CHARLES UNIVERSITY
FACULTY OF MEDICINE IN PILSEN

Microscopic structure of intestinal anastomoses and the use of animal models in experimental intestinal surgery

Ph.D. Thesis

MUDr. Tomáš Kural, MBA

Advisor: Prof. MUDr. Mgr. Zbyněk Tonar, Ph.D.
Consultant: Prof. MUDr. Václav Liška, Ph.D.

Pilsen 2023

Bibliographical information

Author: MUDr. Tomáš Kural, MBA

Title: Microscopic structure of intestinal anastomoses and the use of animal models in experimental intestinal surgery

Language of work: English

Type of thesis: Dissertation for the Ph.D. degree

University: Charles University

Faculty: Faculty of Medicine in Pilsen

Department: Department of Histology and Embryology

Specialty: Anatomy, histology, embryology

Form of study: combined

Advisor: Prof. MUDr. Mgr. Zbyněk Tonar, Ph.D.

Consultant: Prof. MUDr. Václav Liška, Ph.D.

Počet stran:

Keywords: quantitative histology; stereology; intestinal anastomosis; small intestine; large intestine; healing; animal models; pig; human; mouse; rat

Statement

I declare that I have prepared my thesis independently and that I have properly listed and cited all sources and literature used. I also declare that the thesis has not been used to obtain another or the same degree.

I agree to permanently store the electronic version of my thesis in the database of the inter-university project Theses.cz for the purpose of constant checking of the similarity of qualifying theses.

In Pilsen, 29th May 2023

Tomáš Kural

Signature

Abstract

Despite extensive research and the implementation of modern surgical methods, the incidence of anastomotic leaks remains high. The exact pathophysiological mechanisms responsible for these leaks are still unknown, making prevention a challenge. The use of animal models is extensive in the research of intestinal anastomotic leakage. The literature review of this thesis, therefore, presents a brief history of the usage of experimental animals as well as major differences in terms of anatomy and histology between humans and the experimental mammals utilized in intestinal healing studies. The thesis is based on four studies describing the possibilities of using quantitative histological methods in different applications, animal models, and experimental surgical techniques in the research of intestinal anastomotic healing. The conclusions of these four studies can be summarized as follows:

Conclusion 1: TeIGen software is readily accessible to scientists researching fibrous and porous materials using micro-CT analysis. This software aids in producing virtual image sets with defined morphometric attributes, and it can also help with fine-tuning of quantification tools required to examine micro-CT scans. The software also enables the identification of material morphological properties and image characteristics in micro-CT scans that may compromise the results of quantitative analysis. TeIGen software's capacity to generate virtual image sets significantly bolsters the reliability and conclusiveness of measurements, thereby elevating the research's value and reproducibility.

Conclusion 2: Histological research can benefit from the efficient use of scanning conventional slides in digital form combined with unbiased sampling of regions of interest. By adhering to unbiased random sampling principles, researchers follow the "do more less well" rule, leading to more valid, ethical, and efficient results. Digital microscopy has proven particularly useful for proper sampling at the slide level. To attain uniform distribution, one may opt to scan entire slides and carefully select fields of view according to a chosen pattern, or alternatively, use a motorized stage microscope. Such principles are not limited only to quantitative research, but are also crucial in qualitative studies, as they enhance both precision and replicability of the research. Our discoveries indicate that it is imperative for all motorized microscopes and digital histology slide scanners used for scientific purposes to incorporate support for unbiased random sampling.

Conclusion 3: Despite the promising potential of biodegradable nanomaterials, their use in the field of intestinal anastomoses remains largely uncharted. We have found out, that administering of nanomaterials in anastomoses in the small intestine of an animal model did not impede normal healing. A standardized animal follow-up procedure post-surgery was established, completed with a new perianastomotic adhesion scoring system. Furthermore, a robust combination of histological and stereological methods was employed to assess healing. While nanomaterials appear safe, their efficacy in improving anastomosis healing requires further investigation.

Conclusion 4: Through a quantitative histological mapping of various factors, we have discovered the following about porcine small and large intestinal anastomoses: (i) the anastomosis had a higher proliferation index, microvessel density, and collagen volume fraction, but not neutrophil volume fraction; (ii) the healing of porcine small and large intestinal anastomoses was not interchangeable, with the presence of the experimental defect significantly affecting healing despite the healing process being complete at 21 days after the surgery; and (iii) proximity to the anastomosis had a more significant impact on healing in the small intestine than in the large intestine.

To summarize the conclusions of the literature review and presented studies, automated software used in image data analysis must undergo proper calibration. Stereology is a reliable calibration method that can help with validating such data. Our review paper on digital microscopy procedures and multilevel sampling strategies gives practical recommendations and considerations for optimal quantitative histological assessment. Clinical research projects involving surgery of experimental animals are essential to yield reliable results that can be translated into human medicine. The significance of such studies is highlighted in the experimental healing of intestinal anastomoses.

Foreword

The thesis entitled "Microscopic Structure of Intestinal Anastomoses and the Use of Animal Models in Experimental Intestinal Surgery" was prepared at the Department of Histology and Embryology and the Laboratory of Quantitative Histology of the Biomedical Center of the Faculty of Medicine in Pilsen, Charles University, under the supervision of my advisor Prof. MUDr. Mgr. Zbyněk Tonar, Ph.D., surgical issues were consulted with Prof. MUDr. Václav Liška, Ph.D.

The thesis is based on four already published studies in which I participated as follows:

1. Jiřík M., Bartoš M., Tomášek P., Malečková A., **Kural T.**, Horáková J., Lukáš D., Suchý T., Kochová P., Hubálek Kalbáčová M., Králíčková M., Tonar Z. (Microsc Res Tech, 2018): Participation in the literature search of quantitative histology tools and manuscript review.
2. Kolinko Y., Malečková A., Kochová P., Grajciarová M., Blassová T., **Kural T.**, Trailin A., Červenková L., Havránková J., Vištejnová L., Tonarová P., Moulisová V., Jiřík M., Zavaďáková A., Tichánek F., Liška V., Králíčková M., Witter K., Tonar Z. (Anat Histol Embryol, 2022): Participation in the literature search, manuscript revision and preparation of the methodology of one of the systematic sampling examples.
3. Rosendorf J., Horáková J., Klíčová M., Pálek R., Červenková L., **Kural T.,** Hošek P., Kříž T., Tegl V., Moulisová V., Tonar Z., Třeška V., Lukáš D., Liška V. (Sci Rep, 2020): Collaboration on study design, participation in experimental animal operations, literature search, manuscript editing.
4. **Kural T.,** Grajciarová M., Rosendorf J., Pálek R., Červenková L., Malečková A., Šarčevic S., Liška V., Tonar Z. (Ann Anat, 2023): Participation in the study design, experimental animal operations, processing of most photodocumentation, and evaluation of most microphotographs using quantitative histology methods. Interpretation of the statistical evaluation, writing and editing of most of the manuscript.

In Pilsen, 29th May 2023

Acknowledgements

I would like to thank with great humility especially my advisor Prof. MUDr. Mgr. Zbyněk Tonar, Ph.D. and expert consultant Prof. MUDr. Václav Liška, Ph.D. for their guidance of my work, for their boundless patience during consultations and for providing invaluable advice and suggestions, without which the preparation of my first-authored manuscript and this thesis would not have been possible.

Furthermore, I would like to thank Prof. MUDr. Milena Králíčková, Ph.D., MVDr. Martina Grajciarová, Ph.D. and all the colleagues and staff from the Department of Histology and Embryology and the Biomedical Center for their warmth, helpfulness, and utmost collegiality. I am also very grateful for the permission from MUDr. Radovan Hudák to use the images from Memorix Anatomy and Memorix Histology to illustrate my thesis.

I also extend my sincerest appreciation to my wife for her unwavering support and forbearance. It was her understanding and patience that enabled me to accomplish my Ph.D. studies.

Table of Contents

List of Abbreviations

A.D. - Anno Domini

ALP - Alkaline phosphatase

ALT - Alanine aminotransferase

ASA - American Society of Anaesthesiology

AST - Aspartate aminotransferase

ATZ - Anal transitional zone

B.C. - Before Christ

bFGF - Basic fibroblast growth factor

BMI - Body Mass Index

CAL - Colorectal anastomotic leakage

CD - Cluster of differentiation

CRP - C-reactive protein

CT - Computed tomography

EGF - Epithelial growth factor

FGF - Fibroblast growth factor

IBD - Inflammatory bowel disease

IGF - Insulin-like growth factor

IL - Interleukin

MPO - Myeloperoxidase

NSAIDs - Nonsteroidal anti-inflammatory drugs

PAAS - Perianastomotic adhesions amount score

PAI-1 - Plasminogen activator inhibitor-1

PCL - Polycaprolactone

PDGF - Platelet-derived growth factor

PLCL - Polylactic acid-polycaprolactone copolymer

ROI - Region of interest

TGF-β - Transforming growth factor beta

TNF-α - Tumour necrotising factor alpha

tPA - Tissue-type plasminogen activator

VEGF - Vascular endothelial growth factor

vWF - von Willebrand factor

1 Introduction and literature review

1.1 The phenomenon of the anastomotic healing

The most serious complication after an intestinal resection with a consequent reconnection (anastomosis) is an anastomotic leak. Typical clinical symptoms of such complications vary from abdominal discomfort and fever to sepsis. In extreme cases, the anastomotic leak leads to peritonitis, septic shock, or death (Shogan et al., 2015). Especially the prevalence of anastomotic leaks in high-risk regions such as the oesophagus and rectum is considerable (Matthiessen et al., 2007). Colorectal anastomotic leaks occur in about 11% of patients, with higher rates the closer the surgical procedure is to the anus (Shogan et al., 2013). The prevalence rate of an anastomotic leak after surgery in the distal colon can be as high as 30-40%. This leads to the routine of performing a protective colostomy or ileostomy to prevent the spillage of intestinal content in the abdominal cavity in case of an anastomotic leak (Matthiessen et al., 2007). This practice means two possible options – a second high-risk operation to close the protective stoma, with the possibility of developing an anastomotic leak after the second operation, or avoiding the second operation by leaving the stoma as a lifelong solution (Shogan et al., 2015). Anastomotic leaks significantly increase patient's risk of death and result in longer hospital stays. Some of the recent studies have shown that anastomotic leak had a significant effect on local cancer recurrence (Bell et al., 2003). However, the overall prevalence of anastomotic leak fluctuates extensively in the literature. This considerable variation exists partly because of the lack of uniform diagnostic parameters and definition for anastomotic leakage (Shogan et al., 2013).

The healing of intestinal anastomoses involves a temporary decrease in collagen amount and intestinal strength (de Roy van Zuidewijn et al., 1986). Maintaining the collagenous equilibrium is crucial for the anastomosis to remain intact and prevent leakage. If synthesis of collagen is outpaced by collagenolysis, anastomotic leakage comes about (Hesp et al., 1985). Rahbari et al. (2010) defined the anastomotic leakage as a defect in the intestinal wall after the intestinal ends have been reconnected by a suture (hand-sewn or stapled), resulting in communication between the lumen of the intestine and the abdominal cavity. Suture dehiscence, fistulas, and spillage of intestinal contents in the abdominal cavity resulting in peritonitis and possibly sepsis are common outcomes of failed gastrointestinal anastomosis (Kosmidis et al., 2011).

Despite extensive research, anastomotic leaks still appear at a high rate. Many modern surgical methods have been implemented over the years, such as robotics, laparoscopy, and

staplers. However, these techniques have not substantially reduced the frequency of anastomotic leaks. It is still unclear which pathophysiological mechanisms cause anastomotic leaks in the first place, making it difficult to prevent them (Shogan et al., 2013). This is also the reason why the topic of this thesis deals with the phenomenon of intestinal anastomotic healing and the options for further experimental in vivo research in animal models.

1.1.1 Risk factors for colorectal anastomotic leak

There is not a simple pathophysiological explanation of why colorectal anastomotic leakage occurs as there are multiple factors contributing to the development of anastomotic leak. There are numerous studies analyzing the possible risk factors – among others age, gender, height of anastomosis from the anal verge, ASA-Classification, BMI, steroid treatment, preoperative radiotherapy, tumor stage, or immediate perioperative risk factors such as the use of NSAIDs, operative blood loss and transfusion and duration of surgery (Pommergaard et al., 2014). Pommergaard et al. performed a meta-analysis of risk factors for colorectal anastomotic leakage (CAL) with the following results:

1.1.1.1 Age

From 19 observational studies on age as a risk factor for the development of CAL, only two of them found a provable relationship between CAL and age, indicating that age was not a risk factor for CAL. Apparently, biological age matters more than chronological age as there are many elderly patients being entirely healthy. In that sense, the assessment of the possible riskiness of a colorectal operation should not be based only on age (Pommergaard et al., 2014).

1.1.1.2 Gender

From 22 studies dealing with gender as a possible risk factor, only six discovered a relationship between male gender and the development of CAL. The quality of evidence is therefore low. However, it is known that the anatomy of male pelvis is different from female and a narrower pelvis may favour the development of CAL because of the technical complexity of the operation (Pommergaard et al., 2014).

1.1.1.3 Height of the anastomosis from the anal verge

There is quite strong evidence that a low anastomosis presents a serious risk factor for CAL as of 19 studies dealing with the level of anastomosis in colorectal surgery that were included

in the meta-analysis, 13 showed a link between the height of anastomosis and the prevalence of CAL. Low anastomosis was in most of these studies defined as lower than 5 cm from anus. The higher occurrence of anastomotic leak in distal rectum results possibly from complicated anatomical conditions of blood supply in this area (Pommergaard et al., 2014).

1.1.1.4 American Society of Anesthesiology (ASA) classification

Patients undergoing colorectal surgery having various comorbidities, for example pulmonary or cardiovascular disorders, are placed into a higher ASA-category according to ASA. These systemic diseases may have a negative impact on the oxygenation of tissues, thus, impairing the healing tendency. In this sense, it is quite surprising that only two out of 14 studies considering the ASA class as a possible risk factor for CAL showed a statistically significant association. Therefore, there is only very low evidence about the direct correlation between the presence of systemic comorbidities and the risk of developing a CAL (Pommergaard et al., 2014).

1.1.1.5 Body mass index (BMI)

From 13 studies included in the meta-analysis, only one reported BMI outside the normal boundaries (too high or too low) having a negative effect on the outcome of surgery in terms of CAL (Pommergaard et al., 2014). However, the result is quite controversial as the general interpretation of this issue states that obesity and undernutrition of the patients are associated with worse surgical results (Valentijn et al., 2013; Wu et al., 2013). Nevertheless, it remains open to discussion whether the poorer results of colorectal surgery in connection with BMI are not rather related to malnutrition in the sense of vitamin and trace element deficiencies as malnutrition can be found not only in cachectic, but also in obese patients (Kang et al., 2013).

1.1.1.6 Steroid treatment

All three studies included in the overview thematising this topic showed a significant correlation between worse surgical outcomes in terms of CAL and the ongoing treatment with steroids as the anastomotic healing is apparently impaired due to immunosuppression (Pommergaard et al., 2014).

1.1.1.7 Preoperative radiotherapy

Preoperative radiotherapy frequently causes local irritation and scarring resulting in tissue fibrosis. This may negatively influence the risk of CAL. Meta-analysis of two included studies showed that the prevalence of CAL may be related to preoperative radiotherapy (Pommergaard et al., 2014).

1.1.1.8 Tumor stage

There were 15 observational studies describing tumour stage as a risk factor for CAL, only one showed a direct link between CAL and the tumour stage. Therefore, the conclusiveness of the relationship between the poor surgical outcome and a higher tumour stage is questionable (Pommergaard et al., 2014). However, some studies worked rather with the clinical tumour size than with the histopathological staging of the tumour. These studies showed a possible correlation between the higher prevalence of CAL and the tumour size (Eberl et al., 2008; Nisar et al., 2012).

1.1.1.9 Perioperative risk factors

While certain factors such as steroid treatment or preoperative radiotherapy are significant for the surgical outcome, perioperative risks must also be considered. These include the absence of a diverting stoma (Montedori et al., 2010), postoperative use of nonsteroidal anti-inflammatory drugs (NSAIDs) (Klein et al., 2012), blood loss during surgery (Bertelsen et al., 2010), and duration of the procedure (Choi et al., 2006). While these risks are quite well documented, less proven factors such as surgical technique, surgeon experience, and the influence of centralization on the surgical outcome require further exploration. Additionally, patient-related aspects such as socio-economic status, medication, or education must also be considered. The role of minimal-invasive procedures (i.e., robotic and laparoscopic surgery) also remains a topic for future investigation (Pommergaard et al., 2014).

1.1.2 Classification of anastomotic leak in the surgery of rectum

The clinical classification of anastomotic leak can be found in **Table 1.**

Grade of anastomotic leak	Clinical symptoms and possible therapy
Grade A	Asymptomatic, with no elevation of laboratory inflammatory parameters, covered anastomotic leak, only detectable only using radiological methods. There is no need for action either surgically or interventionally.
Grade B	Typically accompanied by abdominal pain, with possible purulent exudation via drains and an increase in laboratory-chemical inflammatory parameters. This condition does not require re-operation and can be well managed using antibiotics, image-guided percutaneous drainage, or a combination of both.
Grade C	This condition results in peritonitis. It is a life-endangering disorder requiring a repeated surgery.

Table 1. Clinical classification of anastomotic leak. After rectum anterior resection, anastomotic leak is divided into three clinical grades according to the classification suggested by the International Rectal Cancer Study Group (Rahbari et al., 2010; Vallance et al., 2017). Anastomotic leak of the grade B and C is related with higher morbidity and mortality, poorer quality of surgical outcomes, need for prolonged inpatient treatment and higher likelihood of the need for a diverting stoma (Ashraf et al., 2013).

1.2 Wound healing in the gastrointestinal tract

The wound healing takes place in three phases with distinctive biochemical processes and occurrence of specific cells at the wound site: (i) inflammation and hemostasis, (ii) proliferative phase and (iii) maturation and remodeling (Brunicardi et al., 2015).

Following an injury, the inflammation begins immediately and extends until 72 hours thereafter. From the third day after the injury, the proliferation commences, and goes on for around fourteen days. Maturation and remodeling of the newly produced tissue begins as early as on the seventh day after the injury and remains active for six to twelve months. The basic healing process is finished by approximately three weeks after the injury when the mucosal repair is finished. However, even after this time an ongoing remodelling and cross-linking of collagen chains at the wound site can still be observed (Brunicardi et al., 2015).

Healing of full thickness injury in the gastrointestinal tract usually begins with surgical reapposition of the intestinal ends. On the serosa, a fibrin seal must form to ensure the early anastomosis integrity. The correct suturing of the ends of the intestinal anastomosis, especially the submucosa, is of great importance, as there is a substantial decline in marginal

strength throughout the first week post-injury due to collagenolysis (Braskén, 1991; Brunicardi et al., 2015).

The cell colonization of the anastomosis follows the pattern at which the different cell populations tolerate hypoxia. Accordingly, the neutrophils are first to enter the anastomosis, after which macrophages arrive. Approximately 48 hours after the injury, fibroblasts invade the anastomotic line in greater number. Because of this effect, a good local blood supply and tissue oxygenation are necessary for normal healing to occur (Kivisaari et al., 1975).

Lactate which is present in significant concentration at the wound site due to the initial hypoxia, appears to have an important role in regulating wound healing. Lactate is a product of aerobic glycolysis typical of fast cell growth and is also a by-product of the oxidative burst of white blood cells (Trabold et al., 2003). Firstly, lactate promotes the secretion of substances through macrophages, thereby stimulating angiogenesis and mitosis (Jensen et al., 1986). Secondly, lactate affects collagen production using a mechanism involving adenosine diphosphate ribosylation. However, the synthesis of collagen occurs only when enough oxygen is present (Hussain et al., 1989).

1.2.1 Hemostasis and inflammation

Vasodilation and edema appear at the anastomotic site after the injury. Immediately after the intestinal trauma, hemostasis takes place. This comes about due to the coagulation cascade activation and aggregation as well as degranulation of thrombocytes. These processes also support the secretion of chemotactic factors into the wound environment. The fibrin clot, a byproduct of hemostasis, also offers a foundation for neutrophils and monocytes to move around the wound (Braskén, 1991).

The first inflammatory cells to be observed at the anastomotic site are neutrophils. These cells are present in the anastomosis as soon as three hours after the injury, and their numbers peak after 12 to 24 hours. Neutrophils serve as the primary agents for phagocytosis of bacteria and tissue debris; however, they do not contribute to the mechanical stability of wounds as they are not involved in collagen synthesis. Conversely, protracted presence of neutrophils can hinder the re-epithelialization of the wounds (Dovi et al., 2003).

Macrophages are crucial for successful healing. Coming from circulating monocytes, macrophages are abundant in the wound by 48 to 96 hours after the injury and remain present until the wound healing is complete. Releasing cytokines and growth factors, macrophages are involved in controlling angiogenesis, collagen production and remodeling, as well as

contributing to the healing process through microbial decontamination and phagocytosis (Clark, 1989; Feiken et al., 1995).

Around the end of the first week after an injury, the amount of T-lymphocytes at the wound site is most abundant, although their numbers are never as high as those of macrophages. T-lymphocytes serve as a bond between the phases of inflammation and proliferation during the wound healing and modulate actively the environment of the wound. A certain balance in the count of CD8+ and CD4+ T-lymphocyte-subgroups is essential so that a physiological wound healing can occur (Barbul et al., 1989; Efron et al., 1990).

Type of cells	Appearance at the anastomotic site after injury	Function	Reference
Neutrophils	First appearance three hours after the injury, peak at 12–24 hours	- phagocytosis of tissue debris and bacteria - cytokine release during the early stages of inflammation, above all TNF-α	(Braskén, 1991; Brunicardi et al., 2015; Dovi et al., 2003; Feiken et al., 1995)
Macrophages	48-96 hours until the completion of wound healing	- enhancement of local angiogenesis and collagen synthesis - wound debridement through phagocytosis - microbial decontamination via synthesis of nitric oxide and oxygen radicals - recruitment and activation of other cells via secretion of growth factors and cytokines, intercellular adhesion, and cell-cell interactions - release of epithelial growth factor (EGF), insulin-like growth factor (IGF), vascular endothelial growth factor (VEGF), transforming growth factor β (TGF-β) and lactate → control of angiogenesis and cell proliferation, matrix synthesis, deposition, and remodelling	(Brunicardi et al., 2015; Clark, 1989; Feiken et al., 1995; Leibovich and Ross, 1975)
T-lymphocytes	Highest numbers approximately seven days after the injury	- bridge between the inflammation and the proliferation - regulation of the wound milieu - downregulation of collagen production through release of IL-1, interferon-γ and TNF-α	(Efron et al., 1990; Rezzonico et al., 1998; Schäffer and Barbul, 1998)
Fibroblasts	24 hours until day 7 after the injury	- activation of fibroblasts through cytokines and growth factors - matrix synthesis and remodelling - production of collagen - matrix contraction	(Braskén, 1991; Brunicardi et al., 2015; Kivisaari et al., 1975)

Table 2. Chronological order of presence of cellular populations during anastomotic healing. There are four basic types of cells present at the anastomotic site during healing – neutrophils, fibroblasts, macrophages, and T-lymphocytes.

1.2.2 Proliferation

The second phase of wound healing begins approximately 72 hours after the injury and lasts until day 14. The tissue continuity is restored during this phase and the fibroblasts are the last cell population to enter the wound. They appear in small numbers as soon as 24 hours after anastomosis, but they do not enter the anastomotic site in greater number until 48 hours after the injury as their ability to tolerate hypoxia is limited. After their proliferation, fibroblasts become activated by cytokines and growth factors and begin to perform the synthesis of extracellular matrix, collagen and remodelling (Brunicardi et al., 2015; Jensen et al., 1986). All the cellular populations found at the anastomotic site are stated in **Table 2.**

1.2.2.1 Extracellular matrix

The extracellular matrix is composed of several substances including fibronectin, proteoglycans and glycosaminoglycans as well as collagen. These substances occur at the site of injury in a specific order. The initial meshwork of fibers is formed by fibronectin and collagen type III. Gradually, proteoglycans and glycosaminoglycans accumulate in the healing wound. Finally, the matrix is completed with collagen type I (Shoulders and Raines, 2009).

1.2.2.1.1 Fibronectin

Fibronectin is an adhesive glycoprotein that binds to cell membrane receptors called integrins. It is important in cell migration, growth, differentiation, and adhesion and plays a key role in embryonic development and wound healing (Pankov and Yamada, 2002). Fibronectin serves during the early healing as scaffolding for the organization of interstitial collagen fibrillogenesis (Clark, 1989). There are two known forms of fibronectin. First, soluble plasma fibronectin is produced by hepatocytes in the liver. Second, insoluble cellular fibronectin in fibrillar form, which is synthesized mainly by fibroblasts, is present abundantly in basement membranes, in the extracellular matrix during the healing process and in the connective tissue (Grinnell et al., 1981; Hsieh and Chen, 1983).

The production and accumulation of fibronectin is the first manifestation of tissue repair. At the colic anastomotic site, the presence of fibronectin is reserved for the submucosa and smooth muscle layers, where it appears in the basal laminas of individual smooth muscle cells (Braskén, 1991). Plasma fibronectin can be detected in the wound hematoma as soon as 1–5 hours after the injury (Grinnell et al., 1981). Correspondingly, plasma fibronectin enters

the wound over the subsequent 48 hours after the injury and binds to exposed elements of connective tissue and cell membranes such as proteoglycans and collagen (Gauperaa and Seljelid, 1986). The occurrence of non-soluble fibronectin in the granulation tissue is associated with the presence of fibroblasts entering the wound site and the highest concentration of fibronectin can be observed on the fifth day after the surgery with a slight decline in fibronectin amount within the next two weeks (Braskén, 1991; Kurkinen et al., 1980). During the maturation of granulation tissue, the amount of fibronectin in the scar declines gradually (Kurkinen et al., 1980).

1.2.2.1.2 Collagen synthesis

Collagen accounts for about one third of total body proteins (Shoulders and Raines, 2009) and is crucial for the successful completion of wound healing. Its synthesis as well as lysis are controlled by growth factors and cytokines (Jensen et al., 1986). Fibril formation and cross-linking of collagen fibrils contribute to collagen insolubility, increased mechanical strength and resistance to enzymatic degradation. Collagen synthesis in the gastrointestinal tract is performed by smooth muscle cells and fibroblasts. There are several systemic factors that strongly contribute to collagen synthesis. The abundance of nutrients (amino acids, carbohydrates and cofactors as vitamins and trace elements), minimal bacterial contamination and sufficient oxygen supply enhance collagen synthesis and deposition (Brunicardi et al., 2015). Immediately after the gastrointestinal injury the collagen as well as laminin concentrations in the intestinal wall drop. This is due to the postoperative edema of the intestinal wall and to the collagenolysis taking place during the first 48 to 72 hours of healing. This emphasizes the importance of good suturing technique to avoid early complications resulting from an anastomotic leak before the synthesis of new collagen occurs (Braskén, 1991). The collagen concentration at the colic anastomotic site falls by 20% to 40% after the injury. When an inverting continuous suture is used, the decrease of collagen concentration is even greater (Cronin et al., 1968; Irvin and Hunt, 1974; Jiborn et al., 1978).

Accumulation of collagen at the wound site begins from the third postoperative day and maximal staining intensities of collagen can be observed on day 7 with only a slight decrease in collagen concentration during the subsequent two weeks. Several months following the injury, mechanical strength of collagen continues to increase even though the amount of collagen maintains plateau levels (Levenson et al., 1965). Scar remodelling continues for 6 to 12 months after the injury, resulting in an acellular and avascular scar.

However, the mechanical properties of the scar never achieve those of the uninjured tissue (Brunicardi et al., 2015). The function, appearance, and the location of synthesis of different proteins during anastomotic healing can be found in **Table 3**.

	Location of accumulation during repair	**Function**	**Time course**	**Reference**
Fibrillar collagens				
Collagen type I and III	- serosal surface, submucosa, repair tissue in the anastomotic line	**Type I collagen:** withstandness against force tension and stretch, enhancement of tensile strength **Type III collagen:** forms a loose supportive scaffolding made up of thin fibers, present in different organs and blood vessels	- day 1 after the injury in the serosa and submucosa - day 2 after the injury in the repair tissue of the anastomotic line - accumulation of fibrillar collagens in greater amount from day 3 onwards - production of collagen III begins earlier than that of type I collagen - strongest synthesis of collagen during the first week after the surgery	(Bailey et al., 1975; Braskén, 1991; Brunicardi et al., 2015; Shoulders and Raines, 2009; Stumpf et al., 2002)
Collagen type V	- distributed uniformly throughout connective tissue - can be found in the epimysium and perimysium of smooth muscle	Type I collagen fibrils have type V collagen at their surface in order to alter its biomechanical properties	- staining intensities are reduced for the period of the first two postoperative days - appears in the anastomotic line on the second day after the injury - maximal staining intensity on day 7 after the surgery	(Birk et al., 1988; Braskén, 1991; Fessler JH, Fessler LI, Mayne R, Burgeon RE, 1987)
Components of basal laminae				
Collagen type IV, Laminin	Basal laminae or its proximity	**Collagen type IV:** main non-fibrillar collagen in the basal laminae of epithelia **Laminin:** main structural glycoprotein of basal laminae, promotion of cell migration and differentiation, cell growth and adhesion	- maximal staining intensity on day 7 after the surgery - correlation of staining intensity with the neoangiogenesis and reepithelization from day 3 onwards	(Braskén, 1991; Brunicardi et al., 2015; Kleinman and Weeks, 1989; Schittny and Yurchenco, 1989)

Table 3. Types of collagen and its synthesis during the anastomotic healing.

1.2.2.1.2.1 Fibrillar collagens

Type I and type III collagen are the essential collagen types for wound healing, although it has been proven there are around 28 different varieties of collagen (Shoulders and Raines, 2009). Type I collagen is the main constituent of the extracellular matrix. Type III collagen becomes

more accentuated and significant during the healing process. The proportion of type I to type III collagen varies not only during the matrix synthesis (Bailey et al., 1975), but the amount of both types of collagen also fluctuates in different tissues (Bornstein and Sage, 1980). Type V collagen forms thin fibrils (Fessler et al., 1987) and is present in the same tissues as fibrillar collagens type I and III (Bornstein and Sage, 1980; Krieg et al., 1988).

1.1.2.1.2.2 Components of basal laminae

Laminin is the main structural glycoprotein of basal laminae. Laminin promotes the cell migration and differentiation, the cell growth and adhesion. These features are due to several biologically active sites of the laminin molecule, where different cell receptors connect (Durbeej, 2010). Laminin becomes particularly abundant in the basal laminae as the re-epithelialization and formation of new blood vessels occurs during the healing process (Clark, 1989). The time course of appearance and synthesis of laminin in the basal laminae throughout the healing process are highly similar to those of collagen type IV. Collagen type IV is the most abundant mammalian non-fibrillar collagen (Martin et al., 1985) present in the basal laminae of epithelia. Its abundance correlates strongly with the neoangiogenesis and mucosal re-epithelization from the third day after the injury (Braskén, 1991).

1.2.2.3 Glycosaminoglycans and proteoglycans

Glycosaminoglycans are an inhomogeneous group of long unbranched polysaccharides consisting of recurrent disaccharide units with widely variable molecular weight and state of sulfation. These polysaccharides form a large part of the granulation tissue (Brunicardi et al., 2015). Chondroitin and dermatan sulphate are the most abundant wound glycosaminoglycans. Interactions of dermatan sulphate with fibroblast growth factors FGF-2 and FGF-7 participate in wound repair and cellular proliferation (Trowbridge and Gallo, 2002). Glycosaminoglycans are synthesized by fibroblasts, mesothelial cells and certain types of stem cells (Laurent et al., 1996). During wound healing, the amount of glycosaminoglycans increases significantly in the first three weeks. After this time, a gradual decline in the amount of glycosaminoglycans can be observed due to scar maturation. It has been suggested that glycosaminoglycans, like fibronectin, form a primary scaffolding for the assembly of collagen fibrils and during this process the level of glycosaminoglycan sulfation is decisive for the final shape of the collagen fibrils (Akgül and Mahendroo, 2014).

1.2.3 Angiogenesis

Cell disruption caused by injury brings about the release of proteolytic enzymes thus degrading proteins and fibronectin. Degradation products are chemotactic for macrophages and endothelial cells. Macrophages then release angiogenic factors, such as FGF. Disruption of mast cells leads to discharge of heparin, which is another chemotactic factor for endothelial cells (Brunicardi et al., 2015).

Fibroblast growth factor and disrupted cells of the injured tissue stimulate endothelial cells to release procollagenase and plasminogen activator. Plasminogen activator initiates the transformation of procollagenase to collagenase and activation of plasminogen to plasmin. This leads to disruption of the basement membrane, a process necessary for the invasion of endothelial cells. There are many additional factors having angiogenic activity such as VEGF, TGF-α, TGF-β and EGF (Brunicardi et al., 2015; Clark, 1989).

Endothelial cells from venules near the injury begin to migrate through the disrupted basement membranes forming capillary buds and producing provisional matrix; this occurs simultaneously with fibroblast ingrowth. Endothelial cells remaining in the original vessel proliferate and subsequently migrate to join the new population in the perivascular space. Finally, capillary sprouts branch to form capillary loops and later on a capillary plexus, enabling normal blood circulation in the injured tissue. Migration of endothelial cells goes hand in hand with ongoing collagen and proteoglycan synthesis. Synthesis of normal extracellular matrix is essential for normal angiogenesis (Clark, 1989). Hypoxia provokes the production of VEGF and supports increased collagen gene expression. In healing wounds, VEGF is primarily produced by macrophages, and the membrane of endothelial cells is where VEGF receptors are found (Ferrara and Davis-Smyth, 1997; Xiong et al., 1998). A study on colic and ileal anastomoses revealed similar levels of angiogenesis between the two types of healing anastomoses, according to angiographic findings (Hesp et al., 1985).

1.2.4 Smooth muscle and wound contraction

Myofibroblasts are cells with smooth-muscle cell-like features (Powell et al., 1999) differentiating from mesenchymal cells (Thornton and Barbul, 1997) and playing a crucial role in wound healing and especially in the wound contraction during the proliferation phase. The contractile capability is due to the presence of stress fibres, mainly alpha smooth-muscle actin in the cytoskeleton. Another necessary component in the cytoskeleton for the wound

contraction is the non-muscle myosin (Chitturi et al., 2015). The transfer of intracellular contractile force to the outside of the cell occurs due to fibronexi. These are transmembrane devices connecting the extracellular matrix with cytoplasmic contractile filaments (Eyden, 2007). Smooth muscle tissue is re-established through the differentiation from undifferentiated mesenchymal cells present in the healing intestinal muscle layer from day 3 to 5 after the injury. These cells differentiate not only into smooth muscle cells but also into phagocyting histiocytes, as indicated by certain studies (Thornton and Barbul, 1997). According to other studies alpha smooth muscle actin cannot be detected until day 6 after the injury and its expression rises further until the end of week 3 after the injury (Darby et al., 1990). Approximately after four weeks, its expression decreases and myofibroblasts undergo apoptosis as an expression of wound maturation and remodelling (Desmoulière et al., 2005). Another study describes the staining intensity of myofibroblasts as most stressed from day 3 to day 7 after the surgery. Upon reaching the seventh day, the alpha smooth muscle actin content present in the myofibroblasts equals that found in the muscular layers of a healthy intestinal wall. This discovery suggests a potential explanation for the decreased likelihood of anastomotic leakage following the seventh day after surgery (Kosmidis et al., 2011). Another study describes the alpha smooth muscle actin undetectable at the wound site until day 6, then increasingly expressed for the next fifteen days of wound healing (Darby et al., 1990).

In addition to wound contraction, myofibroblasts play a crucial part in the repair and synthesis of extracellular proteins, particularly collagen. The synthesis of collagen in healing wounds takes place not only by myofibroblasts but also smooth muscle cells (Nakamura et al., 2016). In healing areas, the expression of alpha smooth muscle actin may be observed not only in myofibroblasts but also in smooth muscle fibres of the muscularis mucosa and muscular layer as well as smooth muscle of vascular walls (Kosmidis et al., 2011). Studies have shown that smooth muscle cells are capable of producing the three distinct types of collagens described in the submucosa. As a result of this discovery, there is a theory that suggests that the matrix of submucosa situated between the muscularis mucosae and the muscular layer originates and is maintained by these two layers of smooth muscle tissue. It has been observed that smooth muscle cells produce a greater amount of collagen type III than collagen type I, in comparison to fibroblasts. This observation serves as evidence supporting the conclusion stated above. One study discovered a 2:1 ratio of collagen type III to collagen type I, which mirrors the proportion described in the media of larger blood vessels. Smooth

muscle cells contain more of collagen type III than type I collagen (Bornstein and Sage, 1980).

1.2.4 Mucosal repair

There are three stages of early epithelial recovery occurring before the epithelial proliferation: (a) villus contraction, (b) epithelial migration and (c) tight junction closure. These steps are to ensure the prompt re-establishment of epithelial continuity and mucosal barrier function. Only then does the mucosal repair occur through re-epithelialization (Blikslager et al., 1997).

First, immediately after injury, individual villi contract, thus reducing the uncovered surface of the basement membrane (Moore et al., 1989). This process is enabled due to three factors: enteric nerves mediating the instantaneous villous contraction, the presence of contractile myofibroblasts and a network of smooth muscle cells in the lamina propria (Joyce et al., 1987; Moore et al., 1989). The ongoing contraction at the site of mucosal injury is mediated by secretion of prostaglandins in the affected tissue (Gookin et al., 2002; Moore et al., 1989).

Following the initial phase of mucosal repair, the migration of enterocytes is the next important phase. These cells temporarily loose their typical characteristics through dedifferentiation and flattening. This is followed by the occurrence of "epithelial crawling" in the direction of the exposed basement membrane (Dignass et al., 1994).

The final stage in the early mucosal repair is the reinstallment of tight junctions among the enterocytes. After epithelial cells have re-established contact with each other, and the uncovered basement membrane is concealed, tight junctions can reform. Subsequently, the mucosal barrier function is restored (Blikslager et al., 1997).

The process of mucosal repair is initiated by the contact of enterocytes with laminin and fibronectin present in the extracellular matrix, along with the stimulation from various growth factors and cytokines such as EGF, PDGF, IGF-1, TGF-β or bFGF, which are produced by monocytes (Brunicardi et al., 2015).

Research has demonstrated that there exists a noteworthy contrast between the rate of repair of ileal and colic mucosa. In rabbits, the mucosal repair of the ileum is finished within a week following surgery. However, in the colon, mucosal repair occurs slower, and tissue necrosis is still evident at the seven-day mark after the procedure (Hesp et al., 1985). No mention of duodenal or jejunal mucosa healing were found in the literature – Medline and Google Search on 18th May 2023 using key words: healing, mucosa, jejunum, duodenum.

1.2.6 Serosal repair

Serosa is the peritoneal extension on the surface of the gastrointestinal tract (Brunicardi et al., 2015) and consists of a thin layer of connective tissue and a simple flat cell layer (mesothelium) covering the muscular layer (Thornton and Barbul, 1997). While the gastrointestinal healing process is relatively uniform, only two layers of the gastrointestinal wall, namely the serosa and mucosa, allow for healing without scar tissue formation (Brunicardi et al., 2015). Studies have shown a higher incidence of anastomotic failure in extraperitoneal parts of the gastrointestinal tract, such as the distal third of rectum, duodenum, or esophagus, emphasizing the key role of the serosa in gastrointestinal healing (Brunicardi et al., 2015; Thornton and Barbul, 1997). Good surgical technique during suturing is essential for maintaining the robustness of anastomosis, above all in the early phases of intestinal healing. Proper serosal apposition is another critical aspect for the formation of a fibrin seal on the serosa, reducing the anastomotic leakage rate. The inverting suture technique is the best way to achieve this (Kosmidis et al., 2011; Thornton and Barbul, 1997).

1.2.7 Submucosal repair

Submucosa is a relatively narrow structure lying between the mucosa and muscular layer of the intestinal wall and consisting of loose connective tissue with infrequent fibroblast-like cells (Brunicardi et al., 2015).

The submucosa has a rich vascular plexus which is disturbed when the intestine is divided, and the blood vessels become dilated by vasoactive substances. Due to this, vascular stasis and subsequently submucosal edema develops. The postoperative edema of the intestinal wall is most accentuated in the submucosa and almost completely disappears within the first week after the surgery. The onset of angiogenesis can be detected as early as on the third day after the injury (Braskén, 1991). Healing of the submucosa begins on the first postoperative day with a strong influx of neutrophils (Brunicardi et al., 2015; Clark, 1989).

The events in order to enable the synthesis of collagen occur immediately after surgery in the submucosa and serosa. The expression of collagen genes can be detected as soon as on day 2 after the surgery. At the same time, we can see the decline in concentration of pre-existing collagen and laminin in the edemic tissue (Braskén, 1991; Cronin et al., 1968; Irvin and Hunt, 1974; Jiborn et al., 1978). This change is most marked in the submucosa where the

formerly dense mesh of collagen fibres loses postoperatively most of its immunoreactivity (Braskén, 1991).

After the synthesis of collagen begins, type I and III fibrillar collagen can be found in three main areas of the intestinal wall – submucosa, anastomotic line and serosa (Brunicardi et al., 2015).

There is a very effective glycolytic metabolism in the healthy intestinal wall. After intestinal trauma, a long-lasting decline in the efficiency of all metabolic processes can be observed, especially in the anastomotic area. These changes are particularly expressed in the mucosa and muscular layer. On the other hand, the submucosal metabolism remains almost intact after the surgery. The metabolic disturbance last as long as three weeks after the surgery (Braskén, 1991).

Similar time course applies to the submucosal inflammation in the anastomotic area – even though the submucosal inflammation with edema of the intestinal wall disappears within three weeks after the surgery, the number of fibroblasts and blood vessels remains greater than in healthy colon (Braskén, 1991).

1.3 Maturation and Remodelling

Maturation and remodelling of extracellular matrix begin during the fibroplastic phase from day 14 onwards (Brunicardi et al., 2015). This process is dynamic and defined by a constant re-organization of previously formed collagen fibres gaining mechanical strength due to stable cross-links between individual collagen chains (Aznan et al., 2016). After a number of weeks since the injury, the quantity of wound collagen remains steady, while the mechanical resistance of the scar increases as collagen fibers continue to cross-link (Levenson et al., 1965). Scar remodelling goes on for the next 6–12 months after injury. Newly built tissue becomes gradually less cellular and an avascular scar made up of collagenous fibres remains (Brunicardi et al., 2015).

The deposition of substances at the wound site proceeds in the same rigid manner: fibronectin and collagen type III together with proteoglycans represent the early matrix and collagen type I embodies the final fibrous tissue of the scar. There are several major substances playing key roles in the remodelling of extracellular matrix such as metalloproteinases, hyaluronidase and the plasminogen activator-plasmin system (Clark, 1989).

It is known that for physiological healing to occur, a strict balance of ongoing collagen synthesis and collagenolysis must be maintained during the healing process. In a recent study performed in rats, it has been shown that commensal intestinal microbes, such as *Enterococcus faecalis*, with the ability to produce collagenases and activate host metalloproteinases following intestinal resection, may lead to an imbalance in these processes and contribute to the pathogenesis of an anastomotic leak (Shogan et al., 2015).

1.4 Adhesions

Among the unresolved challenges of modern medicine, peritoneal adhesions stand out as a frequently occurring complication in abdominal surgeries. The development of peritoneal adhesions is linked to higher rates of both morbidity and mortality, resulting in poorer quality of life of affected patients, prolonged hospitalization time and a significant financial strain of healthcare systems across the globe (Ellis et al., 1999; Husarić et al., 2016). The widespread of adhesions is highly individual depending on the type of surgery and postoperative complications (Monk et al., 1994). The most common postoperative complication caused by peritoneal adhesions is small bowel obstruction (in more than 75% of cases) (Carmichael and Mills, 2006; Lee et al., 2014; Miller et al., 2000; Oyasiji and Helton, 2011; Richards and Williams, 1988).

Peritoneal adhesions are bands of fibrous tissue developing between organs normally lying separately in the peritoneal cavity and/or between abdominal organs and the parietal peritoneum (Brunicardi et al., 2015). The peritoneal adhesions result from previous peritoneal injury or irritation following surgery and exposure to infection, ischemia or foreign materials (Husarić et al., 2016).

The injury of the serosal surface leads to the damage of mesothelial lining and the underlying connective tissue and causes the activation of physiological inflammatory response, i.e. hyperemia, development of tissue edema, invasion of the site of injury by monocytes and platelets leading to activation of complement and coagulation cascades and increased secretion of inflammatory cytokines (Brunicardi et al., 2015).

The cornerstone in the development of peritoneal adhesions is the change in the balance of the fibrinogenesis and fibrinolysis to the side of fibrinogenesis (Zühlke et al., 1990). Fibrin deposition occurs between the opposed damaged peritoneal surfaces. The primary temporary adhesions can be easily dismantled by proteases of the fibrinolytic system resulting in the restoration of normal serosal surface (Brunicardi et al., 2015). Permanent

adhesions result from insufficient fibrinolytic activity, fibroblasts entering the primary fibrin scaffolding and collagen deposition during the first week after the injury (Zühlke et al., 1990). The development of imbalance of the fibrinogenesis and fibrinolysis is due to the reduced fibrinolytic activity because of lower levels of tissue-type plasminogen activator (tPA) in the peritoneal fluid after the surgery and later also due to increased availability of plasminogen activator inhibitor-1 (PAI-1) induced by various cytokines including IL-1, IL-6 or TNF-α (Cheong et al., 2002).

Two major strategies to prevent the formation of adhesions are minimization of peritoneal trauma by careful manipulation with tissues, avoiding tissue desiccation and spare use of retractors and cautery. Many studies have also shown that fewer adhesions form following laparoscopic surgical approach in comparison with open surgery. The second advance in adhesion prevention is the introduction of a number of barrier gels and membranes in order to create a barrier between damaged peritoneal surfaces. However, there is a contraindication of use of these substances in the proximity of intestinal anastomoses due to an elevated risk of anastomotic leak (Zeng et al., 2007).

1.5 Experimental animals

The use of experimental animals is an essential element in the development of biomedical sciences. Experimental animals are animals intended for experiments and may be used provided that no alternative method to determine the required hypotheses exists and the use is not illegal (Franco, 2013). An experiment is any use of an animal, invasive or non-invasive, for scientific or educational purposes (Smith et al., 2018). Natural animal biorhythms are disturbed by human interaction with the animal, which may affect the results of the experiment, particularly if done in wild nature (Bittman et al., 2013; Emmer et al., 2018). Currently, laboratory animals are considerably standardized in terms of genetics and health condition (Kafkafi et al., 2018).

1.5.1 History

Experimental animals have been used for scientific purposes since ancient times. As early as in ancient Egypt, the postulate was formulated that human and animals' function on a similar principle. In Mesopotamia it was found that some diseases were transmitted from animals to human or vice versa. The use of experimental animals was widespread particularly in ancient

Greece. Hippocrates performed anatomical necropsies of animals around 400 B.C. and some of his postulates have remained valid until today – for example, the description of true and false ribs (Craik and Hippocrates, 1998). Aristotle was another important anatomist who compared the anatomy of human and animal organs in his work (Crivellato and Ribatti, 2007). Finally, the anatomical and physiological work of Galen of the 2nd century A.D. should be mentioned, based predominantly on animal necropsies and describing the motor apparatus, the nervous system and the brain (Standring, 2016).

The fall of the ancient empires was associated with a considerable decline of all scientific disciplines and human autopsies were prohibited by the Catholic Church. Therefore, the scientific knowledge of ancient anatomists, especially Aristotle and Hippocrates, was used for the study of medicine until the 14th century.

In the Middle Ages, Persian and Arab physicians used the theories of physicians from ancient Greece in their work and made many medical discoveries. They wrote many writings and books on pharmacology, diseases, and their treatment. These books also included a lot of information about other natural sciences - alchemy, astrology, and mathematics. Important representatives of Persian and Arab medieval medicine were al-Razi, Ibn Sina (Avicenna) and ibn-al Nafis.

Al-Razi was a native of Persia and his works dealt with alchemy, medicine, and philosophy. He lived from 865 to 925 A.D. He was the first physician to describe the differences between measles and smallpox and was also involved in experimental medicine. He is known as the father of pediatrics, and his book "Childhood Diseases" is the first in which pediatrics was set aside as a separate discipline. In other texts he also dealt with ophthalmology, allergies, and immunology. He was the first author to describe fever as a defense mechanism of the immune system in inflammation.

Coming from Persia, Ibn Sina, also known as Avicenna, authored numerous works on various subjects, of which nearly forty were related to medicine. His noteworthy contributions in medicine include the Book of Healing and the Canon of Medicine. The Canon of Medicine holds great significance in the history of medicine as it laid down fundamental principles of the field that were widely adopted in both the Middle East and Europe. Knowledge from Ibn Sina’s works was used in the teaching of medicine by European universities until the 16th century. Ibn Sina was also one of the first physicians to deal with psychology and mental illness.

Ibn al-Nafis was an Arab physician from Damascus, Syria, who lived in the 13th century. He is believed to have made his discoveries based on animal experiments and is credited with the first description of blood circulation in the lungs (Edriss et al., 2017).

The social situation in Europe became less severe in the period of Renaissance, and especially thanks to human autopsies performed by Vesalius in the 16th century, the human skeleton was described for the first time and more than 200 dogmas formulated by Galen were disproven. Vesalius gathered his knowledge in seven books called *De humani corporis fabrica libri septem,* which were used for the teaching of medicine for subsequent 200 years. Thanks to the legacy of Vesalius, the study of human anatomy has become the foundation of the study of medicine and the use of animal models was shifted rather towards physiological experiments (Hildebrand, 1996).

Physiology and anatomy were completely separated in the 18th century under the influence of Albrecht von Haller's work. His work was the first to describe the respiratory mechanics and muscular irritability. Experiments were done using the trial and error method (Frixione, 2006). First experiments characterized by a logical procedure can be encountered in the scientific work of Antoine-Laurent de Lavoisier. Oxygen consumption by animals during respiration was his greatest discovery (Karamanou et al., 2013).

In the 19th century, Claude Bernard described essential principles of food digestion based on animal experiments. This is also the time when domesticated animals started being more widely used for scientific experiments, particularly dogs, pigs and rodents. Standardization of experimental conditions could also be seen thanks to Bernard's publication *Introduction à l'étude de la médecine expérimentale* of 1865, which became a cornerstone of modern scientific experiments (Young, 1957; Zanchetti, 2005).

At the end of the 19th and in the course of the 20th century, experimental and, by extension, also human medicine has seen a huge boom. Many important discoveries were made – for example, description of hormonal regulation, transplant experiments or the gene knockout method, i.e., specific knocking out of a certain gene in mice aimed at simulating a disease. Furthermore, the use of experimental animals for the study of certain diseases became standardized worldwide, and the development of anesthesia made it possible to observe physiology and pathophysiology in living animals.

Currently, experiments are an integral part of scientific work and efforts are focused rather on limiting the use of experimental animals and replacing them with non-animal models (Doke and Dhawale, 2015).

1.5.3 Recent experimental work

In terms of use of the results, research can be classified as basic, applied and translational (Critchfield, 2011). While to a certain extent, basic research is done according to the researcher's preferences and has no immediate application in practice, applied research seeks practical use for knowledge learned precisely through basic research. The purpose of translational research is to utilize research results across various fields (Critchfield, 2011; Lerman, 2003, Fang and Casadevall, 2010).

Research can also be classified as clinical and preclinical. Experimental confirmation of a hypothesis is the tool of preclinical research, although experiments in humans are excluded. Clinical research allows also experiments in humans and has four phases. In the first phase, an experiment is done in a small number of healthy individuals to verify tolerance of a pharmaceutical or medicinal product and its side effects. At the same time, the dosing form and the highest tolerable dose are determined in this phase. In the second phase, therapeutic effects of the study drug are verified. These tests are done in a group of 25 to 100 individuals who have the disease that is to be treated with the given drug. The third phase serves to compare the study drug with known methods or placebo. Placebo may be used only if no harm is caused to the patient by not administering an active substance. Subsequently, the results obtained from the experimental and control groups are compared; adverse effects and contraindications are explored in this phase, as well. In the final phase, the medicinal or pharmaceutical product is used in the new indication but data on adverse effects still continues to be collected, as well as data on interactions with other medicines or on teratogenicity (Lüllmann et al., 2018).

1.5.4 Biomodels

Biomodels are living organisms with a physiological or pathological process analogical to an identical phenomenon in another species, most commonly in human (Dietrich et al., 2020; Wangler et al., 2017). Currently, numerous mutant strains exist, which are used as biomodels of human diseases such as arterial hypertension (Lerman, 2003), obesity (Martins et al., 2022), diabetes (King, 2012), etc. Biomodels are helpful in the study of etiology, pathogenesis and the possibilities of therapy of serious diseases in human and in animals (Vandamme, 2014).

Experiments done in biomodels can also be described as experiments *in vivo*. Given an effort to replace animal models with their alternatives, *in vitro* models are also used in research now. Experiments done *in vitro*, i.e. "in glass", are performed using cell or tissue cultures (Russell and Burch, 1959). Experiments done in an isolated perfused organ can be positioned somewhere between experiments *in vitro* and *in vivo* (Stevens et al., 2020). Another possibility to reduce the number of used experimental animals is offered by mathematical models (Puopolo, 2004). In mathematical models, experiments are done using computer experiments and are called models *in silico* given the presence of silicon in computer processors (Madden et al., 2020). In order to obtain good-quality outputs from mathematical models, one needs to know the exact relationships among input variables in the studied system (McNamara et al., 2016).

1.5.5 The 3R rule

3R denotes Replacement, Reduction and Refinement. Together, these principles represent an effort to replace experimental animals with lower animal species or with an alternative approach, resulting in reduced numbers of used experimental animals and in a refined approach to the same (Maestri, 2021). This principle was presented for the first time in 1959 by Russell and Burch (Russell and Burch, 1959).

"Replacement" means that an experimental animal is replaced with a lower animal species; for example, vertebrates are replaced with invertebrates, with a perfused organ, cell structure or a model *in silico* (Kiani et al., 2022; Yadav and Singh, 2021).

"Reduction" is an effort to reduce the number of experimental animals (Russell and Burch, 1959). This involves sufficient literature search before the experiment, and planning of the study with the minimum number of experimental animals that excludes the statistical type 1 error (Fitts, 2011). Such measures also include an effort to use appropriate statistical methods (Festing and Altman, 2002). Important aspects include, among others, homogeneity of the animal group in terms of sex, age, weight, health condition. (Johnson and Besselsen, 2002). A maximum amount of new information should also be derived from the experimental animal group (Seo et al., 2018). Thanks to advanced imaging methods, the number of experimental animals could be reduced substantially, while at the same time increasing the amount of newly learned information (Heindl et al., 2008).

"Refinement" can be understood as an overall refinement of how the experimental animal is approached (Russell and Burch, 1959). Such measures include minimised duration

of the experiment, sufficient analgesia or minimised social and physical deprivation of the animal (Carbone, 2011).

Currently, about 190 million laboratory animals are used for scientific purposes annually worldwide, and about 40 millions in Europe (Taylor and Alvarez, 2019). Commonly used laboratory animal species include *Drosophila melanogaster*, *Caenorhabditis elegans* or *Danio rerio*. Among vertebrates, the most common animals include the laboratory mouse, laboratory rat, Guinea pig, golden hamster, domestic rabbit, domestic dog, domestic cat, common quail and primates (Hickman et al., 2017; Rosenthal and Brown, 2007). Among vertebrates, rodents are the most commonly used laboratory animals, representing more than 90% (Hickman et al., 2017).

1.5.6 Most used experimental animals, their advantages and disadvantages

The laboratory mouse is the most common experimental species. Currently, more than 450 inbred and knockout strains exist (Sartori et al., 2011), which have been used in pharmacology (Zuberi and Lutz, 2016), to study mammal genetics (Yuan et al., 2011), in virology (Baxter and Griffin, 2016) or oncology (Cekanova and Rathore, 2014). Advantages of the mouse include its short generation time and simple breeding at low costs (Rosenthal and Brown, 2007). Its disadvantages include the small size and the necessity of microsurgical approach in experimental surgery (Wenzel et al., 2021).

The laboratory rat is another widespread species. The most common strains include Wistar and Sprague-Dawley (Johnson, 2022). More than 200 inbred strains are currently used for research purposes (Benavides et al., 2020). Laboratory rats are the most widely used laboratory animals for training purposes thanks their convenient size, simple breeding and intelligence (O'Malley et al., 2022). Similarly, as in other rodents, their short life is a disadvantage, making it impossible to undertake long-term experiments (Aitman et al., 2008).

Laboratory Guinea pigs are used for the study of serology (Winsnes et al., 2009), allergology and immunology (Shomer et al., 2015). Their physiological characteristics predestine them for certain experiments. Sensitivity to *Mycobacterium tuberculosis* is one of these characteristics, making Guinea pigs suitable for microbiological research. Also, Guinea pigs exhibit a number of anatomical and physiological properties similar to human (Shomer et al., 2015), including inner ear structure (Albuquerque et al., 2009), inability to synthesize vitamin C (Čapo et al., 2015) or immune system (Shomer et al., 2015). The limited number of strains is their disadvantage, preventing the conduct of comparative studies.

Laboratory rabbit is also used in experiments thanks to its suitable size and considerable fertility (Mapara et al., 2012). Rabbit has been used predominantly in diabetology (Wang et al., 2010), in pyrogen testing (Ronneberger, 1977) or in serology (Weber et al., 2017).

Domestic pig is a very common animal in experimental surgery (Kobayashi et al., 2012). Minipigs with the weight of 30 kg in adult age are bred for experimental purposes as this weight facilitates their handling (Nunoya et al., 2007). Given that their physiology and anatomy are very similar to those of human (Meurens et al., 2012) and that pig skin is also similar to human skin (Krumpholz et al., 2022), domestic pig finds a broad scale of use in embryology (Kobayashi et al., 2012), teratology (Nunoya et al., 2007), study of ontogenesis (Krause et al., 2021) or in immunology (Pabst, 2020). Novel surgical procedures are also first tried in pig models (Walters and Prather, 2013). The use of domestic pig for experimental purposes is quite expensive, but not as costly as other large animal models (Raval et al., 2022).

Cats, dogs and monkeys were much more commonly used laboratory animals in the past (Research, 1988). Currently, ethical aspects are much more emphasized also in research, and therefore their use in experimental work has been rather declining (Goñi-Balentziaga et al., 2022).

1.6 Interspecies differences in the development, anatomical structure and microstructure of the intestine in human and most used laboratory mammals

1.6.1 Human GIT development

The development of the human gastrointestinal tract begins in the third week of embryonic development with the process of gastrulation (Bhatia et al., 2022). During gastrulation, the formation of three germ sheets occurs – ectoderm, entoderm and mesoderm (Muhr and Ackerman, 2022). The epithelium of the gastrointestinal tract is of entodermal origin, except for the mouth, pharynx and anus (Bhatia et al., 2022). In addition to the GIT, the respiratory system, liver, biliary tract and pancreas are of entodermal origin (Gilbert, 2000). The entoderm is initially directed towards the yolk sac (Muhr and Ackerman, 2022). The mesoderm separates the ectoderm and entoderm from each other everywhere except the oropharyngeal and cloacal membranes (Gilbert, 2000).

By the rotation of the primitive gut, its basic parts form – the pharynx, foregut, midgut and hindgut. The pharynx extends from the oropharyngeal membrane to the laryngotracheal groove. The foregut, with arterial supply via the celiac trunk, arises from the laryngotracheal groove to the hepatic diverticulum. The midgut, supplied by the superior mesenteric artery, extends from the hepatic diverticulum to 2/3 of the transverse colon, and the hindgut, with vascular supply originating from the inferior mesenteric artery, represents the aboral part of the intestine, from the 2/3 of the transverse colon to the cloacal membrane (Sadler, 2018).

As the gastrointestinal tract develops, the stomach turns 90° clockwise around its long axis and the liver heads to the right side. As a result of the rotation of the stomach and the growth of the head of the pancreas, the duodenum turns convexly to the right. By shortening of mesenterium, the duodenum becomes a secondary retroperitoneal organ (Gangane and Borate, 2018).

The midgut is suspended from the dorsal mesogastrium and communicates with the yolk sac via the omphaloenteric (vitelline) duct (Kostouros et al., 2020). The longitudinal axis of the primary intestinal loop is represented by the superior mesenteric artery coming from the aorta. Along this axis the intestine divides into the superior limb and the inferior limb. The superior limb occupies part of the duodenum, the jejunum, and the proximal part of the ileum. The inferior limb covers the terminal ileum, the cecum, the ascending colon and 2/3 of the transverse colon. The midgut initially rotates 90° counterclockwise. The superior limb grows faster than the inferior limb and forms secondary loops (Gangane and Borate, 2018). Between the sixth and tenth week, physiological herniation of the intestine into the umbilicus occurs due to the growth of the liver, which temporarily causes insufficient space in the abdominal cavity (Bogers et al., 2019). The schematic depiction of the physiological herniation can be found in **Figure 1**.

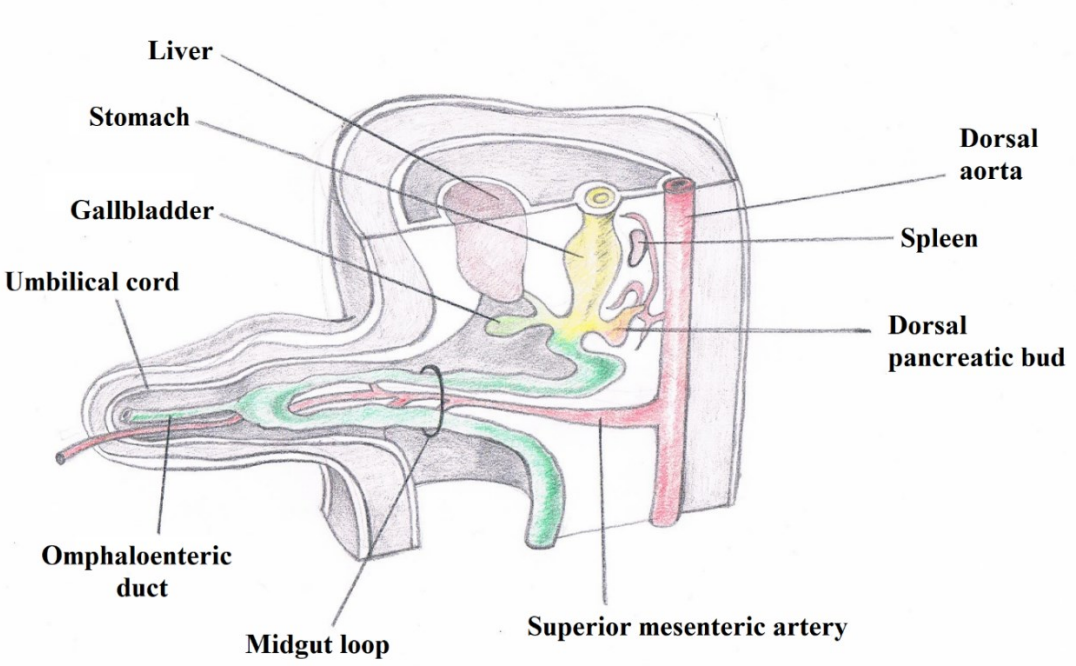

Figure 1. Development of the midgut and physiological herniation. Schematic depiction of physiological herniation in weeks 7 and 8 of embryonic development. Crown-rump length 5 to 15 mm (Verburg et al., 2008). Adapted according to Langmann's Medical Embryology (Sadler, 2018).

In the tenth week, due to the cessation of liver growth and due to the growth of the body, the intestine returns to the abdominal cavity and rotates 180° counterclockwise (Soffers et al., 2015). The intestine returns to the abdominal cavity in proximodistal direction. Thus, the jejunum is placed in the left upper quadrant, the cecum returns last and is placed under the liver. In the next stage, the cecum descends into the right iliac fossa. During the descent into the right lower quadrant, the vermiform appendix is formed (Sadler, 2018). The rotation of the midgut is shown in **Figure 2**.

The hindgut opens at the back of the cloaca, which is terminated by the cloacal membrane. Ventrally, the urogenital sinus is formed and dorsally the anorectal canal is established. These structures are separated by the urorectal septum (Sadler, 2018). The cloacal membrane is thus divided in the anal and urogenital membrane.The caudal part of the rectum is formed from ectoderm and therefore has a different vascular supply (Thakar and Fenner, 2007).

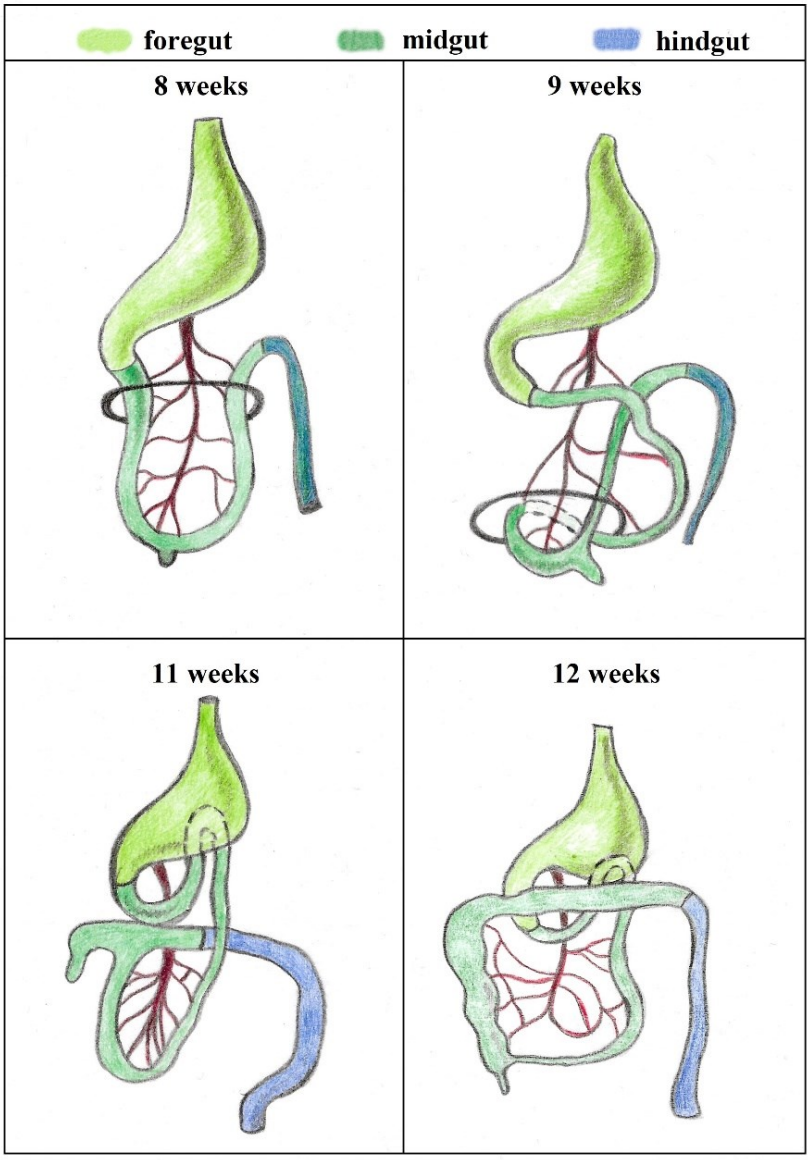

Figure 2. Rotation of the midgut during embryonic development. The black circle in upper images represents the entrance to the physiological herniation. Adapted according to https://www.wikiskripta.eu/w/V%C3%BDvoj_st%C5%99eva#/media/Soubor:Rotace_streva.jpg.

1.6.2 GIT development in humans and laboratory mammals

Research on human intrauterine development is based on the examination of aborted embryos and fetuses (Kawasaki et al., 2020), or on the examination of resected tissues after surgery of premature infants (Stewart et al., 2020). For ethical reasons, there is a ban on culturing human embryos after the second week of development, which prevents scientific research (Cavaliere, 2017). At this point, experimental animal models enter the research (Morris, 2017).

Human and pig embryos show considerable similarities in early development (Li et al., 2020). Considering the different gestation lengths in humans and pigs, the development of

the gastrointestinal tract takes place in relation to the different gestation lengths at the same time periods, making the translation of results from the experimental model easier (Zhang et al., 2013).

	Human	**Pig**	**Rat**	**Mouse**
Gestation period	268 days (Jukic et al., 2013)	approximately 115 days (Vonderohe et al., 2022; Winn et al., 1994)	20–22 days (Bazer and Spencer, 2011)	
Functional maturation of the GIT	Prenatally (Drozdowski et al., 2010; Indrio et al., 2022)	Prenatally, with the exception of tissues of the immune system (Nowland et al., 2019; Pluske, 2016)	Postnatally, in the first 4 weeks after birth (Jena et al., 2020; Walthall et al., 2005)	
GIT maturation hormone	Cortisol (Young et al., 2023)	Cortisol (Young et al., 2023)	Cortisol - cortisol levels minimal in the first two weeks postnatally, a significant increase from the 3rd week postnatally (after weaning) (Boksa, 1997; Vallée et al., 1997)	
Formation of villi	9–10th week of gestation (Drozdowski et al., 2010; Trier and Moxey, 1979)	Around the 40th day of gestation (Huansheng Yang, Xia Xiong, and Yulong Yin, 2013)	From the 14th day of gestation onwards (Walton et al., 2016)	From the 16th day of gestation onwards (Trier and Colony, 2008)
Formation of intestinal crypts	From the 8th to 24th week of gestation (Frazer and Good, 2022)	Between 60 and 90 days of gestation (Alessandra M. M. G. de Castro et al., 2001)	From the 20th day of gestation (Quaroni, 1986)	From 14th postnatally (Chin et al., 2017)
Enteric neurons	Present from the 4th week of gestation, maturation begins from the 8th week in myenteric plexus and 11th week in submucosal plexus and goes on until birth and postnatally (Rao and Gershon, 2018)	Present from the 8th week of gestation, maturation until birth and postnatally (Van Ginneken et al., 1998)	Present from the 8th day of gestation, maturation until birth and postnatally (Rao and Gershon, 2018)	
Differentiation of intestinal epithelium	From the 10th week of gestation (Frazer and Good, 2022)	End of the 3rd month of gestation (Modina et al., 2021)	From the 17th day of gestation (Rubin et al., 1989)	From the 18th day of gestation (Gordon JI, 1989)

Table 4. Comparison of some parameters of embryonic development in human and most used laboratory mammals. Due to the short gestation period, a significant part of the physiological and functional maturation of the gastrointestinal tract in rodents occurs postnatally. Thus, in their case, the milestone of gastrointestinal development is not birth but weaning. At the time of birth, the human gastrointestinal tract is the most mature one in comparison with other experimental mammals.

The study of gastrointestinal pathophysiology has been significantly advanced with the use of rodent models. Nevertheless, it is crucial to recognize the limitations of these models when translating their discoveries to human digestive disease. Overcoming some of these limitations can be achieved by turning to large animal models (Ziegler et al., 2016). Due to

the short duration of gestation, the rodent gastrointestinal tract is immature at birth and functional maturation does not occur until postnatally (Demers-Mathieu, 2022; Weström et al., 2020). Weaning is a significant step in the developmental process of the rodent gastrointestinal tract (Majumbar and Johnson, 1982). Instead of adjusting existing cells, functional maturation happens through cell replacement (Henning, 1981). The progress of mucosa maturation, cell differentiation, and microstructural tissue development advances proximodistally (De Santa Barbara et al., 2003). From a functional point of view, GIT maturation in rodents is completed at approximately four weeks postnatally (Singh et al., 2019). Unlike other mammals such as pigs, the human gut is noticeably more developed both in form and function at birth (Drozdowski et al., 2010). Comparison of the parameters of embryonic development of most used laboratory mammals is stated in the **Table 4**.

1.6.3 Development of the pig spiral colon

The ascending colon in pig is arranged spirally. The ascending colon makes three to five spiral turns centrifugally in the caudal direction and subsequently the same number centripetally going in the cranial direction. The colon then turns dorsally and passes in the prevertebral space to the rectum. Similar to humans, the colon occupies most of the inferior limb of the primary intestinal loop. The inferior limb in pig is compared to humans much longer (40% vs. 15% of the overall length). This leads to convolution of the developing intestine and formation of the spiral colon. Upon return of the intestine from the umbilicus, a360° rotation of the intestinal loop takes place, and the superior limb crosses the posterior limb twice (Lineback, 1916). The formation of the spiral colon begins around the 50th day of gestation (Odlaug and Petterson, 1955). Ascending colon in the pig corresponds to the ascending and transverse colon in humans. The final configuration of the spiral colon is completed in the 4th week postnatally (Lineback, 1916). As time progresses, the spiral tightens and its coils interlock, simultaneously concealing the previously visible portions of the inner coil on the exterior. By adulthood, the apex of the pig's spiral colon has rotated to the left side of the abdominal cavity instead of pointing caudally, completing full four rotations. Subsequently, the inner coil is less exposed than at birth. The previously unapparent sacculations have now fully developed, causing a significant transformation in the spiral colon’s overall appearance (Lineback, 1916). The comparison of spiral colon at four weeks postnatally and in the adult pig is shown in **Figure 3**.

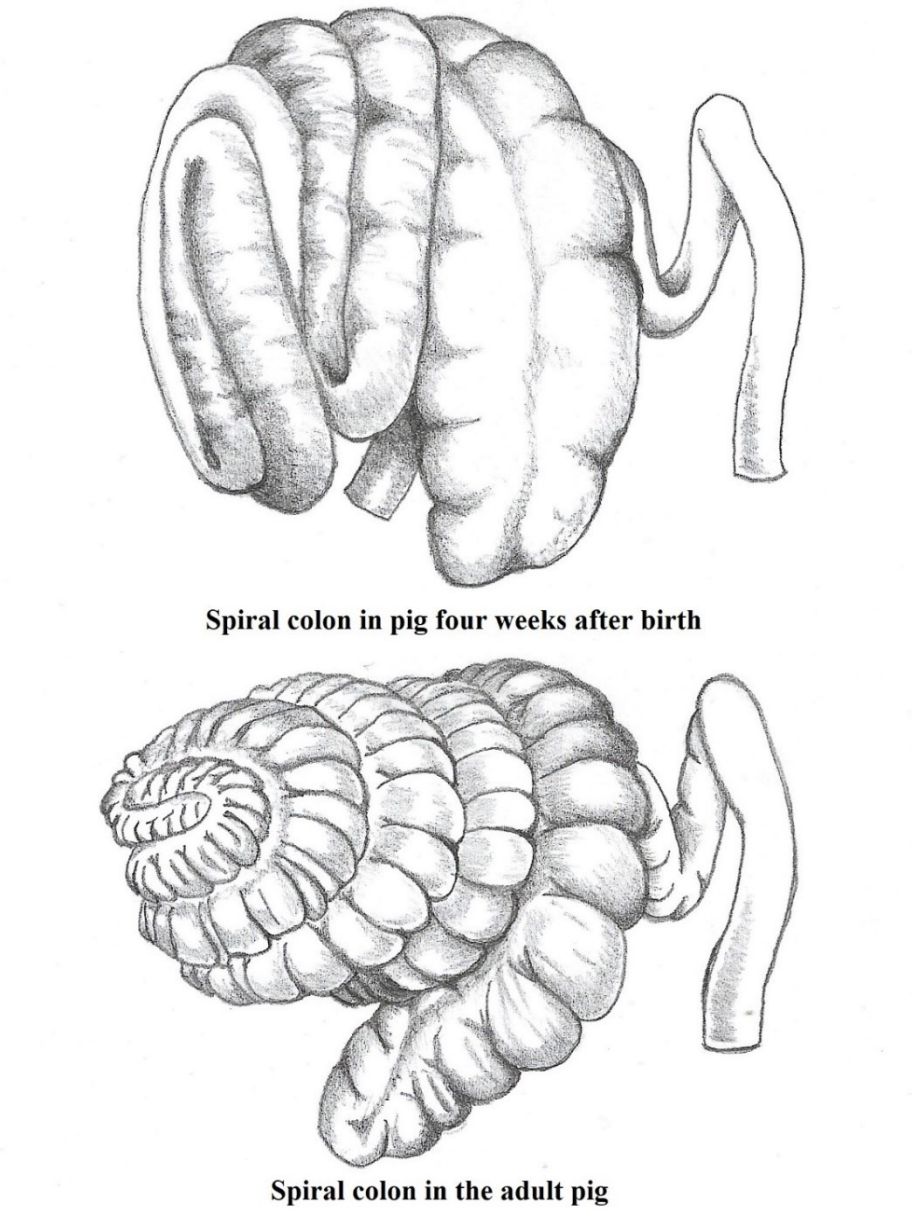

Figure 3. Comparison of the constellation of the spiral colon in pig four weeks postnatally and in an adult pig. Adapted according to Lineback, 1916.

1.7 Anatomy and histology of human small intestine

1.7.1 Anatomy of the small intestine

The small intestine is with its three to five meters the most extensive part of the gastrointestinal tract. Its diameter amounts to two to four centimeters in humans. In anatomical terms, it is partitioned into three distinctive segments: the duodenum, jejunum, and ileum.

The duodenum, extending from the pyloric ostium to the duodenojejunal flexure, is anchored to the retroperitoneum by the duodenal suspensory ligament (of Treitz). Located within the range of L1 to L3 vertebrae, the duodenum encircles the L2 vertebra from right to left, forming a convexity that houses the head of the pancreas. The duodenum has four distinct portions: D1 - superior part, is predominantly located within the peritoneum (its bulb) and represents the first segment of the small intestine following the pylorus of the stomach; D2 - descending part, between the right kidney hilum and the right border of the L2 vertebra; D3 - inferior part and finally D4 - ascending part, that transitions into the jejunum. Parts D2 to D4 are located in the retroperitoneum. The D2 part contains both the major duodenal papilla (of Vater) and minor duodenal papilla (of Santorini), where the pancreatic duct (of Wirsung) and the accessory pancreatic duct (of Santorini) emerge into the duodenum. The celiac trunk branches, specifically the gastroduodenal artery and the anterior and posterior superior pancreaticoduodenal arteries, supply the duodenal upper half with arterial blood. In the distal half, the inferior pancreaticoduodenal artery coming from superior mesenteric artery basin, is responsible for providing vascular supply. The hepatic portal vein receives the venous blood. The parasympathetic system, via the vagal nerve and the sympathetic system, through the sympathetic trunk, provide autonomic innervation. The viscerosensory nerves migrate along with autonomic nerves. The anatomy and vascular supply of the duodenum are shown in **Figure 4.**

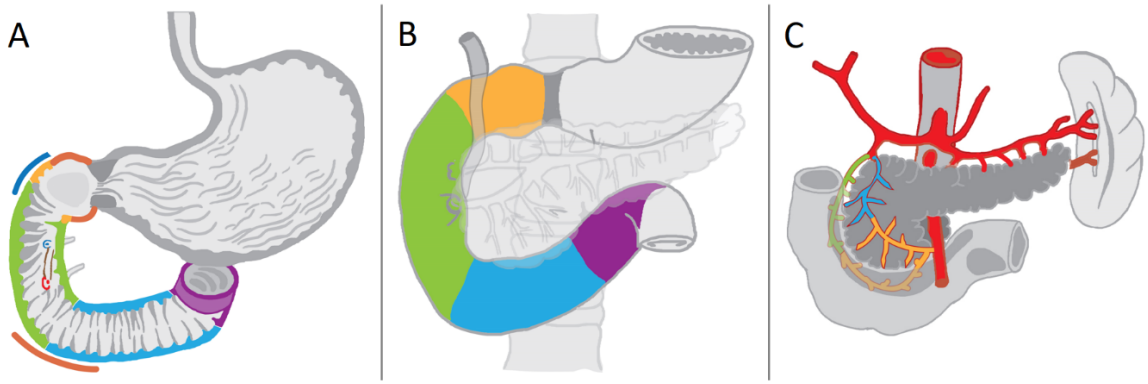

Figure 4. Anatomy of the duodenum. A: position of the major duodenal (light blue) and minor duodenal (red) papilla on the medial side of the duodenum. B: the four parts of duodenum are depicted: D1 (yellow) – superior part; D2 (green) – descending part; D3 (blue) – inferior part; and D4 (violet) – ascending part. C: the arterial blood supply is shown – green and blue branches from the celiac trunk and the yellow branches from the superior mesetenric artery. The illustrations are used with permission from the authors of Memorix Anatomie (Hudák and Kachlík, 2015).

The jejunum represents approximately 40% of the jejuno-ileum's length and its diameter is 3 cm, which is more than that of the ileum. The jejunum starts at the duodenojejunal flexure (fixed by the suspensory ligament of the duodenum) and passes into the ileum with no visible border. Its mucosal folds are high and numerous; vascular supply is provided by one to two series of arcades from jejunal arteries and long arteriolae rectae from the superior mesenteric artery. Venous blood is drained via the superior mesenteric vein. Analogically to the duodenum, autonomic and viscerosensory innervation is ensured by the vagal nerve and splanchnic nerves.

The ileum represents 60% of the jejuno-ileum length and its lumen is approximately 2.5 cm. The beginning of the ileum is not exactly defined; its end is the ileocaecal junction, i.e. the ileal orifice opening into the colon at the border between the cecum and the ascending colon (obsolete term – ileocecal valve of Bauhin). Compared to the jejunum, its mucosal folds are lower and less numerous. The arterial supply is poorer and is provided by two to three series of arcades from ileal arteries and short arterioleae rectae from the superior mesenteric artery. Venous blood drainage and innervation of the ileum are identical to those of the jejunum (Hudák and Kachlík, 2015). The division of the small intestine and the differences in arterial supply of the small intestine are shown in **Figure 5**.

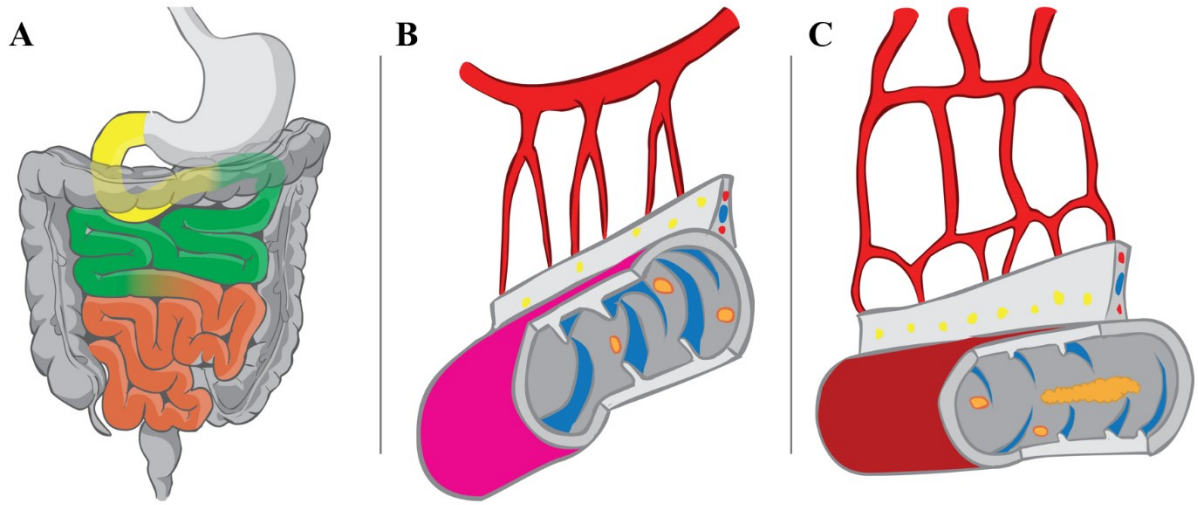

Figure 5. Anatomy and arterial supply of the small intestine mesentery. A: division of the small intestine into three parts: yellow – duodenum, green – jejunum, orange – ileum. B: depiction of the arterial supply in the mesentery with arteriolae rectae coming to the intestine. C: the arcades of arterial supply in the mesentery of the ileum with short arteriolae rectae coming to the ileum are shown. The illustrations are used with permission from the authors of Memorix Anatomie (Hudák and Kachlík, 2015).

1.7.2 Histology of the small intestine

Duodenal length is approximately 30 cm and its diameter is 4 cm. Intestinal folds are highest in the duodenum; however, they are missing completely in the bulb of the duodenum and appear from the descending part on. Intestinal villi are numerous and leaf-shaped. Lymphatic nodules are sparse and solitary. Abundant duodenal glands (of Brunner) are found in the submucosa.

The jejunum is about 2 m long and its lumen is about 3 cm. Its folds are high, but become lower in the aboral direction. Intestinal villi are numerous, long and finger-shaped. Only solitary lymphatic nodules are found in the jejunum, as well.

The ileum is approximately 3 m long, representing the longest segment of the small intestine. At the same time, it is the narrowest part with the lumen of 2.5 cm. The folds are low and are missing completely in the terminal portion. The villi are rather sparse, short and their shape is filamentous. Lymphatic nodules occur isolated (solitary) as well as in clusters (aggregated) in the form of patches of Peyer (Balko et al., 2016). The differences of the structure of mucosa in different parts of the small intestine are shown in **Figure 6**.

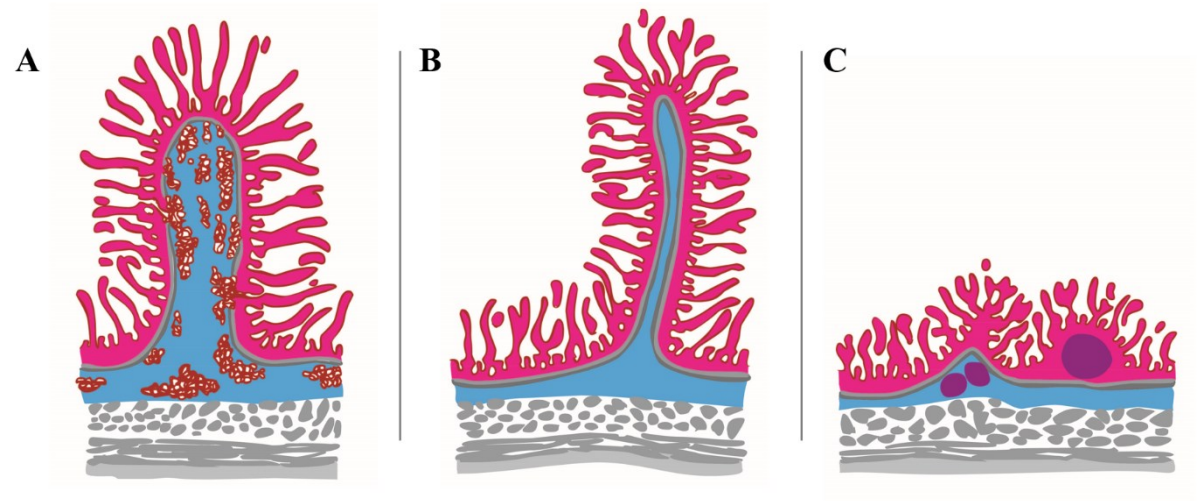

Figure 6. Intestinal villi and submucosa in duodenum, jejunum and ileum. A: the duodenal villus is shown. The villi in duodenum are numerous and leaf-shaped. Lymphatic nodules are scarce and isolated (solitary). Duodenal glands are found in the submucosa. B: jejunal intestinal villi are depicted. They are numerous, long and finger-like. Lymphatic nodules are isolated (solitary). In ileum (C), the villi are rather sparse, short and their shape is filamentous. Lymphatic nodules occur isolated (solitary) as well as in clusters (aggregated) in the form of patches of Peyer. The illustrations are used with permission from the authors of Memorix Histologie (Balko et al., 2016).

1.7.3 Structure of the small intestinal wall

The intestinal wall consists of four basic parts: mucosa, submucosa, muscular layer and serosa.

The mucosa (mucous membrane) is a complex constituent of the intestinal wall. It consists of three distinct sublayers- starting from the lumen of the intestine, these are the epithelium, lamina and muscularis mucosae. The epithelial layer is composed of a simple columnar epithelium with microvilli. Lamina propria contains sparse collagenous connective tissue with lymphocytes and forms the stroma of intestinal villi. Lymphatic nodules are also found in this part of the intestinal wall, either isolated or as solitary lymphoid nodules scattered in the mucosa, or as aggregated lymphatic nodules grouped in patches of Peyer. The last part of the mucosa the muscular mucosae, is composed of smooth muscle cells in one to two layers.

Submucosa is collagenous connective tissue that provides mechanical strength to the intestinal wall. In the duodenum, most of the submucosa is filled with mucinous duodenal glands (of Brunner) that neutralize the acidic chyme from the stomach. The submucosa is also penetrated with submucous nervous plexus (of Meissner), submucous blood plexus and lymphatic vessels.

There are two sub-parts of smooth muscle layer in the intestinal wall - the inner circular and outer longitudinal. Between these two muscle sheets lies the myenteric nerve plexus (of Auerbach).

The serosa is the outer layer of the small intestine that covers most of its surface with the exception of the duodenum, which is covered with adventitia (Balko et al., 2016). The structure of the small intestine is shown in the **Figure 7.**

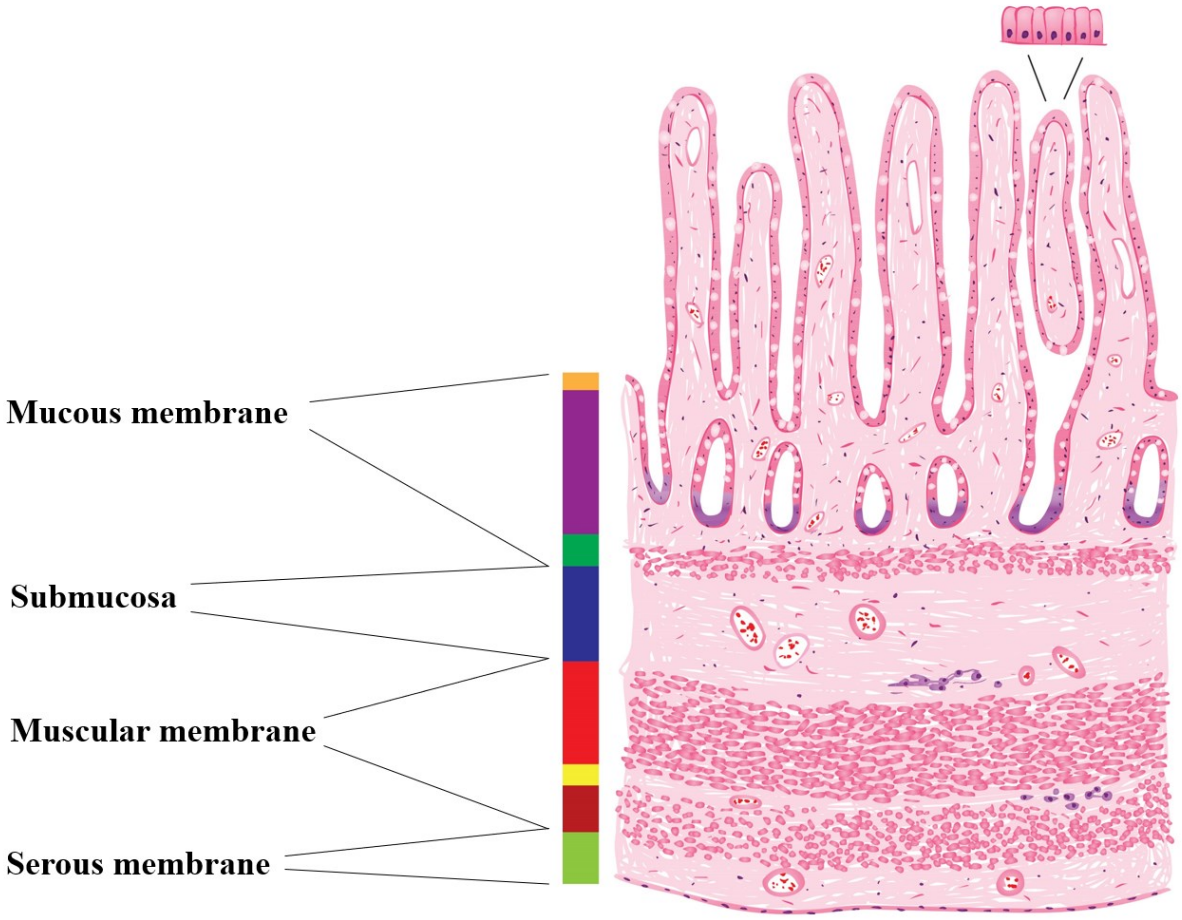

Figure 7. Microstructure of the small intestinal wall. The details regarding the microstructure of the small intestine are stated in the text above. The illustration is used with permission from the authors of Memorix Histologie (Balko et al., 2016).

1.7.4 Cell types of the small intestinal mucosa

Six types of cells are found in the mucosa of the small intestine. According to their staining type, they can be divided as eosinophilic; these cells include enterocytes, goblet cells and M cells, and as basophilic; these include enteroendocrine cells, Paneth cells and undifferentiated stem cells.

Enterocytes are characterized by a highly cylindrical shape; the brush border of microvilli, covered with glycocalyx, is found on their apical surface. Enterocytes are the predominant cellular population of the mucosa. They play are the key element in secretion of digestive enzymes and nutrient absorption. They also form a barrier between the inner environment of the organism and the intestinal lumen. Laterally, they are connected by intercellular junctions such as tight junctions, adherent zonules and desmosomes.

Goblet cells are irregularly shaped and apically, they are filled with numerous mucous granules. Their function is to produce mucus.

M cells have a cylindrical shape with apical protrusions. Basally, they protrude into the lamina propria, which facilitates their contact with lymphocytes. These cells form part of the immune system; they transport antigens and present them to lymphocytes and macrophages. M cells are always found near lymphatic nodules located in the submucosa.

Enteroendocrine cells are characterized by a low cylindrical shape and occur in two variants – as endocrine and paracrine cells. They are usually irregularly scattered among other cells; basally, they are usually in contact with capillaries into which they secrete hormones.

Paneth cells are basophilic, although they have eosinophilic granules in the apical region. Their shape is pyramidal, and they produce lysozyme, phospholipase A2 and defensins that erode the bacterial wall and are involved in maintaining equilibrium of bacterial growth in the intestine. They occur on the bottom of intestinal crypts.

Undifferentiated stem cells have a low cylindrical shape and serve to replace dead cells of other types, into which they differentiate (Balko et al., 2016). The cell types of small intestine are depicted in **Figure 8**.

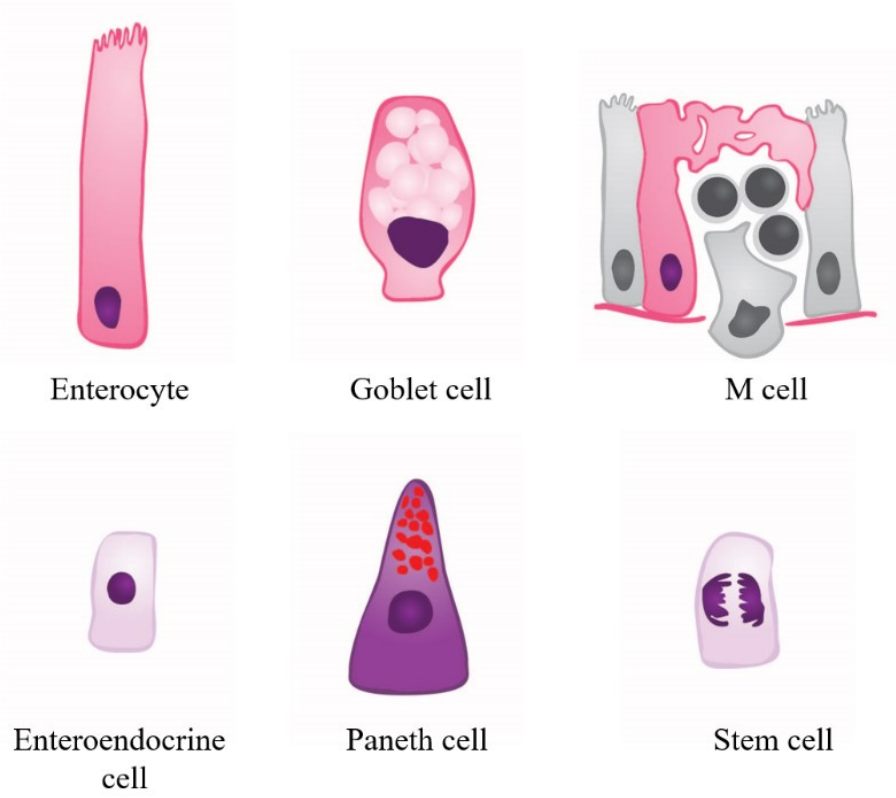

Figure 8. Cell types of the small intestinal mucosa. The details can be found in the text above. The illustrations are used with permission from the authors of Memorix Histologie (Balko et al., 2016).

1.7.5 Structures increasing the absorption area

The overall absorption surface of the small intestine is about 300 square metres. This huge surface is obtained thanks to anatomical structures that include circular intestinal folds, villi, microvilli, and intestinal glands (crypts of Lieberkühn).

The circular intestinal folds (of Kerckring) are most distinctive in the duodenum and gradually become lower in the aboral direction. They consist of mucosa and submucosa.

Intestinal villi are finger-shaped protrusions into the intestinal lumen, approximately 0.5 to 1.5 mm long, composed of the epithelial layer and lamina propria. In the aboral direction, their shape gradually changes from leaf-like to finger-like and they become shorter and less numerous. Every villus contains an afferent arteriole and an efferent venule, and a lymph (chyle) vessel running through the middle. Microvilli form a brush border on the surface of enterocytes.

Intestinal glands, also known as the crypts of Lieberkühn, are tubule-like glandular structures in between the villi. They pass through the lamina propria and reach the muscularis mucosae. They are lined with enterocytes and goblet cells, while Paneth cells and stem cells are found on their bottom. Enteroendocrine cells are scattered in the walls (Balko et al., 2016). The structures increasing the absorption area are depicted below, in the **Figure 9**.

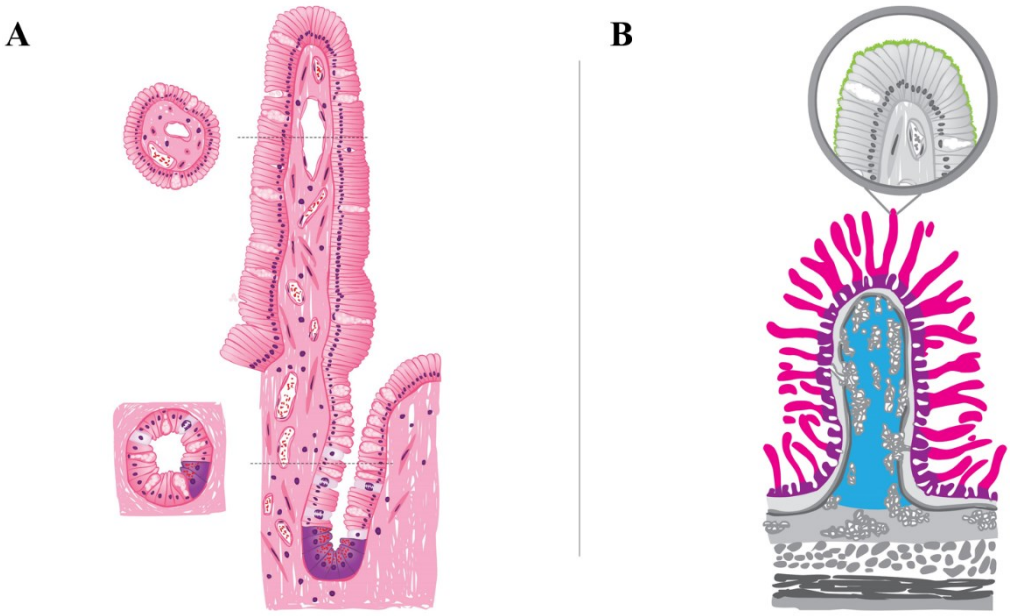

Figure 9. Structures increasing the absorption area of the small intestine. A: villus with the intestinal gland. B: a circular intestinal fold (blue) and brush border formed by microvilli (detail picture in the cutout) are shown. The illustrations are used with permission from the authors of Memorix Histologie (Balko et al., 2016).

1.8 Anatomy and histology of human large intestine

1.8.1 Anatomy of the large intestine

The large intestine is divided in three basic parts: the caecum, colon and rectum. The vermiform appendix is a part of the caecum. The colon is divided in four segments according to their direction – ascending, transverse, and descending colon and the sigmoid colon that continues into the rectum. The rectum is the final segment of the intestine and leads to the anus. The ascending and descending parts of the colon are situated secondarily retroperitoneally, while the remaining parts of the colon are situated intraperitoneally.

Several typical anatomical formations are found on the surface of the large intestine, which make it easy to distinguish the large intestine from the small intestine. These formations include the haustra, taeniae, and omental appendices.

The haustra are derived from the activity of circular and longitudinal smooth muscles of the intestinal wall. The circular muscle layer is responsible for strangulation, while the longitudinal layer creates typical contractions. Grooves between the haustra correspond to internal semilunar folds.

Colic taeniae are three reinforced ribbons of longitudinal muscles of the intestinal wall that are visible on the surface. They include mesocolic taenia that begins where the transverse mesocolon is separated; omental taenia at the place of adhesion with the greater omentum; and free taenia is the freely accessible and visible taenia. In the area of the vermiform appendix, the colic taeniae converge to form a continuous longitudinal mantle. In the area of the rectosigmoid transition zone, the colic taeniae spread out and descend in the aboral direction as two longitudinal muscle strips.

Omental (epiploic) appendices are protrusions of the visceral peritoneum filled with fatty connective tissue (Hudák and Kachlík, 2015). The typical anatomical structures of the large intestine as well as its division are shown in **Figure 10**.

1.8.2 Vascular supply and innervation of the large intestine

Arterial supply of the large intestine is provided from the basin of the superior and inferior mesenteric arteries and from the internal iliac artery. Three branches separate from the superior mesenteric artery, which supply the right half of the large intestine. These are the ileocolic artery, the right colic artery, and the middle colic artery. The ileocolic artery is

responsible for supplying the terminal ileum and caecum. Via appendicular artery, it supplies the vermiform appendix with arterial blood. The right colic artery runs to the ascending colon and the middle colic artery supplies the right two-thirds of the transverse colon.

From the inferior mesenteric artery emanate branches that supply the left half of the colon. These branches encompass the left colic artery that separates into the superior branch, which provides the left third of the transverse colon with arterial blood supply, while the inferior branch is responsible for the descending colon and forms an arterial connection to the cranial sigmoid artery. Further caudally, two to four sigmoid arteries extend from the main trunk of the inferior mesenteric artery towards the sigmoid colon. At the boundary between the right two-thirds and left one-third of the transverse colon, there is an anastomosis of the basins of the superior and inferior mesenteric arteries called Haller's anastomosis, or *anastomosis magna Halleri* in Latin. The last of the branches of inferior mesenteric artery is the superior rectal artery providing blood for the rectal ampulla region. Another arterial anastomosis is formed between the most caudal sigmoid artery and the small branches breaking away from the superior rectal artery.

Since the final segment of the gastrointestinal tube is of ectodermal origin (Sadler, 2018), its vascular supply comes not from the splanchnic vessels but from the arterial branches of internal iliac artery. These branches, supplying the anal canal and anus, are named the middle and inferior rectal arteries.

Venous outflow is provided by veins leading into the inferior mesenteric vein and the internal iliac vein.

Kachlík et al. (2010) have shown in their article on blood supply of the colic wall using corrosion casts that the vascular plexuses are interconnected into a long canal that spans the entire length of the large intestine and can act as a vast collateral blood vessel in times of need. It is important to note that this collateral vessel operates optimally only in cases where there are no underlying developmental defects or damage to the immune and vascular system or diseases relating to connective tissue.

Innervation of the large intestine is ensured by mixed periarterial plexuses of sympathetic and parasympathetic nerves leaving from the coeliac ganglion, and from the superior and inferior mesenteric ganglia. Approximately at two thirds of the transverse colon, at the Cannon-Böhm point, parasympathetic innervation from the vagal nerve passes into innervation of the aboral part of the large intestine from the sacral parasympathetic nerve. Sympathetic innervation of the large intestine is derived from the abdominal aortic plexus and

the superior and inferior hypogastric plexuses (Hudák and Kachlík, 2015). Arterial supply is shown in **Figure 10**.

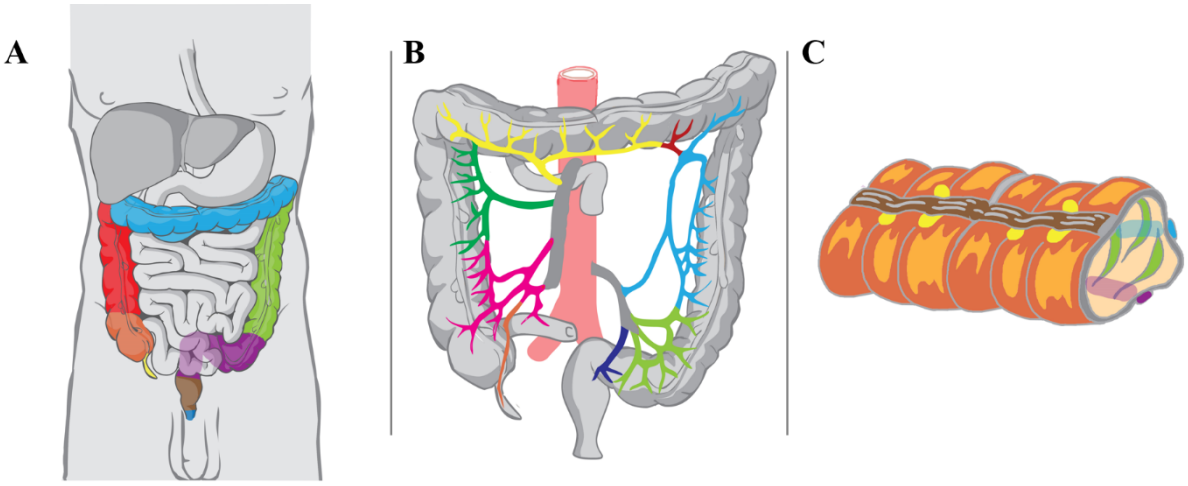

Figure 10. Division, arterial blood supply and typical anatomical structures of the large intestine. A: vermiform appendix (yellow), caecum (orange), ascending colon (red), transverse colon (blue), descending colon (dark green), sigmoid colon (violet), rectum (brown) and anus (dark blue). B: from the superior mesenteric artery come these arterial branches: ileocolic artery (pink), appendicular artery (orange), right colic artery (green), middle colic artery (yellow), Haller's anastomosis (brown); the inferior mesenteric artery produces these branches: left colic artery (light blue), sigmoid arteries (light green), superior rectal artery (dark blue). C: typical structures of the large intestine: taeniae (brown, blue and violet), semilunar folds (green) and omental appendaces (yellow). The illustrations are used with permission from the authors of Memorix Anatomie (Hudák and Kachlík, 2015).

1.8.3 Differences in the structures of human small and large intestinal walls

Similar to the wall of the small intestine, the wall of the large intestine is also composed of four layers – serosa, muscular layer, submucosa and mucosa. Despite that, the structure of the large intestinal wall differs in many aspects.

The mucosa has a smooth surface without villi and circular folds. However, temporary semilunar folds with haustra between them are formed by contraction of the muscles. A considerable number of intestinal glands is also found in the area of the large intestine, which pass through the mucosa almost in its entire thickness. Sparse connective tissue with lymphocytes and lymphatic nodules forming the so-called GALT (gut associated lymphatic tissue) is found in the area of lamina propria. Lymphatic tissue of the large intestine is more developed, which is apparently related to rich bacterial populations.

The serous membrane forms visceral and parietal peritoneum, covering a major part of the intestinal surface, on the outer surface of the large intestine. Peritoneal diverticula filled

with fatty tissue form epiploic appendices on the surface of the large intestine (as seen in Figure 7). The surface of retroperitoneal and subperitoneal parts of the large intestine is covered with adventitia.

Several differences in the intestinal wall structure can be found in the area of the vermiform appendix although its basic structure does resemble the remaining parts of the large intestine. Unlike other parts of the large intestine, Paneth cells are found in the mucosa of the vermiform appendix. Lamina propria contains substantial quantities of lymphatic tissue forming lymphatic nodules (Balko et al., 2016).

1.8.4 Mucosal cells of the vermiform appendix and colon

The cellular populations found in the mucosa of the large intestine, bear similarity to their small intestinal counterparts. Colonocytes are the most abundant constituents of the mucosa. They share a resemblance in structure with enterocytes. However, the density of microvilli on the luminal surface is notably lower in colonocytes. On the contrary, goblet cells are much more numerous in the large intestine; these cells produce mucus that protects the mucosa and facilitates chyme transport in the aboral direction. Similarly to the small intestine, M cells, enteroendocrine cells, and undifferentiated stem cells, situated on the bottom of intestinal glands, are found in the large intestine (Balko et al., 2016). The separate cell types present in the large intestine mucosa are shown in the **Figure 11.**

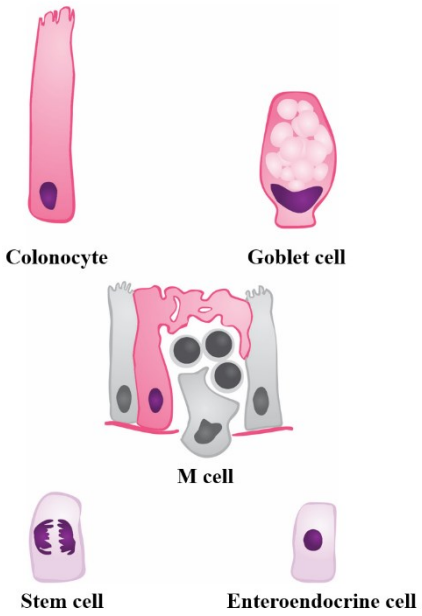

Figure 11. Cell types in the large intestine mucosa. Detailed information can be found in the text above. The illustrations are used with permission from the authors of Memorix Histologie (Balko et al., 2016).

1.8.5 Rectum

The rectum is the last part of the large intestine. Its parts include: the rectal ampulla, the anal canal and the anus.

The structure of the rectal ampulla is similar to that of the colon; the mucosa is movable with respect to submucosa and contains a large amount of goblet cells. Several typical anatomical structures are found in the rectal ampulla – three transverse rectal folds. The upper and lower transverse folds (of Houston) protrude from the left side. Between these two folds, the middle fold (of Kohlrausch) protrudes from the right side. The boundary between the typical mucosa of the large intestine and the anal transitional zone (ATZ) with changing epithelium is called the supratransitional line.

The surgical anal canal is a part of the rectum narrowed by sphincters. Anal columns are found in this area, forming longitudinal mucosal folds. The anatomical anal canal is the short (1,5 cm long) distal and narrowest part. The anus is the external opening of the gastrointestinal tract to the surface of the body (Hudák and Kachlík, 2015). The anatomical structure of rectum is shown in **Figure 12**.

1.8.5.1 Inner structure of the rectum

The inner structure of the rectum is also somewhat different from the rest of the large intestine. The boundary between different types of mucosae in the aboral part of the rectum is called the supratransitional line. The anal transitional zone is an area where the simple columnar epithelium changes into stratified columnar epithelium and subsequently into stratified squamous epithelium. Dentate (pectinate) line is the boundary between the rectal ampulla and the anal canal. The anal squamous zone (anal pecten) corresponds to the extent of the anatomical anal canal fand its epithelium is stratified squamous non-keratinizing. Submucosa in the area of the clinical anal canal contains a rich venous plexus – haemorrhoidal (internal rectal) plexus. The smooth internal anal sphincter originates from the muscular layer; this sphincter is formed by a thickened circular layer in the range of the anal transitional zone and the anatomical anal canal. In the area of the rectum, thanks to its subperitoneal position, the longitudinal smooth muscle layer does not form the intestinal wall of colic taenia, otherwise present in the large intestine. Given the subperitoneal position of the rectum, the external layer is formed predominantly by adventitia, and the rectum is covered with serosa only in the oral part. The external anal sphincter originates from the area of the

pelvic floor; this sphincter is formed by striated muscles, the external anal sphincter muscle (Balko et al., 2016). The histological structure of rectum is shown in **Figure 12**.

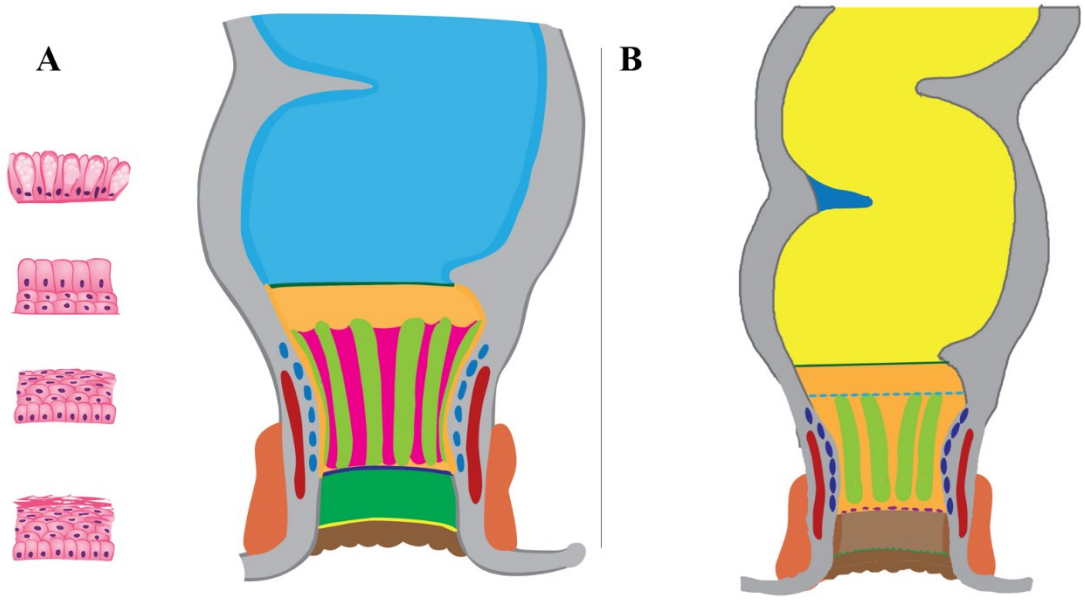

Figure 12. Anatomical and histological structure of rectum. A: one can see the transition of the typical large intestinal mucosa with abundant goblet cells and simple columnar epithelium into stratified columnar epithelium and subsequently into stratified squamous epithelium. The supratransitional line is shown as the green boundary between the rectal ampulla (light blue) and the surgical anal canal (orange). B: the anatomical structure of the rectum is shown: rectal ampulla (yellow), anal canal (orange) and anus (brown). The haemorrhoidal plexus is marked in dark blue; the inner sphincter is red and external sphincter light brown. The anal columns are depicted in light green. Middle trasnverse rectal fold (of Kohlrausch) in the rectal ampulla is light blue. The illustrations are used with permission from the authors of Memorix Histologie (Balko et al., 2016) and Memorix Anatomie (Hudák and Kachlík, 2015).

1.9 Use of experimental animals in gastrointestinal surgery

Metabolic, anatomical, physiological, and biochemical differences between human and animal may distort the experimental results and result in a failure of the entire research. No animal can seamlessly imitate all properties of human; however, the use of a suitable animal model is possible for some purposes (European Commission, 2013). Therefore, it is important to understand interspecies differences. Important factors that differ among individual experimental animal species include internal pH, bile composition, pancreatic juice composition, composition of the mucus produced by goblet cells, intestinal microflora composition, the transit time, lymphatic tissue in the intestinal wall, and the gastrointestinal tract structure (Kararli, 1995).

1.9.1 The pig as a model organism

The use of rodents in gastrointestinal tract research is widespread and enables large-scale studies. However, experimental results must be carefully translated to humans (Casteleyn et al., 2010). For experimental surgery, domestic pigs are commonly utilized, particularly the mini variety weighing 30 kg in adult age, due to their ease of handling (Nunoya et al., 2007). Domestic pigs have similar physiology, anatomy (Meurens et al., 2012), and skin to humans (Krumpholz et al., 2022), making them ideal for studies in embryology (Kobayashi et al., 2012), teratology (Nunoya et al., 2007), ontogenesis (Krause et al., 2021), immunology (Pabst, 2020), and novel surgical procedures (Walters and Prather, 2013). The swine and human intestinal wall share a similar microscopic structure, but the intestinal microflora differs (Zhang et al., 2013). A schematic depiction of the pig gastrointestinal tract is shown in the **Figure 13**.

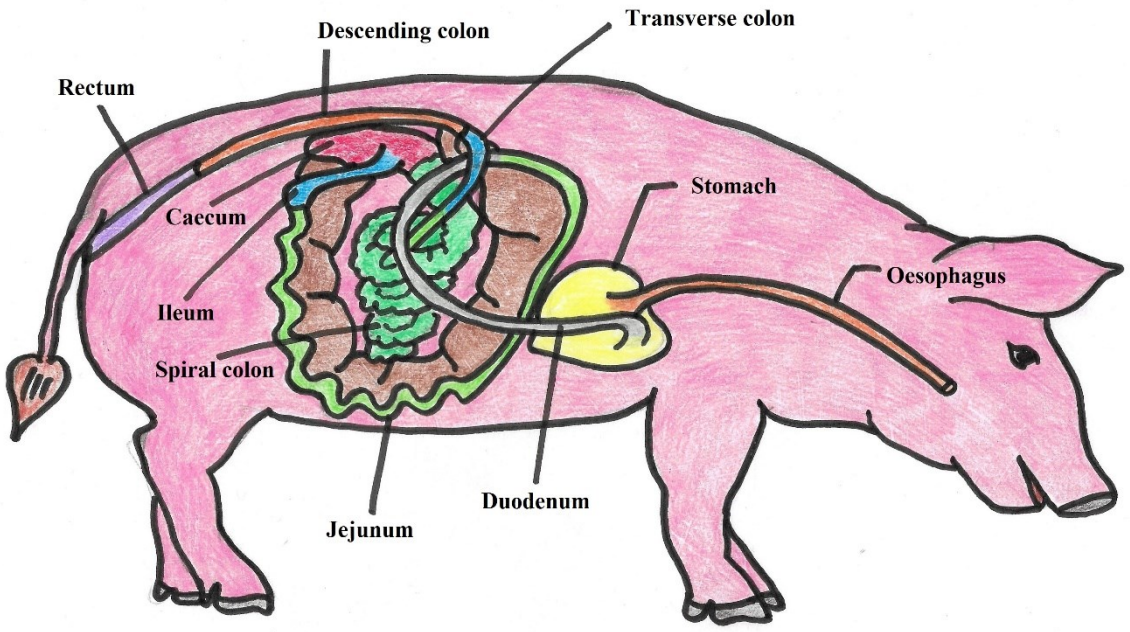

Figure 13. Gastrointestinal tract of the pig. The pig duodenum is considerably longer than that of humans, as well as jejunum. On the other hand, the ileum is much shorter. The ascending colon in pigs form a helix-shaped structure (spiral colon), whereas the transverse and descending colon in pig are significantly shorter. Adapted according to Rieger, 2016.

1.9.2 Differences in pig and human small intestine structure

The overall length of the small intestine in the pig is approximately 15–22 metres (Gonzalez et al., 2015). The duodenum is with 70–95 cm quite short (Al Masri et al., 2015); the jejunum is 14 to 19 m long (Al Masri et al., 2015); and the ileum is only 70 to 100 cm long (Al Masri et al., 2015). The effective surface area of the villus is constant in all common laboratory animals and in humans, about 25 μm^2 (Kararli, 1995). Anatomical structure of the small and large intestinal wall is identical to that in humans (Kararli, 1995). The overview of differences of the small intestine among humans and commonly used laboratory mammals are shown in the **Table 5**.

1.9.2.1 Differences in duodenum structure

In the pig, the pancreatic duct and bile duct enter the duodenum separately (Lærke and Hedemann, 2012); the accessory duodenal papilla (of Santorini) is also present in the pig and represents the orifice of the accessory pancreatic duct (Ferrer et al., 2008). The amount of dudoenal glands (of Brunner) is another difference. While in human, duodenal glands are found in the entire duodenum (Balko et al., 2016) and occupy a major part of the submucosa, in the pig these glands occur from the duodenal bulb to 45–50 cm distal to the pancreatic duct orifice and their abundance decreases in the proximodistal direction (Caeleton, 1935). Both in humans and in pigs, the villi are numerous and leaf-like (Balko et al., 2016; Skrzypek et al., 2005). The length of villi in the pig increases from the duodenum to the center of the jejunum, and subsequently it decreases again towards the terminal ileum (Lærke and Hedemann, 2012); in human, intestinal villi of the duodenum are numerous and leaf-shaped, in the jejunum they are numerous and long, finger-shaped, and in the ileum they are less numerous and short, filamentous (Balko et al., 2016). The overview of differences in the duodenum anatomy and histology among humans and commonly used laboratory mammals are shown in the **Table 6**. The comparison of human and pig duodenum is shown in the **Figure 14**.

1.9.2.2 Differences in jejunum and ileum structure

The pig jejunum is considerably longer compared to human, to the detriment of the ileal length (Al Masri et al., 2015). The transition between the jejunum and ileum is not quite clear; clinically, the boundary can be best revealed based on differences in vascular supply of the jejunum and ileum (Rieger, 2016; Spalding and Heath, 1987). The overview of differences in the jejunum and ileum anatomy and histology among humans and commonly used laboratory

mammals are shown in the **Table 7** and **Table 8**. The comparison of human and pig jejunum is shown in the **Figure 14**.

Figure 14. Comparison of human duodenum (A) and pig duodenum (B) as well as human jejunum (C) and pig jejunum (D). Histological staining with hematoxylin-eosin (A, C, D) and green trichrome (B). Scale 1 mm (A, B) and 2 mm (C, D). A and B: The structure and size of the human and pig duodenum is almost identical. This is partly due to the contraction of tissue during histological staining. The submucosa in both species is to a large extent filled with duodenal glands. C and D: In comparison of human and pig jejunum, one can see the difference in the thickness of the serosa and muscular layer (above all the circular layer of the muscular layer) as well as the submucosa. These layers are thicker in humans than in pigs. Furthermore, the scale of the pig jejunum is smaller than that in humans.

1.9.3 Differences in pig and human large intestine structure

The overall length of the large intestine is about 4–6 m in the pig (Gonzalez et al., 2015), and 120 to 150 cm in human (Hudák and Kachlík, 2015). Comprising of three distinct parts, namely the caecum, colon and rectum, the basic anatomical division of pig's large intestine is identical to humans. Similarly, as in human, the pig colon includes the ascending colon, the transverse colon and the descending colon (Rieger, 2016). However, the sigmoid colon is missing in the pig. The luminal surface of the large intestine has no villi, but taeniae and haustra are found in both (Hedemann et al., 2002). The overview of differences in the large intestine anatomy and histology among humans and commonly used laboratory mammals are shown in the **Table 9**.

1.9.3.1 Differences in caecum structure

The caecum is a cylindrical, blind-ended sac located at the proximal end of the large intestine (Rowan JP et al., 2015). The caecum and the proximal part of the spiral-shaped large intestine have two to three taeniae (Hedemann et al., 2002; Langer and Takács, 2004), forming haustra on the intestinal surface (Hedemann et al., 2002). The area of the caecum is poorly defined in human, while the pig caecum is larger by several orders compared to human (Mochizuki and Makita, 1998). The overview of differences in the caecum anatomy and histology among humans and commonly used laboratory mammals are shown in the **Table 10**.

1.9.3.2 Differences in colon structure

Colon configuration in the pig is different from that in humans, as the main part of the colon forms the so-called spiral colon. The ascending colon coils into three to four centrifugal and centripetal helices. Upon exiting the spiral, the colon moves cranially before making a leftward turn and becoming the transverse colon. The transverse colon then descends caudally, eventually curving inward and transitioning into the rectum (Mochizuki and Makita, 1998). The overview of differences in the colon anatomy among humans and commonly used laboratory mammals are shown in the **Table 11**. The anatomy of the large intestine in pig can be seen in **Figure 3** and **Figure 13.** The comparison of colon in humans and pigs is shown in **Figure 15**.

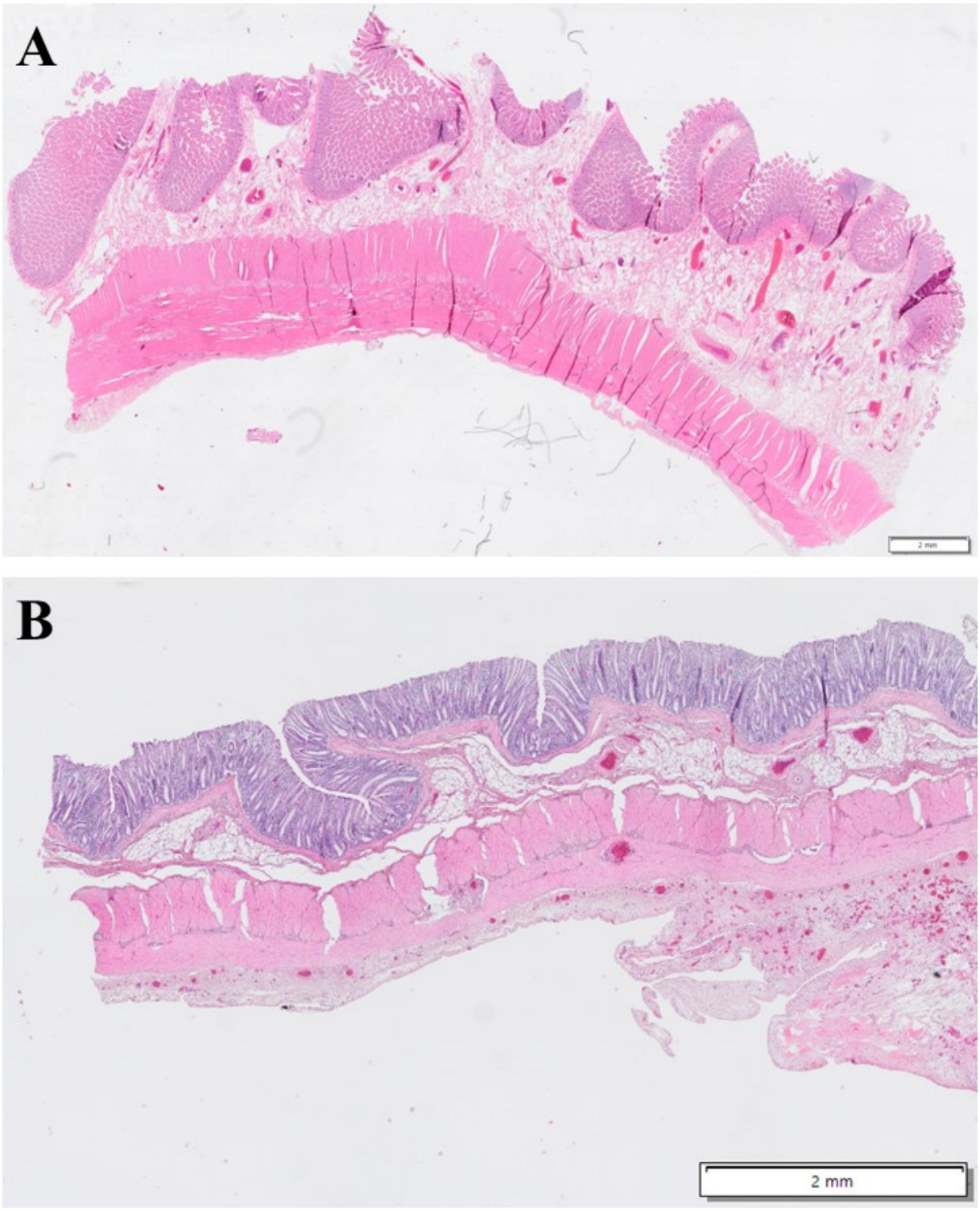

Figure 15. Comparison of human colon (A) and pig colon (B). Histological staining with hematoxylin-eosin. Scale 2 mm (A and B). As well as in jejunum, one can see that the human submucosa is more pronounced than that in pigs. The scale of the pig colon is smaller than in humans.

1.9.3.3 Differences in rectum structure

The pig rectum has a highly similar anatomical and microscopical structure to that in humans. The anus has two sphincters similarly to human, and also an anal transitional zone between the columnar and squamous epithelium (Plakhotnyi et al., 2021). The overview of differences in the rectum anatomy and histology among humans and commonly used laboratory mammals are shown in the **Table 12**.

1.9.4 Other differences in the pig intestine structure

1.9.4.1 Peyer's patches

Peyer's patches are a set of aggregated lymphatic nodules in the lamina propria of the mucosa and in the submucosa of the small intestine, which are separated from the intestinal lumen either by one layer of M cells, or by a combination of M cells and columnar enterocytes. Peyer's patches play a key role in capturing antigens and in inducing of the immune response. The quantity and size of Peyer's patches increase with age, body weight and length of the small intestine. New-born pigs have no Peyer's patches – they become apparent on day 15 from the birth; in human, about 60 patches can be observed already before the 30th week of pregnancy. The patches in the pig ileum are larger and more numerous than in the jejunum. Pig M cells have dense and irregular microvilli on the luminal surface, while human M cells are covered with irregular grooves or folds instead of microvilli (Kararli, 1995).

1.9.4.2 Vascular supply

The anatomy of the main aortic branches in the pig corresponds to that of the human. Instead of arterial arcades in human, we find numerous arteriovenous bundles in the pig, containing up to 500 arteries running radially through the mesentery. The arteries anastomose with each other. Each arteriovenous bundle contains up to 30 arteries when separated, and these arteries merge during the course of the mesenterium, leaving only one to four arteriolae rectae near the intestine. The exact function of the multitude of small arteries in the mesentery remains somewhat unclear. Nevertheless, it is probable that their primary purpose is to regulate blood pressure within the intestinal wall (Spalding and Heath, 1987). The schematic depiction of the arterial supply of the pig intestine is shown in **Figure 16**.

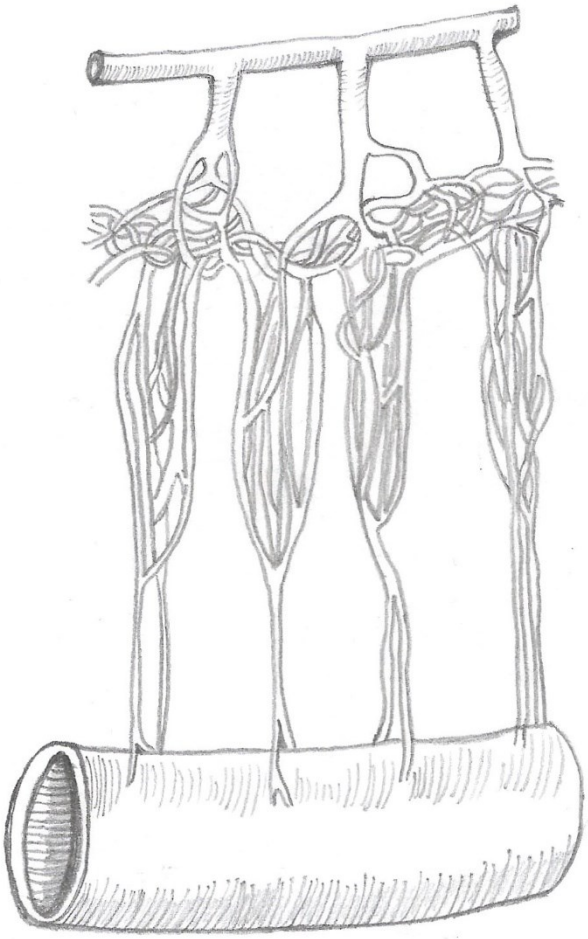

Figure 16. Arterial supply of the pig intestine. Adapted according to Spalding et al., 1987.

1.9.5 Rodent as a model organism

In animal experiments, mice and rats are the most commonly used subjects, accounting for over 90%. Between these two species, mice are the preferred choice for biomedical research because of their small size, which make the process of maintenance and housing much more efficient. Additionally, they possess a relatively mild temperament, short reproductive cycle, and lifespan, as well as a docile nature. Moreover, their anatomy, genetics, biology, and physiology have been widely studied, making them an ideal animal model. Lastly, the possibility of breeding genetically modified and spontaneously-mutated mice further support their position as an excellent research subject (Hickman et al., 2017). The small size (especially in mice) is a disadvantage, as microsurgical methods are required in surgical

experiments (Michel et al., 2020). Nevertheless, rodents are commonly employed in research relating to the gastrointestinal tract, given their efficacy in large-scale studies. Notwithstanding, results from such experiments must be cautiously extrapolated to humans (Casteleyn et al., 2010).

1.9.6 Differences in rodent and human small intestine structure

The small intestine is about 35 cm long in mice and 170 cm in rats. It is divided identically as in human – in the duodenum, jejunum, and ileum. Human mucosa of the small intestine includes permanent circular folds, which are not present in rodents. The other attributes that increase the absorption surface area of the small intestine, i.e., villi, microvilli, and intestinal glands, are present in rodents. In rodents, the villi are roughly two times longer compared to human, which increases their absorption surface area despite the absence of circular folds. The length of the villi in rodents varies depending on their diet, pregnancy and segment of the intestine (Treuting et al., 2017). The overview of differences in the small intestine anatomy among humans and commonly used laboratory mammals are shown in **Table 5**.

	Human	**Pig**	**Rat**	**Mouse**
Length	3–5 m (Hudák and Kachlík, 2015)	15–22 m (Gonzalez et al., 2015)	170 cm (Treuting et al., 2017)	35 cm (Treuting et al., 2017)
Diameter	3–4 cm (Hudák and Kachlík, 2015)	4.2–6.8 mm in neonate piglets (de Castro et al., 2001), value for adult pigs not found – Medline and Google search on 29th March 2023 using keywords diameter, small intestine, small bowel, pig, swine	2.5–5 mm (Kararli, 1995)	4 mm (Gabella, 1987)

Table 5. Interspecies differences in the anatomy of small intestine in human, pig, rat, and mouse.

1.9.6.1 Differences in duodenum structure

In rodents, the duodenum is short; the common bile duct and pancreatic orifices lead to the duodenal papilla, while the pancreatic orifice may even be multiple. Long, leaf-shaped villi and submucous duodenal glands are found in the rodent duodenum, which are bordered with cuboidal epithelium. Given the presence of duodenal glands, the proximal part of the duodenal submucosa is considerably thickened (Treuting et al., 2017). The overview of differences in the duodenum anatomy and histology among humans and commonly used laboratory mammals are shown in **Table 6**.

	Human	Pig	Rat	Mouse
Length	25 cm (Hudák and Kachlík, 2015)	70–95 cm (Al Masri et al., 2015)	9.5–10 cm (Kararli, 1995)	7 cm (Treuting et al., 2017)
Diameter	4 cm (Hudák and Kachlík, 2015)	4.8–6.2 mm in neonate piglets (de Castro et al., 2001), value for adult pigs not found - Medline and Google search on 29th March 2023 using keywords diameter, duodenum, pig, swine	2.5–3 mm (Kararli, 1995)	2.5–2.7 mm (Treuting et al., 2017)
Major duodenal papilla – orifice of the bile and pancreatic ducts	Present, common orifice (Hudák and Kachlík, 2015)	Separate orifice of the bile and pancreatic ducts (Lærke and Hedemann, 2012)	In rodents, the pancreas is diffusely spread throughout the mesentery, so that the pancreatic papillae may be multiple (Treuting et al., 2017)	
Accessory duodenal papilla	Present – orifice of the accessory pancreatic duct (Hudák and Kachlík, 2015)	Present – orifice of the accessory pancreatic duct (Ferrer et al., 2008)		
Villi	Leaf-like, numerous (Balko et al., 2016)	Leaf-like, numerous (Skrzypek et al., 2005)	Leaf-like, tall (Treuting et al., 2017)	
Intestinal glands (of Brunner)	They fill a large part of the submucosa of the entire duodenum (Balko et al., 2016)	Present in the submucosa from the duodenal bulb to 45–50 cm distal to the pancreatic duct orifice. The abundance of duodenal glands in the submucosa decreases in the proximodistal direction (Caeleton, 1935)	Present in the submucosa forming a compact mass beginning at the pyloric sphincter and stretching down the length of duodenum (Krause and Leeson, 1967)	In the oral part, thickening of submucosa due to their presence (Friend, 1965)

Table 6. Interspecies differences in the anatomy and histology of duodenum in human, pig, rat, and mouse.

1.9.6.3 Differences in jejunum and ileum

In human, the jejunum represents about two fifths of the small intestine length and the ileum represents the remaining three fifths (Sensoy, 2021). In rats, the length of jejunum is 100 cm (Sharp and Villano, 2013), whereas in mice jejunum is 31.2 to 33.8 cm (Casteleyn et al.,

2010) long. Rat ileum is much shorter than jejunum, with 2.5 to 3.5 cm (Kararli, 1995). Mouse ileum has 4 to 4.6 cm in length (Casteleyn et al., 2010).

	Human	Pig	Rat	Mouse
Length	up to 2 metres (Hudák and Kachlík, 2015)	14–19 m (Al Masri et al., 2015)	100 cm (Sharp and Villano, 2013)	31.2–33.8 cm (Casteleyn et al., 2010)
Diameter	3 cm (Hudák and Kachlík, 2015)	4.2–6.0 mm in neonate piglets (de Castro et al.,2001), value for adults not found - Medline and Google search on 29th March 2023 using keywords diameter, jejunum, pig, swine	4–5 mm (Kararli, 1995b)	2.7–3 mm (Casteleyn et al., 2010)
Villi	Finger-like, numerous and long (Balko et al., 2016)	The villi become progressively longer from the duodenum towards the center of the jejunum (Lærke and Hedemann, 2012)	High and cylindrical (Treuting et al., 2017), decreasing height in proximodistal direction from duodenum to ileum (Hosoyamada and Sakai, 2005)	
Paneth cells	Present throughout the small intestine, caecum, and vermiform appendix (Balko et al., 2016)	Present, (Myer, 1982; van der Hee et al., 2018), however, the validity of their presence remains disputed (van der Hee et al., 2018; Wallaeys et al. in 2023)	Present mainly in the jejunum (Treuting et al., 2017)	
Lymphatic tissue	Solitary and aggregated (Peyer's patches) lymphatic nodules throughout the small intestine. Increase in abundance of Peyer's patches in proximodistal direction (Cornes J.S., 1965)	Several distinct Peyer's patches in the jejunum and oral ileum (Kararli, 1995)	Peyer's patches most abundant in jejunum, on the antimesenteric side of the intestine (Treuting et al., 2017)	

Table 7. Interspecies differences in the anatomy and histology of jejunum in human, pig, rat, and mouse.

In all species, the superior mesenteric artery is the source of arterial supply for both the jejunum and the ileum (Treuting et al., 2017). The histological composition of the jejunum and ileum is nearly identical, with the exception of the villi and the presence or absence of Paneth cells. Jejunal villi are long and cylindrical, while in the ileum they are short and roll-shaped. Paneth cells are found especially in the jejunum and are characterized by very marked granules, exclusively in the small intestine in rodents. In human, the Paneth cells can be found also in the vermiform appendix and caecum. In rodents, Peyer's patches are most abundant in the jejunum, but in human in the terminal ileum. Rodent submucosa is thin; in human, it includes fat cells and collagenous connective tissue (Treuting et al., 2017). The overview of

differences in the jejunum anatomy and histology among humans and commonly used laboratory mammals are shown in **Table 7**. The comparison of cross-section of jejunum in mouse and rat is shown in **Figure 17**. The overview of interspecies differences in ileum can be found in **Table 8**.

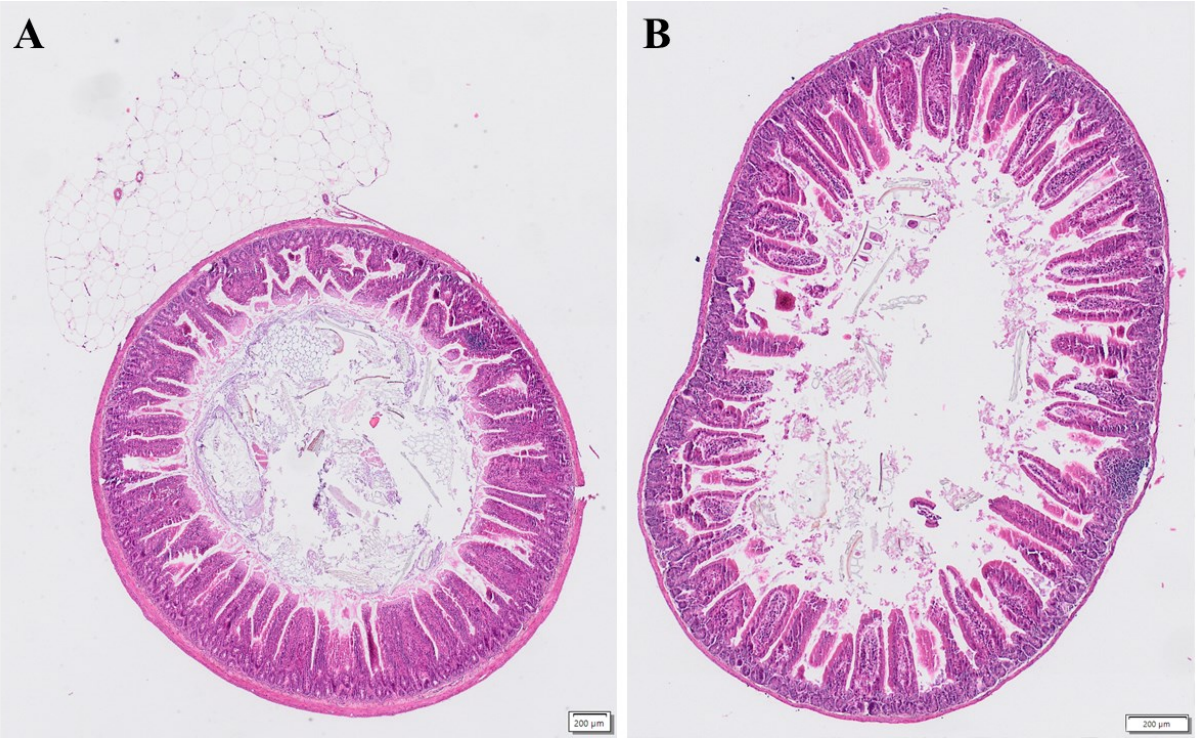

Figure 17. Cross section of rat (A) and mouse (B) jejunum. Histological staining with hematoxylin-eosin. Scale 200 µm. The muscular layer of the rat jejunum is thicker than in mice. The scale of the mouse jejunum is smaller. Otherwise, the structure of the jejunum in both species is very similar.

	Human	**Pig**	**Rat**	**Mouse**
Length	Up to 3 metres (Hudák and Kachlík, 2015)	70–100 cm (Al Masri et al., 2015)	2.5–3.5 cm (Kararli, 1995)	4–4.6 cm (Casteleyn et al., 2010)
Diameter	Approximately 2.5 cm (Hudák and Kachlík, 2015)	4.8–6.5 mm in neonate piglets (de Castro et al., 2001), value for adults not found - Medline and Google search on 29th March 2023 using keywords diameter, ileum, pig, swine	3–5 mm (Kararli, 1995)	2.3–2.5 mm (Casteleyn et al., 2010)
Villi	Few, shorter, filamentous (Balko et al., 2016)	Less numerous, decreasing length from mid jejunum to terminal ileum (Lærke and Hedemann, 2012)	Short, finger-like (Treuting et al., 2017)	
Lymphatic tissue	Solitary and aggregated (Peyer's patches) lymphatic nodules, most abundant in the terminal ileum (Cornes J.S., 1965)	The abundance of lymphatic tissue rises in the proximodistal direction and there is one unbroken Peyer's patch in the terminal ileum (Kararli, 1995)	Separate lymph nodes and Peyer's patches in smaller numbers than in jejunum (Treuting et al., 2017)	

Table 8. Interspecies differences in the anatomy and histology of ileum in human, pig, rat, and mouse.

1.9.7 Differences in rodent and human large intestine structure

Similar to humans, the large intestine of rodents has three parts – the caecum, colon and rectum. The colon is divided in the proximal part that represents about one half of colon length, the middle part and the distal part. The mucosa of rodent large intestine is rich in goblet cells that secrete mucus. The bacterial flora of rodents is rich given its higher importance compared to human. Intestinal wall structure in rodents is similar to that in human. Rodent serosa is smooth, and it has no taenia, haustra and omental appendaces (Treuting et al., 2017). The overview of differences in the large intestine anatomy and histology among humans and commonly used laboratory mammals are shown in **Table 9**.

	Human	**Pigs**	**Rat**	**Mouse**
Length	1.2–1.5 m (Hudák and Kachlík, 2015)	4–6 m (Gonzalez et al., 2015)	22–26 cm (Kararli, 1995)	10.9–12.5 cm (Casteleyn et al., 2010)
Diameter	5 cm (Hudák and Kachlík, 2015)	1.6–3 cm (Hecker and Grovum, 1975)	3–10 mm (Kararli, 1995)	2.7–2.9 mm (Casteleyn et al., 2010)
Haustra	Present (Hudák and Kachlík, 2015)	Present (Hedemann et al., 2002)	Absent, fecal pellets in the aboral colon may mimic the haustra (Treuting et al., 2017)	
Taeniae	Three (Hudák and Kachlík, 2015)	Two (Hedemann et al., 2002) to three (Langer and Takács, 2004)	Absent (Treuting et al., 2017)	Absent (Treuting et al., 2017)
Epiploic appendices	Present (Hudák and Kachlík, 2015)	No mention of omental appendices in pigs in the literature – Medline and Google Search on 26th March 2023 using key words: epiploic appendices, pig, swine large intestine, colon	Absent (Suckow et al., 2011)	Absent (Suckow et al., 2011)
Semilunar fonds	Present, increasing manifestation in the proximodistal direction (Balko et al., 2016)	Present (Langer and Takács, 2004)	Recently has been reported that cotton rats have a single longitudinal mucosal fold throughout the large intestine (Chuluunbaatar et al., 2020)	Absent (Langer and Takács, 2004; Treuting PM et al., 2017)

Table 9. Interspecies differences in the anatomy and histology of large intestine in human, pig, rat, and mouse.

1.9.7.1 Differences in cecum

In rodents, the cecum forms an incurvated blind sac representing approximately one third of the large intestine length. The apical blind end contains a lot of GALT. It works on the principle of a fermentation tank that contains large amounts of bacterial and other protozoan organisms; the degree of bacterial fermentation and also of the size of the cecum depend on rodent diet. Commensal intestinal microflora produces free fatty acids, vitamin K and some B group vitamins in the rodent cecum. In human, the relative size of the cecum is much smaller. Transverse folds are present in the mucosa of the rodent caecum and oral large intestine (Treuting et al., 2017). The overview of differences in the cecum anatomy and histology among humans and commonly used laboratory mammals are shown in **Table 10**.

	Human	**Pig**	**Rat**	**Mouse**
Length	5 cm (Hudák and Kachlík, 2015)	20–30 cm (Mochizuki and Makita, 1998)	5–7 cm (Kararli, 1995)	3.2–3.8 cm (Casteleyn et al., 2010)
Diameter	7 cm (Hudák and Kachlík, 2015)	8–10 cm (Mochizuki and Makita, 1998)	1 cm (Kararli, 1995)	4.9–5.4 mm (Casteleyn et al., 2010)
Vermiform appendix	Present, 6–10 cm in length, redundant immunological function, important gut microbiome storage organ (Girard-Madoux et al., 2018)	Absent (Gonzalez et al., 2015)	Present, the appendix in rat functions as a transitional area that plays a role in regulating the microflora of both the small and large intestines (Shao et al., 2023)	Present, regulatory function of gut microbiota, possible involvement in the development of IBD (Alkadhi et al., 2014)
Functions	Electrolyte and water absorption (Moran and Jackson, 1992)	Minimal (Lloyd et al., 1958)	Fermentation tank principle, large number of bacteria and protozoa – production of fatty acids, vitamin K and B (Treuting et al., 2017)	
GALT	Abundant in the appendix area (Balko et al., 2016)	The cecum is completely covered with lymphatic nodules (Merchant et al., 2011)	Rich (Treuting et al., 2017)	

Table 10. Interspecies differences in the anatomy and histology of cecum in human, pig, rat, and mouse.

1.9.7.2 Differences in colon

Both in mice and rats, the colon exhibits a classical structure of the wall. Fecal pellets in the aboral large intestine of rodents may imitate haustra, which are not present in rodents, though. Characteristic mucosal folds are found in the proximal and distal parts of the rodent colon.

The oral colon of rodents exhibits transverse folding of the mucosa; the middle part is flat, and the aboral colon has longitudinal folds. In the oral colon of rats, transverse folds of the mucosa are visible through the serosa, while in mice these folds are not visible through the whole intestine. Unlike rodents, human mucosa of the large intestine has semilunar folds that become more distinct in the proximodistal direction. Given the thin colonic wall of mice, mucosal herniations occur to a higher extent, especially with an inflammation of the large intestine or at anatomically weaker points such as where blood vessels enter the colonic wall or around lymphatic nodules. Herniations do not occur in rats. The rodent thickness of the muscular layer increases in the proximodistal direction, forming longitudinal folds in the aboral segment of the large intestine (Treuting et al., 2017). The overview of differences in the colon anatomy and histology among humans and commonly used laboratory mammals are shown in **Table 11**.

	Human	**Pig**	**Rat**	**Mouse**
Division	Ascending colon (20–25 cm) Transverse colon (40 cm) Descending colon (20–25 cm) Sigmoid colon (20–25 cm) (Hudák and Kachlík, 2015)	Ascending colon (spiral colon) Transverse colon Descending colon (Mochizuki and Makita, 1998)	Proximal colon (half length) Middle colon Distal colon (Treuting et al., 2017)	
Mucosa	Without villi (Kararli, 1995)			

Table 11. Interspecies differences in the anatomy and histology of colon in human, pig, rat, and mouse.

	Human	**Pig**	**Rat**	**Mouse**
Length	16 – 18 cm (Hudák and Kachlík, 2015)	20 – 22 cm (Plakhotnyi et al., 2021)	8 cm (Kararli, 1995)	1 – 2 mm (Treuting et al., 2017)
Microstructure	Very complex (Hudák and Kachlík, 2015)	Highly similar to the anatomical and microscopical structure of the human rectum (Plakhotnyi et al., 2021)	Identical to the aboral colon - without anal transition zone - simple sphincter (Treuting et al., 2017)	Identical to the aboral colon - without anal transition zone - frequent rectal prolapse - simple sphincter (Treuting et al., 2017)

Table 12. Interspecies differences in the anatomy and histology of rectum in human, pig, rat, and mouse.

1.9.7.3 Differences in rectum

The rodent rectum is relatively short. In mice, it is about 1–2 mm long (Treuting et al., 2017), and 8 cm long in rats (Kararli, 1995). Rectal prolapse can be observed relatively often in mice, while rats are resistant to this phenomenon. The rectum of rodents is straight and difficult to distinguish from the aboral colon; also, the histological structure of its wall is identical to that of the aboral colon. The definition of human anorectal boundaries differs according to medical disciplines, and, for example, it has an impact on the treatment of colorectal cancer. In rodents, a sudden transition of rectal crypts with glandular mucosa into the squamous mucosa of the anal canal can be observed. Thus, unlike human, rodents have no anal transitional zone of the stratified columnar epithelium. Rodents have a large amount of modified sebaceous circumanal glands, while in human, large apocrine glands are found in the perianal region, localized in cutaneous dermis (Treuting et al., 2017). The overview of differences in the rectum anatomy and histology among humans and commonly used laboratory mammals are shown in **Table 12**.

1.9.8 Open issues of the use of experimental models in surgery

A number of obstacles and limits are encountered in experimental work, which prevent perfect translation of experimental results from research in animal models. Among others, these include the very complex immune system with considerable interspecies differences, and the limited possibilities of simulating risk factors in animal models such as, for example, high age, smoking, alcohol abuse, diabetes, hypertension (Herson and Traystman, 2014; van der Worp et al., 2010). Anatomical interspecies differences pose another obstacle, which restrict the use of individual models only for a certain experiment (Akhtar, 2015). Experience and manual dexterity of the surgeon also play a role in surgical experimental work given that technical execution of the surgery may have a considerable impact on the result of the entire experiment, as well (El Boghdady and Ewalds-Kvist, 2021).

In various aspects of human medicine, numerous problems remain unresolved, making experimental animal studies the sole option. Although selecting the most appropriate experimental animal and correctly interpreting the findings necessitate close consideration, they remain a beacon of hope.

2 Aims and hypotheses

This Ph.D. thesis is based on a collection of four studies dealing with quantitative histology using stereological methods and the use of animal models in experimental surgery. The first study was focused on the development of software for generating standardized images with known volumes, surfaces, lengths and numbers of objects to calibrate and set up a system for analysing image data obtained from microtomography. The second paper, a methodological review I contributed to, was on the proper and effective use of multilevel sampling in digital microscopy and stereological studies. The third study was on the topic of experimental anastomosis fortification in porcine small intestine using nanomaterials. My first-authored paper discusses in detail the differences in healing of porcine small and large intestine.

We have defined the following questions:

1. How can the reliability of parametric data obtained by automated image analysis of micro-CT scans be verified? What are the principles of proper calibration of a system for automated image analysis of micro-CT scans?

2. What are the digital microscopy procedures? What are the principles to be followed for correct multilevel sampling in quantitative histology?

3. Is the use of nonwoven nanomaterials made of biodegradable polymers safe in abdominal surgery? How do these nanomaterials affect the healing of intestinal anastomosis in an experimental porcine model?

4. Are there differences in mitotic activity, inflammatory neutrophilic infiltration, microvessel density, and collagen synthesis between anastomotic and non-anastomotic regions of the intestinal wall?

5. Can significant differences be found in mitotic activity, inflammatory neutrophilic infiltration, microvessel density and collagen synthesis between small intestine anastomoses without standardized defect, small intestine anastomoses with defect and large intestine anastomoses with defect?

6. Do the correlation patterns of mitotic activity, inflammatory neutrophilic infiltration, microvessel density, and collagen synthesis in non-anastomotic and anastomotic regions, in small intestine without defect, small intestine with defect, and large intestine with defect coincide

2.1 Generating virtual images for testing and calibration of micro-CT image analysis

2.1.1 Background

Micro-CT is computed tomography with a resolution in the micrometer range. It is an effective and currently widely used method for the non-destructive visualization and analysis of X-ray-contrast two- and three-dimensional structures. When comparing micro-CT with classical microscopy, the greatest advantage of micro-CT is the possibility of imaging continuous and fibrous structures in 3D, without the need to degrade the object under examination by preparing a microscopic slide. The quantitative analysis performed on the basis of scans obtained from micro-CT results in parametric values (lengths, surfaces, volumes or numbers of objects) describing the properties of the investigated structures in 2D and 3D.

The resulting values are often considered to be correct, although they may be biased due to a number of variables. The extent of the bias caused by the processing of the image data is usually unknown. Variables affecting the reliability of the measurement results include, but are not limited to, the resolution of the micro-CT scans, image processing for noise suppression, anisotropy of the imaged structures, or thresholding when converting grayscale image data to a binary, black-and-white system. These adjustments to the image information are necessary due to the similar radio-opacity of the individual components of the materials under study, which results in insufficient contrast in the micro-CT scans. However, it should be kept in mind that even the best possible visual quality of micro-CT scans does not ensure accurate results of the quantitative assessment.

Verification of quantitative results at the microscopic level is either impossible or difficult to achieve, especially for complex three-dimensional structures. At the same time, no clear recommendations for thresholding image data in the study of biological materials have been published yet. For the calibration of a quantitative analysis system, the use of test images is a commonly used procedure in order to avoid significant bias in the acquired data and to increase the reliability of the results.

The motivation for this study was to create a freely available software providing calibration tools in the sense of virtual phantom images from micro-CT, to optimize calibration procedures, image data processing and limit the influence of these variables on the bias of the final quantification analysis outputs.

To the best of our knowledge, there is still no software that allows researchers working with micro-CT to calculate the bias in the analysis of micro-CT image data, based on virtual image sets with previously known object counts, lengths, surfaces or volumes, which would make it possible to demonstrate the effect of image processing on the accuracy of quantitative analysis results.

2.1.2 Aims of the study

The purpose of this investigation was to assemble a software tool called TeIGen (Test Image Generator) generating 3D virtual images with known quantitative specifics like object counts, lengths, area of their surface or known volumes. These virtual simulations were designed to work as calibrations instruments for correct interpretation of micro-CT scans. Additionally, we aimed to tackle potential biases and sources of error in image data and setup-up of measurement tools and provide practical advice on how to get more accurate readings and refine the quantitative analysis.

The main goal of the work was to create new software TeIGen. In this sense, an extensive analysis was carried out to test the accuracy and robustness of the measurement methods in the analysis of data obtained by measuring fibrous and porous structures using micro-CT. Thus, the null hypotheses of this study were not predefined.

2.2 Using digital microscopy to develop multilevel sampling strategies in quantitative histology and stereology

2.2.1 Background

Stereology is a collection of instruments one can use to obtain a quantitative information on objects without the need of prior knowledge of their distribution, shape or size. In order to be able to produce accurate data using stereology, one needs to follow the sampling guidelines correctly. If these guidelines are adhered to, results are always repeatable. For these reasons, stereology has become commonly employed in quantitative studies of histological samples.

Morphological studies often rely on multilevel sampling, which involves collecting tissue samples from organs, in which the histological analysis of the whole organ is impossible to achieve (such as the brain of liver), choosing histological specimens from these samples, and selecting microscopic fields of view for closer examination. Unbiased sampling is a fundamental rule of multilevel sampling - meaning, each region of the studied tissue must

have an equal chance as any other to get studied. Additionally, the sampling process must remain unbiased throughout all stages of multilevel sampling in order to keep the research repeatable and precise. On the other hand, if sampling is performed accurately, it allows the measurement procedure to be optimized so that the study precisely describes those tissue samples where the differences under investigation are most pronounced and, therefore, also require the most detailed sampling possible for a reliable description. With unbiased multilevel sampling, it is also possible to better justify not only the number of individuals that are included in the study, but also the number of tissue samples, histological slides, and number of fields of view that are included in the stereological measurements.

2.2.2 Aims of the study

The aim of the study was to describe the procedures and means used in digital microscopy to improve the efficiency and reproducibility of results in research using stereological quantification. Methodological recommendations were made based on a wide range of tissues and procedures. Thus, no null hypothesis was tested by statistical evaluation. Instead, we compared the pros and cons of different multilevel sampling strategies and made methodological recommendations that can be generally applied.

2.3 Fortification of intestinal anastomoses with nanomaterials in an experimental porcine model

2.3.1 Background

One of the biggest problems in gastrointestinal surgery is anastomotic leak (Hyman et al., 2007; Jex et al., 1987). Although the rate of many GI anastomosis-related complications has been reduced over the years, there is still some anastomotic leakage and persistence of complications associated with this phenomenon. Anastomotic leak often leads to prolonged hospitalization of patients. The clinical severity of anastomotic leak varies widely. Mileski et al. reported that minor anastomotic leaks may be difficult to detect, often only an increase in inflammatory markers is observed (Mileski et al., 1988). Incomplete dehiscence of the anastomosis can very often be treated conservatively with antibiotics and parenteral nutrition until spontaneous healing of the anastomosis without significant complications takes place (Chadi et al., 2016; Sevim et al., 2016; Thomas and Margolin, 2016; Blumetti and Abcarian, 2015). Incomplete dehiscence of the anastomosis often involves elevated C-reactive protein

(CRP) levels, fever, abdominal pain, and increased discharge through drains (Gessler et al. 2017). In worst cases, reoperation is necessary, associated with a high risk of performing of a diverting stoma and increasing patient morbidity and mortality (Paliogiannis et al., 2012; Zhao et al., 2011). Several experimental and clinical studies have investigated different methods of local fortification of gastrointestinal anastomoses to positively influence anastomotic healing and, consequently, reduce the risk of developing anastomotic leakage. Hyaluronic acid derivatives, collagen patches, fibrin patches and other materials have been used (Bonanomi et al., 2004; Fajardo et al., 2012; Khorshidi et al., 2017; Nordentoft et al., 2007; Nordentoft and Holte, 2009; Trotter et al., 2018).

Peritoneal adhesions can develop as a result of any surgery in the abdomen. Their characteristics range from thin membranes to sturdy strands with a high content of fibrous tissue, and even blood vessels. Just like the appearance of the adhesions, their effects are also very diverse. In some patients they cause little or no difficulty, in others the adhesions significantly affect the quality of life. Subjectively, the patients feel abdominal cramps, flatulence, or tendency to constipation and must be very careful about the choice of food. The most serious complication of abdominal adhesions is the development of a mechanical ileus, which may require further surgery with adhesiolysis (Ellis et al., 1997; van Goor, 2007). Currently, there are no reliable products on the market that successfully reduce postoperative adhesions without negatively affecting the healing of gastrointestinal anastomoses.

Nanomaterials have gained the interest of the professional community in the field of tissue engineering due to the similarity of their microscopic structure to the extracellular matrix. The application of nanomaterials in the medical field has been experimentally described in several surgical studies to improve the biomechanical properties of various anatomical structures (Dahlin et al., 2011; Krchova et al., 2014; Yalcin et al., 2014). Whether the use of these materials can reduce the development of peritoneal adhesions has not been studied yet. Horakova et al. (2018) have proven in their investigation that for optimal outcomes, nanomaterials should possess the ability to resorb at a comparable speed as the physiological tissue healing. The basic process of the anastomotic healing lasts for approximately 21 days, even though the phase of scar tissue maturation takes several more months. Numerous biodegradable polymers are already used in human medicine today - e.g. the sutures conventionally used during surgical procedures are made from polycaprolactone and polylactic acid (Gunatillake, 2003).

2.3.2 Aims of the study

The objective of this investigation was to describe the impact of the application of electrospun nanomaterials (polylactic acid and polycaprolactone) on the physiology of the anastomotic healing and the genesis of peritoneal adhesions. In addition, we wanted to design a new scoring system for the classification of adhesions in the proximity of intestinal anastomoses.

2.4 Histological description of intestinal anastomotic healing in a porcine model

2.4.1 Background

Every year, a considerable number of patients undergo gastrointestinal surgery, where an anastomosis is performed. Although research on the development of anastomotic leakage has been going on for many years, the causes of its development have still not been fully described or understood (Binnebösel et al., 2014; Wu et al., 2013). Surgeons have more or less accepted that the exact mechanism of anastomotic failure remains unknown, and that anastomotic leakage cannot be completely prevented.
Pigs are widely used as a large animal experimental model due to their anatomical, physiological, and genetic similarities to humans (Boersema et al., 2017; Bonanomi et al., 2004; Nordentoft, 2015).

The anatomy of the swine intestine is useful for studying the differences in healing of the small and large intestine. The risk of anastomosis failure in the colon is higher than in the small intestine, which is mainly due to three factors: the presence of a rich intestinal flora, a fragile blood supply and the presence of solid stool and gas.

In previous studies (Rosendorf et al., 2021a, 2021b, 2020), small intestinal defects (SID) and large intestinal defects (LID) were assessed using semi-quantitative and quantitative scoring systems (total collagen fraction, volume fraction of von Willebrand factor (vWF) positive cells and MAC387-positive cells). This assessment focused on the entire thickness of the intestinal wall excluding the mucosa. In our study, we quantitatively assessed all layers of the intestinal wall individually except the mucosa.

2.4.2 Aims of the study

The aim of our study was to collect and critically evaluate quantitative histological data to contribute to a better understanding of small and large bowel anastomosis healing and its complications and to outline the possibility of further in vivo experimental studies.

Our objective was to address the problems, which remain unanswered about the intestinal anastomotic healing and, as far as we are aware, have not been mentioned in available literature in large animal models. In doing so, we developed the following hypotheses structured as null hypotheses that can be tested:

H0 (A): There are no significant differences in mitotic activity, inflammatory neutrophilic infiltration, microvessel density and collagen synthesis between anastomotic and non-anastomotic areas.

H0 (B): There are no significant differences in mitotic activity, inflammatory neutrophilic infiltration, microvessel density and collagen synthesis between small intestine anastomoses without standardized defect, small intestine anastomoses with defect and large intestine anastomoses with defect.

H0 (C): There are similar correlation patterns in mitotic activity, inflammatory neutrophilic infiltration, microvessel density, and collagen synthesis in non-anastomotic and anastomotic areas, in small intestine without defect, small intestine with defect, and large intestine with defect.

3 Materials and methods

3.1 Generating virtual images for testing and calibration of micro-CT image analysis

Using Python programming language, a novel software called TeIGen has been created. TeIGen produces virtual image stacks depicting fibrous and porous structures as seen on micro-CT scans. The software is also equipped with a noise generator to simulate realistic image data. Every image stack is defined by a set of specific morphometric parameters - object count, surface area, lengths and volumes. Throughout the phase of software testing and development, a total of 40 virtual image stacks produced by TeIGen, were subjected to a quantitative analysis using CTAn - software designated for micro-CT scans. Following this, we compared the results of the quantitative analysis obtained from CTAn with the previously preset values during the production of virtual images in TeIGen to assess the deviation between the actual and measured results. Based on the outcomes, the dedicated CTAn software could be calibrated to minimize the error in estimating quantitative results from the measurements, especially for colliding and continuous structures. Furthermore, our analysis provided a better understanding of the effect of thresholding, image resolution and background noise on the accuracy of the results.

3.2 Using digital microscopy to develop multilevel sampling strategies in quantitative histology and stereology

A number of digital slides from previous quantitative studies were used to compile our recommendations. For unbiased sampling, the rules of systematic and random selection of fields of view should be followed. The first field of view is selected randomly, and subsequent fields of view are chosen based on a pre-selected sampling interval. When selecting the fields of view, the results of readings are variable at different sampling rates. Thus, the goal of proper study design is to find a sampling frequency that makes the most efficient use of all resources – both material and time. To find the optimal multilevel sampling setting, standard deviation (SD) and coefficient of error (CE) are calculated as measures of variability. Estimates of the coefficient of error for spatially correlated objects are calculated based on the quadratic Matheron approximation (Gundersen and Jensen, 1987; Slomianka and West, 2005).

3.3 Fortification of intestinal anastomoses with nanomaterials in an experimental porcine model

We used a total of 24 piglets in our study. In each piglet, three anastomoses were sewn manually in an end-to-end manner in the small intestine. The contingent of our experimental animals was divided into three groups. In group 1 (n=8), we augmented the suture with a PCL patch, in group 2 (n=8) PLCL copolymer was applied as the fortification of the anastomosis, and group 3 (n=8) served as our control, with no added nanomaterial.

The period of clinical observation lasted 21 days. After three weeks, the tissue samples were surgically removed, and the piglets sacrificed. We developed a fixed plan of blood sample testing and re-alimentation. We analyzed creatinine, urea, albumin, ALP, ALT, AST, bilirubin, and CRP on the preoperative, first, seventh, fourteenth and twenty-first day.

During the second operation, our surgical team resected the tissue samples and examined the clinical and macroscopic evidence - i.e., presence of intestinal dilation or stenosis, peritoneal adhesions, or free intestinal contents in the abdomen. The anastomotic area was then resected, dissected along the long axis of the intestine at the transition of the intestinal serosa to the mesentery, mounted on cork and immersed in 10% formalin.

The evaluation of adhesions has been performed using Perianastomotic Adhesions Amount Score (PAAS), a novel scoring method invented as a part of the present study. The resected tissue samples were partitioned into four equal segments. Based on the degree of adhesions present, each segment was given a score ranging from zero to two. Zero points were awarded if the adhesions in the given segment were completely absent, one point if the segment was partially affected and two points were given for complete coverage.

Several staining techniques were employed in the preparation of histological slides. Histological staining was performed using hematoxylin-eosin, to highlight the connective tissue green trichrome was used. Collagen fibers were stained with picrosirius red for the polarized light microscopy. Additionally, immunohistochemistry with antibodies against the smooth muscle actin (smooth muscle), MAC387 (macrophages) and von Willebrand factor (endothelium) were chosen to complete the range of staining, in order to enable a detailed histological description of the intestinal healing.

Afterwards, stereological assessment of the entire intestinal wall, with the exception of the mucosa, was performed. Dedicated software (Stereologer and Ellipse) was utilized to perform a quantitative evaluation of virtual images of the ROI located 3mm from the center of the anastomosis, both proximally and distally. Utilizing stereological methods, volume

fractions of von Willebrand factor-positive cells, collagen fibers, and MAC387-positive cells were estimated.

3.4 Histological description of intestinal anastomotic healing in a porcine model

We carried out our investigation on 22 piglets of both sexes (female=12, male=10), that were split into three cohorts based on the type of the intestinal anastomoses. The groups included small intestine without defect (n=7), small intestine with defect (n=8), and large intestine with defect (n=7). For our analysis, we utilized histological staining with picrosirius red to observe the amount of type I and type III collagen using polarized light microscopy. Immunohistochemical antibodies were employed to display the cells in the mitotic phase (anti-Ki67), inflammatory infiltration with neutrophils (anti-MPO) and the density of microvessels (anti-vWF).

Digital microphotographs were taken according to the rules of systematic uniform sampling for each layer of the intestinal wall separately, except for the mucosa. Thus, the submucosa, muscle layer and subserosa were photographed. For the purpose of this study, we defined the region of interest (ROI) as the intestinal wall 3 mm proximally and distally from the middle of the anastomosis, with the exception of mucosa. In specimens exhibiting the discontinuity of the muscular layer or a presence of a pseudodiverticulum, the ROI was determined as the area 2 mm proximally and distally from the borders of the deformity. The rest of the specimen on both sides of the anastomosis area (proximally and distally) was considered as the ROI outside of it. Four microphotographs were captured in each layer of the intestinal wall separately in both ROIs, utilizing a 40x objective. In other words, 24 microphotographs were captured per slide. This sampling method was applied in all four staining sessions used. The total number of microphotographs taken was 2112.

Stereological methods were used to calculate the proliferation index, neutrophil volume fraction, type I and III collagen, and total collagen, and two-dimensional density of vascular profiles in each layer and ROI of the anastomosis and outside the anastomosis. Ellipse software (ViDiTo, Košice, Slovakia) was used for the measurements. Statistical processing of the results was performed using Statistica Base 11 software. All differences at $p<0.05$ are reported as significant.

4 Results and discussion

4.1 Generating virtual images for testing and calibration of micro-CT image analysis

4.1.1 Main findings

TeIGen, an open-source program, allows the researchers to create virtual image stacks of fibrous and porous structures with predefined morphometric characteristics, while mimicking the attributes of real scans obtained from micro-CT, such as the image resolution or background noise. Our analysis of the virtual images helped to better understand the effect of noise and resolution on the error in the quantification results. Error increased inversely proportional to image resolution and directly proportional to background noise.

Another possible use of this software is to pre-test the density of stereological grids used in the quantification analysis of the actual micro-CT image sets. The goal of such a stereological grid setup for measurements is to find an optimal compromise between laboriousness, time and reliability of the results.

The outcomes of this study were used for optimizing the parameters of stereological grids used for histological quantification in the main study (4.4).

4.1.2 Publication

Jiřík M., Bartoš M., Tomášek P., Malečková A., **Kural T.,** Horáková J., Lukáš D., Suchý T., Kochová P., Hubálek Kalbáčová M., Králíčková M., Tonar Z. Generating standardized image data for testing and calibrating quantification of volumes, surfaces, lengths, and object counts in fibrous and porous materials using X-ray microtomography. Microsc Res Tech. 2018 Jun;81(6):551-568. doi: 10.1002/jemt.23011.

$IF_{(JCR2017)}$ = 1.087. Q3 (Microscopy) https://pubmed.ncbi.nlm.nih.gov/29476582/

The publication is a part of this dissertation as Supplement I on the page 119.

4.2 Using digital microscopy to develop multilevel sampling strategies in quantitative histology and stereology

4.2.1 Main findings

When planning a histological study with the use of stereology, it is necessary to choose the correct method of selecting the fields of view. It is possible to evaluate either whole slides that have been converted to digital form using a scanner or only representative areas of the slide. If the number of specimens is limited or if the specimens are small in size, evaluation of the whole slide is appropriate. For larger specimens, the choice of sampling frequency also depends on the homogeneity or heterogeneity of the tissue under examination. In general, the magnitude of the sampling error is inversely proportional to the number of fields of view examined. For heterogeneous tissues, it is therefore advisable to first perform a pilot study to reliably determine the optimal sampling frequency.

When using stereological quantification in histology, at least the following criteria must be met: (i) all structures of the histological specimen should be clearly identifiable due to technically perfect histological staining and (ii) the boundaries of the region of interest are clearly defined, either by conventional means or by anatomical structure (Howard and Reed 2005, Mouton 2002). As mentioned above, the method of collection of the tissue under study, the method and frequency of selection of fields of view and the density of the structures studied in the tissue largely influence the results, which, depending on these parameters, can be highly variable, even if the tissue under study is one and the same (Gundersen and Osterby, 1981; Slomianka and West, 2005). When selecting histological sections and fields of view, it is advisable to proceed based on systematic random selection, because only in this way is the distribution of the selected samples that are further processed and evaluated uniform (Mayhew and Lucocq, 2015). To determine the correct sampling frequency at all levels, it is advisable to conduct a pilot study. This will avoid unnecessary time and money without gaining new or more accurate insights (Tschanz et al., 2014).

The outcomes of this study were used for optimizing the sampling of microscopic fields of view for the histological quantification in the main study (4.4).

4.2.2 Publication

Kolinko Y., Malečková A., Kochová P., Grajciarová M., Blassová T., **Kural T.,** Trailin A., Červenková L., Havránková J., Vištejnová L., Tonarová P., Moulisová V., Jiřík M., Zavaďáková A., Tichánek F., Liška V., Králíčková M., Witter K., Tonar Z. Using virtual microscopy for the development of sampling strategies in quantitative histology and design-based stereology. Anat Histol Embryol. 2022 Jan;51(1):3-22. doi: 10.1111/ahe.12765. **IF$_{(JCR2020)}$=1.114. Q3(Veterinary sciences)** https://pubmed.ncbi.nlm.nih.gov/34806204/
The publication is a part of this dissertation as Supplement II on the page 139.

4.3 Fortification of intestinal anastomoses with nanomaterials in an experimental porcine model

4.3.1 Main findings

There was no anastomosis insufficiency and no death of experimental animals during the experiment. Furthermore, there were no significant differences between groups for all measurements. Neither clinically nor histologically were morphological changes detected around the nanomaterial. In the case of adhesions, the differences between groups were not statistically significant, but the absolute numbers suggest that the used nanomaterials might favor adhesion formation.

The use of nanofibrous fortifications in intestinal anastomoses has not yet been described. We accomplished successfully designing a study to investigate the feasibility of using a nanomaterial for this specific objective. The handling of the used nanomaterial was uncomplicated. Throughout the course of our research, no significant issues were encountered, including no mortality. Intestinal obstruction and sepsis were also absent from the clinical evaluations conducted, and no changes in body weight were noted. In prior clinical studies, the majority of patients experienced anastomotic leak during the initial 14-day period following surgery. Our observation period lasted 21 days.

Based on the clinical findings of our investigation, it can be stated that all anastomoses healed entirely. Additionally, no structural alterations were seen neither in the abdominal cavity nor in the proximity of the anastomoses with applied nanomaterial, indicating the usage of the nanomaterial is harmless. Our observations do not provide a conclusive answer to the inquiry regarding the speed of nanomaterial biodegradation, as we always discovered the nanomaterial being visibly present at the site of application during the second operation.

Microscopically, we could observe an empty space in the subserosa, corresponding with the area of nanomaterial application, as it dissolved during the histological processing. This finding suggests, on one hand, the nanomaterial does not tend to dislocate once applied on the serosal surface of the intestine, on the other hand, the half-life of biodegradation is longer than anticipated. Interestingly, no significant morphological or other differences were discovered between the experimental cohorts through the statistical analysis. We pronounced this result to be positive – we came to the conclusion that the process of intestinal healing was not negatively impacted, and the scar tissue in the experimental groups was of comparable quality to scars that healed in a physiological manner.

Our team employed an innovative method to evaluate the degree of peritoneal adhesions in the proximity of the intestinal anastomoses (PAAS). While the variance in the quantity of peritoneal adhesions between the groups did not reach statistical significance, the raw figures indicated that the applied nanomaterial enhanced the development of peritoneal adhesions in its vicinity. This could potentially be attributed to the fibrous microstructure of the substance, which allows the penetration of fibroblasts from both surfaces of the material, as documented by Srouji (Srouji et al., 2005).

We were able to demonstrate the biocompatibility of the nanomaterials utilized in our research through the existence of physiological granulation tissue in its proximity. All laboratory values were in the normal range, which hints at the lack of negative systemic effects caused by the material. Such results were rather unsurprising, considering the fact that the used polymers have been utilized in human medicine for years.

Clinical benefits of nanomaterials may be highlighted in other experimental settings - i.e., in intestines with anastomotic defects, where positive outcomes such as decreased occurrence of major complications could be better recognized.

4.3.2 Publication

Rosendorf, J., Horáková J, Klíčová, M., Pálek, R., Červenková, L., **Kural, T.**, Hošek, P., Kříž, T., Tégl, V., Moulisová, V., Tonar, Z., Třeška, V., Lukáš, D., Liška, V. Experimental fortification of intestinal anastomoses with nanofibrous materials in a large animal model. Sci Rep. 2020 Jan 24;10(1):1134. DOI: 10.1038/s41598-020-58113-4.

$IF_{(JCR2020)}$ = 4.380. Q1 (Multidisciplinary Sciences)

https://pubmed.ncbi.nlm.nih.gov/31980716/

The publication is a part of this dissertation as Supplement III on the page 160.

4.4 Histological description of intestinal anastomotic healing in a porcine model

4.4.1 Main findings

Quantitative histological evaluation using stereological methods showed that the proliferation index, microvessel density and collagen volume fraction were higher in the anastomosis area. Neutrophilic infiltration was comparable in all layers of the intestine in the anastomosis area and outside the anastomosis. The presence of the anastomotic defect significantly affected the healing. However, the healing process seemed to be accomplished three weeks after the primary operation. Our detailed histological analysis has shown substantial discrepancies in the healing of porcine large and small intestine. Based on this finding, we can postulate a recommendation that the results of the healing in the small and large intestine should not be confused with each other. Furthermore, the presence of the anastomosis affected more the healing in the small intestine than the colonic segments.

The anastomosis area showed increased mitotic activity compared to the non-anastomosis area. The presence of neutrophils was comparable in all layers of the intestine, both in and outside the anastomosis area. This finding indicates that the inflammatory phase of healing is concluded after 21 days in the small and large intestine, even though in two of the experimental groups, a standardized defect while suturing the anastomosis has been performed. The proportion of collagen in the subserosa and muscular layer was found to be higher within the anastomotic region than outside of it, implying that a concomitant phenomenon of the amplified proliferation in these parts of the intestinal wall was also the higher matrix synthesis. The presence of an anastomosis defect appears to result in decreased microvessel density and delayed collagen maturation. The healing of submucosa in small intestine anastomoses was different from that of colic anastomoses. Small intestine submucosa showed less proliferation, fewer vascular profiles, and less type I and total collagen than colic anastomoses. This demonstrates that either the mechanisms of healing or the temporal sequence in the colon and small intestine are unmistakable.

Our research demonstrated that the existence of an anastomotic defect in the small intestine had an impact on the microstructure of the intestinal wall, even in non-anastomotic areas. A similar occurrence was observed in the colon, although to a lesser degree, indicating that the healing in non-anastomotic colonic regions is less influenced by the closeness of the

experimental defect. Based on this discovery, we suggest to acquire future tissue samples from non-anastomotic regions of the small intestine at a greater distance from the anastomosis than our initially chosen distance of 3 mm.

Semi-quantitative histological scoring systems (Rosendorf et al., 2021a, 2021b) provide a rapid and robust assessment of intestinal wall integrity. Detailed, yet laborious quantitative histological analysis, however, provides a much deeper understanding of the biological mechanisms of the healing process.

The results of this study showed that experiments on the small intestine of pigs should definitely not be considered interchangeable with results on the large intestine.

When evaluating the results, it is important to keep in mind that healing of intestinal anastomoses in pigs at 12–14 weeks of age is usually much faster than healing in human patients, which often include advanced age or cancer patients (Sparreboom et al., 2018). Studying intestinal anastomoses in the manner we propose, but at multiple time points after the primary surgery, would provide a significant advance in our understanding of gastrointestinal anastomosis healing.

4.4.2 Publication

Kural T., Grajciarová M., Rosendorf J., Pálek R., Červenková L., Malečková A., Šarčevic S., Liška V., Tonar Z. Histological mapping of healing of the small and large intestine - A quantitative study in a porcine model. Ann Anat. 2023 Apr 1;249:152095. doi: 10.1016/j.aanat.2023.152095. Epub ahead of print. PMID: 37011825.

$IF_{(JCR2021)}$ = 2.976. Q1 (Anatomy&Morphology)

https://pubmed.ncbi.nlm.nih.gov/37011825/

The publication is a part of this dissertation as Supplement IV on the page 173.

5 Conclusions

5.1 Generating virtual images for testing and calibration of micro-CT image analysis

The TeIGen software is freely available (available from: https://mjirik.github.io/teigen/) to all scientists involved in micro-CT analysis of fibrous and porous materials. It is used to create virtual image sets with known morphometric characteristics and can also be used to fine tune the quantification tools used to analyze micro-CT scans. The ability to identify combinations of material morphological properties and image characteristics of micro-CT scans that lead to bias in the results of quantitative analysis, based on preliminary measurements on virtual image sets created in TeIGen software, contributes significantly to the reliability and definitive results of the measurements, and consequently increases the value and reproducibility of the overall research.

5.2 Using digital microscopy to develop multilevel sampling strategies in quantitative histology and stereology

The effective use of scanning of conventional histological slides for their conversion to digital form, combined with unbiased sampling, is an effective way to follow the "do more less well" rule in histological research (Gundersen and Osterby, 1981). Digital microscopy has proven to be a very useful tool for streamlining proper sampling at the histological slide level. Uniform distribution can be achieved not only by scanning whole slides followed by systematic random selection of fields of view, but also by using a microscope with a motorized stage. When conducting research, it is crucial to adhere to the guidelines of standard unbiased random sampling. These guidelines are necessary for ensuring the accuracy and repeatability of both quantitative and qualitative studies. In addition, incorporating such principles is vital for maintaining validity, ethics, and efficiency in research results. To sum up our findings, all scientific digital histology slide scanners, and microscopes, featuring a motorized stage, should natively include modules enabling their users to easily follow the principles of standard unbiased random sampling of fields of view.

5.3 Fortification of intestinal anastomoses with nanomaterials in an experimental porcine model

Biodegradable nanomaterials have not yet been used in the field of intestinal anastomosis. Intestinal anastomoses healed normally despite the application of nanomaterials. A standardized protocol for clinical follow-up of animals after primary surgery was established. In addition, a new scoring system was developed to describe perianastomotic adhesions. A robust set of histological and stereological methods was assembled to assess intestinal anastomosis healing. Nanomaterials appear to be safe, but their positive effect on anastomosis healing has not yet been demonstrated.

5.4 Histological description of intestinal anastomotic healing in a porcine model

Quantitative histological mapping of proliferation index, neutrophil volume fraction, microvessel density, and volume fraction of type I, III, and total collagen in porcine small and large intestinal anastomoses yielded the following findings: (i) higher proliferation index, higher microvessel density and higher collagen volume fraction, but not neutrophil volume fraction, were found in the intestinal anastomosis; (ii) porcine large and small intestine are not interchangeable in terms of intestinal anastomosis healing. The presence of the experimental defect largely affected healing, although our findings suggest that healing was complete after 21 days; (iii) the healing process in the small intestine was found to be significantly influenced by the closeness to the anastomotic area, unlike the large intestine.

To summarize the findings of the thesis, the first two scientific papers, focused on the methodology of correct scientific work, have shown the importance of unbiased random sampling and truthful image analysis for the reproducibility and accuracy of the study results. The third study described and innovative application of biodegradable nanomaterials in the field of intestinal anastomosis healing. Although nanomaterials are believed to be safe, their potential to enhance anastomosis healing has yet to be proven. In my first-authored article, a plethora of histological and immunohistochemical staining methods as well as a thorough quantitative analysis using stereological methods have been used. We have shown that a detailed analysis of morphology of the intestinal wall can bring new findings even though the first impression of the study design might have appeared quite trivial.

6 References

Aitman, T.J., Critser, J.K., Cuppen, E., Dominiczak, A., Fernandez-Suarez, X.M., Flint, J., Gauguier, D., Geurts, A.M., Gould, M., Harris, P.C., Holmdahl, R., Hubner, N., Izsvák, Z., Jacob, H.J., Kuramoto, T., Kwitek, A.E., Marrone, A., Mashimo, T., Moreno, C., Mullins, J., Mullins, L., Olsson, T., Pravenec, M., Riley, L., Saar, K., Serikawa, T., Shull, J.D., Szpirer, C., Twigger, S.N., Voigt, B., Worley, K., 2008. Progress and prospects in rat genetics: a community view. Nat Genet 40, 516–522. https://doi.org/10.1038/ng.147

Akgül Y., Mahendroo M., 2014. Cervical Changes Accompanying Birth, in: The Guide to Investigation of Mouse Pregnancy. Elsevier, p. 391.

Akhtar, A., 2015. The Flaws and Human Harms of Animal Experimentation. Camb Q Health Ethics 24, 407–419. https://doi.org/10.1017/S0963180115000079

Al Masri, S., Hünigen, H., Al Aiyan, A., Rieger, J., Zentek, J., Richardson, K., Plendl, J., 2015. Influence of age at weaning and feeding regimes on the postnatal morphology of the porcine small intestine. Journal of Swine Health and Production 23, 186–203.

Albuquerque, A.A.S., Rossato, M., de Oliveira, J.A.A., Hyppolito, M.A., 2009. Understanding the anatomy of ears from guinea pigs and rats and its use in basic otologic research. Brazilian Journal of Otorhinolaryngology 75, 43–49. https://doi.org/10.1016/S1808-8694(15)30830-2

Alkadhi, S., Kunde, D., Cheluvappa, R., Randall-Demllo, S., Eri, R., 2014. The murine appendiceal microbiome is altered in spontaneous colitis and its pathological progression. Gut Pathog 6, 25. https://doi.org/10.1186/1757-4749-6-25

Ashraf, S.Q., Burns, E.M., Jani, A., Altman, S., Young, J.D., Cunningham, C., Faiz, O., Mortensen, N.J., 2013. The economic impact of anastomotic leakage after anterior resections in English NHS hospitals: are we adequately remunerating them? Colorectal Dis 15, e190-198. https://doi.org/10.1111/codi.12125

Aznan, M.I., Khan, O.H., Unar, A.O., Tuan Sharif, S.E., Khan, A.H., Syed Abd Aziz, S.H., Zakaria, A.D., 2016. Effect of Tualang honey on the anastomotic wound healing in large bowel anastomosis in rats-A randomized controlled trial. BMC Complement Altern Med 16, 28. https://doi.org/10.1186/s12906-016-1003-6

Bailey, A.J., Sims, T.J., Le Lous, O., Bazin, S., 1975. Collagen polymorphism in experimental granulation tissue. Biochem Biophys Res Commun 66, 1160–1165. https://doi.org/10.1016/0006-291x(75)90480-5

References

Balko J., Tonar Z., Varga I., 2016. Memorix histologie, 1st Edition. Triton, Prague.

Barbul, A., Breslin, R.J., Woodyard, J.P., Wasserkrug, H.L., Efron, G., 1989. The effect of in vivo T-helper and T-suppressor lymphocyte depletion on wound healing. Ann Surg 209, 479–483. https://doi.org/10.1097/00000658-198904000-00015

Baxter, V.K., Griffin, D.E., 2016. Animal Models. Viral Pathogenesis 125–138. https://doi.org/10.1016/B978-0-12-800964-2.00010-0

Bazer, F.W., Spencer, T.E., 2011. Chapter 5 - Hormones and Pregnancy in Eutherian Mammals, in: Norris, D.O., Lopez, K.H. (Eds.), Hormones and Reproduction of Vertebrates. Academic Press, London, pp. 73–94. https://doi.org/10.1016/B978-0-12-374928-4.10005-7

Bell, S.W., Walker, K.G., Rickard, M.J.F.X., Sinclair, G., Dent, O.F., Chapuis, P.H., Bokey, E.L., 2003. Anastomotic leakage after curative anterior resection results in a higher prevalence of local recurrence. Br J Surg 90, 1261–1266. https://doi.org/10.1002/bjs.4219

Benavides, F., Rülicke, T., Prins, J.-B., Bussell, J., Scavizzi, F., Cinelli, P., Herault, Y., Wedekind, D., 2020. Genetic quality assurance and genetic monitoring of laboratory mice and rats: FELASA Working Group Report. Lab Anim 54, 135–148. https://doi.org/10.1177/0023677219867719

Bertelsen, C.A., Andreasen, A.H., Jørgensen, T., Harling, H., Danish Colorectal Cancer Group, 2010. Anastomotic leakage after anterior resection for rectal cancer: risk factors. Colorectal Dis 12, 37–43. https://doi.org/10.1111/j.1463-1318.2008.01711.x

Bhatia, A., Shatanof, R.A., Bordoni, B., 2022. Embryology, Gastrointestinal, in: StatPearls. StatPearls Publishing, Treasure Island (FL).

Birk, D.E., Fitch, J.M., Babiarz, J.P., Linsenmayer, T.F., 1988. Collagen type I and type V are present in the same fibril in the avian corneal stroma. J Cell Biol 106, 999–1008. https://doi.org/10.1083/jcb.106.3.999

Bittman, E.L., Kilduff, T.S., Kriegsfeld, L.J., Szymusiak, R., Toth, L.A., Turek, F.W., 2013. Animal Care Practices in Experiments on Biological Rhythms and Sleep: Report of the Joint Task Force of the Society for Research on Biological Rhythms and the Sleep Research Society. J Am Assoc Lab Anim Sci 52, 437–443.

Blikslager, A.T., Roberts, M.C., Rhoads, J.M., Argenzio, R.A., 1997. Is reperfusion injury an important cause of mucosal damage after porcine intestinal ischemia? Surgery 121, 526–534. https://doi.org/10.1016/s0039-6060(97)90107-0

References

Bogers, H., Baken, L., Cohen-Overbeek, T.E., Koning, A.H.J., Willemsen, S.P., van der Spek, P.J., Exalto, N., Steegers, E.A.P., 2019. Evaluation of First-Trimester Physiological Midgut Herniation Using Three-Dimensional Ultrasound. Fetal Diagn Ther 45, 332–338. https://doi.org/10.1159/000489260

Boksa, P., 1997. Early Developmental Profiles of Plasma Corticosterone Are Altered by Birth Condition in the Rat: A Comparison of Vaginal Birth, Cesarean Section, and Cesarean Section with Added Anoxia. Pediatr Res 41, 34–43. https://doi.org/10.1203/00006450-199701000-00006

Bornstein, P., Sage, H., 1980. Structurally distinct collagen types. Annu Rev Biochem 49, 957–1003. https://doi.org/10.1146/annurev.bi.49.070180.004521

Braskén, P., 1991. Healing of experimental colon anastomosis. Eur J Surg Suppl 1–51.

Brunicardi, F. C., Hunter, J. G., Billiar, T. R., Andersen, D. K., Matthews, J. B., Dunn, D. L., & Pollock, R. E. (2014). Schwartz's Principles of Surgery, 10th edition. McGraw-Hill Education / Medical.

Caeleton, A., 1935. 25. The Distribution of Brunner's Glands in the Duodenum of Mammals. Proceedings of the Zoological Society of London 105, 385–390. https://doi.org/10.1111/j.1469-7998.1935.tb06255.x

Čapo, I., Hinić, N., Lalošević, D., Vučković, N., Stilinović, N., Marković, J., Sekulić, S., 2015. Vitamin C Depletion in Prenatal Guinea Pigs as a Model of Lissencephaly Type II. Vet Pathol 52, 1263–1271. https://doi.org/10.1177/0300985814561270

Carbone, L., 2011. Pain in Laboratory Animals: The Ethical and Regulatory Imperatives. PLoS One 6, e21578. https://doi.org/10.1371/journal.pone.0021578

Carmichael, J.C., Mills, S., 2006. Reoperation for small bowel obstruction-how critical is the timing? Clin Colon Rectal Surg 19, 181–187. https://doi.org/10.1055/s-2006-956438

Casteleyn, C., Rekecki, A., Van der Aa, A., Simoens, P., Van den Broeck, W., 2010. Surface area assessment of the murine intestinal tract as a prerequisite for oral dose translation from mouse to man. Lab Anim 44, 176–183. https://doi.org/10.1258/la.2009.009112

Cavaliere, G., 2017. A 14-day limit for bioethics: the debate over human embryo research. BMC Medical Ethics 18, 38. https://doi.org/10.1186/s12910-017-0198-5

Cekanova, M., Rathore, K., 2014. Animal models and therapeutic molecular targets of cancer: utility and limitations. Drug Des Devel Ther 8, 1911–1922. https://doi.org/10.2147/DDDT.S49584

References

Cheong, Y.C., Laird, S.M., Shelton, J.B., Ledger, W.L., Li, T.C., Cooke, I.D., 2002. The correlation of adhesions and peritoneal fluid cytokine concentrations: a pilot study. Hum Reprod 17, 1039–1045. https://doi.org/10.1093/humrep/17.4.1039

Chin, A.M., Hill, D.R., Aurora, M., Spence, J.R., 2017. Morphogenesis and maturation of the embryonic and postnatal intestine. Seminars in Cell & Developmental Biology, Development of the digestive organs 66, 81–93. https://doi.org/10.1016/j.semcdb.2017.01.011

Chitturi, R.T., Balasubramaniam, A.M., Parameswar, R.A., Kesavan, G., Haris, K.T.M., Mohideen, K., 2015. The role of myofibroblasts in wound healing, contraction and its clinical implications in cleft palate repair. J Int Oral Health 7, 75–80.

Choi, H.-K., Law, W.-L., Ho, J.W.C., 2006. Leakage after resection and intraperitoneal anastomosis for colorectal malignancy: analysis of risk factors. Dis Colon Rectum 49, 1719–1725. https://doi.org/10.1007/s10350-006-0703-2

Chuluunbaatar, T., Ichii, O., Nakamura, T., Irie, T., Namba, T., Islam, M.R., Otani, Y., Masum, M.A., Okamatsu-Ogura, Y., Elewa, Y.H.A., Kon, Y., 2020. Unique Running Pattern and Mucosal Morphology Found in the Colon of Cotton Rats. Front Physiol 11, 587214. https://doi.org/10.3389/fphys.2020.587214

Clark, R.A., 1989. Wound repair. Curr Opin Cell Biol 1, 1000–1008. https://doi.org/10.1016/0955-0674(89)90072-0

Cornes J.S., 1965. Number, size, and distribution of Peyer's patches in the human small intestine: Part II The effect of age on Peyer's patches. Gut 6, 230–233. https://doi.org/10.1136/gut.6.3.230

Craik, E.M., Hippocrates, 1998. The Hippocratic treatise "On Anatomy." Class Q 48, 135–167. https://doi.org/10.1093/cq/48.1.135

Critchfield, T.S., 2011. To a Young Basic Scientist, About to Embark on a Program of Translational Research. Behav Anal 34, 137–148.

Crivellato, E., Ribatti, D., 2007. A portrait of Aristotle as an anatomist: historical article. Clin Anat 20, 447–485. https://doi.org/10.1002/ca.20432

Cronin, K., Jackson, D.S., Dunphy, J.E., 1968. Changing bursting strength and collagen content of the healing colon. Surg Gynecol Obstet 126, 747–753.

Darby, I., Skalli, O., Gabbiani, G., 1990. Alpha-smooth muscle actin is transiently expressed by myofibroblasts during experimental wound healing. Lab Invest 63, 21–29.

References

De Castro A.M.M.G., Alvares E.P., Zocoller-Seno M.C., Neves M.F., Passipiéri M., 2001. Morphological Study of The Small Intestine of Moura Pigs (Sus scrofa - Lineaus, 1758) during Fetal Development. Braz. J. morphol. Sci 18, 95–101.

De Roy van Zuidewijn, D.B., Wobbes, T., Hendriks, T., Klompmakers, A.A., de Boer, H.M., 1986. The effect of antineoplastic agents on the healing of small intestinal anastomoses in the rat. Cancer 58, 62–66. https://doi.org/10.1002/1097-0142(19860701)58:1<62::aid-cncr2820580112>3.0.co;2-x

De Santa Barbara, P., Van Den Brink, G.R., Roberts, D.J., 2003. Development and differentiation of the intestinal epithelium. Cell Mol Life Sci 60, 1322–1332. https://doi.org/10.1007/s00018-003-2289-3

Demers-Mathieu, V., 2022. The immature intestinal epithelial cells in preterm infants play a role in the necrotizing enterocolitis pathogenesis: A review. Health Sciences Review 4, 100033. https://doi.org/10.1016/j.hsr.2022.100033

Desmoulière, A., Chaponnier, C., Gabbiani, G., 2005. Tissue repair, contraction, and the myofibroblast. Wound Repair Regen 13, 7–12. https://doi.org/10.1111/j.1067-1927.2005.130102.x

Dietrich, M.R., Ankeny, R.A., Crowe, N., Green, S., Leonelli, S., 2020. How to choose your research organism. Stud Hist Philos Biol Biomed Sci 80, 101227. https://doi.org/10.1016/j.shpsc.2019.101227

Dignass, A., Lynch-Devaney, K., Kindon, H., Thim, L., Podolsky, D.K., 1994. Trefoil peptides promote epithelial migration through a transforming growth factor beta-independent pathway. J Clin Invest 94, 376–383. https://doi.org/10.1172/JCI117332

Doke, S.K., Dhawale, S.C., 2015. Alternatives to animal testing: A review. Saudi Pharm J 23, 223–229. https://doi.org/10.1016/j.jsps.2013.11.002

Dovi, J.V., He, L.-K., DiPietro, L.A., 2003. Accelerated wound closure in neutrophil-depleted mice. J Leukoc Biol 73, 448–455. https://doi.org/10.1189/jlb.0802406

Drozdowski, L.A., Clandinin, T., Thomson, A.B., 2010. Ontogeny, growth and development of the small intestine: Understanding pediatric gastroenterology. World J Gastroenterol 16, 787–799. https://doi.org/10.3748/wjg.v16.i7.787

Durbeej, M., 2010. Laminins. Cell Tissue Res 339, 259–268. https://doi.org/10.1007/s00441-009-0838-2

Eberl, T., Jagoditsch, M., Klingler, A., Tschmelitsch, J., 2008. Risk factors for anastomotic leakage after resection for rectal cancer. Am J Surg 196, 592–598. https://doi.org/10.1016/j.amjsurg.2007.10.023

Edriss, H., Rosales, B.N., Nugent, C., Conrad, C., Nugent, K. Islamic Medicine in the Middle Ages. Am J Med Sci. 2017 Sep;354(3):223-229. doi: 10.1016/j.amjms.2017.03.021

Efron, J.E., Frankel, H.L., Lazarou, S.A., Wasserkrug, H.L., Barbul, A., 1990. Wound healing and T-lymphocytes. J Surg Res 48, 460–463. https://doi.org/10.1016/0022-4804(90)90013-r

El Boghdady, M., Ewalds-Kvist, B.M., 2021. The innate aptitude's effect on the surgical task performance: a systematic review. Updates Surg 73, 2079–2093. https://doi.org/10.1007/s13304-021-01173-6

Ellis, H., Moran, B.J., Thompson, J.N., Parker, M.C., Wilson, M.S., Menzies, D., McGuire, A., Lower, A.M., Hawthorn, R.J., O'Brien, F., Buchan, S., Crowe, A.M., 1999. Adhesion-related hospital readmissions after abdominal and pelvic surgery: a retrospective cohort study. Lancet 353, 1476–1480. https://doi.org/10.1016/S0140-6736(98)09337-4

Emmer, K.M., Russart, K.L.G., Walker, W.H., Nelson, R.J., DeVries, A.C., 2018. Effects of Light at Night on Laboratory Animals and Research Outcomes. Behav Neurosci 132, 302–314. https://doi.org/10.1037/bne0000252

European Commission, 2013. Seventh Report on the Statistics on the Number of Animals Used for Experimental and Other Scientific Purposes in the Member States of the European Union. Brussels.

Eyden, B., 2007. The myofibroblast: a study of normal, reactive and neoplastic tissues, with an emphasis on ultrastructure. J Submicrosc Cytol Pathol 7–166.

Fang, F.C., Casadevall, A., 2010. Lost in translation--basic science in the era of translational research. Infect Immun 78, 563–566. https://doi.org/10.1128/IAI.01318-09

Feiken, E., Rømer, J., Eriksen, J., Lund, L.R., 1995. Neutrophils express tumor necrosis factor-alpha during mouse skin wound healing. J Invest Dermatol 105, 120–123. https://doi.org/10.1111/1523-1747.ep12313429

Ferrara, N., Davis-Smyth, T., 1997. The biology of vascular endothelial growth factor. Endocr Rev 18, 4–25. https://doi.org/10.1210/edrv.18.1.0287

Ferrer, J., Scott, W.E., Weegman, B.P., Suszynski, T.M., Sutherland, D.E.R., Hering, B.J., Papas, K.K., 2008. Pig Pancreas Anatomy: Implications for Pancreas Procurement,

Preservation, and Islet Isolation. Transplantation 86, 1503–1510. https://doi.org/10.1097/TP.0b013e31818bfda1

Fessler J.H., Fessler L.I., Mayne R., Burgeon R.E., 1987. Type V collagen, in: Structure and Function of Collagen Types. Academic Press Inc., London, pp. 81–103.

Festing, M.F.W., Altman, D.G., 2002. Guidelines for the design and statistical analysis of experiments using laboratory animals. ILAR J 43, 244–258. https://doi.org/10.1093/ilar.43.4.244

Fitts, D.A., 2011. Ethics and Animal Numbers: Informal Analyses, Uncertain Sample Sizes, Inefficient Replications, and Type I Errors. J Am Assoc Lab Anim Sci 50, 445–453.

Franco, N.H., 2013. Animal Experiments in Biomedical Research: A Historical Perspective. Animals (Basel) 3, 238–273. https://doi.org/10.3390/ani3010238

Frazer, L.C., Good, M., 2022. Intestinal epithelium in early life. Mucosal Immunology 15, 1181–1187. https://doi.org/10.1038/s41385-022-00579-8

Friend, D.S., 1965. The fine structure of Brunner's glands in the mouse. J Cell Biol 25, 563–576. https://doi.org/10.1083/jcb.25.3.563

Frixione, E., 2006. Albrecht von Haller (1708-1777). J Neurol 253, 265–266. https://doi.org/10.1007/s00415-006-0998-x

Gabella, G., 1987. The number of neurons in the small intestine of mice, guinea-pigs and sheep. Neuroscience 22, 737–752. https://doi.org/10.1016/0306-4522(87)90369-1

Gangane S.D., Borate S.M., 2018. Textbook of Embryology for Undergraduate Students. Thieme Medical Publishers, New Delhi.

Gauperaa, T., Seljelid, R., 1986. Plasma fibronectin is sequestered into tissue damaged by inflammation and trauma. Acta Chir Scand 152, 85–90.

Gilbert, S.F., 2000. Endoderm. Developmental Biology. 6th edition.

Girard-Madoux, M.J.H., Gomez de Agüero, M., Ganal-Vonarburg, S.C., Mooser, C., Belz, G.T., Macpherson, A.J., Vivier, E., 2018. The immunological functions of the Appendix: An example of redundancy? Semin Immunol 36, 31–44. https://doi.org/10.1016/j.smim.2018.02.005

Goñi-Balentziaga, O., Ortega-Saez, I., Vila, S., Azkona, G., 2022. A survey on the use of mice, pigs, dogs and monkeys as animal models in biomedical research in Spain. Lab Anim Res 38, 14. https://doi.org/10.1186/s42826-022-00124-5

References

Gonzalez, L.M., Moeser, A.J., Blikslager, A.T., 2015. Porcine models of digestive disease: the future of large animal translational research. Transl Res 166, 12–27. https://doi.org/10.1016/j.trsl.2015.01.004

Gookin, J.L., Rhoads, J.M., Argenzio, R.A., 2002. Inducible nitric oxide synthase mediates early epithelial repair of porcine ileum. Am J Physiol Gastrointest Liver Physiol 283, G157-168. https://doi.org/10.1152/ajpgi.00005.2001

Gordon J.I., 1989. Intestinal epithelial differentiation: new insights from chimeric and transgenic mice. J Cell Biol 108, 1187–1194.

Grinnell, F., Billingham, R.E., Burgess, L., 1981. Distribution of fibronectin during wound healing in vivo. J Invest Dermatol 76, 181–189. https://doi.org/10.1111/1523-1747.ep12525694

Hecker, J.F., Grovum, W.L., 1975. Rates of passage of digesta and water absorption along the larg intestines of sheep, cows and pigs. Aust J Biol Sci 28, 161–167. https://doi.org/10.1071/bi9750161

Hedemann, M.S., Kristiansen, E., Brunsgaard, G., 2002. Morphology of the large intestine of the pig: haustra versus taenia. Ann Anat 184, 401–403. https://doi.org/10.1016/S0940-9602(02)80065-6

Heindl, C., Hess, A., Brune, K., 2008. Refinement and reduction in animal experimentation: options for new imaging techniques. ALTEX 25, 121–125. https://doi.org/10.14573/altex.2008.2.121

Henning, S.J., 1981. Postnatal development: coordination of feeding, digestion, and metabolism. Am J Physiol 241, G199-214. https://doi.org/10.1152/ajpgi.1981.241.3.G199

Herson, P.S., Traystman, R.J., 2014. Animal models of stroke: translational potential at present and in 2050. Future Neurol 9, 541–551. https://doi.org/10.2217/fnl.14.44

Hesp, W.L., Hendriks, T., Schillings, P.H., Lubbers, E.J., de Boer, H.H., 1985. Histological features of wound repair: a comparison between experimental ileal and colonic anastomoses. Br J Exp Pathol 66, 511–518.

Hickman, D.L., Johnson, J., Vemulapalli, T.H., Crisler, J.R., Shepherd, R., 2017. Commonly Used Animal Models. Principles of Animal Research for Graduate and Undergraduate Students 117–175. https://doi.org/10.1016/B978-0-12-802151-4.00007-4

Hildebrand, R., 1996. [Illustration of humans in the anatomy of the Renaissance: Andrea Vesalius' De humani corporis fabrica libri septem, Basel 1543]. Ann Anat 178, 375–384.

Hosoyamada, Y., Sakai, T., 2005. Structural and mechanical architecture of the intestinal villi and crypts in the rat intestine: integrative reevaluation from ultrastructural analysis. Anat Embryol (Berl) 210, 1–12. https://doi.org/10.1007/s00429-005-0011-y

Hsieh, P., Chen, L.B., 1983. Behavior of cells seeded in isolated fibronectin matrices. J Cell Biol 96, 1208–1217. https://doi.org/10.1083/jcb.96.5.1208

Yang H., Xiong X., Yin Y., 2013. Development and Renewal of Intestinal Villi in Pigs, in: Nutritional and Physiological Functions of Amino Acids in Pigs. Springer-Verlag, Wien.

Hudák R., Kachlík D., 2015. Memorix anatomie, 3rd Edition. Triton, Prague.

Husarić, E., Hasukić, Š., Hotić, N., Halilbašić, A., Husarić, S., Hasukić, I., 2016. Risk factors for post-colectomy adhesive small bowel obstruction. Acta Med Acad 45, 121–127. https://doi.org/10.5644/ama2006-124.167

Hussain, M.Z., Ghani, Q.P., Hunt, T.K., 1989. Inhibition of prolyl hydroxylase by poly(ADP-ribose) and phosphoribosyl-AMP. Possible role of ADP-ribosylation in intracellular prolyl hydroxylase regulation. J Biol Chem 264, 7850–7855.

Indrio, F., Neu, J., Pettoello-Mantovani, M., Marchese, F., Martini, S., Salatto, A., Aceti, A., 2022. Development of the Gastrointestinal Tract in Newborns as a Challenge for an Appropriate Nutrition: A Narrative Review. Nutrients 14, 1405. https://doi.org/10.3390/nu14071405

Irvin, T.T., Hunt, T.K., 1974. Reappraisal of the healing process of anastomosis of the colon. Surg Gynecol Obstet 138, 741–746.

Jena, A., Montoya, C.A., Mullaney, J.A., Dilger, R.N., Young, W., McNabb, W.C., Roy, N.C., 2020. Gut-Brain Axis in the Early Postnatal Years of Life: A Developmental Perspective. Front Integr Neurosci 14, 44. https://doi.org/10.3389/fnint.2020.00044

Jensen, J.A., Hunt, T.K., Scheuenstuhl, H., Banda, M.J., 1986. Effect of lactate, pyruvate, and pH on secretion of angiogenesis and mitogenesis factors by macrophages. Lab Invest 54, 574–578.

Jiborn, H., Ahonen, J., Zederfeldt, B., 1978. Healing of experimental colonic anastomoses. I. Bursting strength of the colon after left colon resection and anastomosis. Am J Surg 136, 587–594. https://doi.org/10.1016/0002-9610(78)90315-x

Jiřík, M., Bartoš, M., Tomášek, P., Malečková, A., **Kural, T.,** Horáková, J., Lukáš, D., Suchý, T., Kochová, P., Hubálek Kalbáčová, M., Králíčková, M., Tonar, Z. Generating standardized image data for testing and calibrating quantification of volumes, surfaces, lengths, and object counts in fibrous and porous materials using X-ray microtomography. Microsc Res Tech. 2018 Jun;81(6):551-568. DOI: 10.1002/jemt.23011.

Johnson, M., 2022. Laboratory Mice and Rats. Materials and Methods.

Johnson, P.D., Besselsen, D.G., 2002. Practical aspects of experimental design in animal research. ILAR J 43, 202–206. https://doi.org/10.1093/ilar.43.4.202

Joyce, N.C., Haire, M.F., Palade, G.E., 1987. Morphologic and biochemical evidence for a contractile cell network within the rat intestinal mucosa. Gastroenterology 92, 68–81. https://doi.org/10.1016/0016-5085(87)90841-9

Jukic, A.M., Baird, D.D., Weinberg, C.R., McConnaughey, D.R., Wilcox, A.J., 2013. Length of human pregnancy and contributors to its natural variation. Hum Reprod 28, 2848–2855. https://doi.org/10.1093/humrep/det297

Kachlík, D., Baca, V., Stingl, J., 2010. The spatial arrangement of the human large intestinal wall blood circulation. J Anat 216, 335–343. https://doi.org/10.1111/j.1469-7580.2009.01199.x

Kafkafi, N., Agassi, J., Chesler, E.J., Crabbe, J.C., Crusio, W.E., Eilam, D., Gerlai, R., Golani, I., Gomez-Marin, A., Heller, R., Iraqi, F., Jaljuli, I., Karp, N.A., Morgan, H., Nicholson, G., Pfaff, D.W., Richter, S.H., Stark, P.B., Stiedl, O., Stodden, V., Tarantino, L.M., Tucci, V., Valdar, W., Williams, R.W., Würbel, H., Benjamini, Y., 2018. Reproducibility and replicability of rodent phenotyping in preclinical studies. Neuroscience & Biobehavioral Reviews 87, 218–232. https://doi.org/10.1016/j.neubiorev.2018.01.003

Kang, C.Y., Halabi, W.J., Chaudhry, O.O., Nguyen, V., Pigazzi, A., Carmichael, J.C., Mills, S., Stamos, M.J., 2013. Risk factors for anastomotic leakage after anterior resection for rectal cancer. JAMA Surg 148, 65–71. https://doi.org/10.1001/2013.jamasurg.2

Karamanou, M., Tsoucalas, G., Androutsos, G., 2013. Hallmarks in the study of respiratory physiology and the crucial role of Antoine-Laurent de Lavoisier (1743-1794). Am J Physiol Lung Cell Mol Physiol 305, L591-594. https://doi.org/10.1152/ajplung.00142.2013

Kararli, T.T., 1995. Comparison of the gastrointestinal anatomy, physiology, and biochemistry of humans and commonly used laboratory animals. Biopharm Drug Dispos 16, 351–380. https://doi.org/10.1002/bdd.2510160502

Kawasaki, H., Yamada, T., Wada, T., Kosugi, S., 2020. Current status and legal/ethical problems in the research use of the tissues of aborted human fetuses in Japan. Congenital Anomalies 60, 166–174. https://doi.org/10.1111/cga.12381

Kiani, A.K., Pheby, D., Henehan, G., Brown, R., Sieving, P., Sykora, P., Marks, R., Falsini, B., Capodicasa, N., Miertus, S., Lorusso, L., Dondossola, D., Tartaglia, G.M., Ergoren, M.C., Dundar, M., Michelini, S., Malacarne, D., Bonetti, G., Dautaj, A., Donato, K., Medori, M.C., Beccari, T., Samaja, M., Connelly, S.T., Martin, D., Morresi, A., Bacu, A., Herbst, K.L., Kapustin, M., Stuppia, L., Lumer, L., Farronato, G., Bertelli, M., 2022. Ethical considerations regarding animal experimentation. J Prev Med Hyg 63, E255–E266. https://doi.org/10.15167/2421-4248/jpmh2022.63.2S3.2768

Kivisaari, J., Vihersaari, T., Renvall, S., Niinikoski, J., 1975. Energy metabolism of experimental wounds at various oxygen environments. Ann Surg 181, 823–828. https://doi.org/10.1097/00000658-197506000-00011

Klein, M., Gögenur, I., Rosenberg, J., 2012. Postoperative use of non-steroidal anti-inflammatory drugs in patients with anastomotic leakage requiring reoperation after colorectal resection: cohort study based on prospective data. BMJ 345, e6166. https://doi.org/10.1136/bmj.e6166

Kleinman, H.K., Weeks, B.S., 1989. Laminin: structure, functions and receptors. Curr Opin Cell Biol 1, 964–967. https://doi.org/10.1016/0955-0674(89)90066-5

Kobayashi, E., Hishikawa, S., Teratani, T., Lefor, A.T., 2012. The pig as a model for translational research: overview of porcine animal models at Jichi Medical University. Transplant Res 1, 8. https://doi.org/10.1186/2047-1440-1-8

Kolinko, Y., Malečková, A., Kochová, P., Grajciarová, M., Blassová, T., **Kural, T.,** Trailin, A., Červenková, L., Havránková, J., Vištejnová, L., Tonarová, P., Moulisová, V., Jiřík, M., Zavaďáková, A., Tichánek, F., Liška, V., Králíčková, M., Witter, K., Tonar, Z. Using virtual microscopy for the development of sampling strategies in quantitative histology and designbased stereology. Anat. Histol. Embryol. 2022 Jan;51(1):3-22. DOI: 10.1111/ahe.12765.

Kosmidis, C., Efthimiadis, C., Anthimidis, G., Basdanis, G., Apostolidis, S., Hytiroglou, P., Vasiliadou, K., Prousalidis, J., Fahantidis, E., 2011. Myofibroblasts and colonic

anastomosis healing in Wistar rats. BMC Surg 11, 6. https://doi.org/10.1186/1471-2482-11-6

Kostouros, A., Koliarakis, I., Natsis, K., Spandidos, D.A., Tsatsakis, A., Tsiaoussis, J., 2020. Large intestine embryogenesis: Molecular pathways and related disorders (Review). Int J Mol Med 46, 27–57. https://doi.org/10.3892/ijmm.2020.4583

Krause, A., Kreiser, M., Puppe, B., Tuchscherer, A., Düpjan, S., 2021. The effect of age on discrimination learning and self-control in a marshmallow test for pigs. Sci Rep 11, 18287. https://doi.org/10.1038/s41598-021-97770-x

Krause, W.J., Leeson, C.R., 1967. The origin, development and differentiation of Brunner's glands in the rat. J Anat 101, 309–320.

Krieg, T., Hein, R., Hatamochi, A., Aumailley, M., 1988. Molecular and clinical aspects of connective tissue. Eur J Clin Invest 18, 105–123. https://doi.org/10.1111/j.1365-2362.1988.tb02400.x

Krumpholz, L., Clarke, J.F., Polak, S., Wiśniowska, B., 2022. An open-access data set of pig skin anatomy and physiology for modelling purposes. Database (Oxford) 2022, baac091. https://doi.org/10.1093/database/baac091

Kural T., Grajciarová M., Rosendorf J., Pálek R., Červenková L., Malečková A., Šarčevic S., Liška V., Tonar Z. Histological mapping of healing of the small and large intestine - A quantitative study in a porcine model. Ann Anat. 2023 Apr 1;249:152095. doi: 10.1016/j.aanat.2023.152095.

Kurkinen, M., Vaheri, A., Roberts, P.J., Stenman, S., 1980. Sequential appearance of fibronectin and collagen in experimental granulation tissue. Lab Invest 43, 47–51.

Lærke H.N., Hedemann M.S., 2012. The digestive system of the pig, in: Nutritional Physiology of Pigs. Videncenter for Svineproduktion, Aarhus.

Langer, P., Takács, A., 2004. Why are taeniae, haustra, and semilunar folds differentiated in the gastrointestinal tract of mammals, including man? J Morphol 259, 308–315. https://doi.org/10.1002/jmor.10176

Laurent, T.C., Laurent, U.B., Fraser, J.R., 1996. The structure and function of hyaluronan: An overview. Immunol Cell Biol 74, A1-7. https://doi.org/10.1038/icb.1996.32

Lee, S.Y., Park, K.J., Ryoo, S.-B., Oh, H.-K., Choe, E.K., Heo, S.C., 2014. Early postoperative small bowel obstruction is an independent risk factor for subsequent adhesive small bowel obstruction in patients undergoing open colectomy. World J Surg 38, 3007–3014. https://doi.org/10.1007/s00268-014-2711-z

Leibovich, S.J., Ross, R., 1975. The role of the macrophage in wound repair. A study with hydrocortisone and antimacrophage serum. Am J Pathol 78, 71–100.

Lerman, D.C., 2003. From the laboratory to community application: translational research in behavior analysis. J Appl Behav Anal 36, 415–419. https://doi.org/10.1901/jaba.2003.36-415

Levenson, S.M., Geever, E.F., Crowley, L.V., Oates, J.F., Berard, C.W., Rosen, H., 1965. The healing of rat skin wounds. Ann Surg 161, 293–308. https://doi.org/10.1097/00000658-196502000-00019

Li, F., Wang, D., Song, R., Cao, C., Zhang, Z., Wang, Yu, Li, Xiaoli, Huang, J., Liu, Q., Hou, N., Xu, B., Li, Xiao, Gao, X., Jia, Y., Zhao, J., Wang, Yanfang, 2020. The asynchronous establishment of chromatin 3D architecture between in vitro fertilized and uniparental preimplantation pig embryos. Genome Biology 21, 203. https://doi.org/10.1186/s13059-020-02095-z

Lineback, P.E., 1916. The development of the spiral coil in the large intestine of the pig. American Journal of Anatomy 20, 483–503. https://doi.org/10.1002/aja.1000200308

Llloyd L.E., Dale D.E., Crampton E.W., 1958. Role of the Caecum in Nutrient Utilization by the Pig | Journal of Animal Science | Oxford Academic [WWW Document]. https://academic.oup.com/jas/article-abstract/17/3/684/4739845?redirectedFrom=fulltext (accessed 4.2.23).

Lüllmann H., Mohr K., Hein L., 2018. Color atlas of pharmacology, 5th Edition. Thieme, Stuttgart.

Madden, J.C., Enoch, S.J., Paini, A., Cronin, M.T.D., 2020. A Review of In Silico Tools as Alternatives to Animal Testing: Principles, Resources and Applications. Altern Lab Anim 48, 146–172. https://doi.org/10.1177/0261192920965977

Maestri, E., 2021. The 3Rs Principle in Animal Experimentation: A Legal Review of the State of the Art in Europe and the Case in Italy. BioTech (Basel) 10, 9. https://doi.org/10.3390/biotech10020009

Majumdar, A.P., Johnson, L.R., 1982. Gastric mucosal cell proliferation during development in rats and effects of pentagastrin. Am J Physiol 242, G135-139. https://doi.org/10.1152/ajpgi.1982.242.2.G135

Mapara, M., Thomas, B.S., Bhat, K.M., 2012. Rabbit as an animal model for experimental research. Dent Res J (Isfahan) 9, 111–118. https://doi.org/10.4103/1735-3327.92960

Matthiessen, P., Hallböök, O., Rutegård, J., Simert, G., Sjödahl, R., 2007. Defunctioning stoma reduces symptomatic anastomotic leakage after low anterior resection of the rectum for cancer: a randomized multicenter trial. Ann Surg 246, 207–214. https://doi.org/10.1097/SLA.0b013e3180603024

McNamara, J.P., Hanigan, M.D., White, R.R., 2016. Invited review: Experimental design, data reporting, and sharing in support of animal systems modeling research1. Journal of Dairy Science 99, 9355–9371. https://doi.org/10.3168/jds.2015-10303

Merchant, H.A., McConnell, E.L., Liu, F., Ramaswamy, C., Kulkarni, R.P., Basit, A.W., Murdan, S., 2011. Assessment of gastrointestinal pH, fluid and lymphoid tissue in the guinea pig, rabbit and pig, and implications for their use in drug development. Eur J Pharm Sci 42, 3–10. https://doi.org/10.1016/j.ejps.2010.09.019

Meurens, F., Summerfield, A., Nauwynck, H., Saif, L., Gerdts, V., 2012. The pig: a model for human infectious diseases. Trends Microbiol 20, 50–57. https://doi.org/10.1016/j.tim.2011.11.002

Michel, P.A., Kronenberg, D., Neu, G., Stolberg-Stolberg, J., Frank, A., Pap, T., Langer, M., Fehr, M., Raschke, M.J., Stange, R., 2020. Microsurgical reconstruction affects the outcome in a translational mouse model for Achilles tendon healing. J Orthop Translat 24, 1–11. https://doi.org/10.1016/j.jot.2020.04.003

Miller, G., Boman, J., Shrier, I., Gordon, P.H., 2000. Etiology of small bowel obstruction. Am J Surg 180, 33–36. https://doi.org/10.1016/s0002-9610(00)00407-4

Mochizuki, S., Makita, T., 1998. Differences in intestinal length between specific-pathogen-free (SPF) and conventional swine. J Vet Med Sci 60, 545–548. https://doi.org/10.1292/jvms.60.545

Modina, S.C., Aidos, L., Rossi, R., Pocar, P., Corino, C., Di Giancamillo, A., 2021. Stages of Gut Development as a Useful Tool to Prevent Gut Alterations in Piglets. Animals (Basel) 11, 1412. https://doi.org/10.3390/ani11051412

Monk, B.J., Berman, M.L., Montz, F.J., 1994. Adhesions after extensive gynecologic surgery: clinical significance, etiology, and prevention. Am J Obstet Gynecol 170, 1396–1403. https://doi.org/10.1016/s0002-9378(94)70170-9

Montedori, A., Cirocchi, R., Farinella, E., Sciannameo, F., Abraha, I., 2010. Covering ileo- or colostomy in anterior resection for rectal carcinoma. Cochrane Database Syst Rev CD006878. https://doi.org/10.1002/14651858.CD006878.pub2

Moore, R., Carlson, S., Madara, J.L., 1989. Villus contraction aids repair of intestinal epithelium after injury. Am J Physiol 257, G274-283. https://doi.org/10.1152/ajpgi.1989.257.2.G274

Moran, B.J., Jackson, A.A., 1992. Function of the human colon. Br J Surg 79, 1132–1137. https://doi.org/10.1002/bjs.1800791106

Morris, S.A., 2017. Human embryos cultured in vitro to 14 days. Open Biol 7, 170003. https://doi.org/10.1098/rsob.170003

Muhr, J., Ackerman, K.M., 2022. Embryology, Gastrulation, in: StatPearls. StatPearls Publishing, Treasure Island (FL).

Myer, M.S., 1982. The presence of Paneth cells confirmed in the pig. Onderstepoort J Vet Res 49, 131–132.

Nakamura, H., Yokoyama, Y., Uehara, K., Kokuryo, T., Yamaguchi, J., Tsuzuki, T., Nagino, M., 2016. The effects of bevacizumab on intestinal anastomotic healing in rabbits. Surg Today 46, 1456–1463. https://doi.org/10.1007/s00595-016-1342-4

Nisar, P.J., Lavery, I.C., Kiran, R.P., 2012. Influence of neoadjuvant radiotherapy on anastomotic leak after restorative resection for rectal cancer. J Gastrointest Surg 16, 1750–1757. https://doi.org/10.1007/s11605-012-1936-0

Nowland, T.L., Plush, K.J., Barton, M., Kirkwood, R.N., 2019. Development and Function of the Intestinal Microbiome and Potential Implications for Pig Production. Animals (Basel) 9, 76. https://doi.org/10.3390/ani9030076

Nunoya, T., Shibuya, K., Saitoh, T., Yazawa, H., Nakamura, K., Baba, Y., Hirai, T., 2007. Use of Miniature Pig for Biomedical Research, with Reference to Toxicologic Studies. Journal of Toxicologic Pathology 20, 125–132. https://doi.org/10.1293/tox.20.125

O'Malley, C., Hubley, R., Moody, C., Turner, P., 2022. Use of nonaversive handling and training procedures for laboratory mice and rats: Attitudes of American and Canadian laboratory animal professionals. Frontiers in Veterinary Science 9. https://doi.org/10.3389/fvets.2022.1040572

Oyasiji, T., Helton, S.W., 2011. Survey of opinions on operative management of adhesive small bowel obstruction: laparoscopy versus laparotomy in the state of Connecticut. Surg Endosc 25, 2516–2521. https://doi.org/10.1007/s00464-011-1579-3

Pabst, R., 2020. The pig as a model for immunology research. Cell Tissue Res 380, 287–304. https://doi.org/10.1007/s00441-020-03206-9

Pankov, R., Yamada, K.M., 2002. Fibronectin at a glance. J Cell Sci 115, 3861–3863. https://doi.org/10.1242/jcs.00059

Plakhotnyi, R.O., Kerechanyn, I.V., Fedoniuk, L.Y., Kovalchuk, N.V., Dehtiariova, O.V., Singh, G., 2021. Comparative structure of mucosa coat of the pig's and the human's rectum. Wiad Lek 74, 1718–1723.

Pluske, J.R., 2016. Invited review: Aspects of gastrointestinal tract growth and maturation in the pre- and postweaning period of pigs. Journal of Animal Science 94, 399–411. https://doi.org/10.2527/jas.2015-9767

Pommergaard, H.C., Gessler, B., Burcharth, J., Angenete, E., Haglind, E., Rosenberg, J., 2014. Preoperative risk factors for anastomotic leakage after resection for colorectal cancer: a systematic review and meta-analysis. Colorectal Dis 16, 662–671. https://doi.org/10.1111/codi.12618

Powell, D.W., Mifflin, R.C., Valentich, J.D., Crowe, S.E., Saada, J.I., West, A.B., 1999. Myofibroblasts. II. Intestinal subepithelial myofibroblasts. Am J Physiol 277, C183-201. https://doi.org/10.1152/ajpcell.1999.277.2.C183

Puopolo, M., 2004. Biostatistical approaches to reducing the number of animals used in biomedical research. Ann Ist Super Sanita 40, 157–163.

Quaroni, A., 1986. Fetal characteristics of small intestinal crypt cells. Proc Natl Acad Sci U S A 83, 1723–1727. https://doi.org/10.1073/pnas.83.6.1723

Rahbari, N.N., Weitz, J., Hohenberger, W., Heald, R.J., Moran, B., Ulrich, A., Holm, T., Wong, W.D., Tiret, E., Moriya, Y., Laurberg, S., den Dulk, M., van de Velde, C., Büchler, M.W., 2010. Definition and grading of anastomotic leakage following anterior resection of the rectum: a proposal by the International Study Group of Rectal Cancer. Surgery 147, 339–351. https://doi.org/10.1016/j.surg.2009.10.012

Rao, M., Gershon, M.D., 2018. Enteric nervous system development: what could possibly go wrong? Nat Rev Neurosci 19, 552–565. https://doi.org/10.1038/s41583-018-0041-0

Raval, N.R., Nasser, A., Madsen, C.A., Beschorner, N., Beaman, E.E., Juhl, M., Lehel, S., Palner, M., Svarer, C., Plavén-Sigray, P., Jørgensen, L.M., Knudsen, G.M., 2022. An in vivo Pig Model for Testing Novel Positron Emission Tomography Radioligands Targeting Cerebral Protein Aggregates. Front Neurosci 16, 847074. https://doi.org/10.3389/fnins.2022.847074

Research, N.R.C. (US) and I. of M. (US) C. on the U. of L.A. in B. and B., 1988. Patterns of Animal Use, Use of Laboratory Animals in Biomedical and Behavioral Research. National Academies Press (US).

Rezzonico, R., Burger, D., Dayer, J.M., 1998. Direct contact between T lymphocytes and human dermal fibroblasts or synoviocytes down-regulates types I and III collagen production via cell-associated cytokines. J Biol Chem 273, 18720–18728. https://doi.org/10.1074/jbc.273.30.18720

Richards, W.O., Williams, L.F., 1988. Obstruction of the large and small intestine. Surg Clin North Am 68, 355–376. https://doi.org/10.1016/s0039-6109(16)44482-8

Rieger J., 2016. The Intestinal Mucosal Network in the Pig: A Histological View on Nutrition-Microbiota-Pathogen-Host-Interactions. Freie Universität Berlin, Berlin.

Ronneberger, H.J., 1977. Comparison of the pyrogen tests in rabbits and with limulus lysate. Dev Biol Stand 34, 27–36.

Rosendorf, J., Horáková J, Klíčová, M., Pálek, R., Červenková, L., **Kural, T.**, Hošek, P., Kříž, T., Tégl, V., Moulisová, V., Tonar, Z., Třeška, V., Lukáš, D., Liška, V. Experimental fortification of intestinal anastomoses with nanofibrous materials in a large animal model. Sci Rep. 2020 Jan 24;10(1):1134. DOI: 10.1038/s41598-020-58113-4.

Rosenthal, N., Brown, S., 2007. The mouse ascending: perspectives for human-disease models. Nat Cell Biol 9, 993–999. https://doi.org/10.1038/ncb437

Rowan J.P., Durrance K.L., Combs G.E., Fisher L.Z., 2015. The Digestive Tract of the Pig.

Rubin, D.C., Ong, D.E., Gordon, J.I., 1989. Cellular differentiation in the emerging fetal rat small intestinal epithelium: mosaic patterns of gene expression. Proc Natl Acad Sci U S A 86, 1278–1282.

Russell, W.M.S., Burch, R.L., 1959. The principles of humane experimental technique. Methuen, London.

Sartori, S.B., Landgraf, R., Singewald, N., 2011. The clinical implications of mouse models of enhanced anxiety. Future Neurol 6, 531–571. https://doi.org/10.2217/fnl.11.34

Schäffer, M., Barbul, A., 1998. Lymphocyte function in wound healing and following injury. Br J Surg 85, 444–460. https://doi.org/10.1046/j.1365-2168.1998.00734.x

Schittny, J.C., Yurchenco, P.D., 1989. Basement membranes: molecular organization and function in development and disease. Curr Opin Cell Biol 1, 983–988. https://doi.org/10.1016/0955-0674(89)90069-0

Sensoy, I., 2021. A review on the food digestion in the digestive tract and the used in vitro models. Curr Res Food Sci 4, 308–319. https://doi.org/10.1016/j.crfs.2021.04.004

Seo, S., Jeon, S., Ha, J.K., 2018. Guidelines for experimental design and statistical analyses in animal studies submitted for publication in the Asian-Australasian Journal of Animal Sciences. Asian-Australas J Anim Sci 31, 1381–1386. https://doi.org/10.5713/ajas.18.0468

Shao, C., Song, X., Wang, L., Zhang, H., Liu, Y., Wang, C., Chen, S., Ren, B., Wen, S., Xiao, J., Tang, L., 2023. Microbiome Structure and Mucosal Morphology of Jejunum Appendix and Colon of Rats in Health and Dysbiosis. Curr Microbiol 80, 127. https://doi.org/10.1007/s00284-023-03224-0

Sharp P., Villano J.S., 2013. The Laboratory Rat, 2nd Edition. CRC Press.

Shogan, B.D., Belogortseva, N., Luong, P.M., Zaborin, A., Lax, S., Bethel, C., Ward, M., Muldoon, J.P., Singer, M., An, G., Umanskiy, K., Konda, V., Shakhsheer, B., Luo, J., Klabbers, R., Hancock, L.E., Gilbert, J., Zaborina, O., Alverdy, J.C., 2015. Collagen degradation and MMP9 activation by Enterococcus faecalis contribute to intestinal anastomotic leak. Sci Transl Med 7, 286ra68. https://doi.org/10.1126/scitranslmed.3010658

Shogan, B.D., Carlisle, E.M., Alverdy, J.C., Umanskiy, K., 2013. Do we really know why colorectal anastomoses leak? J Gastrointest Surg 17, 1698–1707. https://doi.org/10.1007/s11605-013-2227-0

Shomer, N.H., Holcombe, H., Harkness, J.E., 2015. Biology and Diseases of Guinea Pigs. Laboratory Animal Medicine 247–283. https://doi.org/10.1016/B978-0-12-409527-4.00006-7

Shoulders, M.D., Raines, R.T., 2009. Collagen structure and stability. Annu Rev Biochem 78, 929–958. https://doi.org/10.1146/annurev.biochem.77.032207.120833

Singh, P., Ochoa Allemant, P., Brown, J., Perides, G., Freedman, S.D., Martin, C.R., 2019. Effect of polyunsaturated fatty acids on postnatal ileum development using the fat-1 transgenic mouse model. Pediatr Res 85, 556–565. https://doi.org/10.1038/s41390-019-0284-0

Skrzypek, T., Valverde Piedra, J.L., Skrzypek, H., Woliński, J., Kazimierczak, W., Szymańczyk, S., Pawłowska, M., Zabielski, R., 2005. Light and scanning electron microscopy evaluation of the postnatal small intestinal mucosa development in pigs. J Physiol Pharmacol 56 Suppl 3, 71–87.

Smith, D., Anderson, D., Degryse, A.-D., Bol, C., Criado, A., Ferrara, A., Franco, N.H., Gyertyan, I., Orellana, J.M., Ostergaard, G., Varga, O., Voipio, H.-M., 2018. Classification and reporting of severity experienced by animals used in scientific procedures: FELASA/ECLAM/ESLAV Working Group report. Lab Anim 52, 5–57. https://doi.org/10.1177/0023677217744587

Soffers, J.H., Hikspoors, J.P., Mekonen, H.K., Koehler, S.E., Lamers, W.H., 2015. The growth pattern of the human intestine and its mesentery. BMC Dev Biol 15, 31. https://doi.org/10.1186/s12861-015-0081-x

Spalding, H., Heath, T., 1987. Arterial supply to the pig intestine: an unusual pattern in the mesentery. Anat Rec 218, 27–29. https://doi.org/10.1002/ar.1092180106

Standring, S., 2016. A brief history of topographical anatomy. J Anat 229, 32–62. https://doi.org/10.1111/joa.12473

Stevens, L.J., Donkers, J.M., Dubbeld, J., Vaes, W.H.J., Knibbe, C.A.J., Alwayn, I.P.J., van de Steeg, E., 2020. Towards human ex vivo organ perfusion models to elucidate drug pharmacokinetics in health and disease. Drug Metabolism Reviews 52, 438–454. https://doi.org/10.1080/03602532.2020.1772280

Stewart, C.J., Estes, M.K., Ramani, S., 2020. Establishing Human Intestinal Enteroid/Organoid Lines from Preterm Infant and Adult Tissue. Methods Mol Biol 2121, 185–198. https://doi.org/10.1007/978-1-0716-0338-3_16

Stumpf, M., Cao, W., Klinge, U., Klosterhalfen, B., Kasperk, R., Schumpelick, V., 2002. Collagen distribution and expression of matrix metalloproteinases 1 and 13 in patients with anastomotic leakage after large-bowel surgery. Langenbecks Arch Surg 386, 502–506. https://doi.org/10.1007/s00423-001-0255-9

Suckow M., Stevens K., Wilson R., 2011. The Laboratory Rabbit, Guinea Pig, Hamster, and Other Rodents, 1st Edition. ed. Academic Press.

Taylor, K., Alvarez, L.R., 2019. An Estimate of the Number of Animals Used for Scientific Purposes Worldwide in 2015. Altern Lab Anim 47, 196–213. https://doi.org/10.1177/0261192919899853

Thakar, R., Fenner, D.E., 2007. Anatomy of the Perineum and the Anal Sphincter, in: Sultan, A.H., Thakar, R., Fenner, D.E. (Eds.), Perineal and Anal Sphincter Trauma: Diagnosis and Clinical Management. Springer, London, pp. 1–12. https://doi.org/10.1007/978-1-84628-503-5_1

Theron O. Odlaug, Carl Petterson, 1955. Laboratory Anatomy of the Fetal Pig, 2nd Edition. ed. Wm C Brown.

Thornton, F.J., Barbul, A., 1997. Healing in the gastrointestinal tract. Surg Clin North Am 77, 549–573. https://doi.org/10.1016/s0039-6109(05)70568-5

Trabold, O., Wagner, S., Wicke, C., Scheuenstuhl, H., Hussain, M.Z., Rosen, N., Seremetiev, A., Becker, H.D., Hunt, T.K., 2003. Lactate and oxygen constitute a fundamental regulatory mechanism in wound healing. Wound Repair Regen 11, 504–509. https://doi.org/10.1046/j.1524-475x.2003.11621.x

Treuting P.M., Dintzis S., Montine K.S., 2017. Comparative Anatomy and Histology: A Mouse, Rat, and Human Atlas, 2nd Edition. Academic Press.

Trier, J., Colony, P., 2008. Morphogenesis of the Small Intestine During Fetal Development. Ciba Foundation symposium 70, 3–29. https://doi.org/10.1002/9780470720530.ch2

Trier, J.S., Moxey, P.C., 1979. Morphogenesis of the Small Intestine during Fetal Development. Ciba Found Symp 3–29. https://doi.org/10.1002/9780470720530.ch2

Trowbridge, J.M., Gallo, R.L., 2002. Dermatan sulfate: new functions from an old glycosaminoglycan. Glycobiology 12, 117R–25R. https://doi.org/10.1093/glycob/cwf066

Sadler T.W., 2018. Langman's Medical Embryology, 11th Edition. Wolters Kluwer, Philadelphia.

Valentijn, T.M., Galal, W., Tjeertes, E.K.M., Hoeks, S.E., Verhagen, H.J., Stolker, R.J., 2013. The obesity paradox in the surgical population. Surgeon 11, 169–176. https://doi.org/10.1016/j.surge.2013.02.003

Vallance, A., Wexner, S., Berho, M., Cahill, R., Coleman, M., Haboubi, N., Heald, R.J., Kennedy, R.H., Moran, B., Mortensen, N., Motson, R.W., Novell, R., O'Connell, P.R., Ris, F., Rockall, T., Senapati, A., Windsor, A., Jayne, D.G., 2017. A collaborative review of the current concepts and challenges of anastomotic leaks in colorectal surgery. Colorectal Dis 19, O1–O12. https://doi.org/10.1111/codi.13534

Vallée, M., Mayo, W., Dellu, F., Le Moal, M., Simon, H., Maccari, S., 1997. Prenatal Stress Induces High Anxiety and Postnatal Handling Induces Low Anxiety in Adult Offspring: Correlation with Stress-Induced Corticosterone Secretion. J Neurosci 17, 2626–2636. https://doi.org/10.1523/JNEUROSCI.17-07-02626.1997

Van der Hee, B., Loonen, L.M.P., Taverne, N., Taverne-Thiele, J.J., Smidt, H., Wells, J.M., 2018. Optimized procedures for generating an enhanced, near physiological 2D

culture system from porcine intestinal organoids. Stem Cell Res 28, 165–171. https://doi.org/10.1016/j.scr.2018.02.013

Van der Worp, H.B., Howells, D.W., Sena, E.S., Porritt, M.J., Rewell, S., O'Collins, V., Macleod, M.R., 2010. Can animal models of disease reliably inform human studies? PLoS Med 7, e1000245. https://doi.org/10.1371/journal.pmed.1000245

Van Ginneken, C., Van Meir, F., Sommereyns, G., Sys, S., Weyns, A., 1998. Nitric oxide synthase expression in enteric neurons during development in the pig duodenum. Anat Embryol (Berl) 198, 399–408. https://doi.org/10.1007/s004290050192

Vandamme, T.F., 2014. Use of rodents as models of human diseases. J Pharm Bioallied Sci 6, 2–9. https://doi.org/10.4103/0975-7406.124301

Verburg B.O., Steegers E.A., De Ridder M., Snijders R.J., Smith E., Hofman A., Moll H.A., Jaddoe V.W., Witteman J.C.. New charts for ultrasound dating of pregnancy and assessment of fetal growth: longitudinal data from a population-based cohort study. Ultrasound Obstet Gynecol. 2008 Apr;31(4):388-96. doi: 10.1002/uog.5225.

Vonderohe, C., Guthrie, G., Stoll, B., Hebib, V.M., Dawson, H., Burrin, D., 2022. Increased Circulating Cortisol After Vaginal Birth Is Associated With Increased FGF19 Secretion in Neonatal Pigs. Endocrinology 164, bqac188. https://doi.org/10.1210/endocr/bqac188

Wallaeys, C., Garcia-Gonzalez, N., Libert, C., 2023. Paneth cells as the cornerstones of intestinal and organismal health: a primer. EMBO Mol Med 15, e16427. https://doi.org/10.15252/emmm.202216427

Walters, E.M., Prather, R.S., 2013. Advancing Swine Models for Human Health and Diseases. Mo Med 110, 212–215.

Walthall, K., Cappon, G.D., Hurtt, M.E., Zoetis, T., 2005. Postnatal development of the gastrointestinal system: A species comparison. Birth Defects Research Part B: Developmental and Reproductive Toxicology 74, 132–156. https://doi.org/10.1002/bdrb.20040

Walton, K.D., Whidden, M., Kolterud, Å., K. Shoffner, S., Czerwinski, M.J., Kushwaha, J., Parmar, N., Chandhrasekhar, D., Freddo, A.M., Schnell, S., Gumucio, D.L., 2016. Villification in the mouse: Bmp signals control intestinal villus patterning. Development 143, 427–436. https://doi.org/10.1242/dev.130112

Wang, J., Wan, R., Mo, Y., Zhang, Q., Sherwood, L.C., Chien, S., 2010. Creating a Long-Term Diabetic Rabbit Model. Exp Diabetes Res 2010, 289614. https://doi.org/10.1155/2010/289614

Wangler, M.F., Yamamoto, S., Chao, H.-T., Posey, J.E., Westerfield, M., Postlethwait, J., Hieter, P., Boycott, K.M., Campeau, P.M., Bellen, H.J., 2017. Model Organisms Facilitate Rare Disease Diagnosis and Therapeutic Research. Genetics 207, 9–27. https://doi.org/10.1534/genetics.117.203067

Weber, J., Peng, H., Rader, C., 2017. From rabbit antibody repertoires to rabbit monoclonal antibodies. Exp Mol Med 49, e305. https://doi.org/10.1038/emm.2017.23

Wenzel, N., Blasczyk, R., Figueiredo, C., 2021. Animal Models in Allogenic Solid Organ Transplantation. Transplantology 2, 412–424. https://doi.org/10.3390/transplantology2040039

Weström, B., Arévalo Sureda, E., Pierzynowska, K., Pierzynowski, S.G., Pérez-Cano, F.-J., 2020. The Immature Gut Barrier and Its Importance in Establishing Immunity in Newborn Mammals. Front Immunol 11, 1153. https://doi.org/10.3389/fimmu.2020.01153

Winn, R.J., Baker, M.D., Merle, C.A., Sherwood, O.D., 1994. Individual and combined effects of relaxin, estrogen, and progesterone in ovariectomized gilts. II. Effects on mammary development. Endocrinology 135, 1250–1255. https://doi.org/10.1210/endo.135.3.8070370

Winsnes, R., Sesardic, D., Daas, A., Terao, E., Behr-Gross, M.-E., 2009. Collaborative study on a Guinea pig serological method for the assay of acellular pertussis vaccines. Pharmeur Bio Sci Notes 2009, 27–40.

Wu, X.-S., Wu, W.-G., Li, M.-L., Yang, J.-H., Ding, Q.-C., Zhang, L., Mu, J.-S., Gu, J., Dong, P., Lu, J.-H., Liu, Y.-B., 2013. Impact of being overweight on the surgical outcomes of patients with gastric cancer: a meta-analysis. World J Gastroenterol 19, 4596–4606. https://doi.org/10.3748/wjg.v19.i27.4596

Xiong, M., Elson, G., Legarda, D., Leibovich, S.J., 1998. Production of vascular endothelial growth factor by murine macrophages: regulation by hypoxia, lactate, and the inducible nitric oxide synthase pathway. Am J Pathol 153, 587–598. https://doi.org/10.1016/S0002-9440(10)65601-5

Yadav, S., Singh, V., 2021. Alternatives to Animal Experiments in Research and Regulatory Testing. pp. 137–156. https://doi.org/10.1007/978-981-16-0987-9_7

Young, R., Lewandowska, D., Long, E., Wooding, F.B.P., De Blasio, M.J., Davies, K.L., Camm, E.J., Sangild, P.T., Fowden, A.L., Forhead, A.J., 2023. Hypothyroidism impairs development of the gastrointestinal tract in the ovine fetus. Front Physiol 14, 1124938. https://doi.org/10.3389/fphys.2023.1124938

Yuan, R., Peters, L.L., Paigen, B., 2011. Mice as a Mammalian Model for Research on the Genetics of Aging. ILAR J 52, 4–15.

Zeng, Q., Yu, Z., You, J., Zhang, Q., 2007. Efficacy and safety of Seprafilm for preventing postoperative abdominal adhesion: systematic review and meta-analysis. World J Surg 31, 2125–2131; discussion 2132. https://doi.org/10.1007/s00268-007-9242-9

Zhang, Q., Widmer, G., Tzipori, S., 2013. A pig model of the human gastrointestinal tract. Gut Microbes 4, 193–200. https://doi.org/10.4161/gmic.23867

Ziegler, A., Gonzalez, L., Blikslager, A., 2016. Large Animal Models: The Key to Translational Discovery in Digestive Disease Research. Cell Mol Gastroenterol Hepatol 2, 716–724. https://doi.org/10.1016/j.jcmgh.2016.09.003

Zuberi, A., Lutz, C., 2016. Mouse Models for Drug Discovery. Can New Tools and Technology Improve Translational Power? ILAR J 57, 178–185. https://doi.org/10.1093/ilar/ilw021

Zühlke, H.V., Lorenz, E.M., Straub, E.M., Savvas, V., 1990. [Pathophysiology and classification of adhesions]. Langenbecks Arch Chir Suppl II Verh Dtsch Ges Chir 1009–1016.

8 List of tables

9 List of images

10 Publication activity of the author

10.1. Publications supporting the thesis

Jiřík, M., Bartoš, M., Tomášek, P., Malečková, A., **Kural, T.,** Horáková, J., Lukáš, D., Suchý, T., Kochová, P., Hubálek Kalbáčová, M., Králíčková, M., Tonar, Z. Generating standardized image data for testing and calibrating quantification of volumes, surfaces, lengths, and object counts in fibrous and porous materials using X-ray microtomography. Microsc Res Tech. 2018 Jun;81(6):551-568. DOI: 10.1002/jemt.23011.
$IF_{(JCR2017)}$ = 1.087. Q3 (Microscopy) https://pubmed.ncbi.nlm.nih.gov/29476582/

Kolinko, Y., Malečková, A., Kochová, P., Grajciarová, M., Blassová, T., **Kural, T.,** Trailin, A., Červenková, L., Havránková, J., Vištejnová, L., Tonarová, P., Moulisová, V., Jiřík, M., Zavaďáková, A., Tichánek, F., Liška, V., Králíčková, M., Witter, K., Tonar, Z. Using virtual microscopy for the development of sampling strategies in quantitative histology and designbased stereology. Anat. Histol. Embryol. 2022 Jan;51(1):3-22. DOI: 10.1111/ahe.12765.
$IF_{(JCR2020)}$ = 1.114. Q3 (Veterinary sciences) https://pubmed.ncbi.nlm.nih.gov/34806204/

Rosendorf, J., Horáková J, Klíčová, M., Pálek, R., Červenková, L., **Kural, T.**, Hošek, P., Kříž, T., Tégl, V., Moulisová, V., Tonar, Z., Třeška, V., Lukáš, D., Liška, V. Experimental fortification of intestinal anastomoses with nanofibrous materials in a large animal model. Sci Rep. 2020 Jan 24;10(1):1134. DOI: 10.1038/s41598-020-58113-4.
$IF_{(JCR2020)}$ = 4.380. Q1 (Multidisciplinary Sciences) https://pubmed.ncbi.nlm.nih.gov/31980716/

Kural T., Grajciarová M., Rosendorf J., Pálek R., Červenková L., Malečková A., Šarčevic S., Liška V., Tonar Z. Histological mapping of healing of the small and large intestine - A quantitative study in a porcine model. Ann Anat. 2023 Apr 1;249:152095. doi: 10.1016/j.aanat.2023.152095. Epub ahead of print. PMID: 37011825.
$IF_{(JCR2021)}$ = 2.976. Q1 (Anatomy&Morphology) https://pubmed.ncbi.nlm.nih.gov/37011825/

10.2 Publications not related to the topic of the thesis

Tomášek, P., Tonar, Z., Grajciarová, M., **Kural, T.,** Turek D., Horáková, J., Pálek, R., Eberlová, L., Králíčková, M., Liška, V. Histological mapping of porcine carotid arteries – An animal model for the assessment of artificial conduits suitable for coronary bypass grafting in humans. Ann. Anat. 2020 Mar;228:151434. DOI: 10.1016/j.aanat.2019.151434.

$IF_{(JCR2019)}$ = 2.388. Q1(Anatomy&Morphology) https://pubmed.ncbi.nlm.nih.gov/31704146/

Tonar, Z., **Kural, T.**, Kochová, P., Nedorost, L., Witter, K. Vasa vasorum quantification in human varicose great and small saphenous veins. Ann Anat. 2012 Sep;194(5):473-81. DOI: 10.1016/j.aanat.2012.02.019.

$IF_{(JCR2012)}$ = 1.960. Q2 (Anatomy&Morphology)

https://pubmed.ncbi.nlm.nih.gov/22559999/

11 Supplements

11.1 Supplement I

Jiřík, M., Bartoš, M., Tomášek, P., Malečková, A., **Kural, T.,** Horáková, J., Lukáš, D., Suchý, T., Kochová, P., Hubálek Kalbáčová, M., Králíčková, M., Tonar, Z. Generating standardized image data for testing and calibrating quantification of volumes, surfaces, lengths, and object counts in fibrous and porous materials using X-ray microtomography. Microsc Res Tech. 2018 Jun;81(6):551-568. DOI: 10.1002/jemt.23011.

$IF_{(JCR2017)}$ = 1.087. Q3 (Microscopy) https://pubmed.ncbi.nlm.nih.gov/29476582/

Received: 15 November 2017 | Revised: 22 January 2018 | Accepted: 12 February 2018

DOI: 10.1002/jemt.23011

RESEARCH ARTICLE

WILEY MICROSCOPY RESEARCH & TECHNIQUE

Generating standardized image data for testing and calibrating quantification of volumes, surfaces, lengths, and object counts in fibrous and porous materials using X-ray microtomography

Miroslav Jiřík[1*] | Martin Bartoš[2*] | Petr Tomášek[3] | Anna Malečková[1,3] | Tomáš Kural[3] | Jana Horáková[4] | David Lukáš[4] | Tomáš Suchý[5] | Petra Kochová[6] | Marie Hubálek Kalbáčová[1,7] | Milena Králíčková[1,3] | Zbyněk Tonar[1,3]

[1]Biomedical Center, Faculty of Medicine in Pilsen, Charles University, Pilsen, 323 00, Czech Republic

[2]Institute of Dental Medicine, First Faculty of Medicine, Charles University and General University Hospital in Prague, Prague 2, 128 01, Czech Republic

[3]Department of Histology and Embryology, Faculty of Medicine in Pilsen, Charles University in Prague, Pilsen, 301 66, Czech Republic

[4]Faculty of Textile Engineering, Technical University of Liberec, Liberec 1, 461 17, Czech Republic

[5]Department of Composites and Carbon Materials, Institute of Rock Structure and Mechanics, Academy of Sciences of the Czech Republic, Prague 8, Czech Republic

[6]European Centre of Excellence NTIS, Faculty of Applied Sciences, University of West Bohemia, Univerzitní 22, Pilsen, 306 14, Czech Republic

[7]Institute of Pathological Physiology, First Faculty of Medicine, Charles University, U nemocnice 5, 128 53 Prague, Czech Republic

Correspondence
Zbynek Tonar, Department of Histology and Embryology, Faculty of Medicine in Pilsen, Charles University, Karlovarska 48, 301 66 Pilsen, Czech Republic.
Email: zbynek.tonar@lfp.cuni.cz

Funding information
National Sustainability Program I (NPU I) Nr. LO1503 provided by the Ministry of Education, Youth and Sports of the Czech Republic, by the Progres Q39 and Progres Q29/LF1 (MB) projects of the Charles University, Grant/Award Numbers: SVV 260390/2017 and SVV 260392/2017 and UNCE/MED/006 projects of the Charles University. PK was supported by project LO1506 of the Czech Ministry of Education, Youth and Sports under program NPU I. ZT was also supported by the Ministry of Education, Youth and Sports under the project, Grant/Award Number: CZ.02.1.01/0.0/0.0/16_019/0000787. Technological development of post doc programs, Grant/Award Number: CZ.1.05/41.00/16.0346, Research and Development for Innovations Operational Programme (RDIOP)

Review Editor: Prof. George Perry

Abstract

Quantification of the structure and composition of biomaterials using micro-CT requires image segmentation due to the low contrast and overlapping radioopacity of biological materials. The amount of bias introduced by segmentation procedures is generally unknown. We aim to develop software that generates three-dimensional models of fibrous and porous structures with known volumes, surfaces, lengths, and object counts in fibrous materials and to provide a software tool that calibrates quantitative micro-CT assessments. Virtual image stacks were generated using the newly developed software TeIGen, enabling the simulation of micro-CT scans of unconnected tubes, connected tubes, and porosities. A realistic noise generator was incorporated. Forty image stacks were evaluated using micro-CT, and the error between the true known and estimated data was quantified. Starting with geometric primitives, the error of the numerical estimation of surfaces and volumes was eliminated, thereby enabling the quantification of volumes and surfaces of colliding objects. Analysis of the sensitivity of the thresholding upon parameters of generated testing image sets revealed the effects of decreasing resolution and increasing noise on the accuracy of the micro-CT quantification. The size of the error increased with decreasing resolution when the voxel size exceeded 1/10 of the typical object size, which simulated the effect of the smallest details that could still be reliably quantified. Open-source software for calibrating quantitative micro-CT assessments by producing and saving virtually generated image data sets with known morphometric data was made freely available to researchers involved in morphometry of three-dimensional fibrillar and porous structures in micro-CT scans.

*The first two authors contributed equally to the manuscript.

KEYWORDS
fibers, Python, pores, scaffolds, spatial statistics, stereology, textile

1 | INTRODUCTION

1.1 | Assessment of the three-dimensional structure of fibrous and porous biomaterials using micro-CT: Present state and methodological problems

High-resolution quantitative X-ray microtomography (micro-CT) has become a method of choice for three-dimensional and quantitative (Schladitz, 2011) characterization of tissue-engineered scaffolds (Ho & Hutmacher, 2006) used, e.g., to support the healing of organs.

Newly manufactured biomaterials, such as electrospun nanofibrous scaffolds (Szentivanyi, Chakradeo, Zernetsch, & Glasmacher, 2011; Zhong, Zhang, & Lim, 2012) or fiber-polymer composite foams (Shen, Nutt, & Hull, 2004) undergo morphometric assessments before being used in vitro or in vivo. A good correlation between micro-CT and histology was found in bone research (Particelli et al., 2012). Software supplied by manufacturers of micro-CT facilities supports a plethora of morphometric parameters characterizing volume fractions, outer and inner surfaces (Pyka, Kerckhofs, Schrooten, & Wevers, 2014), porosities in bone and dental research (De Souza et al., 2013; Draenert et al., 2012; Karageorgiou & Kaplan, 2005; Tonar, Khadang, Fiala, Nedorost, & Kochová, 2011), pore size and distribution in bone scaffolds (Montufar, Vojtova, Celko, & Ginebra, 2017) and synthetic bone model foams (Gómez, Vlad, López, Navarro, & Fernández, 2013) and the topology of multiple phases of tissue scaffolds in user-defined regions of interest (ROIs). The three-dimensional and quantitative nature of the micro-CT makes it a tool of choice for estimating shrinkage of materials (Burey et al., 2018) and propagation of material fractures and cavitation (Neves, Coutinho, Alves, & de Assis, 2015). Some of the estimates are based on or fully compatible with stereological principles and spatial statistics (Baddeley & Jensen, 2004; Mouton, 2002; Stoyan, Kendall, & Mecke, 1995) and may be assessed automatically, provided the image data have a sufficient contrast (Ji˜rík et al., 2016; Mouton et al., 2017). However, surfaces are especially potentially sensitive to the settings of the micro-CT scanning and further image postprocessing, such as resolution, noise, preferential spatial arrangement (anisotropy), filtration, and thresholding during binarization of grayscale images. The amount of potential bias introduced by these variables is generally unknown. The sensitivity of micro-CT to steps performed during thresholding might become an issue, especially in biomaterials combining multiple phases with similar or overlapping radiological opacity, such as partially mineralized collagen scaffolds combined with other substances, such as glycosaminoglycans. To the best of our knowledge, there are currently no published guidelines or fixed routines for thresholding biological samples, which is understandable due to the growing number of newly manufactured biomaterials and rapidly developing methodology of micro-CT. However, the entire measurement is as weak as its weakest link. Moreover, a precise knowledge of the morphometry of tissue-engineered materials would be necessary to test the consistency of their production and biodegradation once implanted. The motivation of the work presented in this article is the absence of a freely accessible and reliable source of calibration tools for use as realistic phantoms that simulate the micro-CT image stacks. As far as we know, the manufacturers of micro-CT facilities do not provide users with such software, which could be used by micro-CT operators to (i) calculate the bias and error during the processing of micro-CT scanned stacks using phantom image series with known volumes, surfaces, lengths, and numbers of objects and (ii) demonstrate the impact of changes to the thresholding routines on the results of quantitative micro-CT.

1.2 | Preprocessing and segmentation of micro-CT images of biomaterials

Before quantification of the structure and composition of biomaterials, the micro-CT images undergo segmentation. This is not a straightforward and routinely standardized procedure due to the low contrast and overlapping radioopacity of biological materials. Although sophisticated approaches are now available for noise suppression or removal (Maia et al., 2015; Rau, Wu€rfel, Lenarz, & Majdani, 2013), in micro-CT, the noise might overlap with the smallest nanofibers and microfibers of the tissue scaffolds. Currently used micro-CT devices (in our study, Bruker micro-CT, Belgium) are usually provided with a software package that is applicable for acquisition of projection images, their reconstruction into cross-section images, visualization of datasets (both in 2D and 3D), resizing, and production of a region or volume of interest (ROI, VOI), and finally, imageameters are commonly available (e.g., Bruker). Currently, employment of operations for image processing is usually very convenient and user-friendly since the typical micro-CT user is neither an information-technology scientist nor a biomathematician. This has to be considered along with subjectivity in the assessment of many procedural parameters in image processing and binarization because exact evaluation of these processes and their calibration is not achievable to date. Manuals and detailed descriptions of both two-dimensional parameters (evaluation of each separate cross-section image in a dataset) and three-dimensional analysis (evaluation of the entire dataset) require image binarization (i.e., conversion of a grayscale image into a black and white image, where white pixels represent objects and black pixels represent the background), e.g., (Burghardt et al., 2007; Zhang, Yan, Chui, & Ong, 2010). This step is crucial, with substantial effect on image analysis results; its sensitivity is dependent on object properties (e.g., size, shape, density, and connections) that we would like to examine in our study. Two basic approaches can be differentiated: subjective threshold values assessment (especially in life sciences) and automatic threshold assessment leading to higher reproducibility (in material or technical sciences) (Stock, 2009).

Influences of threshold variations were assessed in several studies mostly focused on bone micro-CT 3D morphometry (Hara, Tanck, Homminga, & Huiskes, 2002; Jones et al., 2007; Parkinson, Badiei, & Fazzalari, 2008; Yan, Qi, Qiu, Teo, & Lei, 2012). We should consider progressive development of micro-CT devices (Landis & Keane, 2010), resulting in better spatial resolution and lower noise level, thus reducing (not eliminating) the dependency of result variations on threshold values. Possibilities of image binarization in CTAn software (Bruker Corporation, 2017) are as follows: global-threshold, adaptive threshold (mean, median, mean of minimal and maximal values), and Otsu threshold (automatic and automatic multi-level) (Otsu, 1979).

Usually, the signal to noise ratio has to be enhanced. This can be performed by, e.g., using filtering procedures—sharpening or smoothing in 2D or 3D (e.g., Gaussian blur, median, uniform, Kuwahara, unsharp mask). These are usually applied in grayscale images, but binary images can be filtered as well. After binarization, despeckle operations in 2D or 3D are used to remove white "noise" pixels (e.g., remove white/black speckles less than X pixels/voxels, remove pores, sweep—remove all object except the largest one). Many other procedures are offered by CTAn, e.g., morphological operations (dilatation, erosion, opening, and closing procedures), bitwise and arithmetical operations and geometrical transformations. Demonstration of image processing prior to micro-CT analysis is available in, e.g., (Buie, Campbell, Klinck, MacNeil, & Boyd, 2007). Eventually, we decided to perform image processing and binarization in the simplest manner (filtering, automatic thresholding, and despeckle) to minimize the number of variable processes influencing the results and enhance the time efficacy.

To summarize the main problem of quantitative imaging of biomaterials, the combination of various steps using mathematical morphology can affect the morphometric results in an significant but unpredictable manner. A good visual representation of the thresholded structures in micro CT scans does not always guarantee accuracy and precision in a quantitative sense. A solution to this problem would be generating virtual (phantom) data mimicking the real micro-CT examination and comparing the results of the thresholding routines to the a priori known results.

1.3 | Options in calibrating quantitative micro-CT

Micro-CT analysis results in 2D and 3D structural parameters values. However, verification of these values is generally not possible or hardly achievable in complex structures. Micro-CT results are very often presented as precise values even though they may be inaccurate or biased. Phantom models available for common micro-CT users with known parameters would allow calibration of micro-CT analysis procedure and assessment of its accuracy. To date such phantoms are lacking, since it is not possible to produce these phantoms (especially in case of complex interconnected structures and material porosity) at micrometer-scale with adequate level of confidence in its structural parameters. Calibration phantoms exist for material X-ray density assessment (Bone Mineral Density based on X-ray attenuation coefficient calibration) applicable e.g., in bone biology.

Using test images for calibration is a commonly used practice in imaging techniques. One of the most known test image is the Shepp-Logan phantom (Shepp & Logan, 1974). The discrete version of this image can also be generated using the SheppLogan plugin of the public domain ImageJ software (Schneider, Rasband, & Eliceiri, 2012). Several other ImageJ plugins are available for generating test images, such as Random Ovals, Fractal Generator, and RandomJ plugins. However, these algorithms generate two-dimensional images only and do not allow for modeling different object shapes. This prevents these plugins from being suitable for calibration of three-dimensional micro-CT. Spatial test objects can be generated using the freely available Gensei software (Cimrman, 2010; Tonar, Kochova, Cimrman, Witter, Janacek & Rohan, 2011). However, Gensei is limited to ellipsoids only.

1.4 | Aims of the study

The commercially available software packages supplied with most of the micro-CT facilities are notably efficient in thresholding the structures of interest, creating visual reconstructions, and quantitatively describing their geometry and composition. These software packages do provide the operator with sufficient feedback on how the final quantitative data might be affected by numerous combinations of procedures involving filtration, operations of mathematical morphology, and thresholding. Therefore, the aims of our study are as follows:

- To develop open-source software that generates three-dimensional models of fibrous and porous structures with known volumes, surfaces, lengths, and object counts in fibrous materials and to provide a software tool for calibrating quantitative micro-CT assessments.
- To identify combinations of object and image stack properties, which may easily lead to biased results using thresholding procedures of fibrous biomaterials in microCT.
- To provide practical recommendations on how to avoid potential pitfalls during segmentation in quantitative X-ray microtomography of fibrous and porous biomaterials.
- To help users of micro-CT understand where errors can occur, ensuring that micro-CT segmentation procedures can be proved to be valid and correct.

2 | MATERIALS AND METHODS

2.1 | Parameters used for spatial statistics of generated objects

The choice of the basic parameters to be quantified by our software generator was based on studies with real micro-CT (Ji˜rík et al., 2016). This includes volume, surface, length, and number of objects, which are often expressed as relative densities calculated per ROI. The definitions, abbreviations, and possible biological interpretations in the context of biomaterials are summarized in Table 1. The simulation of biomaterials was inspired by real tissue scaffolds, namely: (i)

TABLE 1 Stereological parameters used for spatial statistics of artificially generated objects simulating biomaterials for in-vivo implantation

Parameter	Abbreviation	Unit	Definition	Possible biological interpretation in biomaterials
Volume density (fraction)	V_V	(−)	Volume of objects per Reference volume	measure of the in-vivo degradation of the total mass of a biomaterial
Surface density	S_V	(mm^{-1})	Surface of objects per Reference volume	relative surface area available for the release of substances; thrombogenicity
Length density	L_V	(mm^{-2})	Length of objects per Reference volume	fragmentation of fibers into shorter fragments as a measure of in-vivo material degradation
Numerical density	N_V	(mm^{-3})	Number of objects per Reference volume	showing the degree of branching and connectivity of the biomaterial or its remnants after some period of in-vivo degradation

electrospun polyesters (polycaprolactone) or polypropylene meshes used for manufacturing artificial vascular prostheses or reinforcement of scars (Horakova et al., 2018; Plencner et al., 2014) and consisting of fibers with diameters of 1–6 μm, occupying 25–70% of the volume fraction; and (ii) composite porous scaffolds (Gómez, Vlad, López, & Fernández, 2016; Prosecká et al., 2015; Suchý et al., 2015) manufactured for healing of bone defects and consisting of collagen, polyDL-lactide sub-micron fibers, and sodium hyaluronate, containing typically 70%–80% porosities.

2.2 | Generating virtual objects and image stacks: Algorithm and software development

The program was written in the Python programming language. The software runs under Linux, Windows or Mac OS operating systems. The TeIGen application is designed to generate structures ranging in shape from very elongated fibers to spheres. The output is an image stack that mimics the data obtained using micro-CT and metadata describing the parameters of the generated 3D structure. The application can be used through a graphical user interface, noninteractively from the command line, or directly from the Python environment.

The graphical user interface is created using the pyqt module, the numpy, scipy and scikit modules are used for the calculations, 3D modeling is performed using the VTK package, and the pandas and seaborn packages are used for data processing. Loading and storing data is mediated by our io3d package, which uses SimpleITK and pydicom. 3D noise was generated by the ndnoise package created for this purpose.

The basic concept of the algorithm (Table 2) includes the definition of objects to generate, the generation of the framework of the fiber structure, the surface representation, the quantitative description, the volume representation, and finally the file storage.

The basic element used in this task is a tube. It is a cylindrical body that ends with hemispheres. The user can set parameters for object length, object radius, and parameters that affect the direction and isotropy of objects. The concept and implementation of quantitative measured isotropy was done according to Kochová, Cimrman, Janáček, Witter, and Tonar (2011). The fibrous structure is created by repeatedly inserting these objects into the sample area and can be affected by allowing the overlay of the objects. The collision detection algorithm is based on minimum distance computation, and it is preprocessed by a bounding box collision detection algorithm (Jiménez, Thomas, & Torras, 2001; Moore & Wilhelms, 1988). This process ends when the object number, volume density, or maximum number of iterations defined by the user is reached.

To determine the geometrical properties of the generated objects, a triangulated model of the surface of each tube is created using the VTK package (Schroeder, Avila, & Hoffman, 2000; Schroeder, Martin, & Lorensen, 1998). The measurement_resolution parameter affects the number of triangulation points and hence the accuracy of the measurement and the computation time. By using the vtkBooleanOperation PolyDataFilter function, a connection of two objects is made in the case of a contact. The vtkMassProperties functions are used to determine the numeric volume and numeric body surface.

The intensities of the volume representation are controlled by the background_intensity parameters and the intensity_profile function, which defines the intensity depending on the relative distance from the center of the tube to its edge. The volume representation process begins by creating a 3D array with a homogeneous intensity corresponding to the selected background intensity. Tube-shaped objects are placed in this array in the first iteration. The radius and intensity of an object correspond to the intensity profile (Supporting Information S4A) with the highest relative radius. The second iteration places the same objects with different radius and intensity that correspond to the second largest relative radius of the intensity profile. The entire process is repeated until all the intensity profile values are used. Then, intensity filtering by a Gaussian filter with user-defined parameters is performed.

The next step is to add noise. For this purpose, the ndnoise module was created. The noise parameters are the minimum and maximum noise wavelengths in millimeters and the exponent that controls the ratio of the individual components to the wavelength.

Volumetric data are stored using the imtools package. Data can be stored in a single DICOM or RAW file or as a file series in JPG, PNG, TIFF, DICOM, etc. format. Together with volumetric data, the surface model in VTK and metadata are stored. Metadata contain information about the configuration and quantitative data for all object segments. They are exported in the open and human-readable YAML format or as

TABLE 2 Outline of the steps of the algorithm of the TeIGen software

Input: Parameters defined by the user
1. Type of the generator: Objects or Porosities (Figure 2 and Supporting Information S4)
2. Definition of the objects to be generated 2.1. Properties of objects 2.1.1 Separate objects or Intersecting objects 2.1.2 Number of objects and volume fraction 2.1.3 Distribution of radii and lengths of cylinders and spheres 2.1.4 Isotropy of the objects 2.1.5 Intensity profiles of the objects on virtual micro-CT sections 2.2. Properties of generated virtual micro-CT stacks 2.2.1 Resolution and size in three dimensions (X × Y × Z) 2.2.2 Gaussian blur of the objects (optional) 2.2.3 Generating noise (parametric settings, optional) 2.2.4 Number of iterations for calculation of the numerical estimates of spatial statistics 2.2.5 Setting connected component seed (optional) 2.3 Saving all the parameters listed in steps 1.1-1.2 to a configuration file (YAML)
3. Generating the skeleton and envelopes of the objects (repeat step 2 until the desired values are reached) 3.1. Defining the empty sample area 3.2 Inserting a tube into the sample area according to the defined parameters 3.3. Quantitative analysis of the objects 3.3.1. Calculating analytical lengths, radii, volumes, surfaces 3.3.2. Numeric lengths, radii, volumes and surfaces calculation 3.3.3 Preview of the values for the user
4. Generating and saving virtual micro-CT stacks (volumetric data) (repeat step 2 until all intensity profile values are used) 4.1. Creating the initial volumetric array with the defined background intensity 4.2. Inserting tubes with intensity and radius according to the intensity profile from a high relative radius to a zero radius 4.3 Gaussian filtering 4.4. Inserting the noise 4.5. Image saving to a defined file format
Output: Three-dimensional volumetric data with a known voxel size and known values of quantitative parameters (volume fractions, surface densities, length densities, numerical densities). Export of the 3D model into VTK format. Export of the image stacks (DICOM, JPEG). Export of the morphometric results (CSV file).

CSV files. These are either readable by spreadsheet applications or processed by data scripts.

The computation time depends mainly on the dimensions of the requested volumetric representation and the measurement_resolution. To process a stack from our dataset consisting of 500 × 500 × 500 voxels with a measurement_resolution of 35 and element_number using a computer with an 8x Intel(R) Core(TM) i5-2520M CPU at 2.50 GHz, 8 GB RAM, and an NVIDIA GF119M NVS 4200M graphical adapter, the computation time is approximately 4 min. The minimum and maximum time on this dataset is 1 and 34 min, respectively.

2.3 | Evaluating numerical estimates of volume and surface vs. values calculated using analytic geometry

The parameters evaluated in the objects of our measurements are the surface, volume, length of cylindrical part l and radius of the spherical surfaces and cylindrical part r. From the specified length and radius, the analytical expression of surface $S_{analytic}$ and volume $V_{analytic}$ is given by the following equations.

$$S_{analytic} = 2\pi r l + 4\pi r^2 \quad (1)$$

$$V_{analytic} = \frac{4}{3}\pi r^3 + \pi r^2 l \quad (2)$$

One of our goals is also the modeling of connected objects. Analytical expressions of surfaces and volumes of such bodies are generally difficult and often do not have a definitive solution. For this reason, we use a numerical solution to this problem, which is based on the triangulation of the tube object. The base of the cylindrical part consists of a regular polygon. The number of its sides is given by the measure_resolution parameter. The hemispheres are replaced by triangles with triangulation points located at the intersections of imaginary meridians and parallels. The triangulated tube is inscribed in the original object. Its surface and volume asymptotically approximate the analytically measured values with increasing measurement_resolution. This method of triangulation is further referred to as "inscribed."

To increase the accuracy, we perform some compensation. The radius of the regular inscribed polygon that is the base of the cylindrical model is chosen so that the body on it has the same surface (volume, respectively) as the model cylinder. The compensated surface and volume radii are not the same. The hemisphere parts are unchanged. This method of triangulation with the compensation of the cylindrical part is referred to as "surface" and "volume." The calculation is given by the following equation, where r is the radius of the model tube, n is the measurement_resolution, r_{eqsurf} is the radius of the surface compensated polygon, and r_{eqvol} is the radius of the polygon for volume compensation:

$$r_{eqSurf} = \frac{pr}{n \sin\frac{p}{n}} \quad (3)$$

$$r_{eqVol} = \sqrt{\frac{2pr^2}{n \sin\frac{2p}{n}}} \quad (4)$$

Compensation of the spherical part is performed by experimental measurement using the equation for calculating the radius of the spherical part with knowledge of the surface or volume. r_c is the compensated factor, and r_0 is the model radius. These compensation methods are further referred to as "surface – sphere error" and "volume – sphere error."

$$r_c = \frac{1}{2}\sqrt{\frac{S}{p}} \quad (5)$$

$$r_0 r_c = \sqrt[3]{\frac{3V}{4p}} \quad (6)$$

Similarly, experimental measurements were made to estimate the compensation factor for the error compensation from the connection of the cylindrical and spherical parts. This is referred to as "volume – sphere error – joint error" and "volume – sphere error – joint error." However, these corrections did not increase the precision of either volume or surface estimates and therefore were not included.

2.4 | Evaluating morphometric values using image processing on a micro-CT console

CTAn software (Skyscan CT analyzer (21)) was applied for image processing and subsequent 3D analysis using a "custom processing" mode. A universal procedure (a "standard" procedure) of image processing leading to acceptable and reproducible outcomes was found for datasets with the following variable parameters: *count, isotropy, noise*, and *resolution*. However, *noise* and resolution datasets required modification of the procedure based on the value of the variable parameter.

Standard procedure was based on filtering using Gaussian blur in 3D (with a radius of 2 voxels). Binarization was performed by an automatic Otsu threshold method to eliminate subjectivity in assessment of the threshold value. Noise reduction was achieved by a despeckle function (remove white speckles less than 12 voxels in 3D). *Resolution* variable datasets were filtered using Gaussian blur in 3D with reduction of the value of the radius (from 2 voxels to one voxel; for a pixel size of 80 μm and higher, this operation was not performed). Binarization was achieved by an automatic Otsu threshold method in 3D. Despeckle was performed with decreasing value of the defined volume limit for object elimination (12 voxels and less; for a pixel size of 80 μm and higher, this operation was not performed).

Image processing in datasets with a *noise* variable was based on Gaussian blur in 3D with a gradual increase in the radius value (from 2 to 5 voxels). The generated noise intensity was set to zero, but the standard deviation of the noise intensity gradually increased. Binarization was performed by a global threshold with an increase in the lower gray threshold value from 87 to 135 as noise was intensified. A despeckle operation was performed with an increase of the defined volume (remove white speckles less than: from 12 to 250 μm. According to preliminary results, noise reduction was preferred over object volume preservation, resulting in noise being binarized as an object.

Procedures in *noise* and *resolution* variables were modified regarding object count and subjective assessment (more in 4.1). 3D analysis of the entire dataset and 3D analysis of all individual objects in the dataset were performed in each dataset after the described image processing. The following parameters were evaluated based on analysis: object count, mean and total object length, mean and total object volume, mean and total object surface, surface density (total object surface/dataset volume), and mean object diameter. Objects and volumes are calculated via the marching cubes method (Lorensen & Harvey, 1987). Object length was defined as the furthest distance between two points within the analyzed object volume. Mean diameter was calculated as structure thickness, which is based on object medial axis computation and a subsequent sphere-fitting algorithm. Because these spheres finally have known diameters, it can be used for structure thickness evaluation (Bruker Corporation, 2017; Hildebrand & Ruegsegger, 2003; Remy & Thiel, 2002). Typical time costs for performing the despeckle operation using a computer recommended for micro-CT SkyScan1272 (Bruker) application (Intel(R) Xeon (R) CPU E5-2687W 3.1GHz (2 processors), 128 GB RAM, NVIDIA Quadro – Tesla graphical adapter) were approximately 1–2 min (depending on number of selected parameters in analysis results).

3 | RESULTS

3.1 | Open-source software for generation of three-dimensional objects and virtual micro-CT image stacks

The source code of our software named TeIGen, which was written in the Python programming language, all of the files necessary for its launch, the calculation of the results, and the production of all graph types have been made openly available to the scientific community (Ji˜rík, 2017). The source data and configurations for generation of the following results and all the data sets described in this article can be downloaded as Supporting Information S1–S3. The documentation can be downloaded as well (Ji˜rík & Tonar, 2018). The basic concept of the algorithm (Figure 1, Table 2) is to gather the required parameters of the phantom data from the user; generate, visualize and measure the data; receive approval from the user; and then save image stacks with all configuration files and quantitative results to disc. The software allows for the generation of noncolliding tubes, colliding tubes (for simulating of branching fibers and a greater volume fraction of the material), and isolated or connected (overlapping) porosities (Figure 2). Most of the application functions can be performed noninteractively using command line parameters.

3.2 | Comparing the numerical estimates of volume and surface with known true values calculated using analytic geometry

After implementing the corrections described above, there was very good agreement between the surfaces and volumes of tubes precisely

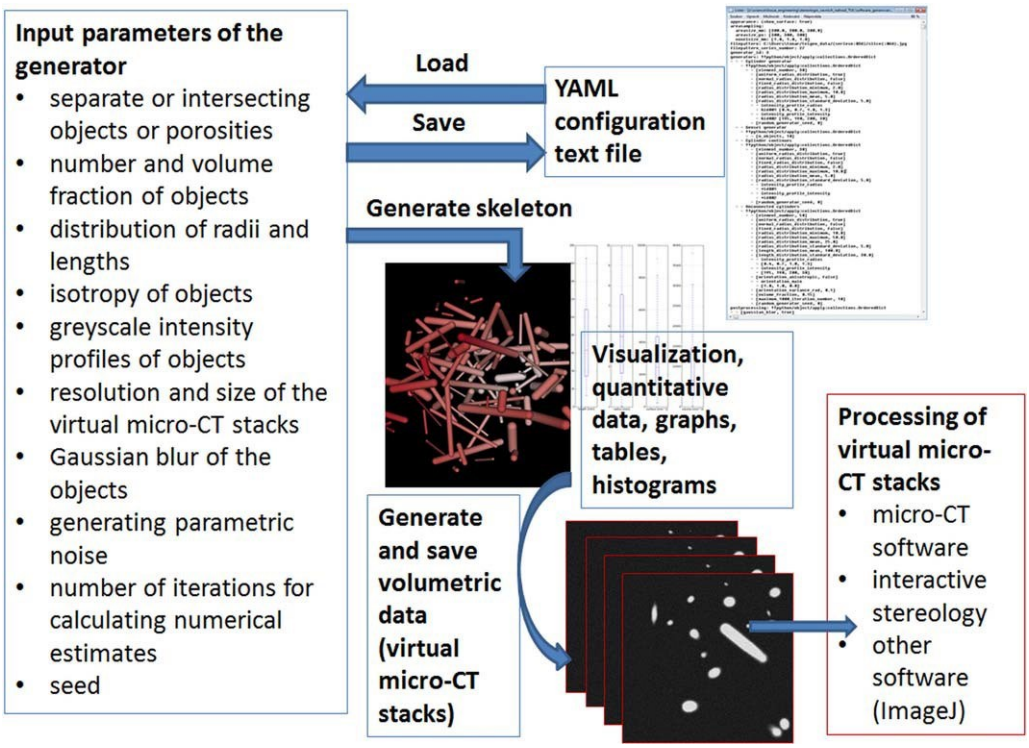

FIGURE 1 Main steps during the setting, generation, and processing of the fibrillar and porous three-dimensional objects and corresponding virtual micro-CT stacks. The user sets the required input parameters (see Table 2 for details) either manually or from a previously saved YAML configuration text file. The skeleton of the objects is generated together with a quantitative description of the objects (volumes, surfaces, and lengths), and the data can be visually checked by the user in the form of three-dimensional skeletons. Once the data meets the required settings, full volumetric data are generated and saved to disk as image sequences mimicking micro-CT stacks together with a three-dimensional model (VTK format) and tables containing all the morphometric results (CSV files). The resulting virtual micro-CT stacks can be loaded into any type of software supporting DICOM or JPEG image stacks [Color figure can be viewed at wileyonlinelibrary.com]

calculated using analytic geometry and the measurement done by the TeIGen software (Figure 3 with source data provided as Supporting Information S1).

3.3 | Analysis of the sensitivity of surface error and volume error on the numbers of generated objects and measurement resolution

Based on these results and the computational time, the accuracy of surface and volume measurement was strongly dependent on the measurement resolution parameter and the radius compensation method. Compared to uncompensated methods (inscribed), methods using radius compensation provide improvement, especially for low values of measure_resolution. The lowest relative surface errors, expressed as 100$\frac{3}{1}$(true value-numerical estimate), were achieved by implementing the cylinder surface$\frac{1}{1}$sphere error corrections. When combined with increasing resolution, the surface error was gradually reduced to values below 0.1 (Figure 4a–d). The volume error was successfully minimized by using the cylinder volume compensation or cylinder volume$\frac{1}{1}$-sphere error compensation (Figure 4e–h), converging to an error below 0.1 even at lower resolutions than the surface (Figure 4h vs. Figure 4d). Based on these experiments and the time costs of the computations, we recommend using the "cylinder surface" method for surface measurement. For volume measurement, we recommend the "cylinder volume$\frac{1}{1}$sphere error" method.

3.4 | Evaluating known morphometric values with analysis based on thresholding on the micro-CT console

For testing the sensitivity of the segmentation procedures using the SkyScan Bruker console micro-CT software, 40 image stacks were generated, representing low to high numbers of objects (Figure 5a), isotropy of objects (Figure 5b), resolution of stacks (Figure 5c), and noise (Figure 5d). After processing these phantom stacks (see Figure 6 for the main steps), situations leading to possible bias were identified (Figure 7). This included thresholding of the gradual transition of grayscale values between the objects and their background (Figure 7a), reduction of object count caused by peripheral sections of objects (Figure 7b), occasionally colliding objects (Figure 7c), and fragmentation due to binarization (Figure 7d).

There was on overall good agreement between the known surface and volume densities of generated objects and the results obtained on the micro-CT console within most of the range of values typical for biomaterials (Figure 8a,b). As shown in the Bland-Altman plots (Figure 8c, d), the disagreement between both measures gradually increased with increasing values of the densities.

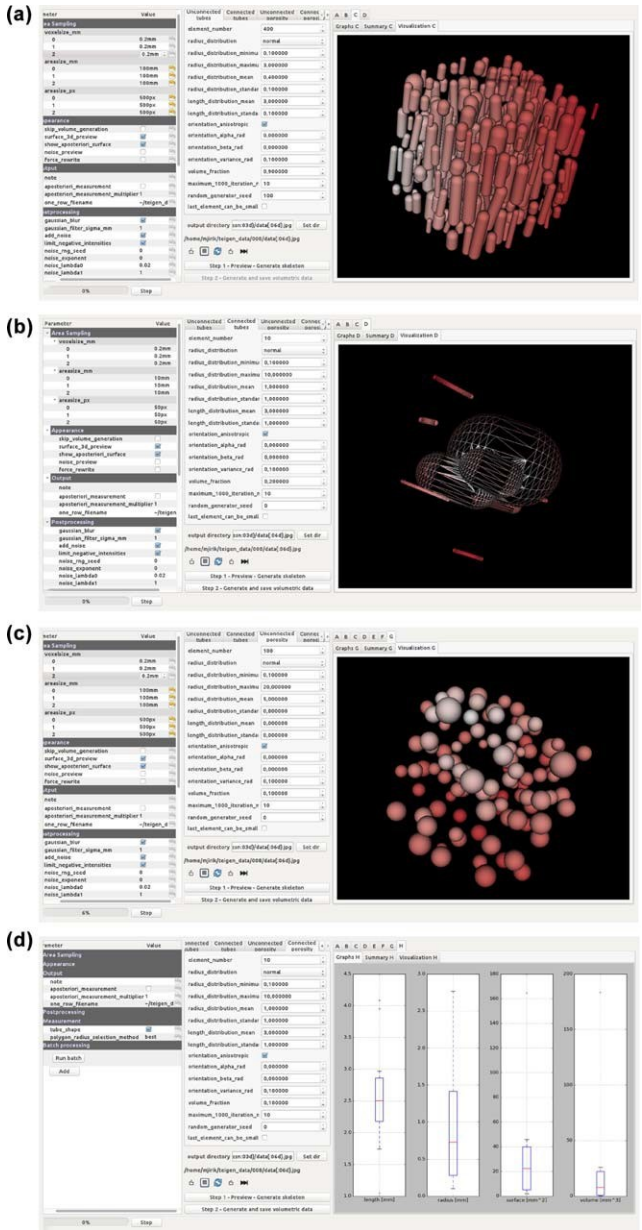

FIGURE 2 Graphical user interface of the four types of generators in the TeIGen software. (a) Generating unconnected tubes, in this example with a highly anisotropic orientation. (b) Generating connected (colliding) tubes, in this example within a wide range of diameters. (c) Generating unconnected porosities, which may have shape of spheres or tubes. (d) Generating connected (overlapping) porosities, overview of morphometric data on length, radius, surface, and volume distribution in the preview window [Color figure can be viewed at wileyonlinelibrary.com]

A detailed analysis of sensitivity of the thresholding upon various values of parameters of generated testing image sets revealed that the changes in object count and the value of isotropy did not affect the accuracy of the micro-CT quantification (Figure 9a,b). The number of objects was underestimated by the micro-CT, and the volumes, surfaces, and length densities had a tendency toward being overestimated. The size of the error significantly increased with decreasing resolution when the voxel size exceeded 1/10 of the typical object size (Figure 9c), which simulated the effect of the smallest details that could still be reliably quantified. Similarly, the results became unreliable when the standard deviation of the noise intensity (mean 50) exceeded 37 arbitrary units, and more filtering and higher threshold values were necessary (see Methods).

3.5 | Examples of practical applications

Verification of micro-CT analysis results of specimen microstructure is hard to achieve or even not possible as was mentioned in 1.3. TeIGen software enables evaluation of micro-CT analysis accuracy, image processing effect and bias quantification. Despite the fact, that 3D structures generated by TeIGen are simplification of studied specimen, it provides important and unique information, which may improve decision making in image processing and analyzes understanding. The benefit of using the TeIGen software will be illustrated in three examples.

3.5.1 | Evaluation of global thresholding effect

A fundamental approach in image thresholding is the use of Global threshold. Separating objects from their background requires a manual selection of grayscale value, which is usually based on operator's subjective assessment. Since there is a gradual transition between object and background, this decision often lacks accuracy and repeatability (typical situations are shown in Figure 10a,b). A solution is as follows: First, TeIGen software is employed for generating a dataset with a known structure similar to the specimen under study. Second, a series of different global thresholding values are applied for binarization using the micro-CT analysis. Third, the results of the micro-CT analysis are compared with known structural parameters generated in the first step. Four, the most accurate settings are used for further specimen analysis and bias introduced by micro-CT analysis is quantified (e.g., discrepancy between objects volume and surface accuracy). An example of such a simple analysis which required approximately 20 min of work is shown in Table 3.

3.5.2 | Effect of image noise quantification

Image noise is found in all micro-CT scans. However, the effect of image noise on results is usually not considered. TeIGen software is used for generating dataset of structures similar to studied specimen with similar level of image noise (Figure 6, see also section 4.1.4). By analyzing the same dataset with and without applying noise reduction algorithms, any bias introduced by noise and micro-CT analysis is quantified, because the impact of noise reduction and filtering is compared with the known structural parameters generated by the TeiGen software.

3.5.3 | Image 2D binarization did introduce bias into quantification of object number in isotropic tubular structures

Tissue engineering scaffold based on microfibers is subjected to micro-CT 3D analysis. 2D or 3D threshold is considered. Assessment of thresholding effect based on subjective visual evaluation is usually

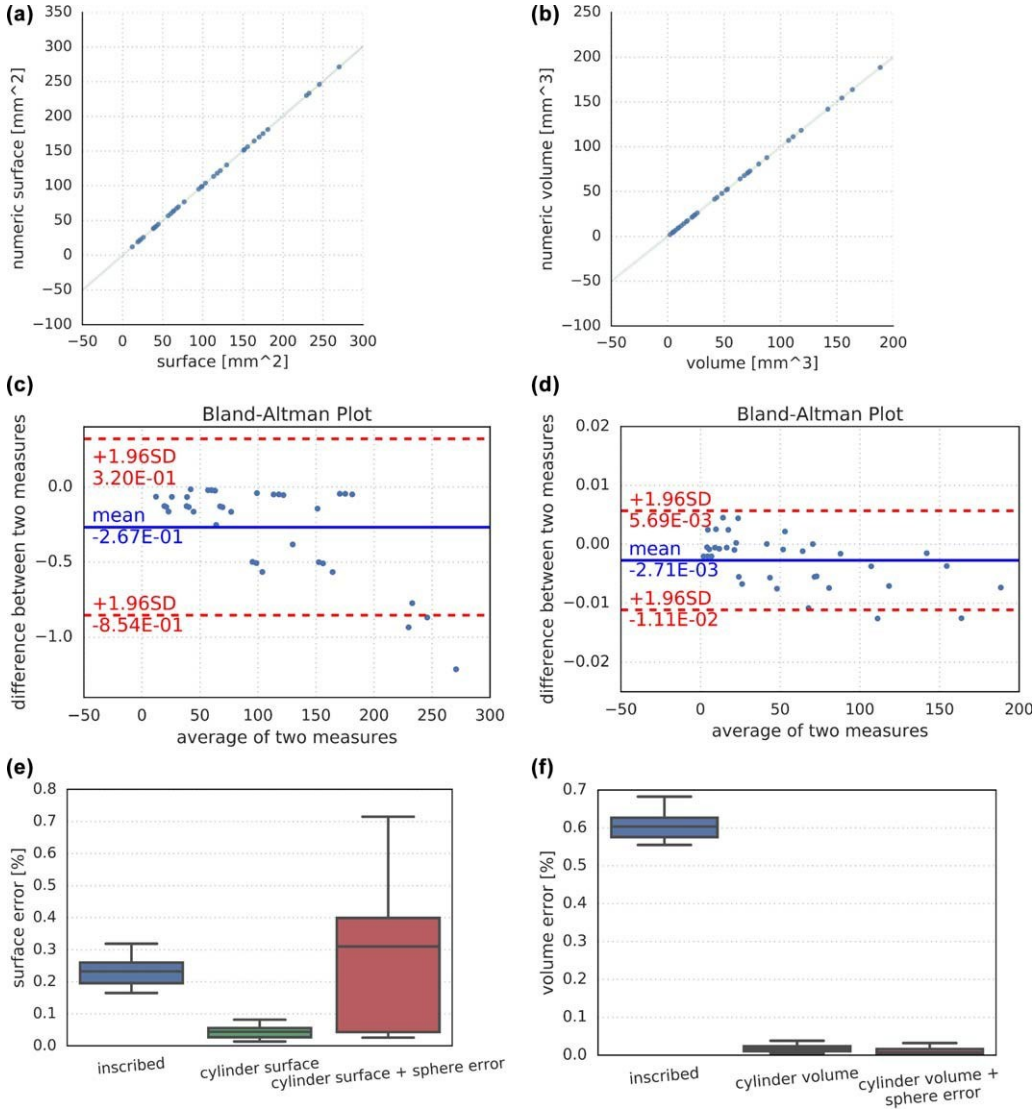

FIGURE 3 Comparing known volumes and surfaces with numerically estimated values. The source data for the graphs are available as Supporting Information S1. (a) Correlation scatter plot displaying the numerically estimated surfaces (Y-axis) against the precisely known surfaces (X-axis) of testing objects. (b) Correlation scatter plot displaying the numerically estimated volumes (Y-axis) against the precisely known volumes (X-axis) of testing objects. (c) Bland-Altman plot displaying the agreement between the numerically estimated surfaces and known surfaces of testing objects. The difference between both values (Y-axis) is plotted against their average (X-axis). The mean difference is shown as a blue line accompanied by a ±1.96 standard deviation of the difference. (d) Bland-Altman plot (Altman and Bland, 1983) displaying the agreement between the numerically estimated volumes and known volumes of testing objects. The difference between both values (Y-axis) is plotted against their average (X-axis). The mean difference is shown as a blue line accompanied by a ±1.96 standard deviation of the difference. (e) Box plot showing the impact of three methods used for compensation of the surface errors. (f) Box plot showing the impact of three methods used for compensation of the volume errors. In E and F, the relative error was calculated as 100×(value-numerical estimate)/value. The box spans the lower limits of the 2nd quartile (Q2) and the upper limits of the 3rd quartile (Q3), and the whiskers span the Q1-1.5×(Q3-Q1) and Q3 + 1.5×(Q3-Q1) values (Q1 is the 1st quartile) [Color figure can be viewed at wileyonlinelibrary.com]

insufficient and inaccurate. To improve analysis, TeIGen software is applied to generate dataset of tubular structures with known parameters. For example, a two-dimensional thresholding resulted in a significant overestimation of number of objects (Figure 7d, see also section 4.1.2) as well as inaccurate surface and volume estimates. In this case, using a three-dimensional thresholding was justified despite its computational time costs, as it provided more accurate results.

4 | DISCUSSION

4.1 | Image processing prior to micro-CT 3D analysis

4.1.1 | Image processing optimization: Aims and basics

Image processing optimization was based on many preliminary analyzes. We aimed to find a simple process (low number of variables

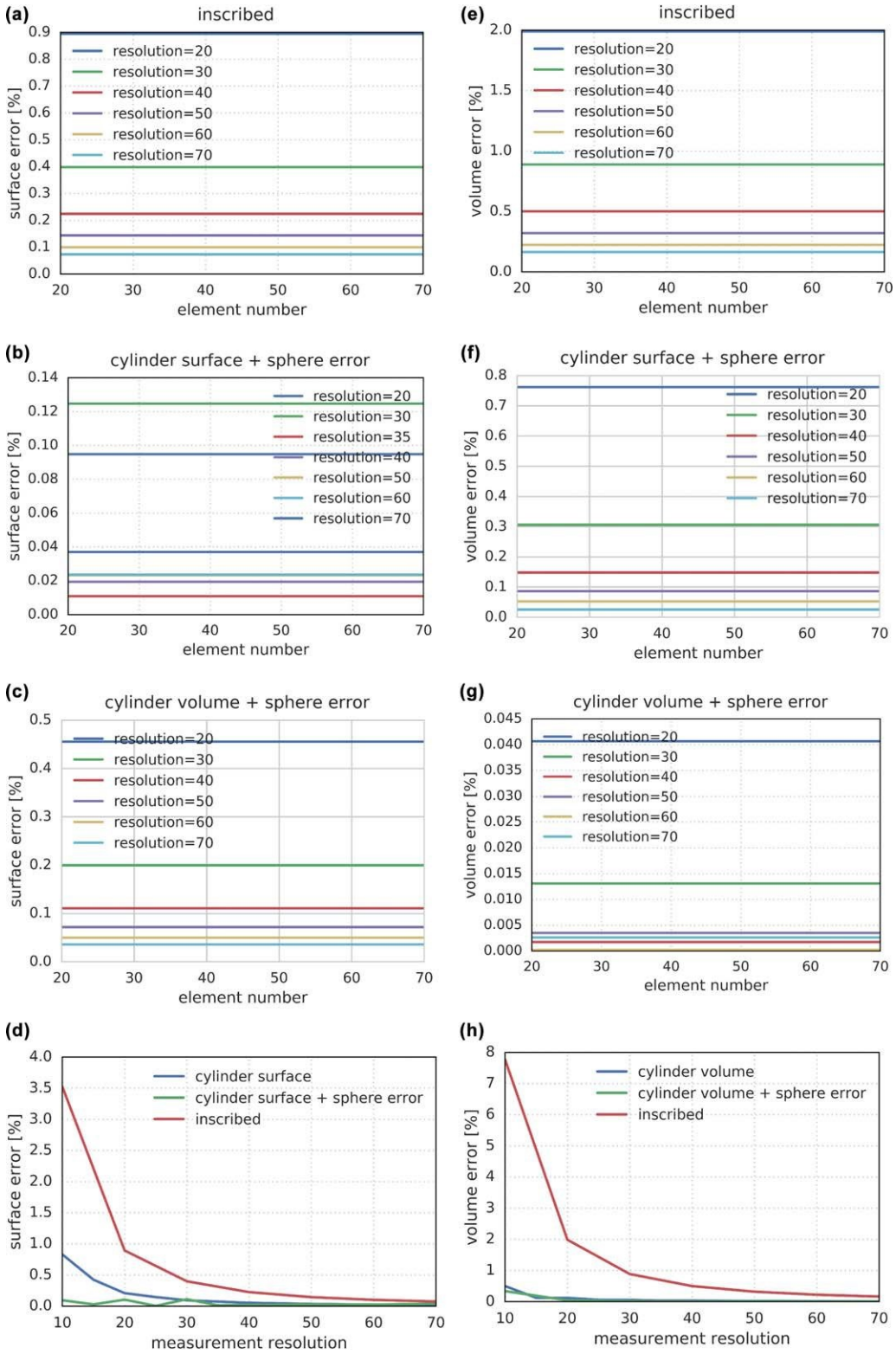

FIGURE 4 Analysis of the sensitivity of surface errors (a–d) and volume errors (e–h) to the number of generated objects (element number, a–c, e–g) and resolution at which the numerical estimates of the surface and volume were performed (d, h). The relative error plotted on the Y-axis was calculated as 100**3**(true value-numerical estimate)/value. The results are displayed without compensation (a,e) and for several methods of error compensation described in the Methods, namely: a,e—surface and volume error when no compensation is used (the colored lines show various resolutions), b,d—cylinder surface and sphere errors are compensated, c,g—cylinder volume and sphere errors are compensated. d,h—surface and volume measurement errors depending on the measurement resolution [Color figure can be viewed at wileyonlinelibrary.com]

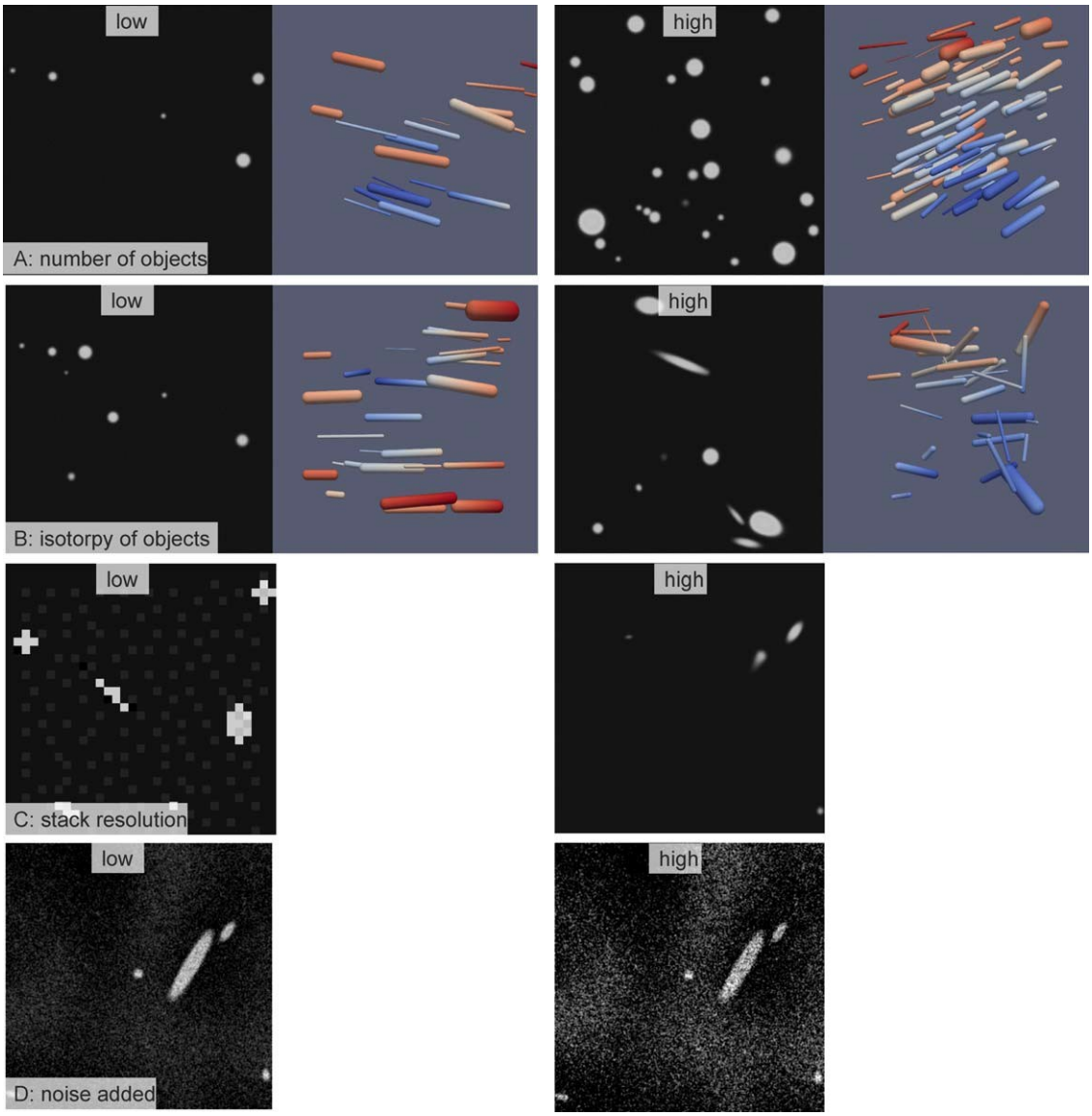

FIGURE 5 Examples of structures generated with various settings of parameters. For every parameter, ten sets of images were generated with values increasing from relatively low to relatively high, namely: (a) number of objects, (b) isotropy of objects, (c) resolution of image stacks, and (d) amount of noise added to the image data. In a-b, both two-dimensional sections and three-dimensional views are presented [Color figure can be viewed at wileyonlinelibrary.com]

influencing outcomes and convenient time efficacy) with satisfactory and reproducible results in all variable parameters of tested datasets. Datasets with the variable *count* were generally uncomplicated compared to *isotropy*, *noise*, and *resolution*, where we encountered more complications that had to be managed.

Image processing modifications by CTAn software were often performed based on subjective assessment by an experienced micro-CT user. This approach is very common in micro-CT analysis (especially in life sciences applications), and therefore it has been chosen for our study. However, this is considered one of the major drawbacks of micro-CT analysis. Reduction of subjectivity was reached by an automated threshold procedure and object count evaluation, which will be described further. This was achievable when assessing various values of object *count*, *isotropy d*atasets, whereas *noise* and *resolution* dataset evaluation was more influenced by subjectivity because individualization of the image processing approach was needed.

Object number count was important in process optimization. A user performing micro-CT analysis would not be aware of dataset parameters generated by TeIGen software. Therefore, the object number count is the only parameter where differences between analysis results and dataset 3D visualization (CTVox, Bruker) are noticeable. There is no option for the evaluation of the other parameters (e.g., volume, surface, length) from this point of view.

The following procedures were used in the image processing optimization process. A universally accurate procedure ("standard" procedure) was found for *count* and *isotropy*. For *resolution* and *noise* variables, an individual approach had to be employed. Standard procedure was based of image filtering (Gaussian blur in 3D, radius **5** 2

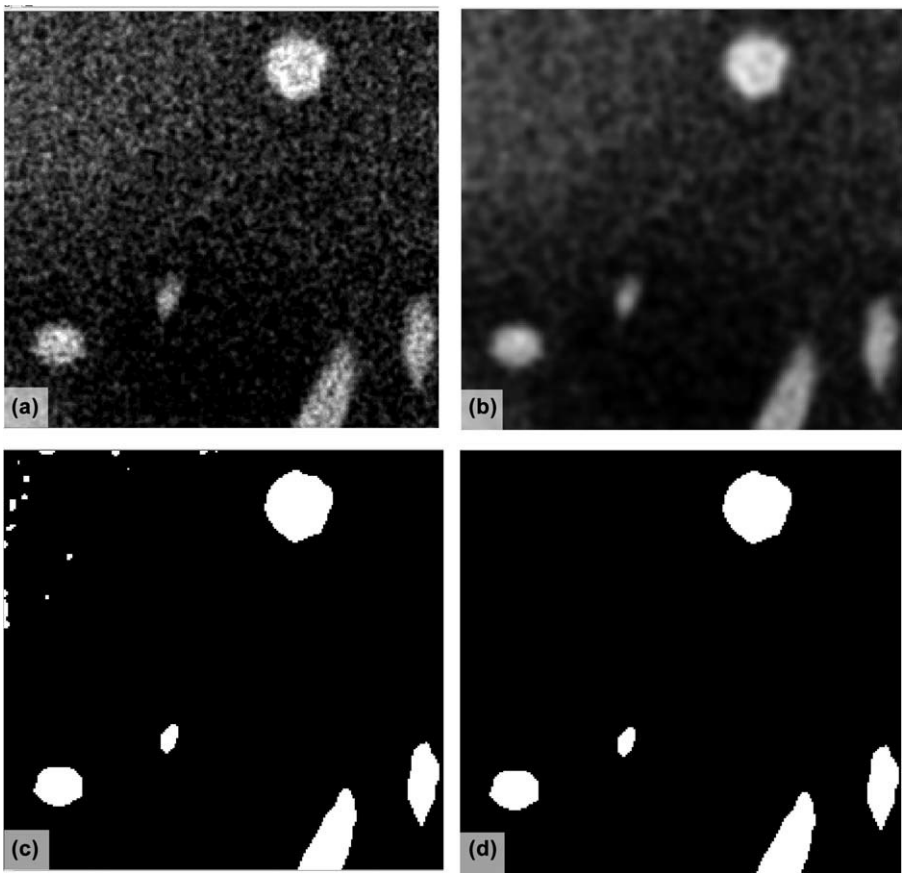

FIGURE 6 Main steps during the image processing of the virtual CT image stacks prior to analysis using the SkyScan 1272 (Bruker) console software. (a) Grayscale cross-section image (NOISE dataset). (b) Application of Gaussian blur in 3D. (c) Image after the binarization procedure (Global threshold). There are white speckles in the upper left corner as a result of image noise. We can observe irregular shapes of all objects as a result of noise and object interaction. (d) Image after performing a despeckle operation in 3D (remove white speckles of less than 50 voxels)

voxels), because some datasets had a gray pixel pattern on the background, and in some cases, they were evaluated as the objects using automatic binarization (Figure 7b). This pattern can imitate image noise in real micro-CT data. An automatic Otsu threshold in 3D was used for image binarization to reduce the influence of subjectivity. A despeckle operation in 3D was performed (remove white speckles less than 12 voxels—more in 4.1.2).

4.1.2 | Number of objects and its variability

Object number count was the only dataset parameter that could be employed in image processing optimization. Reduction of the object count number was observed in many cases, but usually less than 10% of the expected object count. Two causes were identified and explored. First, many datasets presented few relatively small objects, which were presented within a volume of interest only by their edge, so their grayscale values were not sufficient for recognition as an object. We have to consider that the transition from an object to the background is gradual, as we can see in the profile line (Figure 7a,b). In such objects, Gaussian filtering can even reduce their grayscale value, thus increasing the probability of being eliminated by binarization. Second, collision between objects was occasionally observed (Figure 7c), so two former objects were recognized as one. TeIGen should prevent these situations; however, regarding Figure 7a, we can estimate that two objects can be connected just by a gradual transition from object to background, even though their "core" structures are separate. In addition, Gaussian blur can enhance object collisions by creating a connection between the transition areas of two objects.

In contrast, the object count number increase was usually more substantial, i.e., from tens to hundreds of percent of the expected object count. Several causes were identified. In preliminary evaluation of an *isotropy* dataset, we found that objects with relatively small diameter that are almost parallel to the transversal plane were fragmented by the binarization process in 2D (tested for better time efficacy) into many smaller objects (Figure 7d). These objects could be roughly divided into two groups: small objects with volumes of a few voxels and large objects of higher volume but still much smaller than generated objects. These isolated voxels may be connected to the original object by a side or vertex; however, this is not sufficient to be recognized as one object since object voxels are, in CTAn, considered to be connected only when they are in contact via their faces. We decided to employ automatic Otsu thresholding in 3D, which led to significant improvement. However, the object count number was still much higher

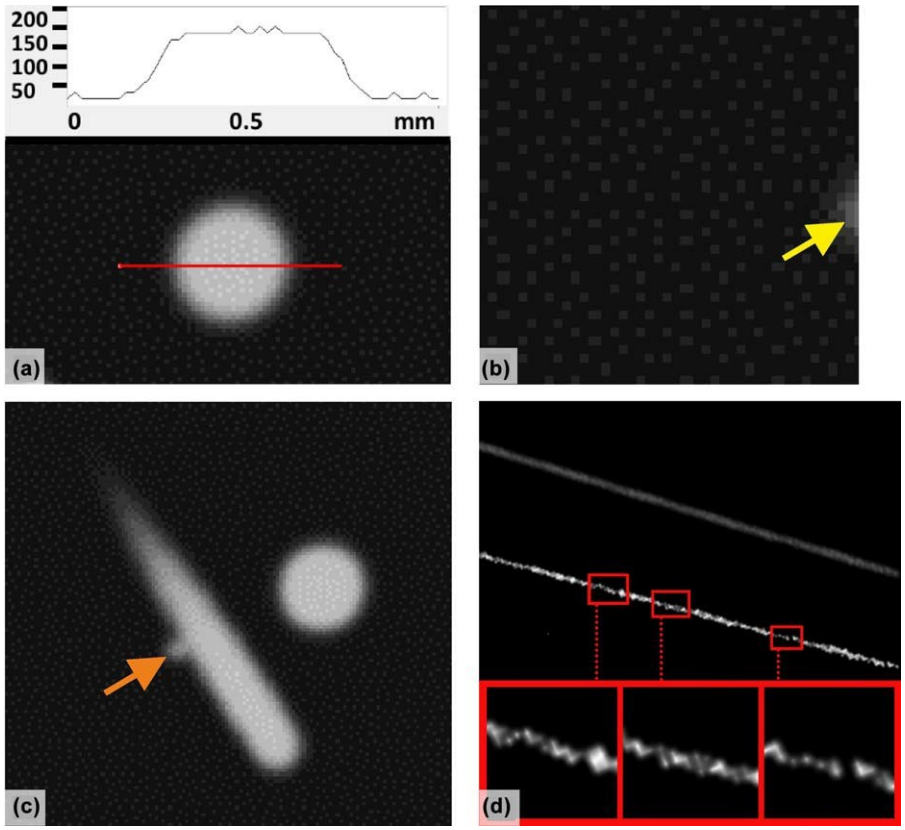

FIGURE 7 Illustration of situations leading to bias in analysis during the image processing. (a) Profile line (red line) presenting the image grayscale value (0–255). A gradual transition is apparent, which is similar to real micro-CT data. This phenomenon is a fundamental problem in image binarization. (b) Object count reduction caused by the peripheral section of an object (yellow arrow), where the grayscale value is not sufficient to be evaluated as an object by the automatic threshold. A pattern of gray pixels is visible in the background; in some datasets, they were recognized as an object, and thus they have to be eliminated by a filtering procedure. (c) Object count reduction caused by the collision of two objects (orange arrow). These are connected by their transition areas even though their core structures are separate. (d) Object count reduction caused by object fragmentation by the binarization process (especially in 2D). The upper object presents a grayscale 3D model (CTVox), and the lower object is the same object after automatic image binarization in 2D; three areas are enlarged to depict fragmentation. According to Individual Object Analysis, there are 37 objects (!) from the original one [Color figure can be viewed at wileyonlinelibrary.com]

than expected. Individual Object Analysis was performed in 3D, and object volume distribution was achieved and examined. We found that a great number of objects are below 12 voxels in volume, and thus they were considered to be noise and removed by a despeckle operation in 3D (remove white speckles of less than 12 voxels). Modification of these two processes led to accurate dataset analysis regarding object number count.

4.1.3 | Resolution parameter and image processing

In *resolution* variable datasets (pixel size from 10 μm to 500 μm in a 10 × 10 × 10-mm³ volume), we observed an increase of the object number count with an increase of pixel size. Substantial changes resulted from a shift from 100 μm to 200 μm for pixel size. Objects with defined parameters are generated by TeIGen software and subsequently voxelized. In lower resolution, objects can be fragmented as mentioned above (4.1.2). We did not succeed in finding a solution for image processing using CTAn for a pixel size of 200 μm or more for 10 × 10 × 10-mm³ dataset volumes. An optimization process regarding object count evidently led to unacceptable changes in object volume and vice versa. The pixel size value had to be considered for the parameter of filtering and despeckle operations in means of reduction of its value; for a pixel size of 80 μm or more, these operations were not applied.

4.1.4 | Noise parameter and image processing

Noise datasets (Figure 6a) needed higher individualization (and thus a more subjective approach) since these presented (together with *resolution* datasets) the most variable image data. Because of this, comparison with datasets processed by the "standard" approach is less applicable. The main problem was the gradual decrease of the signal to noise ratio in image data, so the outcome is always a compromise between noise reduction and object number and volume preservation. Filtration was achieved by Gaussian blur in 3D and was used with a gradual increase of the radius from 2 to 5 voxels (Figure 6b). An automatic Otsu threshold in 3D failed to provide reliable binarization because, in some datasets, noise was recognized as an object. A global threshold had to be employed with a progressive increase in the lower threshold value from 87 to 135 as the noise was intensified (Figure 6c). Interaction between noise and generated objects can lead to an

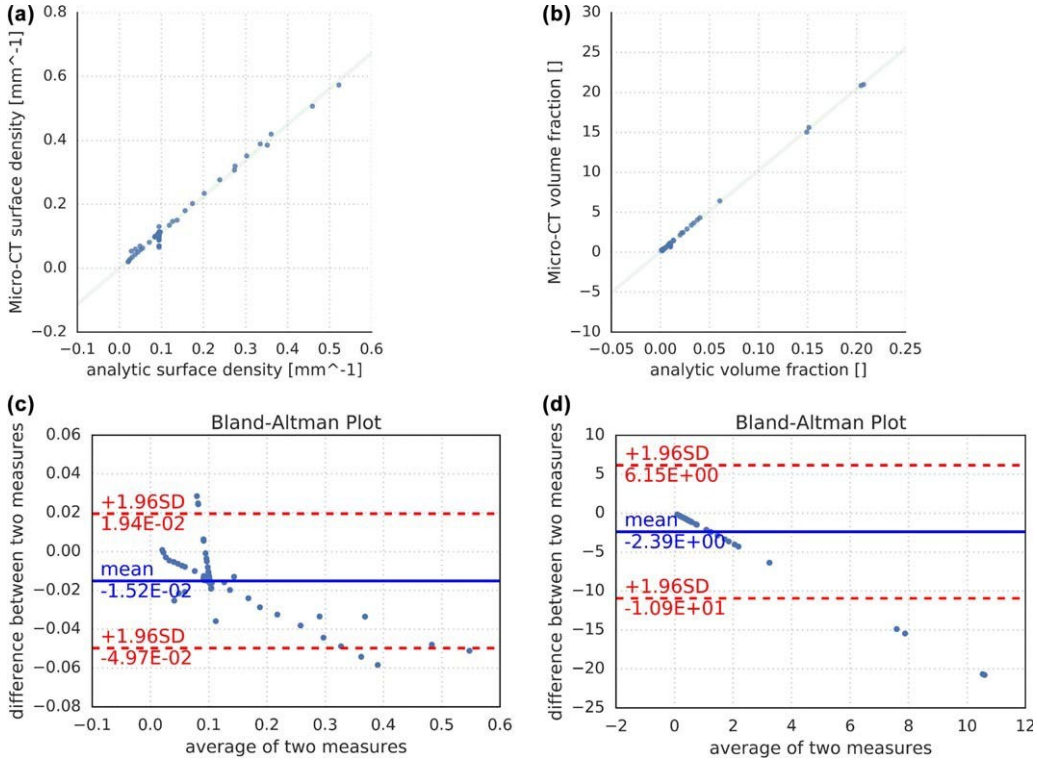

FIGURE 8 Comparing known surface and volume densities of generated objects with the results obtained after thresholding on the micro-CT console. The source data for the graphs are provided as Supporting Information S2. Data sets with known surface and volume densities were processed by the micro-CT software as described above. (a,b) correlation scatter plots displaying the values from micro-CT (Y-axis) against the precisely known surface and volume densities (X-axis) of testing objects. (c,d) Bland-Altman plots displaying the agreement between the surface and volume densities estimated on micro-CT and known values of the same testing objects. The difference between both values (Y-axis) is plotted against their average (X-axis). The mean difference is shown as a blue line accompanied by a ±1.96 standard deviation of the difference [Color figure can be viewed at wileyonlinelibrary.com]

alteration of volume, surface and object shape, which is noticeable in Figure 6c. A higher threshold value resulted in a reduction in object number count and object volume. A despeckle operation was performed with an increase of defined volume (removing white speckles less than: from 12 to 250 mm; Figure 6d).

4.2 | Novelty of the present approach

When compared to the ImageJ plugins mentioned in 1.3., the TeIGen software allows for generating 3D objects as test images. When compared with the Gensei software (Cimrman, 2010), TeIGen provides colliding and noncolliding fibrous structures, the geometric characteristics of which can be set by the user. Moreover, TeIGen generates also porosities and allows for modeling various types of realistic noise. The application includes both graphical user interface with 3D visualization which facilitates data preparation, as well as batch processing option.

It is recommended that the user performs a real object analysis first, using a micro-CT or scanning electron microscopy, thus estimating the typical range of the quantitative characteristics (i.e., total volumes, surfaces, lengths, and number of objects inside ROI). However, the error between the true and estimated data is unknown. In the second step, the data are used as input data of the TeIGen software defining the objects to be generated. In this second step, phantom objects with geometrical properties statistically similar to the real material are generated, but this time, the geometrical characteristics are precisely known. In the third step, the measurement of these phantom data is repeated and the error between the true known and estimated data is quantified. This can be used for calibration of the whole measurement and for identifying any major sources of bias.

In general, using traceable standard reference materials has always belonged to good laboratory practice. The TeIGen software offers a solution by generating virtual standard reference materials. These might either mimic the real materials or be generated according to the best qualified estimates currently available.

4.3 | Further development of the TeIGen software and its relevance to manufacturing and characterization of biomaterials

Further development of the TeIGen software incorporates improvements in the highest values of filling the space with unconnected objects of increasing volume fraction. This task has theoretical limits that cannot be exceeded (Zidek et al., 2016), but the present algorithm starts to require unacceptable computational time costs when reaching the value of approx. 30% volume fraction. Should more space be filled with the tubes, collisions have to be allowed in the settings.

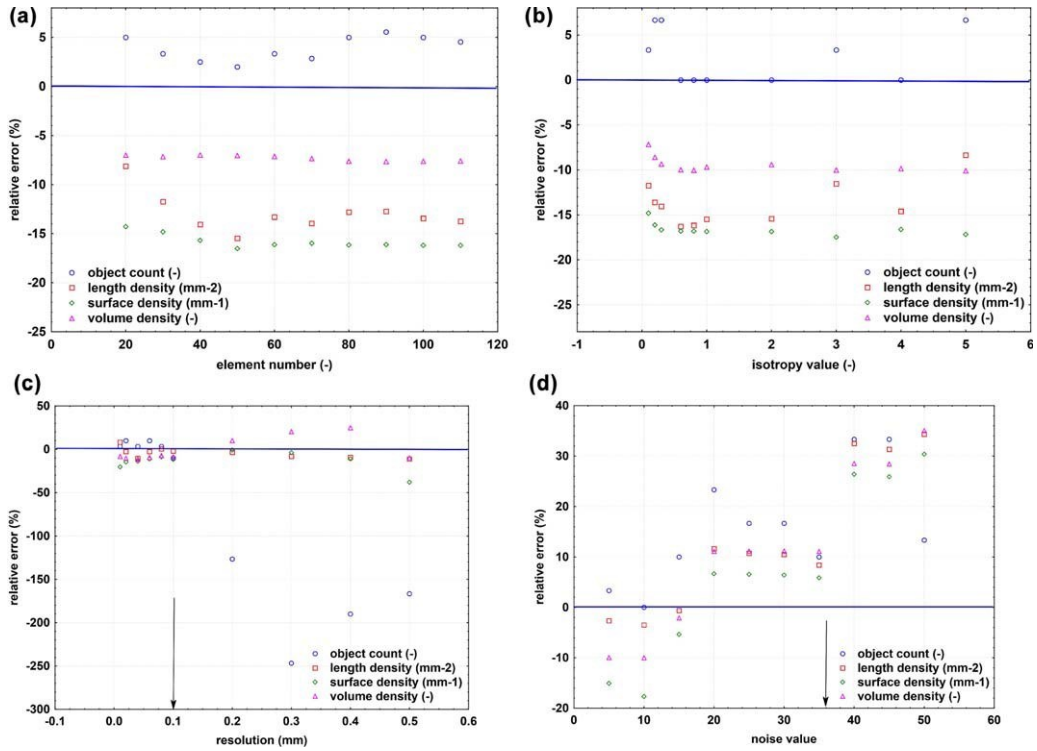

FIGURE 9 Analysis of the sensitivity of the thresholding to various values of parameters in generated image sets. Data sets with known numbers of objects, length densities, surface densities, and volume densities were processed by the micro-CT software as described above. After the morphometry on the micro-CT console was done, the relative errors (Y-axis) were calculated as 100∗(true value-numerical estimate)/value and plotted against gradually changing values of the number of objects (a), isotropy (b), image resolution (c), and noise value (d). (a) Various object counts did not affect the size of the relative error. While the numbers of objects were underestimated by the microCT, the volumes, lengths and surfaces were slightly overestimated. (b) The value of isotropy did not affect the size of the error. (c) The size of the error dramatically increased when the voxel size exceeded 0.1 mm (arrow) in virtual stacks of 10 × 10 × 10 mm containing objects with a mean diameter of 1 mm. (d) The size of the error increased when the noise value exceeded 37 (arrow) [Color figure can be viewed at wileyonlinelibrary.com]

Another challenge for the future would be using the sections of generating objects to simulate the optimum sampling of numbers of image sections and their thicknesses. The TeIGen software can become a useful tool for planning of the sampling design of studies in microscopy, including manual and interactive measurements of objects with known size, where the research aim is to find the number and thickness of sections that are necessary for reliable measurements of numbers, surfaces, and volumes of tubular or spherical objects in studies using stereological counting rules (Mouton et al., 2017).

We greatly acknowledge the wide use of the ImageJ software (Schneider et al., 2012) and its contribution to the scientific community worldwide. Although ImageJ currently supports Python scripting, it

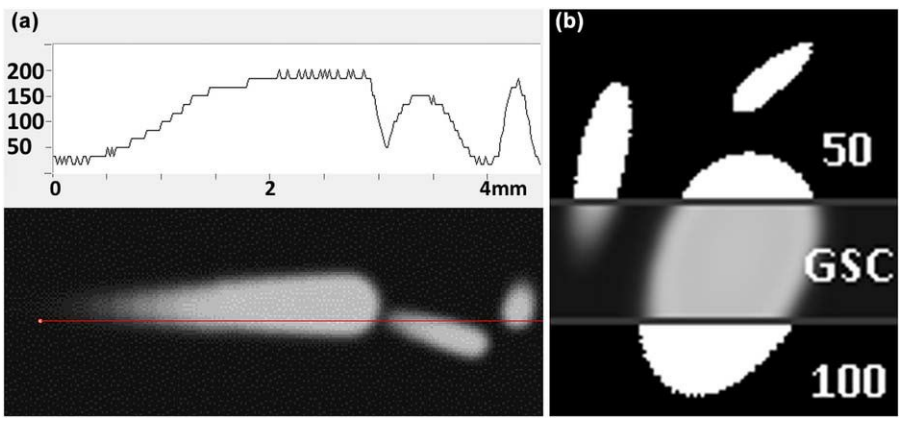

FIGURE 10 Illustration of global thresholding effect. (a) Profile line cutting tubular structures with grayscale value. (b) Different global threshold values (50 and 100; values were chosen to provide apparent differences in this figure) combined with original grayscale image (GSC). Binarized structures appear larger or smaller based on threshold value used [Color figure can be viewed at wileyonlinelibrary.com]

TABLE 3 Example of practical application of the TeIGen software

	Object number	Tot.V. (mm^3)	M.Obj.V. (mm^3)	Tot.S. (mm^2)	M.Obj.S. (mm^2)
TeiGen (true value)	30	11.33	0.38	113.39	3.78
Global threshold **5** 50	28	16.00	0.57	136.89	4.89
Global threshold **5** 75	30	12.42	0.41	116.20	3.87
Global threshold **5** 100	29	10.33	0.36	102.17	3.52

Illustration of the effect of Global threshold used during micro-CT processing on analysis results in selected parameters: Tot.V.—total volume of all objects, M.Obj.V.—mean object volume, Tot.S.—total surface of all objects, M.Obj.S.—mean object surface. For details see Figure 10 and section 3.5. This analysis required approximately 20 min of time and revealed the preferred Global threshold settings **5** 75.

currently does not allow for using libraries that are not part of the language kernel (for example, *scipy, numpy, scikit-image* librares, and several others). Should the ImageJ support these libraries in the future, the TeiGen software can be incorporated as an ImageJ plugin, thus benefiting from the ImageJ interface and a plethora of other functions. At present TeIGen can cooperate with ImageJ by reading and saving image data from/into the commonly supported file formats.

5 | CONCLUSION

Open-source software for the generation of three-dimensional models of fibrous and porous structures with known volumes, surfaces, lengths and object counts was developed and made freely available to the scientific community. This study provides a software tool for calibrating quantitative micro-CT assessments by producing and saving virtually generated image datasets with known morphometric data on noncolliding tubes, colliding tubes, or material porosities. This tool is useful for identifying combinations of object and image stack properties, which may easily lead to biased results using thresholding procedures of fibrous biomaterials in microCT. Some of these situations were extensively tested in the present article to help users of micro-CT understand where errors can occur, ensuring that micro-CT segmentation procedures can be proved to be valid and correct. We identified combinations of object and image stack properties that may easily lead to biased results using thresholding procedures in microCT. A solution to this problem could be more frequent application of design-based stereological methods during micro-CT analyzes. This method is openly available to researchers involved in morphometry of three-dimensional fibrillar and porous structures in micro-CT scans.

HUMAN AND ANIMAL RIGHTS STATEMENT

This article does not contain any studies with human participants or animals performed by any of the authors. This article does not contain patient data.

ACKNOWLEDGMENTS

The authors thank the following research projects. ZT, PS, and MHK were supported by AZV MZ CR Project No. 15-25813A. MJ, TK, AM, PT, PS, MHK, and MK were also supported by the National Sustainability Program I (NPU I) Nr. LO1503 provided by the Ministry of Education, Youth and Sports of the Czech Republic, by the Progres Q39 and Progres Q29/LF1 (MB) projects of the Charles University, and by the SVV 260390/2017 and SVV 260392/2017 projects of the Charles University. PK was supported by project LO1506 of the Czech Ministry of Education, Youth and Sports under program NPU I. ZT was also supported by the Ministry of Education, Youth and Sports under the project FIND No. CZ.02.1.01/0.0/0.0/16_019/0000787. The micro-CT part of the study is a result of the project implementation: "Technological development of post doc programs," registration number CZ.1.05/41.00/16.0346, supported by Research and Development for Innovations Operational Programme (RDIOP) co-financed by the European regional development fund and the state budget of the Czech Republic. MJ and ZT were also supported by the Charles University Research Centre program UNCE/MED/006 University Center of Clinical and Experimental Liver Surgery.

CONFLICT OF INTEREST

The authors declare that they have no conflicts of interest.

ORCID

Zbyněk Tonar http://orcid.org/0000-0002-7200-9894

REFERENCES

Altman, D. G., & Bland, J. M. (1983). Measurement in medicine: The analysis of method comparison studies. *The Statistician*, *32*(3), 307–317.

Baddeley, A., & Jensen, E. B. (2004). *Stereology for statisticians*. Boca Raton: Chapman & Hall/CRC.

Bruker Corporation. (2017). *Morphometric parameters measured by SkyscanTM CT-analyser software*. Billerica: Bruker Corporation.

Buie, H. R., Campbell, G. M., Klinck, R. J., MacNeil, J. A., & Boyd, S. K. (2007). Automatic segmentation of cortical and trabecular compartments based on a dual threshold technique for in vivo micro-CT bone analysis. *Bone*, *41*(4), 505–515.

Burey, A., Dos Reis, P. J., Santana, Vicentin B. L., Dezan Garbelini, C. C., Grama Hoeppner, M., & Appoloni, C. R. (2018). Polymerization shrinkage and porosity profile of dual cure dental resin cements with different adhesion to dentin mechanisms. *Microscopy Research and Technique*, *71*(1), 88–96.

Burey, A., Dos Reis, P. J., Santana Vicentin, B. L., Dezan Garbelini, C. C., Grama Hoeppner, M., & Appoloni, C. R. (in press). Polymerization shrinkage and porosity profile of dual cure dental resin cements with different adhesion to dentin mechanisms. *Microscopy Research and Technique*. https://doi.org/10.1002/jemt.22960.

Burghardt, A. J., Kazakia, G. J., & Majumdar, S. (2007). A local adaptive threshold strategy for high resolution peripheral quantitative computed tomography of trabecular bone. *Annals of Biomedical Engineering*, *35*(10), 1678.

Cimrman, R. (2010). Gensei – GENerate serial images. Retrieved from https://github.com/rc/gensei

De Souza, E. T., Nunes Tameirao, M. D., Roter, J. M., De Assis, J. T., De Almeida Neves, A., & De-Deus, G. A. (2013). Tridimensional quantitative porosity characterization of three set calcium silicate-based repair cements for endodontic use. *Microscopy Research and Technique*, *76*(10), 1093–1098.

Draenert, M. E., Draenert, A. I., Forriol, F., Cerler, M., Kunzelmann, K. H., Hickel, R., & Draenert, K. (2012). Value and limits of μ-CT for nondemineralized bone tissue processing. *Microscopy Research and Technique*, *75*(4), 416–424.

Gómez, S., Vlad, M. D., López, J., & Fernández, E. (2016). Design and properties of 3D scaffolds for bone tissue engineering. *Acta Biomaterialia*, *42*, 341–350.

Gómez, S., Vlad, M. D., López, J., Navarro, M., & Fernández, E. (2013). Characterization and three-dimensional reconstruction of synthetic bone model foams. *Materials Science & Engineering. C, Materials for Biological Applications*, *33*(6), 3329–3335.

Hara, T., Tanck, E., Homminga, J., & Huiskes, R. (2002). The influence of microcomputed tomography threshold variations on the assessment of structural and mechanical trabecular bone properties. *Bone*, *31*(1), 107–109.

Hildebrand, T., & Ruegsegger, P. (2003). A new method for the model independent assessment of thickness in three dimensional images. *Journal of Microscopy*, *185*, 67–75.

Ho, S. T., & Hutmacher, D. W. (2006). A comparison of micro CT with other techniques used in the characterization of scaffolds. *Biomaterials*, *27*(8), 1362–1376.

Horakova, J., Mikes, P., Saman, A., Svarcova, T., Jencova, V., Suchy, T., … Prochazkova, R. (2018). Comprehensive assessment of electrospun scaffolds hemocompatibility. *Materials Science & Engineering. C, Materials for Biological Applications*, *82*, 330–335.

Jiměnez, P., Thomas, F., & Torras, C. (2001). 3D collision detection: A survey. *Computers & Graphics*, *25*, 269–285.

Ji˜rík, M. (2017). Teigen – TEst Image GENerator software. Retrieved from https://mjirik.github.io/teigen/

Ji˜rík, M., & Tonar, Z. (2018). User manual for the Teigen – TEst Image GENerator software. Retrieved from https://github.com/mjirik/teigen/blob/master/user_manual.md

Ji˜rík, M., Tonar, Z., Králíčková, A., Eberlová, L., Mírka, H., Kochová, P., … Li˜ska, V. (2016). Stereological quantification of microvessels using semiautomated evaluation of X-ray microtomography of hepatic vascular corrosion casts. *International Journal of Computer Assisted Radiology and Surgery*, *11*(10), 1803–1819.

Jones, A. C., Arns, C. H., Sheppard, A. P., Hutmacher, D. W., Milthorpe, B. K., & Knackstedt, M. A. (2007). Assessment of bone ingrowth into porous biomaterials using Micro-CT. *Biomaterials*, *28* (15), 2491–2504.

Karageorgiou, V., & Kaplan, D. (2005). Porosity of 3D biomaterial scaffolds and osteogenesis. *Biomaterials*, *26*(27), 5474–5491.

Kochová, P., Cimrman, R., Janáček, J., Witter, K., & Tonar, Z. (2011). How to asses, visualize and compare the anisotropy of linear structures reconstructed from optical sections - a study based on histopathological quantification of human brain microvessels. *Journal of Theoretical Biology*, *286*(1), 67–78.

Landis, E. N., & Keane, D. T. (2010). X-ray microtomography. *Materials Characterization*, *61*(12), 1305–1316.

Lorensen, W. E., & Harvey, E. C. (1987). Marching cubes: A high resolution 3d surface construction algorithm. *ACM Siggraph Computer Graphics*, *21*(4), 163–169.

Maia, R. S., Jacob, C., Hara, A. K., Silva, A. C., Pavlicek, W., & Ross, M. J. (2015). An algorithm for noise correction of dual-energy computed tomography material density images. *International Journal of Computer Assisted Radiology and Surgery*, *10*(1), 87–100.

Montufar, E. B., Vojtova, L., Celko, L., & Ginebra, M. P. (2017). Calcium phosphate foams: Potential scaffolds for bone tissue modeling in three dimensions. *Methods in Molecular Biology (Clifton, N.J.)*, *1612*, 79–94.

Moore, M., & Wilhelms, J. (1988). Collision detection and response for computer animation. *Computer Graphics*, *22*(4), 289–298.

Mouton, P. R. (2002). *Principles and practices of unbiased stereology. An introduction for bioscientists*. Baltimore: The Johns Hopkins University Press.

Mouton, P. R., Phoulady, H. A., Goldgof, D., Hall, L. O., Gordon, M., & Morgan, D. (2017). Unbiased estimation of cell number using the automatic optical fractionator. *Journal of Chemical Neuroanatomy*, *80*, A1–A8.

Neves, A. A., Coutinho, E., Alves, H. D., & de Assis, J. T. (2015). Stress and strain distribution in demineralized enamel: A micro-CT based finite element study. *Microscopy Research and Technique*, *78*(10), 865–872.

Otsu, N. (1979). A threshold selection method from gray-level histograms. *IEEE Transactions on Systems, Man, and Cybernetics*, *9*(1), 62–66.

Parkinson, I. H., Badiei, A., & Fazzalari, N. L. (2008). Variation in segmentation of bone from micro-CT imaging: Implications for quantitative morphometric analysis. *Australasian Physical & Engineering Sciences in Medicine*, *31*(2), 160–164.

Particelli, F., Mecozzi, L., Beraudi, A., Montesi, M., Baruffaldi, F., & Viceconti, M. (2012). A comparison between micro-CT and histology for the evaluation of cortical bone: Effect of polymethylmethacrylate embedding on structural parameters. *Journal of Microscopy*, *245*(3), 302–310.

Plencner, M., East, B., Tonar, Z., Otáhal, M., Prosecká, E., Rampichová, M., … Amler, E. (2014). Abdominal closure reinforcement by using polypropylene mesh functionalized with poly-e-caprolactone nanofibers and growth factors for prevention of incisional hernia formation. *International Journal of Nanomedicine*, *9*, 3263–3277.

Prosecká, E., Rampichová, M., Litvinec, A., Tonar, Z., Králíčková, M., Vojtová, L., … Amler, E. (2015). Collagen/hydroxyapatite scaffold enriched with polycaprolactone nanofibers, thrombocyte-rich solution and mesenchymal stem cells promotes regeneration in large bone defect in vivo. *Journal of Biomedical Materials Research Part A*, *103*(2), 671–682.

Pyka, G., Kerckhofs, G., Schrooten, J., & Wevers, M. (2014). The effect of spatial micro-CT image resolution and surface complexity on the morphological 3D analysis of open porous structures. *Materials Characterization*, *87*, 104–115.

Rau, T. S., Wu€rfel, W., Lenarz, T., & Majdani, O. (2013). Three-dimensional histological specimen preparation for accurate imaging and

spatial reconstruction of the middle and inner ear. *International Journal of Computer Assisted Radiology and Surgery*, *8*(4), 481–509.

Remy, E., & Thiel, E. (2002). Medial axis for chamfer distances: Computing look-up tables and neighbourhoods in 2D or 3D. *Pattern Recognition Letters*, *23*(6), 649–661.

Schladitz, K. (2011). Quantitative micro-CT. *Journal of Microscopy*, *243*(2), 111–117.

Schneider, C. A., Rasband, W. S., & Eliceiri, K. W. (2012). NIH Image to ImageJ: 25 years of image analysis. *Nature Methods*, *9*(7), 671–675.

Schroeder, W. J., Avila, L. S., & Hoffman, W. (2000). Visualizing with VTK: A tutorial. *IEEE Computer Graphics and Applications*, *20*(5), 20–27.

Schroeder, W., Martin, K. M., & Lorensen, W. E. (1998). *The visualization toolkit (2nd ed.): An object-oriented approach to 3D graphics*. Upper Saddle River: Prentice-Hall.

Shen, H., Nutt, S., & Hull, D. (2004). Direct observation and measurement of fiber architecture in shor fiber-polymer composite foam through micro-CT imaging. *Composites Sci Technol*, *64*(13–14), 2113–2120.

Shepp, L. A., & Logan, B. F. (1974). The Fourier reconstruction of a head section. *IEEE Transactions on Nuclear Science*, *21*(3), 21–43.

Stock, S. R. (2009). *MicroComputed tomography methodology and applications*. Boca Raton: CRC Press.

Stoyan, D., Kendall, W. S., & Mecke, J. (1995). *Stochastic geometry and its applications*. New York: John Wiley & Sons.

Suchý, T., Šupová, M., Sauerová, P., Verdánová, M., Sucharda, Z., Rýglová, Š., … Kalbáčová, M. H. (2015). The effects of different cross-linking conditions on collagen-based nanocomposite scaffolds-an in vitro evaluation using mesenchymal stem cells. *Biomedical Materials (Bristol, England)*, *10*(6), 065008.

Szentivanyi, A., Chakradeo, T., Zernetsch, H., & Glasmacher, B. (2011). Electrospun cellular microenvironments: Understanding controlled release and scaffold structure. *Advanced Drug Delivery Reviews*, *63*(4–5), 209–220.

Tonar, Z., Khadang, I., Fiala, P., Nedorost, L., & Kochová, P. (2011). Quantification of compact bone microporosities in the basal and alveolar portions of the human mandible using osteocyte lacunar density and area fraction of vascular canals. *Annals of Anatomy*, *193*(3), 211–219.

Tonar, Z., Kochova, P., Cimrman, R., Witter, K., Janacek, J., & Rohan, V. (2011). Microstructure oriented modelling of hierarchically perfused porous media for cerebral blood flow evaluation. *Key Engineering Materials*, *465*, 286–289.

Yan, Y. B., Qi, W., Qiu, T. X., Teo, E. C., & Lei, W. (2012). The effect of threshold value on the architectural parameters and stiffness of human cancellous bone in micro-CT analysis. *Journal of Mechanics in Medicine and Biology*, *12*(05), 1250092.

Zhang, J., Yan, C. H., Chui, C. K., & Ong, S. H. (2010). Fast segmentation of bone in CT images using 3D adaptive thresholding. *Computers in Biology and Medicine*, *40*(2), 231–236.

Zhong, S., Zhang, Y., & Lim, C. T. (2012). Fabrication of large pores in electrospun nanofibrous scaffolds for cellular infiltration: A review. *Tissue Engineering Part B, Reviews*, *18*(2), 77–87.

Zidek, J., Vojtova, L., Abdel-Mohsen, A. M., Chmelik, J., Zikmund, T., Brtnikova, J., … Kaiser, J. (2016). Accurate micro-computed tomography imaging of pore spaces in collagen-based scaffold. *Journal of Materials Science: Materials in Medicine*, *27*(6), 110.

SUPPORTING INFORMATION

Additional Supporting Information may be found online in the supporting information tab for this article.

How to cite this article: Ji~rík M, Barto~s M, Tomášek P, et al. Generating standardized image data for testing and calibrating quantification of volumes, surfaces, lengths, and object counts in fibrous and porous materials using X-ray microtomography. *Microsc Res Tech*. 2018;00:1–18. https://doi.org/10.1002/jemt.23011

11.2 Supplement II

Kolinko, Y., Malečková, A., Kochová, P., Grajciarová, M., Blassová, T., **Kural, T.,** Trailin, A., Červenková, L., Havránková, J., Vištejnová, L., Tonarová, P., Moulisová, V., Jiřík, M., Zavaďáková, A., Tichánek, F., Liška, V., Králíčková, M., Witter, K., Tonar, Z. Using virtual microscopy for the development of sampling strategies in quantitative histology and designbased stereology. Anat. Histol. Embryol. 2022 Jan;51(1):3-22. DOI: 10.1111/ahe.12765. **$IF_{(JCR2020)}$=1.114. Q3(Veterinary sciences)**
https://pubmed.ncbi.nlm.nih.gov/34806204/

Received: 29 September 2021 | Accepted: 31 October 2021

DOI: 10.1111/ahe.12765

ANATOMIA HISTOLOGIA EMBRYOLOGIA JOURNAL OF VETERINARY MEDICINE WILEY

REVIEW

Using virtual microscopy for the development of sampling strategies in quantitative histology and design-based stereology

Yaroslav Kolinko[1,2] | Anna Malečková[3] | Petra Kochová[3] | Martina Grajciarová[1,2] | Tereza Blassová[1,2] | Tomáš Kural[1] | Andriy Trailin[2] | Lenka Červenková[2,4] | Jiřina Havránková[1,2] | Lucie Vištejnová[1,2] | Pavla Tonarová[2] | Vladimíra Moulisová[2] | Miroslav Jiřík[2,3] | Anna Zavaďáková[2] | Filip Tichánek[2,5] | Václav Liška[2,6] | Milena Králíčková[1,2] | Kirsti Witter[7] | Zbyněk Tonar[1,2]

[1]Department of Histology and Embryology, Faculty of Medicine in Pilsen, Charles University, Pilsen, Czech Republic

[2]Faculty of Medicine in Pilsen, Biomedical Center, Charles University, Pilsen, Czech Republic

[3]Faculty of Applied Sciences, European Centre of Excellence NTIS, University of West Bohemia, Pilsen, Czech Republic

[4]Department of Pathology, Third Faculty of Medicine, Charles University, Prague, Czech Republic

[5]Department of Pathological Physiology, Faculty of Medicine in Pilsen, Charles University, Pilsen, Czech Republic

[6]Department of Surgery and Biomedical Center, Faculty of Medicine in Pilsen, Charles University, Pilsen, Czech Republic

[7]Institute of Morphology, Department of Pathobiology, University of Veterinary Medicine Vienna, Vienna, Austria

Correspondence
Zbyněk Tonar, Department of Histology and Embryology, Faculty of Medicine in Pilsen, Charles University, Karlovarská 48, 301 66 Pilsen, Czech Republic.
Email: Zbynek.Tonar@lfp.cuni.cz

Funding information
Horizon 2020 Framework Programme, Grant/Award Number: 856620; Ministerstvo Zdravotnictví Ceské Republiky, Grant/Award Number: 15–29241A and AZV NU20J-08-00009; Ministerstvo Školství, Mládeže a Tělovýchovy, Grant/Award Number: LO1503; Univerzita Karlova v Praze, Grant/Award Number: GACR No. 1313420, Progres Q39, SVV 260 536 and UNCE/MED/006; European Regional Development Fund, Grant/Award Number: AMTMI CZ.02.1.01/0.0/0.0/17_048/0007280 and FIND CZ.02.1.01/0.0/0.0/16_019/0000787

Abstract

Only a fraction of specimens under study are usually selected for quantification in histology. Multilevel sampling or tissue probes, slides and fields of view (FOVs) in the regions of interest (ROIs) are required. In general, all parts of the organs under study should be given the same probability to be taken into account; that is, the sampling should be unbiased on all levels. The objective of our study was to provide an overview of the use of virtual microscopy in the context of developing sampling strategies of FOVs for stereological quantification. We elaborated this idea on 18 examples from multiple fields of histology, including quantification of extracellular matrix and muscle tissue, quantification of organ and tumour microvessels and tumour-infiltrating lymphocytes, assessing osseointegration of bone implants, healing of intestine anastomoses and osteochondral defects, counting brain neurons, counting nuclei in vitro cell cultures and others. We provided practical implications for the most common situations, such as exhaustive sampling of ROIs, sampling ROIs of different sizes, sampling the same ROIs for multiple histological methods, sampling more ROIs with variable intensities or using various objectives, multistage sampling and virtual sampling. Recommendations were provided for pilot studies on systematic uniform random sampling of FOVs as a part of optimizing the efficiency of histological quantification to prevent over- or undersampling. We critically discussed the pros and cons of using virtual sections for sampling FOVs from whole scanned sections. Our review

demonstrated that whole slide scans of histological sections facilitate the design of sampling strategies for quantitative histology.

KEYWORDS
histological slides, quantitative microscopy, sampling, stereology, study design, veterinary histology

1 | INTRODUCTION

Virtual microscopy or digital microscopy is the digital conversion of light microscopic specimens at full resolution and their presentation over a computer network. The term 'virtual' refers to the examination of the specimens without direct contact with the object slide or the light microscope (Smart In Media AG, 2021). Virtual microscopy makes samples accessible to specialists without needing to be present and without needing to have extensive equipment (Saliba et al., 2012). It is discussed intensively in the frame of diagnosis and treatment of different diseases (telepathology, more than 1400 Scopus entries in September 2021) in human as well as in veterinary medicine (e.g. Bertram & Klopfleisch, 2017), resulting in the first guidelines by the respective expert groups (Jahn et al., 2020).

Another huge field of application for virtual microscopy is education and training, fuelled even more by the increased demand for remote learning during the COVID-19 pandemic (for reviews, see, e.g., Bertram & Klopfleisch, 2017; Kuo & Leo, 2019).

In addition, virtual microscopy is also a powerful tool for research. Our review demonstrates how whole slide scans of histological sections facilitate the design of sampling strategies for quantitative histology and how they can be compared to other technical options.

1.1 | Design-based stereology

Design-based stereology is a set of tools that allows quantification without making assumptions regarding the shape, size, distribution or orientation of the structures of interest (Howard & Reed, 2005; Mouton, 2002). Strict sampling rules have to be followed to achieve this independence; that is, stereology includes detailed prescriptions of the sampling procedure and guidelines on how to test its quality. Stereology has become the gold standard in morphometry due to its reproducibility and assumption-free design. A number of both general and organ-specific protocols, recommendations and algorithms have been published to facilitate planning and conducting quantitative histology studies (Table 1).

1.2 | Sampling in an integral part of design-based stereology

All the guidelines mentioned in Table 1 refer to sampling strategies on all levels of any reduction of material in histological studies. Only a fraction of specimens under study are usually selected for quantification in histology. This multilevel sampling includes (i) taking tissue probes from large macroscopic organs that cannot be processed completely (i.e. porcine liver, human brain); (ii) selecting histological slides from tissue blocks that undergo exhaustive sectioning (not all slides are selected for further analysis); and (iii) selecting microscopic fields of view (FOVs) that are captured and analysed to represent various regions of interest (ROIs). In general, all parts of the organs under study should have the same probability of being taken into account; that is, the sampling should be unbiased on all levels (Howard & Reed, 2005; Tschanz et al., 2014). One of the advantages of stereological concepts in morphometry is that sampling is inherent to stereology. The attention given to the sampling is comparable to that paid to the analysis of micrographs, as sampling actually is part of any unbiased estimation. If design-based stereology, including sampling, is not used for quantitation in histology, the lack of standardized sampling threatens the repeatability of research. More than 70% of researchers encounter problems when trying to repeat another scientist's experiments (Baker 2016). More than 90 researchers from five continents have recently formulated a strategy to improve the reproducibility of research based on light microscopy (Nelson et al., 2021). We propose that proper sampling of microscopic specimens might be a significant contribution to this issue. Citing the paper by Hsia et al. (2010), "the only effective way to avoid bias and ensure accuracy is via standardization of sampling".

1.3 | Sampling strategies and their benefits with regard to magnification

Sampling is of cardinal importance and a practical necessity in morphometrics (Mayhew & Lucocq, 2015). Depending on the uniformity of the distribution of the item of interest, the sampling intensity would have to be greater (in the case of heterogeneous samples) or smaller (in the case of homogeneous samples). Unfortunately, the biological variability of the microscopic structures on the scale of large organs is mostly unknown in human organs as well as in large animal models. There is ongoing work to map the variability in histopathology to enable researchers to plan the sampling of tissue probes, slides and fields of view efficiently. The theoretical foundations for predicting the efficiency of systematic sampling are quite well known (Gundersen & Jensen, 1987; Gundersen et al., 1999; Gundersen & Osterby, 1981). In

TABLE 1 Examples of studies with recommendations and guidelines for quantitative studies in histology

Research field	Brief characteristics	Reference
General guidelines for microanatomy	Planning, volumetry and sampling as crucial steps for a successful study in quantitative anatomy	Tschanz et al., 2014 Vatsos et al., 2021
Cardiovascular microanatomy	Quantitative 3D morphology in cardiac research Quantification of vascular beds Vascularization of organs 3D characterization of capillary networks Numbers and lengths of brain capillaries	Mühlfeld et al., 2010 Dockery & Fraher, 2007 Mühlfeld, 2014 Eržen et al., 2011 Lokkegaard et al., 2001; Kubíková et al., 2018
Neuroanatomy and neurohistology	Total number of neurons in the subdivisions of the hippocampus Assessment of developmental neurotoxicity Morphometry of brain Morphometry of grey and white matter of spinal cord Morphometry of the pineal gland	West et al., 1991 Bolon et al., 2011 Selcuk & Tipirdamaz, 2020; Sadeghinezhad et al., 2020 Sadeghinezhad & Nyengaard, 2021; Cakmak & Karadag, 2019 Bolat et al., 2018
Gastrointestinal microanatomy	Practical stereology of the stomach and intestine. Morphometry of the oesophagus Volumes and numbers in the liver 3D counting of hepatocytes Quantification of hepatic connective tissue Morphometry of intestinal mucosa in nutritional studies	Nyengaard & Alwasel, 2014 Goodarzi et al., 2019 Marcos et al., 2012; Junatas et al., 2017; Mik et al., 2018 Van Ginneken et al., 2002; Casteleyn et al., 2010
Respiratory system	Policy Statement of the American Thoracic Society/ European Respiratory Society on quantitative assessment of lung structure Quantitative microscopy of the lung Study designs in diseases of the respiratory tract	Hsia et al., 2010 Ochs & Mühlfeld, 2013; Knudsen et al., 2021 Mühlfeld & Ochs, 2013
Urinary system	Application of stereology in kidney research	Nyengaard, 1999
Genital system	Stereology tools in testicular research	Noorafshan, 2014 Ferreira et al., 2021
Skeletal system	Stereology of femoral cartilage Standardized nomenclature for bone histomorphometry Quantification of bone microporosities	Noorafshan et al., 2016 Dempster et al., 2013, Parfitt et al., 1987 Tonar et al., 2011
Embryology	Stereology of the human placenta	Mayhew, 2014

Note: Papers compatible with design-based stereology are listed.

the past and in contrast, for example, to biochemistry, standards for sampling in histology seemed to have been neglected; not all authors customarily referred to sampling strategies, numbers of tissue probes, sections, FOVs or any repeatable rules for their selections. Currently, the sampling issue receives more attention as a part of quantitative morphomics that describes the 3D biological structures from gross anatomy to the micro- or even nanomorphome (Mayhew & Lucocq, 2015).

In microscopy, FOV sampling is closely related to the magnification used. When increasing the magnification, the area of the image field decreases quadratically, and the number of FOVs necessary to cover the same original area increases quadratically (Figure S1). Traditionally, it was recommended that the lowest magnification that enables the detection of the structures of interest be used (Howard & Reed, 2005; Mouton, 2002) to maximize the area of the FOVs. Introducing virtual slides into the research might seem to be a 'game changer'. However, whole slide sampling with automated quantitation still requires validation by humans to ensure that the readouts are correct. Combining the benefits of using slide scanners with a clever sampling strategy might be a very efficient tool in quantitative histology.

The aim of our paper was to provide an overview of the use of virtual microscopy in the context of developing sampling strategies for stereological quantification. We elaborated this idea on a number of examples from multiple fields of histology. We critically discussed the pros and cons of using virtual sections for sampling image fields (FOVs and ROIs) from whole scanned sections in quantitative histological studies.

2 | MATERIALS AND METHODS

2.1 | Origin of tissue blocks and histological staining

This paper uses examples of virtual slides from a number of studies representing various fields of quantitative histology. All the original illustrations were newly prepared from archive specimens for the purpose of this review. The origin of the specimen and their use for studying biological questions is summarized in Table 2. The staining methods used in the examples presented in this paper are summarized in Table 3.

TABLE 2 Origin of tissue samples and basic processing of the examples presented in this paper

Example	Origin	Biological question studied (Reference)
#1	Virtually generated standardized image datasets	Testing and calibrating quantification of volumes, surfaces, lengths and object counts (Jiřík et al., 2016, 2018).
#2	Human mesenchymal stem cells (hMSCs) isolated from bone marrow of healthy donors (A)	Metabolic activity assay comparing the ATP production rate and % of glycolysis and oxidative phosphorylation in hMSCs (Tonarova et al., 2021).
#S2	hMSCs isolated from bone marrow of healthy donors (B)	Cell growth assay and metabolic activity assay when studying the effects of different cross-linking conditions on collagen-based nanocomposite scaffolds; an in vitro evaluation using mesenchymal stem cells (Suchý et al., 2015).
#S3	Soft palate of an adult dog fixed in formalin, archive of (C)	Quantitation of connective tissue in the soft palate of the dog; pilot study to assess sampling intensity (unpublished results). This was motivated by assessment of operative outcome of veloplasty (e.g. Arai et al., 2016; Crosse et al., 2015; Dupré & Heidenreich, 2016; Pichetto et al., 2015; Tamburro et al., 2019).
#3	Porcine femurs with titan implants after 6 months of healing, (B)	Assessing osseointegration of titan implants with four different surface composition using quantification of bone-implant contact (BIC) according to Babuska et al. (2016).
#S4	Condylar cartilage and bone of rabbit femur (B)	Estimation of healing of osteochondral defects of condylar cartilage stimulated by three different tissue-engineered scaffolds (unpublished results).
#S5	Brains of female C57B1/6 mice (C)	Tracking the transduction of various viral vectors in neurons after being injected into mice brains (Hlavatý et al., 2017).
#4	Porcine liver (B)	Describe the propagation of the rupture caused by blunt trauma within liver parenchyma with respect to the liver microstructure, namely, the reticular fibres. Does the rupture propagate randomly or does the rupture follow some pattern through the tissue? (Malečková et al., 2021).
#S6	Porcine common carotid arteries (B)	Quantification of type I and type III collagen within tunica intima and media in porcine common carotid artery (Tomášek et al., 2020).
#S7	Archived canine lymph nodes and core biopsies from canine lymph nodes (C)	Quantification of microvessels in canine lymph nodes. Does the density of microvessels correlate with vascular endothelial growth factor expression? (Tonar et al., 2008; Wolfesberger et al., 2008).
	Patient-derived murine xenografts of mantle cell lymphoma (A)	Histological validation of quantitative in vivo monitoring of hypoxia and vascularization of patient-derived murine xenografts of mantle cell lymphoma using photoacoustic and ultrasound imaging (Keša et al., 2021).
#5	Small intestine of 12 to 14-week-old pigs used in research on healing of intestinal anastomoses (B)	Histological validation of healing of intestinal anastomosis, quantification of vascularization, inflammatory infiltration, and collagen formation (Rosendorf et al., 2020, 2021a, 2021b).
#S8	Human and ewe perineal body used for mechanical testing and microstructure quantification (D)	Quantification of volume fraction of smooth muscle, skeletal muscle, adipose cells, elastin, and type I collagen of the perineal body. Does the structure differ along the perineal body? (Kochová et al., 2019a, 2019b). Does the structure differ between the pregnant and post-menopausal ewe perineal bodies? (Kochová et al., 2019b)
#6	Resected human liver with hepatocellular carcinoma (E)	Quantification of CD8+ T cells in different regions of interest (tumour centre, inner and outer invasive margin, peritumoural area and non-tumour liver) can reflect the overall reaction of the immune system to tumour growth, penetration of immune cells through tumour border and expression of pro- and antiapoptotic factors by tumour cells and microenvironment (Andryi Trailin, unpublished results).
#S9	Mouse ovaries (B)	Discover the effects of exposure to bisphenol A analogs during breastfeeding on ovarian capacity of offspring. The quantification of primordial, primary, preantral, antral and atretic follicles (Nevoral et al., 2021).
#S10	The cerebellum of 3-month-old mouse model with degeneration of Purkinje cells (B)	Quantitative validation of potential abnormalities in total number of microvessels in the cerebellum layers of adult mice with degeneration of Purkinje cells (Kolinko et al., 2016).
#S11	Samples of human aortae collected during surgery for abdominal aortic aneurysm (AAA) repair (F)	Comparison of the expression of structural proteins, osteoprotegerin, and pentraxin 3 and the presence of immune factors (T and B lymphocytes, neutrophils and macrophages), microvessels and hypoxic cells in AAA and non-aneurysmatic aortic walls and exploration of their relationships (Blassova et al., 2019).

(Continues)

TABLE 2 (Continued)

Example	Origin	Biological question studied (Reference)
#7	Decellularized porcine liver tissue (B)	Quantitative analysis of morphological preservation of liver extracellular matrix (ECM) after decellularization with the purpose of generation a high-quality biological scaffold for liver tissue engineering (Moulisová et al., 2020)
#S12	3D collagen scaffolds containing dermal fibroblasts used as an in vitro model of dermis (B)	Development of a new method of total cell count determination in 3D collagen scaffolds in order to quantify cell proliferation (unpublished results).

Note: Most examples are based on studies already published, so references are provided for further details on the study design. All in vivo procedures were performed in compliance with the law of the Czech Republic, which is compatible with the legislation of the European Union and, wherever appropriate, were approved by the Ethics Committees in the following institutions where the samples originated: A – First Faculty of Medicine, Charles University; B – Faculty of Medicine in Pilsen, Charles University; C – Institute of Morphology, University of Veterinary Medicine Vienna, Austria; D – Centre for Surgical Technologies, KU Leuven, Leuven, Belgium; E – Department of Pathology, Faculty of Medicine in Pilsen, Czech Republic; and F – Department of Surgery, University Hospital in Pilsen. The examples are numbered according to their appearance in the Results section.

TABLE 3 Histological staining methods used in examples presented in the study

Example	Staining	Purpose and visualization of tissue components
#1	None (computer-generated virtual image).	Virtual sections through three-dimensional objects (spheres and cylinders) mimicking tissue components in X-ray microtomography.
#2	DAPI nuclear staining (Sigma-Aldrich).	Visualization of nuclei.
#S2	DAPI nuclear staining (Sigma-Aldrich, Burlington, MA) and Phalloidin-Alexa Fluor 488 (Life Technologies, Rockford, IL).	Visualization of nuclei and actin microfilaments.
#S3	Aniline blue and nuclear fast red.	Clear distinction of collagen fibres from other tissue components for automated quantitation.
#3	20% Giemsa's azur eosin methylene blue solution	New bone and connective tissue around titan implants within porcine femur.
#S4	Alcian blue staining and PAS reaction.	Detection of acidic and neutral glycosaminoglycans in newly formed cartilage.
#S5	Immunohistochemistry for enhanced green fluorescent protein (EGFP) (Chemicon International, Temecula, CA), counterstained with haematoxylin.	Identification of cells expressing the EGFP as a reporter gene detecting the cells transduced by a viral vector.
#4	Reticulin kit (BioGnost Ltd, Zagreb, Croatia).	Reticular fibres (collagen III) – component of extracellular matrix of connective tissue located in the interlobular septa and in the delicate network, that separates the hepatic sinusoids and hepatocytes
#S6	Picrosirius red (Direct Red 80, Sigma-Aldrich, Munich, Germany).	Type I collagen (yellow–red colour) and type III collagen (green colour) visualized in polarized light (Rich & Whittaker, 2005).
#S7	Immunohistochemical detection of von Willebrand factor (polyclonal rabbit anti-human antibody, Dako, Glostrup, Denmark) combined with lectin histochemistry (WGA, Vector laboratories, Burlingame, CA). Avidin-biotin-peroxidase complex detection (Vector Laboratories). Counterstaining Mayer's haematoxylin.	Endothelium of blood microvessels within canine lymph nodes.
	Immunohistochemical detection of CD31 (rabbit anti-mouse CD31 monoclonal IgG, clone SP38, Thermo Fisher Scientific, Rockford, IL). Counterstained with haematoxylin.	Endothelium of blood microvessels within patient-derived murine xenografts of mantle cell lymphoma.
#5	Immunohistochemical detection of von Willebrand factor (ab6994Abcam, Cambridge, UK).	Endothelium of blood microvessels

(Continues)

TABLE 3 (Continued)

Example	Staining	Purpose and visualization of tissue components
	Immunohistochemical detection of Calprotectin (Monoclonal Antibody—MAC387Invitrogen MA1-81381, Thermo Fisher Scientific). Counterstaining Mayer's haematoxylin.	Granulocytes and tissue macrophages.
	Picrosirius Red.	Collagen observed in circularly polarized light.
#S8	Verhoeff's haematoxylin and green trichrome (Kocová, 1970).	Overall morphology; smooth and skeletal muscle of the perineal body.
	Orcein (Tanzer's orcein, Bowley Biochemical Inc., Danvers, MA, USA).	Adipose cells and elastin of the perineal body.
.	Picrosirius red (Direct Red 80, Sigma-Aldrich, Munich, Germany)	Type I collagen of perineal body was observed in polarized light.
#6	Immunohistochemical detection of CD8+ T cells (BOND™ Ready-to-Use monoclonal primary anti-CD8 Antibody 4B11, Leica Biosystems Newcastle Ltd, UK). Counterstaining Mayer's haematoxylin.	Tumour-infiltrating cytotoxic T cells as actors of antitumour immunity.
#S9	Haematoxylin and eosin	Primordial, primary, preantral, antral and atretic follicles within mice ovaries.
#S10	Immunohistochemical detection of laminin (polyclonal rabbit anti-laminin antibody, Dako, Glostrup, Denmark), counterstained with haematoxylin.	Detection of microvessels in individual layers of the cerebellar cortex in a mouse model of neurodegeneration.
#S11	Immunohistochemical detection of pentraxin 3 (polyclonal rabbit anti-human pentraxin3 antibody, Thermo Fischer Scientific) and MAC387 (monoclonal mouse anti-human macrophages/monocytes antibody, Thermo Fisher Scientific). Counterstaining Gill's haematoxylin.	Detection of Pentraxin 3, a protein produced in response to inflammatory signals in aortic wall. Detection of macrophages infiltrating the aortic wall in abdominal aortic aneurysms.
#7	Haematoxylin & eosin	Visualization of ECM proteins (stained reddish with eosin) and absence of cell nuclei in decellularized samples (lack of blue haematoxylin stain).
#S12	DAPI nuclear staining (Thermo Fisher Scientific, Rockford, IL)	Staining cell nuclei as countable structures for cell counting.

2.2 | Scanning virtual slides

As the paper focuses mainly on the sampling strategies in the context of various histological studies, the devices and techniques used for acquiring the images in the paper are briefly summarized in Table 4.

2.3 | Systematic uniform random sampling of microscopic FOVs

Multistage sampling in quantitative microscopy comprises several levels (Mayhew & Lucocq, 2015). During each step, a sample size divided by the whole specimen size represents the sampling fraction. In this paper, two levels will be considered: If, for example, every 10th histological section is selected from an exhaustively sectioned tissue block, and the position of the 1st section was selected randomly, the section sampling fraction (ssf) is 1/10. When considering a single slide, selecting 5 FOVs out of the 50 FOVs covering the whole section would represent an area sampling fraction (asf) of 1/10. The rules for the systematic uniform random sampling (SURS) are simple, regardless of the technical implementation (slide scanners, motorized microscope stages, manual sampling). The position of the first FOV within the ROI is chosen randomly, for example, by multiplying the maximum ranges of XY coordinates of the ROI by randomly generated numbers (RND function in MS Excel). A previously selected pattern, named a sampling interval, determines the positions of the other FOVs (see, e.g., Mayhew & Lucocq, 2015 for review).

2.4 | Stereological techniques

The sampling strategies illustrated among the examples that follow were part of histological quantitative studies. All the quantitative morphometric parameters used in the examples presented in this study are explained in Table 5.

2.5 | Statistics of sampling density and evaluating the variability of the sampling

The sampling in histology introduces an error into the resulting data. Increasing the sampling frequency reduces the variability of the data but also increases the labour needed to complete the research.

TABLE 4 Devices and techniques used for acquisition of examples demonstrated in this study

Device and manufacturer	Properties, settings, software	Used in Example #:
Aperio ScanScope CS2 automatic slide scanner (Leica Biosystems, Vienna, Austria).	Bright field transmitted light microscope, 20× and 40× lens. Scanning time of 1 cm^2 approx. 60 s (20× objective) or 90 s (40× objective) Automatic white balance Autofocus No immersion, no Z-stack tools ScanScope 12.4.3 software. *SVS document format readable with freely downloadable ImageScope software, tiled images universally viewable in browsers. *.SVS can also be opened directly with ImageJ (Schneider et al., 2012) with the Bio-Formats Plugin or with FIJI (Schindelin et al., 2012).	#S3, #S5
Eclipse Ti-U microscope (Nikon, Tokyo, Japan), XYZ stepper motor focus drives Prior H117E1N4/F and PS3H122R_NB (Prior Scientific Instruments, Fulbourn, UK), Prior ProScan III stepper motor controller, digital camera Nikon DS-Fi2.	Bright field, polarized light and fluorescence microscopy 2×, 4×, 10×, 20×, 40×, 60× (oil immersion) objectives Scanning time of 1 cm^2 approx. 25 min (10× objective) or 3.5 h (20× objective) Scanning and montage controlled by the NIS Elements ar software (v 5.11.03) *ND2 document format readable with freely downloadable nIS-Elements Viewer software Scanning in *XY* plane and in *Z*-axis. Export to universal format TIFF images.	#2, #S2, #S4,#5, #S6, #S9, #S10
Zeiss Axio Scan.Z1 Slide Scanner (Zeiss, Jena, Germany).	Bright field microscopy 20× and 40× objectives Scanning time of 1 cm^2 approx. 5–10 min (20× objective) Scanning controlled by ZEISS Zen Blue software ZEISS Zen microscopy free software offers both basic image analysis, as well as export functionality of the scanned images into TIFF or JPG file formats. Native pyramidal*.CZI files readable with FIJI.	#4, #S8, #S11, #7
Olympus CX41 microscope (Olympus, Tokyo, Japan) with Promicam 3-3CP camera (Promicra, Prague, Czech Republic).	Bright field and polarized light microscopy 2×, 4×, 10×, 20×, 40×, 60× (oil immersion) objectives Manual stage Scanning time of 1 cm^2 takes approx. 30 min (10× objective) of manual work Stitching virtual slides manually using the ImageStithing module of the QuickPhoto Industrial 3.2 software (Promicra, Prague, Czech Republic) Export to TIFF.	#3, #S6, #S7

Stereologists are used to calculate the variability on each level of the sampling to identify the major source of potential bias and to optimize the sampling procedures in terms of time and material costs, provided that enough precision remains to draw conclusions on a pre-determined level of confidence. Several measures of variability are illustrated for this purpose, such as standard deviations (SD), coefficient of error (CE; standard error of the mean of repeated estimates divided by the mean) and the estimates of CE for spatially correlated objects using the Matheron quadratic approximation method with various smoothness constants (Gundersen & Jensen, 1987; Slomianka & West, 2005). The relative percentage error used for comparing the data based on whole slide analysis vs. various levels of subsampling was calculated as 100 × (measured value-expected value)/expected value.

3 | EXAMPLES

A number of combinations of imaging approaches, uses of virtual slides, scanners, or individually sampled micrographs with various magnifications are presented in sequence corresponding to Tables 2, 3 and 5. The examples were tailored to facilitate the solving of biological problems described in Table 2, and the strong and weak points are illustrated. Due to the number of possible combinations, the examples are ordered approximately in increasing complexity.

3.1 | Whole slide analysis vs. density of sampling multiple micrographs

Figure 1 (Example #1) demonstrates the effect of the intensity of sampling on the accuracy of the quantitative results. This can be done in virtually generated scenes. Considering the whole slide as the 'true expected value', the relative error increases with decreasing sampling intensity. In this case, intermediate sampling would provide results with an acceptable relative error. Similarly, Figure 2 (Example #2) compares automated counting of cell nuclei in a single well of a cell culture miniplate with counting based on 15 image fields. In cases of a more homogeneous distribution (Figure S2, Example #S2), the relative error of the sample is acceptably low. It is worth performing a pilot study of heterogeneous histological samples with multiple tissue components (Figure S3, Example #S3) that shows how the moving average depends on the sampling intensity.

TABLE 5 Quantitative morphometric parameters used in the examples presented in this study

Example	Quantitative parameter abbreviation (units)	Definition, reference area, interpretation	Objective used	Image fields sampled per slide	Typical area sampling fraction
#1	V_V (objects, section) (−)	The volume fraction of objects within a virtually generated section.	Not applicable	6	6/54 (0.11)
#2	Q_A (nuclei, well) (mm^{-2})	Two-dimensional density of cell nuclei per area of the well bottom in an 8-well XPf cell culture miniplate (Agilent, Santa Clara, CA).	4×	Whole image processed	Whole image processed
			40×	15	15/160 (0.093)
#S2	Q_A (nuclei, well) (mm^{-2})	Two-dimensional density of cell nuclei per area of the well bottom in a 48-well cell culture plate (Thermo Scientific, Waltham, MA).	10×	Whole image processed	Whole image was processed
			40×	9	9/22 (0.41)
#S3	A_A (connective tissue, palate) (−)	Mean area fraction of connective tissue in whole histological sections of the soft palate of a dog (pilot study).	20× (whole slide scan)	Analysis of whole slide scan	One whole slide scan analysis 0.003 to 0.005 in relation to one complete palatal half
#3	BIC	Bone-implant contact as the ratio of the profile length of direct contact between the implant profile and bone tissue and the total profile length of the implant surface.	10×	15	15/70 (0.214) related to the whole scan 15/15 (1.00) related to the bone-implant interface
#S4	V_V (cartilage, defect) (−)	The volume fraction of Alcian blue and PAS-positive cartilage within the healing bone defect.	10×	22	21/22 (0.95)
#S5	N (EGFP-positive neurons, brain) (−)	Absolute number of EGFP-positive neurons in the injected half of mouse brain.	40× (oil immers)	45–55	1/1 (exhaustive sampling)
#4	P'_L (interlobular septa) and P_L (interlobular septa) (mm^{-1})	Real number of intersections of interlobular septa with rupture and predicted number of intersections based on the total length of the interlobular septa	Whole slide scan	Not applicable	Whole slide scan
	P'_L (reticular fibres) and P_L (reticular fibres) (mm^{-1})	Real number of intersections of reticular fibres with rupture and predicted number of intersections based on the total length of the reticular fibres	40×	10	Between 10/40 (0.25) and 10/50 (0.2)
#S6	A_A (type I collagen, int + med) (−)	The area fraction of type I collagen within the tunica intima and media ROI	40×	4	Between 4/23 (0.17) and 4/37 (0.11)
	A_A (type III collagen, int + med) (−)	The area fraction of type III collagen within the tunica intima and media ROI	40×	4	Between 4/23 (0.17) and 4/37 (0.11)
#S7	Q_A(vWF and WGA-positive microvessels, lymph node) (mm^{-2})	The number of profiles of stained microvessels per sectional area of the lymph node.	40×	50–70	Between 50/1800 (0.028) and 70/2500 (0.03)
	L_V (CD31+ microvessels, lymphoma) (mm^{-2})	The length density of stained microvessels per volume unit of lymphoma	40×	10	Between 10/40 (0.25) and 10/80 (0.125)
#5	V_V (objects, intestinal wall without mucosa located 3 mm proximally and distally from the anastomosis centre) (−)	The volume fraction of vWF positive cells within the ROI	20×	5–38 vWF	Between 1/5 (0.20) and 1/3 (0.35)
		The volume fraction of MAC387-positive cells within the ROI	20×	12–53 MAC387	Approx. 1/2 (0.49)
		The volume fraction of collagen within the ROI	20×	8–24 PSR	Between 1/3 (0.33) and 1/5 (0.22)

TABLE 5 (Continued)

Example	Quantitative parameter abbreviation (units)	Definition, reference area, interpretation	Objective used	Image fields sampled per slide	Typical area sampling fraction
#S8	V_V (smooth muscle; skeletal muscle, perineal body)	The volume fraction of smooth muscle and skeletal muscle within the ROI	10×	12	12/42 (0.3)
	V_V (adipose cells; elastin, perineal body)	The volume fraction of adipose cells and elastin within the ROI	10×	12	12/42 (0.3)
	V_V (type I collagen, perineal body)	The volume fraction of type I collagen within the ROI	10×	12	12/42 (0.3)
#6	Q_A(CD8-positive T cells, liver) (mm^{-2})	The number of profiles of stained CD8+ T cells per sectional area of the ROI of the liver.	20×	8 per ROI 40 per slide	8/133 0.064 in TC and NT ROIs: 8/25 (0.32) in IL, OL and PT ROIs
#S9	N (different types of follicles)	The number of primordial, primary, preantral, antral and atretic follicles	20×	14	14/25 (0.56)
#S10	V_V (cerebellar layers, cerebellum) (–)	The volume fractions of histological layers of cerebellum.	20×	4–7	0.33
	N (microvessels, cerebellum) (–)	Number of microvessels calculated from the number of branching nodes according to Gundersen et al. (1993).	60×	20–40	0.33
#S11	A_A (pentraxin 3, wall) (–)	The area fraction of the pentraxin 3-positive cells within the whole wall reference area	40×	4	Between 4/112 (0.035) and 4/328 (0.012)
	A_A (MAC387, wall) (–)	The area fraction of the MAC387-positive macrophages within the whole wall reference area.	20×	4	Between 4/28 (0.143) and 4/82 (0.049)
#7	L (skeleton length, liver) (mm) L_A (ECM fibres, liver) (mm^{-2}) Q_A (ECM branches, liver) (mm^{-2})	Length and 2D length density of the ECM within liver lobules. Number of EMC branching nodes per sectional area of liver lobules. Both parameters refer to the quality of network structure of sinusoidal vessel ECM in the decellularized scaffold.	40×	10	Typically 5/100 (0.05)
#S12	N (nuclei, scaffold) (–)	Total cell number in the whole scaffold estimated from cell number in 1 column.	10×	9 columns from the 3D scaffold	9 × 1.4 μl/200 μl = 0.063 (9 columns per scaffold)

Note: The magnification of the microscope objective, which was an approximate equivalent to the sampled image field area used for quantification of each parameter, is provided. The number of image fields that were sampled in each study is shown as well.

Abbreviations: A_A (*component*, *space*), Area fraction of the respective components within their reference spaces; BIC, bone-implant contact; L_V (*component*, *space*), Length density of objects per reference volume; N_V (*component*, *space*), Numerical density of objects per reference volume; Q_A (*component*, *space*), number of object profiles per section area; V_V (*component*, *space*), Volume fraction of the respective components within their reference spaces.

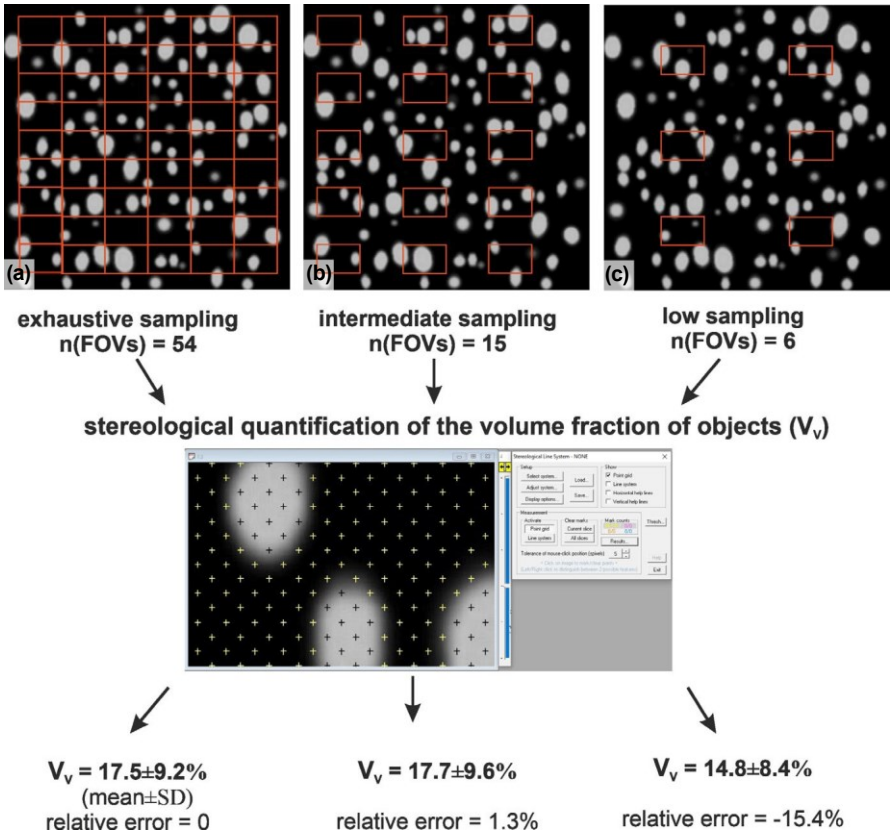

FIGURE 1 Example #1 demonstrates the effect of the intensity of sampling on the quantitative results in virtually generated slides with precisely known volume fractions of objects. A virtual slide was generated using teigen software (Jiřík et al., 2018) with a precisely known volume fraction (V_V) of the white objects on the black background, mimicking the sectional profiles of cell bodies or matrix fibres. The scene was sampled with simulated fields of view (FOVs) exhaustively (a), with intermediate (b) and low (c) intensity. After stereological quantification using the point grid, the V_V was expressed as the mean ± standard deviation (SD), and the relative percentage error of the estimate was calculated for each sampling intensity

3.2 | Slides requiring exhaustive sampling of the ROIs

In some studies, it is advisable to evaluate the complete ROI. This strategy prevails when the number of slides available is limited, such as in ground sections of bone implants (Figure 3, Example #3). Similar situations occur when the ROI has small dimensions, for example central regions of experimental bone defects in small animal models (Figure S4, Example #S4). Exhaustive sampling might also be needed in cases with significant biological variability among the study groups when counting every few cells matters, such as in counting virus-transduced neurons in mouse brains (Figure S5, Example #S5).

3.3 | Using the same sampling count but in ROIs of different absolute sizes

In some study designs without excessive biological variability, it is possible to maintain the same number of FOVs (Figure 4, Example #4). When the size of the specimens and ROI varies, this will result in a variable sampling density (the numerator is the same, the denominator varies), as in samples of proximal vs. distal segments of blood vessels (Figure S6, Example #S6) or large vs. small lymph nodes (Figure S7B, Example #S7). The case presented in Figure S7A (Example #S7) shows a very extensive sampling, the ex post analysis of which identified as an unnecessary and laborious oversampling when compared to Figure S7B.

3.4 | Sampling the same ROI for more histological staining methods

Quantifying the volume fractions of tissue components within the same ROI might require more histological staining. Figure 5 (Example #5) shows three stains within the same ROI and objective. It is of great advantage when the sampling is facilitated by a map that helps adjust the sampling density according to the variability of the structures under study, as provided by the estimates of CE in the Stereologer software (v11.0; SRC Biosciences, Tampa, Florida, USA) (Figure 5H-I). When the CE becomes unacceptably high (Figure 5I), it is recommended to increase the ssf, asf or the density of the stereological grid. Figure S8 (Example #S8) shows a similar design.

3.5 | Sampling one or more ROIs with a variable intensity or using various objectives

Figure 6 (Example #6) illustrates a complex sampling problem that would be difficult to solve without planning on virtual slides. There were five ROIs in every slide, representing the tumoural area, three zones of the tumour invasive margin and healthy non-tumorous tissue. In all five ROIs, multiple structures of interest were identified immunohistochemically (CD8+ T lymphocytes shown, CD3+ T lymphocytes only discussed), and their occurrence within these ROIs was very variable and with different biological interpretations. To maintain the feasibility of such a complex task, two sampling densities were chosen, and part of the sampling variability was

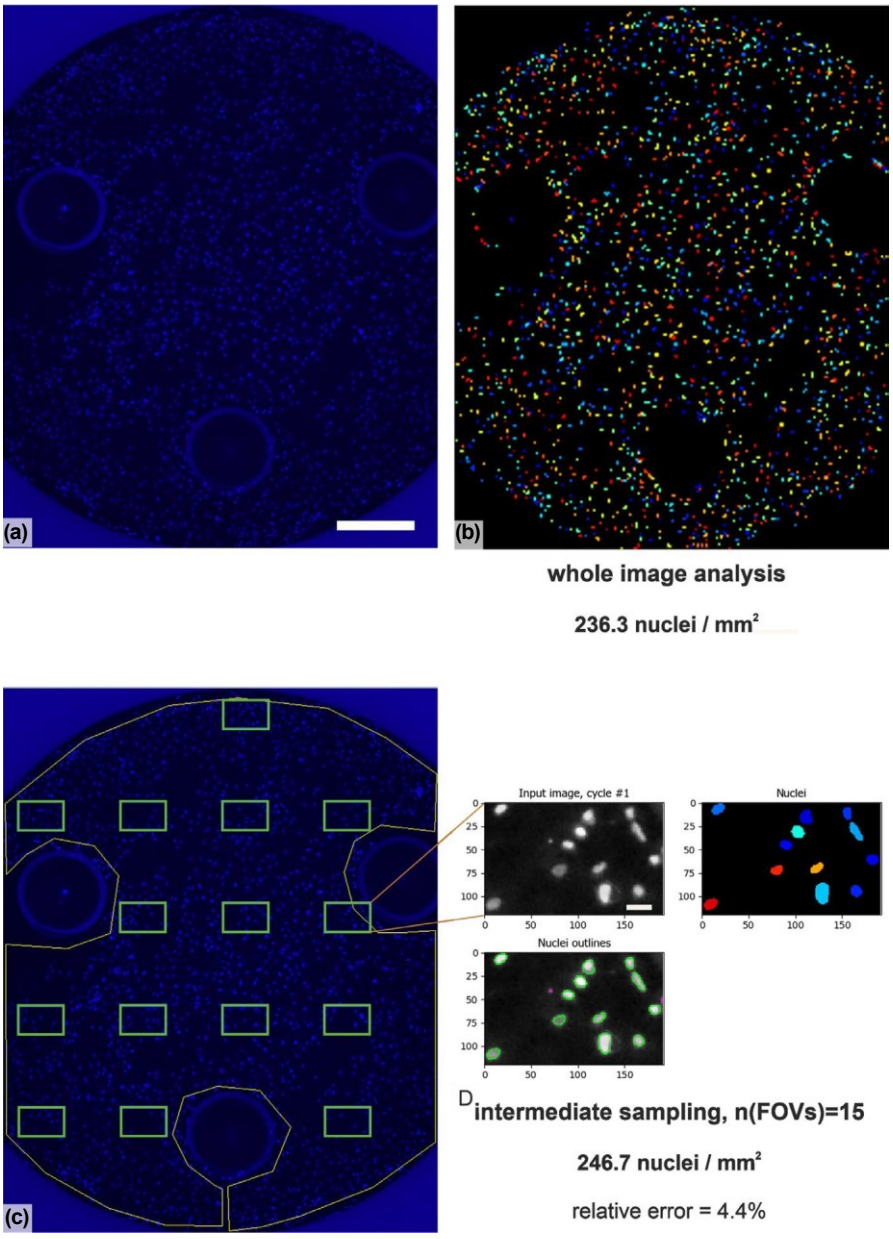

FIGURE 2 Example #2 compares automated counting of cell nuclei in a composite image of a single well in a 8-well XFp cell culture miniplate (captured and stitched with a 4× objective) vs. automated counting in 15 image fields taken from the same well with a 40× objective after 24 h of cultivation (seeding cell density 70,000/cm^2). (a) Raw image stitched from two fields of view of a 4× objective shows most of the well microplate. (b) All the nuclei were segmented, counted and highlighted using a watershed algorithm in CellProFiler 4.2.1 software (McQuin et al., 2018). The obvious benefit of this procedure was that the quantification was based on counting nearly 1900 nuclei. (c) As an alternative approach, 15 fields of view (FOVs) were sampled with a 40× objective (green rectangles) in a systematic uniform random manner from the well (outlined with a yellow polygon). The three rounded spaces for inserting sensor probes that were part of the well bottom profile were avoided. (d) Example of one of the 15 images that were processed in the same way as in b. The analysis provided a value of density of nuclei with a 4.4% error relative to the whole image analysis (b). The benefits of the sampling (c-d) were that the 40× objective provided a greater optical resolution. Fluorescence images, cell nuclei in blue stained with DAPI. Scale bars 500 μm (a–c), and 40 μm (d)

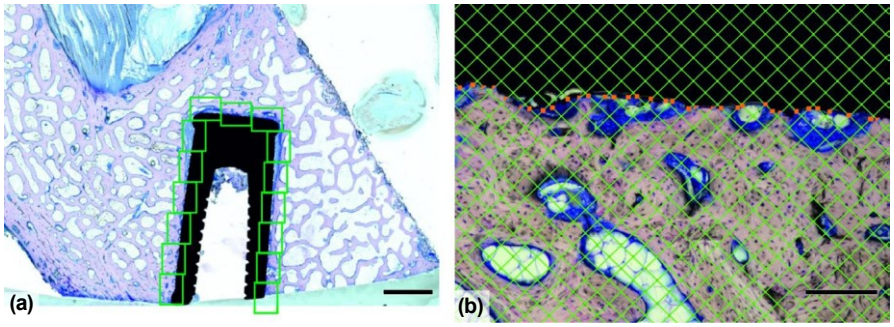

FIGURE 3 Example #3 shows the strategy of exhaustive sampling of an ROI in quantification of bone-implant contact (Babuska et al., 2016). (a) Fifteen ROIs from the bone-implant interface were taken from each slide. All adjacent fields showing the implant surface (black), bone (purple) and connective tissue (blue) were captured exhaustively. (b) Stereological grid randomly positioned over the micrograph; intersections between the test lines and the implant surface (orange points) and intersections between the implant-bone interface and test lines (light blue points). Giemsa's azur eosin methylene blue solution. Scale bar: 2 mm (a), 200 μm (b)

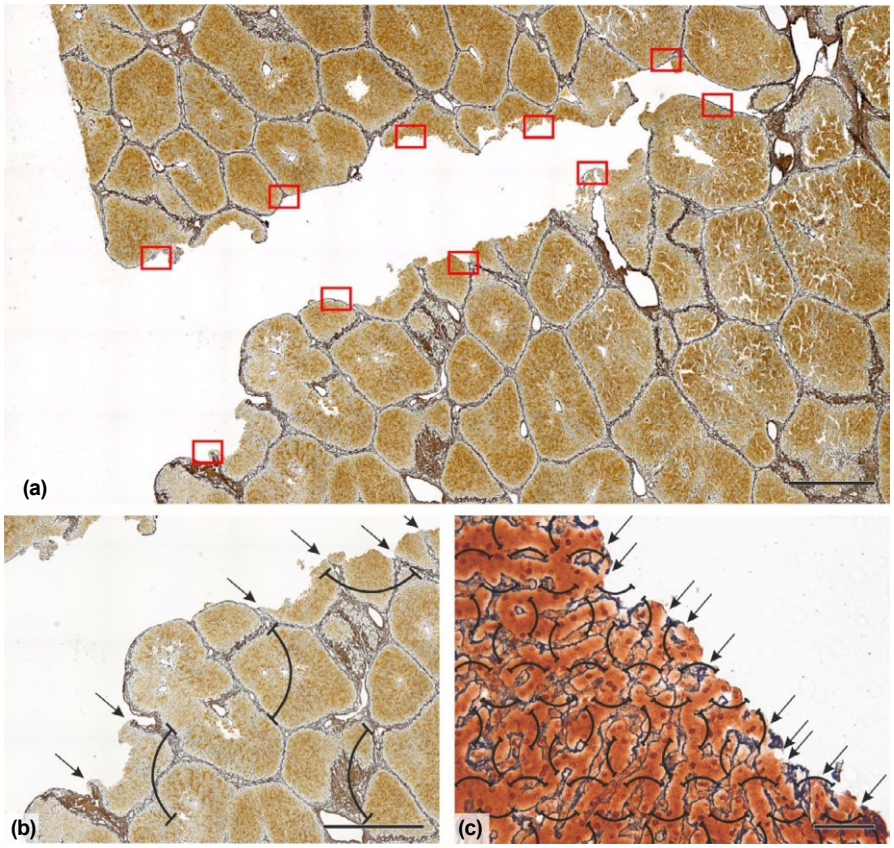

FIGURE 4 Example #4 shows the strategy of tissue sampling for the evaluation of rupture propagation through the porcine liver (Maleckova et al., 2021). (a) An overview of the scanned porcine liver sample showing a rupture in full length. The scanned samples were used to assess the spatial relationship of the rupture and the interlobular septa (analysis was performed along the entire length of the rupture [b]) and the spatial relationship of the rupture and the reticular fibres (analysis was performed in 10 fields of view taken in a systematic manner [red rectangles, C]). (b) Close-up of a part of the rupture-spatial relationship of the rupture and the interlobular septa that were assessed in 7 scanned histological slides (c) An actual field of view taken with a 40× objective shows spatial relationship of the rupture and the reticular fibres. This was determined by comparing the number of the intersections of the interlobular septa/reticular fibres with the rupture (arrows) and the theoretical intersection intensity based on the length density of the interlobular septa/reticular fibres. The length density was estimated using circular arc probes (black curves) as available in the ellipse stereological software (ViDiTo). Reticulin kit staining was used for reticular fibre visualization. Scale bar: 1000 μm (a, b), 50 μm (c)

compensated with more or less dense counting grids (Figure 6B-D). Similarly, Figure S9 (Example #S9) demonstrates that the present settings were suitable for frequently occurring types of ovarian follicles but too low for the rare types. Figure S10 (Example #S10) shows a solution using lower magnification and less intense sampling for the volume fractions of histological layers of cerebellum but a greater magnification and more intense sampling for counting cerebellar microvessels within the layers. Similarly, Figure S11 (Example #S11) shows two magnifications useful for two different components of the aortic wall.

FIGURE 5 Example #5 demonstrates three different sampling densities used for quantification of three parameters when evaluating the healing of intestinal anastomoses. The sampling was facilitated using Stereologer software (Rosendorf et al., 2020, 2021a, 2021b). (a) Scanned slide shows the porcine small intestine. The centre of the healing anastomosis is highlighted with a dashed line. The green outline shows the ROI under study comprising the submucosa, muscularis, and serosa no more than 3 mm proximally and distally (dashed arrows) from the centreline. (b-d) Pan window maps of the scanned areas are screenshots captured from the Stereologer software used for planning the sampling. The green polygon outlines the ROI, from which image fields of 20× objectives (green rectangles) were sampled in a systematic random uniform manner. The red rectangle shows the simulated image field of a 2× objective used for overview. The XY sampling step was 1500 μm for quantification of vWF and collagen (b, d, e, g) or 1000 μm for quantification of MAC387 (c, f). (e-g) Actual fields of view of 2× objectives for all three staining methods. The planned sampling for the 20× objectives is shown (green rectangles). (h–i) Actual fields of view of the 20× objectives for each staining method. Unbiased counting frames and the stereological point grid method were used for quantification of the volume fractions of individual components of the intestinal wall. On the bottom, recommendations on the total sampling variability (coefficient of error, CE, also considering the number of sections) are shown as provided in the Stereologer protocol. In vWF (h) and picrosirius red (i), the CE was sufficiently low. In MAC387, a greater point density is recommended due to the spatial variability of the distribution of inflammatory cells. Gomori trichrome kit (a), vWF immunohistochemistry (e, h), MAC387 immunohistochemistry (f, i), picrosirius red in bright field (g) and circularly polarized light (j). Scale bars 1 mm (a), 500 μm (e–g) and 50 μm (h–j)

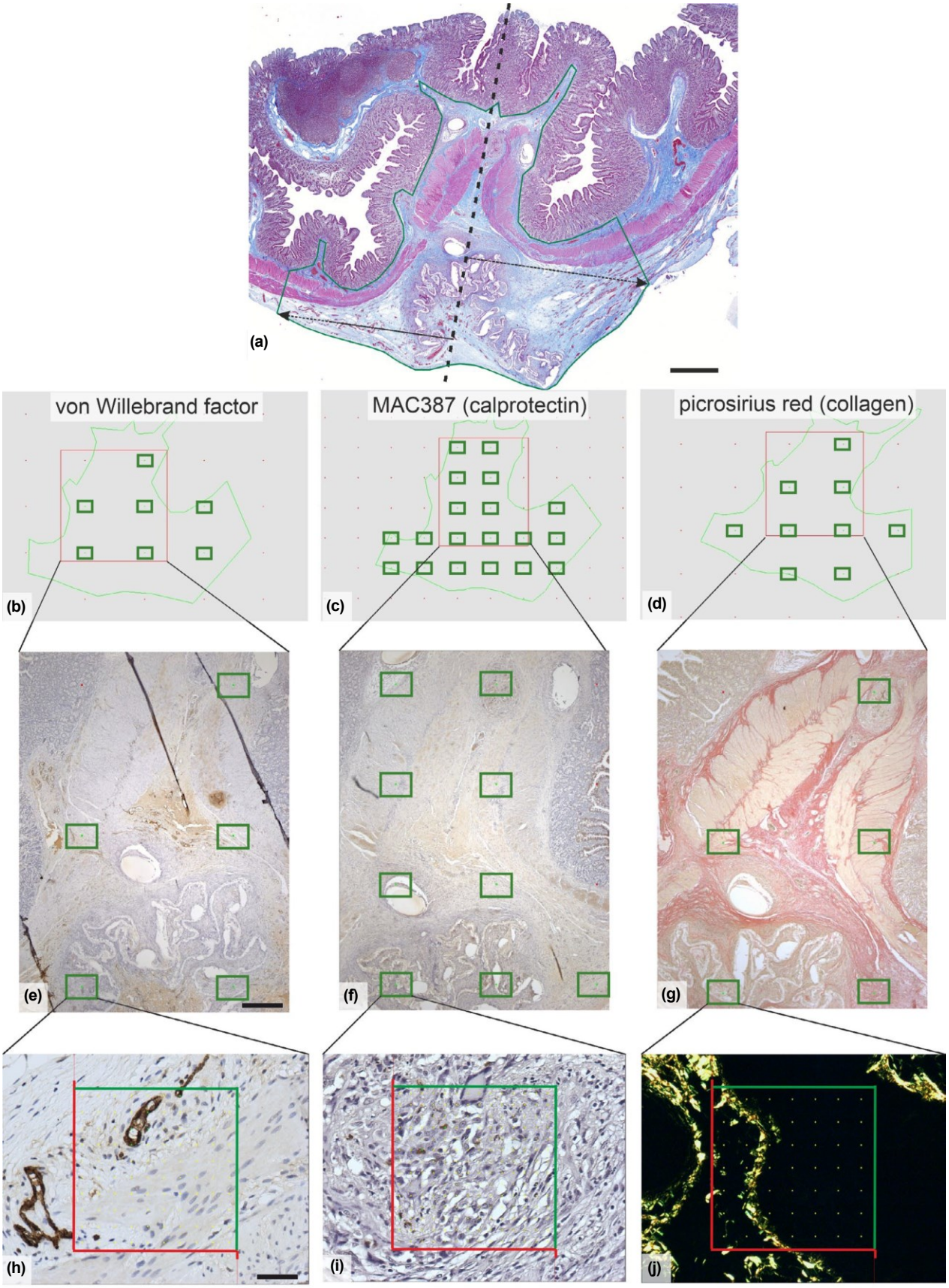
(a)
von Willebrand factor
MAC387 (calprotectin)
picrosirius red (collagen)
(b)
(c)
(d)
(e)
(f)
(g)
(h)
(i)
(j)
Probe Volume Fraction (vWF)
CE 0.1294
Recommendations CE is acceptable.
Probe Volume Fraction (MAC387)
CE 0.2595
Recommendations Decrease the Area per Point.
Probe Volume Fraction (collagen)
CE 0.1188
Recommendations CE is acceptable.

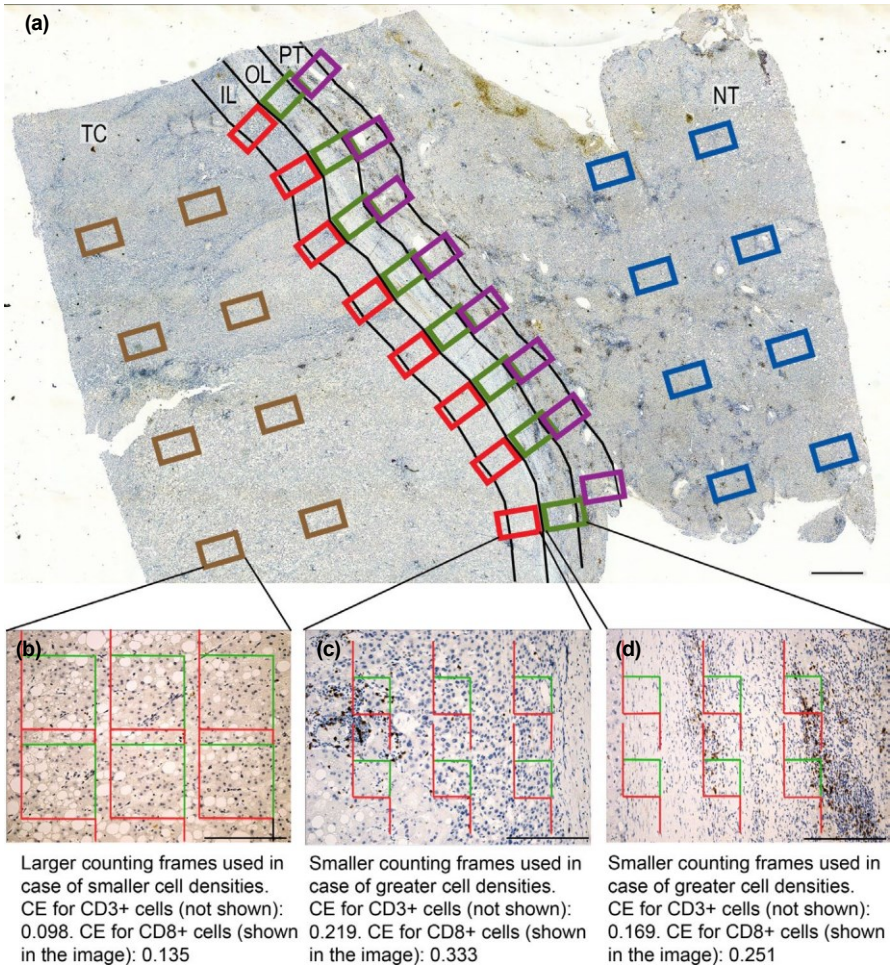

FIGURE 6 Example #6 demonstrates different sampling strategies in multiple ROIs for quantification of tumour-infiltrating CD8+ T cell infiltration in resected samples of human hepatocellular carcinoma. (a) Scanned slide with multiple ROIs: tumour centre (TC), inner layer (IL) of tumour invasive margin (TIM), outer layer (OL) of TIM, peritumoural area (PT) and non-tumour area (NT). The inner TIM and outer TIM were defined as 500 μm on each side of the border separating the malignant cell nests and adjacent non-tumour liver tissue or fibrous capsule (Hendry et al., 2017) towards TC or non-tumour liver, respectively. The TC represented the remaining tumour area. The PT region was defined as the 500 mcm thick region immediately adjacent to the OL. Using a 20× objective, eight equidistant fields of view (FOVs) were taken from each ROI using systematic uniform random sampling (SURS). (b-d) CD8-immunopositive cell profiles were counted using unbiased counting frames. The choice of the number and size of unbiased counting frames (UCFs) varied depending on the cell density at a glance. For TC and NT, areas of UCF (from 8700 to 34,801 μm^2) and their number (6–9) per image varied according to the lymphocytic density, and therefore, sampling fraction per ROI varied as well. Six UCFs per image were used for the inner and outer TIM and for the PT region. The coefficients of error (CE) calculated for the whole population of CD3+ T lymphocytes (not shown in the micrographs) and for the CD8+ subpopulation separately (shown on the micrographs). CD8 immunohistochemistry (a-d). Scale bars 1000 μm (a), 200 μm (b-d)

3.6 | Multistage sampling of FOVs and virtual sampling

Figure 7 (Example #7) shows a special case of multiscale sampling and analysis performed by a semiautomatic software tool when evaluating the quality and composition of decellularized liver. This demonstrates that tailoring a software tool to a specific problem might increase the efficiency of the whole work significantly, especially when the sampling of FOVs is an integral part of the quantification procedure. Figure S12 (Example #S12) demonstrates virtual sampling when counting fibroblasts within a 3D scaffold in vitro; such an approach requires programming skills, but the users are rewarded by a reasonable mapping of the variability of their results.

4 | DISCUSSION

4.1 | Sampling FOVs is only a part of a 3D multistage sampling

For any quantification, at least two criteria are to be met: (i) the staining should allow for a clear identification of all the structures under study, and (ii) borders of the reference space are clearly defined, either anatomically or by convention (Howard & Reed, 2005; Mouton, 2002). We would like to point out explicitly that the sampling of FOVs in virtual scanned sections illustrated above represents only a small part of the whole multistage sampling in quantitative histology. Therefore, the variability of results affected

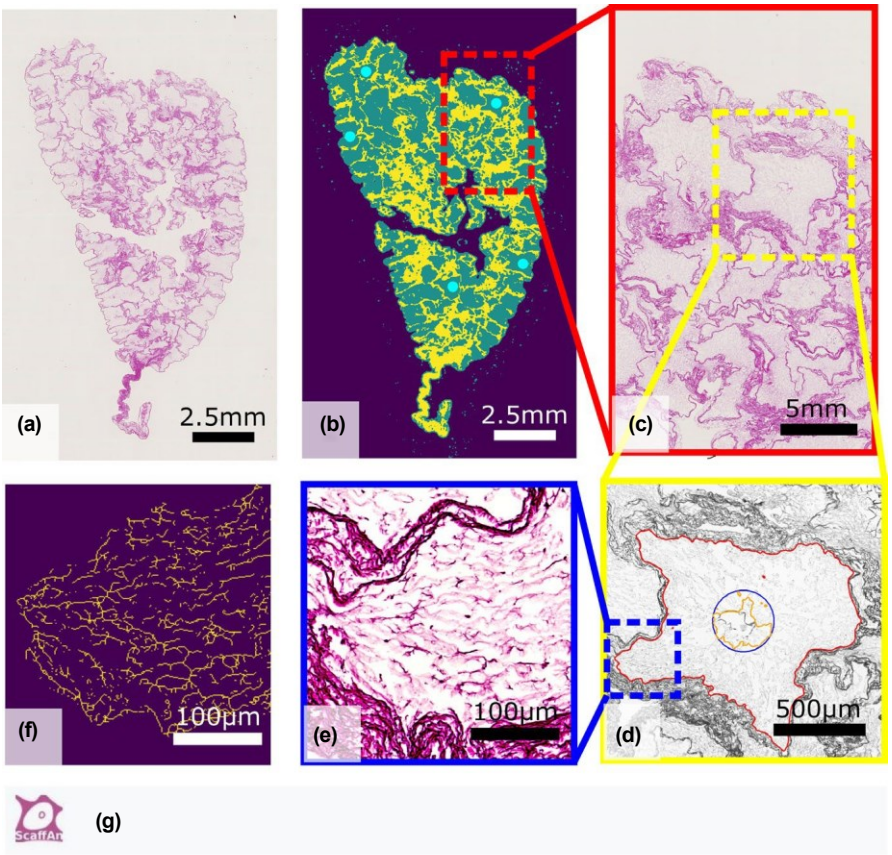

PIG-003_J-18-0170_HE.ndpi

	Skeleton length	Branch number	Area [mm^2]	Scan Segmentation Empty Area [mm^2]	Scan Segmentation Septum Area [mm^2]	Scan Segmentation Sinusoidal Area [mm^2]
0	49.284	23278	0.953975	74.561654	25.290709	89.24516
1	39.998	19469	0.835566	74.561654	25.290709	89.24516
2	50.942	24941	0.939373	74.561654	25.290709	89.24516

FIGURE 7 Example #7 shows a quantitative assessment of the morphological quality of decellularized porcine liver to be used as a high-quality scaffold for liver tissue engineering. (a) Slide scans are evaluated by in-house developed open source software ScaffAn (http://scaffan.kky.zcu.cz/) as an integral part of a multiscale analysis (Moulisová et al., 2020). The resulting parameters describe the level of ECM structure preservation within individual lobules. It is a two-step procedure: (b) The first step is a whole scan analysis separating the lobules (segmentation to distinguish the sinusoidal ECM from more dense interlobular septa, triads and vessels) (Jirik et al., 2020, 2021). Typically, 5 lobules are then selected either manually by the end user or automatically (marked with cyan dots in b). The sampling is defined by a single lobule area and is not random, but it systematically reflects the morphological diversity of the sample (e.g. large vessels that are not the subject of analysis). (c) A close-up of a part of the analysed area. (d) The second step is lobular network analysis calculating parameters for individual lobules. Output parameters such as structure/skeleton lengths (mm) or branching points characterize the integrity of the sinusoidal vessel ECM network (detailed in e). These parameters are generated by using a set of algorithms, including image segmentation by the active contour model (Kass et al., 1988), texture analysis by the grey level cooccurrence matrix (Haralick, 1979) and skeletonization of the sinusoidal network (f). (g) An example of the online software output data

by the sampling of FOVs in a single slide represents only a small part of the total variability of data in the whole study. Other levels of sampling should also be emphasized, such as the number of subjects per study group, the sampling of tissue probes from organs, and the sampling of slides. We highly recommend classical papers on this topic (Gundersen & Osterby, 1981; Slomianka & West, 2005).

The importance of proper sampling of sections is elaborated in Figure S3. We found that the tissue composition of the canine soft palate was so heterogeneous that a whole half of the velum had to be sampled using a minimum of 10–15 sections distributed approximately uniformly throughout the complete tissue block to obtain reliable and robust results. Single sections cannot be used as 'representative' of this organ. Justifying the number of sections required

for a valid quantitative histological study is suggested in Figure S3D-E. However, even when a single slide is available (e.g. in archive material), the repeatability, reliability and correctness, even of simple quantification, might greatly benefit from correct FOV sampling.

4.2 | Choosing the FOV sampling intensity and practical implications

In all the examples presented, our effort was to spread the sampling items evenly and widely throughout the ROIs and specimens. This strategy is called systematic uniform random sampling, and it is superior and more efficient than simple (independent) random sampling, as it covers all parts under study uniformly (Mayhew & Lucocq, 2015). The examples illustrated above do not involve all possible situations in 2D sampling of FOVs in quantitative histology but might provide clues to the reader to most of these. We included mostly examples of sampling optimized in pilot studies but also problematic cases. Unnecessary intensive sampling (oversampling), for example in Figure 1A and Figure S7A, makes the work more laborious and expensive without providing new information. In contrast, insufficient sampling (undersampling), for example in Figure 1C and Figure S9C, Figure S10B,C, might compromise the study design and make it difficult to reach a pre-determined level of significance when testing statistical hypotheses, although biological differences might be present in the samples under study.

As the sampling error (introduced by all levels of the sampling procedure), represented by CE estimates, sums up with the biological variance (i.e. the differences between the samples themselves), according to Tschanz et al. (2014), it is always advisable to perform a pilot study on typical samples and groups under research. This allows for calculating a power sample analysis. Mapping both the total variability of our data and its components is an essential step when designing further studies on the same material, which involves calculating the minimum number of samples needed to compare the groups under study. Descriptive statistics of the pilot data (mean and standard deviation) are useful for the power sample analysis (Chow et al., 2008); for example, when planning an experiment and expecting one of the histological quantitative parameters to be increased by 20%, the minimum number of samples required per group would be calculated using the typical test power $\beta = 0.8$ (the type II error) and $\alpha = 0.05$ (type I error).

4.3 | Whole slide scanning vs. taking multiple micrographs

Currently, researchers have more technical options for acquiring virtual slides and planning the sampling of FOVs. The pros and cons of whole slide scanning vs. taking multiple individual micrographs are summarized in Table 6. An inexpensive alternative for acquiring virtual slides with large areas but high resolution might

TABLE 6 Pros and cons of two technical ways of sampling: Whole slide scanning vs. sampling multiple individual micrographs

Scanning whole slides	Sampling multiple individual micrographs
Histological scanner required.	Can be done even on routine microscopes with motorized or manual stage.
The data from the whole slide are always available, so more ROIs can be added when necessary.	Usually, is done once.
Can be fast and efficient when automated. However, issues occurring during the automated scanning do not appear until checked.	Usually, takes more time to be done. Any technical issues can be seen and solved immediately.
Problems with atypical size of archive slides might occur (Leica Biosystems, 2021). Either the holders are not adapted, or the slides might get stuck within the device.	Can be performed even if archive slides sometimes do not fit the feeding trays or holders of scanners (uniform slide dimensions and thickness required).
In some scanners, only bright field illumination technique and a limited choice of objectives are available. The use of immersion oil objectives is rare.	Can be done using any observation technique available of the microscope, for example fluorescence imaging, phase contrast, polarizing microscopy. No issues with using oil immersion easily.
Generates large datasets (typically 0.5–2 GB per typical histological slide). The pyramidal architecture of the files is usually optimized for viewing.	No special data infrastructure required.
Corresponds to state-of-the art of the whole-mount pathology (Look Hong et al., 2016; Rashid et al., 2019).	Does not permit whole-mount analysis (or this becomes extremely laborious).
In some scanners, multiplane (z-stack) scanning is possible to reflect the thickness of the slide. This might depend on the availability of high-aperture oil immersion objectives. Depth of focus problems might occur that cannot be solved automatically by the scanner software.	Optical sections could be captured in stacks using oil immersion objectives with high numerical aperture. Multiplane scanning might be crucial for studies involving confocal microscopy and requiring not only lateral resolution but also 3D information.
Using automated image-processing methods, the texture pattern of the whole sampling area can be analysed.	Analysing the whole slide would be very laborious or impossible. Texture patterns that exceed the size of individual micrographs are lost and cannot be analysed.

be image stitching, supported currently by stitching modules in most of the proprietary camera software solutions (extra costs in Nikon nIS eleMentS Br; ZeISS Zen Core, leica laS). Moreover, free ImageJ (Schneider et al., 2012) and FIJI software can be used as well (Schindelin et al., 2012). However, stitched images do not support the pyramidal file architecture, and they may require more RAM than the optimized file formats of the slide scanners. Stitching algorithm also fail in case of optically empty regions.

5 | CONCLUSION

We conclude that combining scanning virtual slides in histology with efficient use of unbiased sampling is fully compatible with the plethora of data from quantitative microscopy, which can be expressed as the 'Do less well' rule (Gundersen & Osterby, 1981). Virtual microscopy proved to be extremely helpful to facilitate correct sampling at the level of individual slides. Uniform distribution of FOVs can also be reached using motorized microscope stages. Principles of SURS are beneficial not only for validity, efficiency and ethics of quantitative studies but also for improving accuracy and repeatability in qualitative studies. We suggest that modules supporting the SURS of FOVs with variable settings of ROIs and sampling intensity should be natively supported by all virtual slide scanners intended for scientific use.

ACKNOWLEDGEMENTS

This study was supported by the National Sustainability Program I (NPU I) Nr. LO1503 provided by the Ministry of Education, Youth and Sports of the Czech Republic and by the Charles University Research Fund (Progres Q39). LC, AT, VL, VM and MJ also received support from the Ministry of Education, Youth and Sports under the project FIND No. CZ.02.1.01/0.0/0.0/16_019/0000787 and from the European Regional Development Fund–Project 'Application of Modern Technologies in Medicine and Industry' (No. CZ.02.1.01/0.0/0.0/17_048/0007280). JH was supported by the Ministry of Health of the Czech Republic (Grant no: 15–29241A) and by the grant SVV–2020-2022 No. 260 536. MG was supported by the Charles University Grant Agency, project No. 1313420 and SVV 260 536. LC and VL received support from the Charles University grant UNCE/MED/006, and by the grant of Ministry of Health of the Czech Republic – AZV NU20J-08-00009. AT has received funding from the European Union's Horizon 2020 research and innovation programme under grant agreement Nº856620. The analysis demonstrated in example O represented a pilot study for the dissertation project of Violeta García-Espín, supervised by Prof. Monika Egerbacher and Prof. Gilles Dupré (all University of Veterinary Medicine Vienna, Austria). The help of Dr. Stephan Handschuh (University of Veterinary Medicine Vienna) with the whole slide image analysis is gratefully acknowledged.

CONFLICT OF INTEREST

The authors declare no conflict of interest.

DATA AVAILABILITY STATEMENT

Primary data supporting the calculations in the examples can be requested from the authors or have been already published in the papers that were cited appropriately.

ORCID

Zbyněk Tonar https://orcid.org/0000-0002-7200-9894

REFERENCES

Arai, K., Kobayashi, M., Harada, Y., Hara, Y., Michishita, N., Ohkusu-Tsukada, K., & Takahashi, K. (2016). Histopathologic and immunohistochemical features of soft palate muscles and nerves in dogs with an elongated soft palate. *American Journal of Veterinary Research*, *77*(1), 77–83. https://doi.org/10.2460/ajvr.77.1.77

Babuska, V., Moztarzadeh, O., Kubikova, T., Moztarzadeh, A., Hrusak, D., & Tonar, Z. (2016). Evaluating the osseointegration of nanostructured titanium implants in animal models: Current experimental methods and perspectives (Review). *Biointerphases*, *11*, 030801. https://doi.org/10.1116/1.4958793

Baker, M. (2016). 1,500 scientists lift the lid on reproducibility. *Nature*, *533*, 452–454. https://doi.org/10.1038/533452a

Bertram, C. A., & Klopfleisch, R. (2017). The Pathologist 2.0: An update on digital pathology in veterinary medicine. *Veterinary Pathology*, *54*, 756–766. https://doi.org/10.1177/0300985817709888

Biosystems, L. (2021). *Tips for digital pathology slide scanning*. https://www.leicabiosystems.com/resources/four–tips–for–digital–pathology–slide–scanning

Blassova, T., Tonar, Z., Tomasek, P., Hosek, P., Hollan, I., Treska, V., & Molacek, J. (2019). Inflammatory cell infiltrates, hypoxia, vascularization, pentraxin 3 and osteoprotegerin in abdominal aortic aneurysms – A quantitative histological study. *PLoS One*, *14*, e0224818. https://doi.org/10.1371/journal.pone.0224818

Bolat, D., Kürüm, A., & Canpolat, S. (2018). Morphology and quantification of sheep pineal glands at pre–pubertal, pubertal and post–pubertal periods. *Anatomia, Histologia, Embryologia*, *47*(4), 338–345. https://doi.org/10.1111/ahe.12359

Bolon, B., Garman, R. H., Gundersen, H. J. G., Allan Johnson, G., Kaufmann, W., Krinke, G., Little, P. B., Makris, S. L., Mellon, R. D., Sulik, K. K., & Jensen, K. (2011). Continuing education course #3: Current practices and future trends in neuropathology assessment for developmental neurotoxicity testing. *Toxicologic Pathology*, *39*(1), 289–293. https://doi.org/10.1177/0192623310386247

Cakmak, G., & Karadag, H. (2019). A stereological study on calculation of volume values regarding lumbosacral segments of quails. *Anatomia, Histologia, Embryologia*, *48*, 164–174. https://doi.org/10.1111/ahe.12437

Casteleyn, C., Rekecki, A., Van Der Aa, A., Simoens, P., & Van Den Broeck, W. (2010). Surface area assessment of the murine intestinal tract as a prerequisite for oral dose translation from mouse to man. *Laboratory Animals*, *44*(3), 176–183. https://doi.org/10.1258/la.2009.009112

Chow, S. C., Wang, H., & Shao, J. (2008). *Sample size calculations in clinical research*, 2nd ed. Chapman & Hall/CRC Biostatistics Series.

Crosse, K. R., Bray, J. P., Orbell, G. M. B., & Preston, C. A. (2015). Histological evaluation of the soft palate in dogs affected by brachycephalic obstructive airway syndrome. *New Zealand Veterinary Journal*, *63*(6), 319–325. https://doi.org/10.1080/00480169.2015.1061464

Dempster, D. W., Compston, J. E., Drezner, M. K., Glorieux, F. H., Kanis, J. A., Malluche, H., Meunier, P. J., Ott, S. M., Recker, R. R., & Parfitt, A. M. (2013). Standardized nomenclature, symbols, and units for bone histomorphometry: A 2012 update of the report of the ASBMR

Histomorphometry Nomenclature Committee. *Journal of Bone and Mineral Research*, *28*(1), 2–17. https://doi.org/10.1002/jbmr.1805

Dockery, P., & Fraher, J. (2007). The quantification of vascular beds: A stereological approach. *Experimental and Molecular Pathology*, *82*, 110–120. https://doi.org/10.1016/j.yexmp.2006.12.011

Dorph-Petersen, K. A., Nyengaard, J. R., & Gundersen, H. J. (2001). Tissue shrinkage and unbiased stereological estimation of particle number and size. *Journal of Microscopy*, *204*, 232–246. https://doi.org/10.1046/j.1365-2818.2001.00958.x

Dupré, G., & Heidenreich, D. (2016). Brachycephalic syndrome. *Veterinary Clinics of North America: Small Animal Practice*, *46*(4), 691–707. https://doi.org/10.1016/j.cvsm.2016.02.002

Eržen, I., Janáček, J., & Kubínová, L. (2011). Characterization of the capillary network in skeletal muscles from 3D data. *Physiological Research*, *60*, 1–13. https://doi.org/10.33549/physiolres.931988

Ferreira, V. F., Dias, F. C. R., Costa, K. L. C., da Matta, S. L. P., de Melo, F. R., & de Melo, F. C. S. A. (2021). Descriptive morphometry and stereology in accessing the testis structure and function of the marsupial *Philander frenatus* (Olfers, 1818) (Didelphimorphia: Didelphidae). *Anatomia*, *Histologia*, *Embryologia*, *50*, 379–386. https://doi.org/10.1111/ahe.12642

Goodarzi, N., Akbari Bazm, M., Naseri, L., & Hosseinipour, M. (2019). Histomorphometrical and stereological study of the oesophagus in the adult male Persian squirrel (*Sciurus anomalus*). *Anatomia*, *Histologia*, *Embryologia*, *48*, 444–448. https://doi.org/10.1111/ahe.12465

Greiner, C., Grainger, S., Farrow, S., Davis, A., Su, J. L., Saybolt, M. D., Wilensky, R., Madden, S., & Sum, S. T. (2021). Robust quantitative assessment of collagen fibers with picrosirius red stain and linearly polarized light as demonstrated on atherosclerotic plaque samples. *PLoS One*, *16*, e0248068. https://doi.org/10.1371/journal.pone.0248068

Gundersen, H. J., Boyce, R. W., Nyengaard, J. R., & Odgaard, A. (1993). The Conneulor: Unbiased estimation of connectivity using physical disectors under projection. *Bone*, *14*, 217–222. https://doi.org/10.1016/8756-3282(93)90144-y

Gundersen, H. J., & Jensen, E. B. (1987). The efficiency of systematic sampling in stereology and its prediction. *Journal of Microscopy*, *147*, 229–263. https://doi.org/10.1111/j.1365-2818.1987.tb02837.x

Gundersen, H. J., & Osterby, R. (1981). Optimizing sampling efficiency of stereological studies in biology: Or 'do more less well!'. *Journal of Microscopy*, *121*, 65–73. https://doi.org/10.1111/j.1365-2818.1981.tb01199.x

Gundersen, H. J. G., Vedel Jensen, E. B., Kieu, K., & Nielsen, J. (1999). The efficiency of systematic sampling in stereology reconsidered. *Journal of Microscopy*, *193*, 199–211. https://doi.org/10.1046/j.1365-2818.1999.00457.x

Haralick, R. M. (1979). Statistical and structural approaches to texture. *Proceedings of the IEEE*, *67*, 786–804. https://doi.org/10.1109/PROC.1979.11328

Hendry, S., Salgado, R., Gevaert, T., Russell, P. A., John, T., Thapa, B., Christie, M., van de Vijver, K., Estrada, M. V., Gonzalez-Ericsson, P. I., Sanders, M., Solomon, B., Solinas, C., den Van Eynden, G. G. G. M., Allory, Y., Preusser, M., Hainfellner, J., Pruneri, G., Vingiani, A., … Fox, S. B. (2017). Assessing tumor-infiltrating lymphocytes in solid tumors: A Practical review for pathologists and proposal for a standardized method from the International Immunooncology Biomarkers Working Group: Part 1: Assessing the host immune response, TILs in invasive breast carcinoma and ductal carcinoma in situ, metastatic tumor deposits and areas for further research. *Advances in Anatomic Pathology*, *24*, 235–251. https://doi.org/10.1097/PAP.0000000000000162

Hlavatý, J., Tonar, Z., Renner, M., Panitz, S., Petznek, H., Schweizer, M., Schüle, S., Kloke, B. P., Moldzio, R., & Witter, K. (2017). Tropism, intracerebral distribution, and transduction efficiency of HIV– and SIV–based lentiviral vectors after injection into the mouse brain: A qualitative and quantitative in vivo study. *Histochemistry and Cell Biology*, *148*, 313–329. https://doi.org/10.1007/s00418-017-1569-1

Howard, C. V., & Reed, M. G. (2005). *Unbiased stereology: Three-dimensional measurement in microscopy*, 2nd ed. Garland Science.

Hsia, C. C. W., Hyde, D. M., Ochs, M., & Weibel, E. R. (2010). An official research policy statement of the American Thoracic Society/European Respiratory Society: Standards for quantitative assessment of lung structure. *American Journal of Respiratory and Critical Care Medicine*, *181*(4), 394–418. https://doi.org/10.1164/rccm.200809-1522ST

Jahn, S. W., Plass, M., & Moinfar, F. (2020). Digital pathology: Advantages, limitations and emerging perspectives. *Journal of Clinical Medicine*, *9*(11), 3697. https://doi.org/10.3390/jcm9113697

Jiřík, M., Bartoš, M., Tomášek, P., Malečková, A., Kural, T., Horáková, J., Lukáš, D., Suchý, T., Kochová, P., Hubálek Kalbáčová, M., Králíčková, M., & Tonar, Z. (2018). Generating standardized image data for testing and calibrating quantification of volumes, surfaces, lengths, and object counts in fibrous and porous materials using X–ray microtomography. *Microscopy Research and Techniques*, *81*, 551–568. https://doi.org/10.1002/jemt.23011

Jirik, M., Gruber, I., Moulisova, V., Schindler, C., Cervenkova, L., Palek, R., Rosendorf, J., Arlt, J., Bolek, L., Dejmek, J., Dahmen, U., Zelezny, M., & Liska, V. (2021). Semantic segmentation of intralobular and extralobular tissue from liver scaffold H&E images. *Sensors*, *20*, 7063. https://doi.org/10.3390/s20247063

Jirik, M., Moulisova, V., Schindler, C., Cervenkova, L., Palek, R., Rosendorf, J., Arlt, J., Bolek, L., Dejmek, J., Dahmen, U., Jirikova, K., Gruber, I., Liska, V., & Zelezny, M. (2020). MicrAnt: Towards regression task oriented annotation tool for microscopic images. *Lecture Notes in Computer Science*, *12148*, 209–218. https://doi.org/10.1007/978-3-030-51002-2_15

Jiřík, M., Tonar, Z., Králíčková, A., Eberlová, L., Mírka, H., Kochová, P., Gregor, T., Hošek, P., Svobodová, M., Rohan, E., Králíčková, M., & Liška, V. (2016). Stereological quantification of microvessels using semiautomated evaluation of X–ray microtomography of hepatic vascular corrosion casts. *International Journal of Computer Assisted Radiology and Surgery*, *11*, 1803–1819. https://doi.org/10.1007/s11548-016-1378-3

Junatas, K. L., Tonar, Z., Kubíková, T., Liška, V., Pálek, R., Mik, P., Králíčková, M., & Witter, K. (2017). Stereological analysis of size and density of hepatocytes in the porcine liver. *Journal of Anatomy*, *230*, 575–588. https://doi.org/10.1111/joa.12585

Kass, M., Witkin, A., & Terzopoulos, D. (1988). Snakes: Active contour models. *International Journal of Computer Vision*, *1*, 321–331. https://doi.org/10.1007/BF00133570

Keša, P., Pokorná, E., Grajciarová, M., Tonar, Z., Vočková, P., Trochet, P., Kopeček, M., Jakša, R., Šefc, L., & Klener, P. (2021). Quantitative in vivo monitoring of hypoxia and vascularization of patient-derived murine xenografts of mantle cell lymphoma using photoacoustic and ultrasound imaging. *Ultrasound in Medicine & Biology*, *47*, 1099–1107. https://doi.org/10.1016/j.ultrasmedbio.2020.12.010

Knudsen, L., Brandenberger, C., & Ochs, M. (2021). Stereology as the 3D tool to quantitate lung architecture. *Histochemistry and Cell Biology*, *155*, 163–181. https://doi.org/10.1007/s00418-020-01927-0

Kochová, P., Cimrman, R., Jansová, M., Michalová, K., Kališ, K., Kubíková, T., & Tonar, Z. (2019). The histological microstructure and in vitro mechanical properties of the human female postmenopausal perineal body. *Menopause - The Journal of the North American Menopause Society*, *26*, 66–77. https://doi.org/10.1097/GME.0000000000001166

Kochová, P., Hympánová, L., Rynkevic, R., Cimrman, R., Tonar, Z., Deprest, J., & Kališ, V. (2019). The histological microstructure and in vitro mechanical properties of pregnant and postmenopausal ewe perineal body. *Menopause - The Journal of the North American*

Menopause Society, *26*, 1289–1301. https://doi.org/10.1097/GME.0000000000001395

Kocová, J. (1970). Overall staining of connective tissue and the muscular layer of vessels. *Folia Morphologica*, *18*, 293–295.

Kolinko, Y., Cendelin, J., Kralickova, M., & Tonar, Z. (2016). Smaller absolute quantities but greater relative densities of microvessels are associated with cerebellar degeneration in Lurcher mice. *Frontiers in Neuroanatomy*, *10*, 35. https://doi.org/10.3389/fnana.2016.00035

Kubíková, T., Kochová, P., Tomášek, P., Witter, K., & Tonar, Z. (2018). Numerical and length densities of microvessels in the human brain: Correlation with preferential orientation of microvessels in the cerebral cortex, subcortical grey matter and white matter, pons and cerebellum. *Journal of Chemical Neuroanatomy*, *88*, 22–32. https://doi.org/10.1016/j.jchemneu.2017.11.005

Kuo, K.-H., & Leo, J. M. (2019). Optical versus virtual microscope for medical education: A systematic review. *Anatomical Sciences Education*, *12*(6), 678–685. https://doi.org/10.1002/ase.1844

Lokkegaard, A., Nyengaard, J. R., & West, M. J. (2001). Stereological estimates of number and length of capillaries in subdivisions of the human hippocampal region. *Hippocampus*, *11*, 726–740. https://doi.org/10.1002/hipo.1088

Look Hong, N. J., Clarke, G. M., Yaffe, M. J., & Holloway, C. M. B. (2016). Cost–effectiveness analysis of whole–mount pathology processing for patients with early breast cancer undergoing breast conservation. *Current Oncology*, *23*, S23–S31. https://doi.org/10.3747/co.23.2917

Malečková, A., Kochová, P., Pálek, R., Liška, V., Mik, P., Bońkowski, T., Horák, M., & Tonar, Z. (2021). Blunt injury of liver: Mechanical response of porcine liver in experimental impact test. *Physiological Measurement*, *42*, 025008. https://doi.org/10.1088/1361-6579/abdf3c

Marcos, R., Monteiro, R. A., & Rocha, E. (2012). The use of design–based stereology to evaluate volumes and numbers in the liver: A review with practical guidelines. *Journal of Anatomy*, *220*, 303–317. https://doi.org/10.1111/j.1469-7580.2012.01475.x

Mayhew, T. M. (2014). Estimating oxygen diffusive conductances of gas–exchange systems: A stereological approach illustrated with the human placenta. *Annals of Anatomy*, *196*, 34–40. https://doi.org/10.1016/j.aanat.2012.08.002

Mayhew, T. M., & Lucocq, J. M. (2015). From gross anatomy to the nanomorphome: Stereological tools provide a paradigm for advancing research in quantitative morphomics. *Journal of Anatomy*, *226*, 309–321. https://doi.org/10.1111/joa.12287

McQuin, C., Goodman, A., Chernyshev, V., Kamentsky, L., Cimini, B. A., Karhohs, K. W., Doan, M., Ding, L., Rafelski, S. M., Thirstrup, D., Wiegraebe, W., Singh, S., Becker, T., Caicedo, J. C., & Carpenter, A. E. (2018). Cell profiler 3.0: Next–generation image processing for biology. *PLoS Biology*, *16*(7), e2005970. https://doi.org/10.1371/journal.pbio.2005970

Mik, P., Tonar, Z., Malečková, A., Eberlová, L., Liška, V., Pálek, R., Rosendorf, J., Jiřík, M., Mírka, H., Králíčková, M., & Witter, K. (2018). Distribution of connective tissue in the male and female porcine liver: Histological mapping and recommendations for sampling. *Journal of Comparative Pathology*, *162*, 1–13. https://doi.org/10.1016/j.jcpa.2018.05.004

Moulisová, V., Jiřík, M., Schindler, C., Červenková, L., Pálek, R., Rosendorf, J., Arlt, J., Bolek, L., Šůsová, S., Nietzsche, S., Liška, V., & Dahmen, U. (2020). Novel morphological multi–scale evaluation system for quality assessment of decellularized liver scaffolds. *Journal of Tissue Engineering*, *11*, 2041731420921121. https://doi.org/10.1177/2041731420921121

Mouton, P. R. (2002). *Principles and practices of unbiased stereology. An introduction for bioscientists*. The Johns Hopkins University Press.

Mühlfeld, C. (2014). Quantitative morphology of the vascularisation of organs: A stereological approach illustrated using the cardiac circulation. *Annals of Anatomy*, *196*, 12–19. https://doi.org/10.1016/j.aanat.2012.10.010

Mühlfeld, C., Nyengaard, J. R., & Mayhew, T. M. (2010). A review of state–of–the–art stereology for better quantitative 3D morphology in cardiac research. *Cardiovascular Pathology*, *19*, 65–82. https://doi.org/10.1016/j.carpath.2008.10.015

Mühlfeld, C., & Ochs, M. (2013). Quantitative microscopy of the lung: A problem–based approach. Part 2: Stereological parameters and study designs in various diseases of the respiratory tract. *American Journal of Physiology*, *Lung Cellular and Molecular Physiology*, *305*, L205–L221. https://doi.org/10.1152/ajplung.00427.2012

Nelson, G., Boehm, U., Bagley, S., Bajcsy, P., Bischof, J., Brown, C. M., Dauphin, A., Dobbie, I. M., Eriksson, J. E., Faklaris, O., Fernandez-Rodriguez, J., Ferrand, A., Gelman, L., Gheisari, A., Hartmann, H., Kukat, C., Laude, A., Mitkovski, M., Munck, S., … Nitschke, R. (2021). QUAREP-LiMi: A community-driven initiative to establish guidelines for quality assessment and reproducibility for instruments and images in light microscopy. *Journal of Microscopy*, *284*, 56–73. https://doi.org/10.1111/jmi.13041

Nevoral, J., Havránková, J., Kolinko, Y., Prokešová, Š., Fenclová, T., Monsef, L., Žalmanová, T., Petr, J., & Králíčková, M. (2021). Exposure to alternative bisphenols BPS and BPF through breast milk: Noxious heritage effect during nursing associated with idiopathic infertility. *Toxicology and Applied Pharmacology*, *413*, 115409. https://doi.org/10.1016/j.taap.2021.115409

Noorafshan, A. (2014). Stereology as a valuable tool in the toolbox of testicular research. *Annals of Anatomy*, *196*, 57–66. https://doi.org/10.1016/j.aanat.2012.07.008

Noorafshan, A., Niazi, B., Mohamadpour, M., Hoseini, L., Hoseini, N., Owji, A. A., Rafati, A., Sadeghi, Y., & Karbalay-Doust, S. (2016). First and second order stereology of hyaline cartilage: Application on mice femoral cartilage. *Annals of Anatomy*, *208*, 24–30. https://doi.org/10.1016/j.aanat.2016.07.011

Nyengaard, J. R. (1999). Stereologic methods and their application in kidney research. *Journal of the American Society of Nephrology*, *10*, 1100–1123. https://doi.org/10.1681/ASN.V1051100

Nyengaard, J. R., & Alwasel, S. H. (2014). Practical stereology of the stomach and intestine. *Annals of Anatomy*, *196*, 41–47. https://doi.org/10.1016/j.aanat.2013.10.007

Ochs, M., & Mühlfeld, C. (2013). Quantitative microscopy of the lung: A problem–based approach. Part 1: Basic principles of lung stereology. *American Journal of Physiology*, *Lung Cellular and Molecular Physiology*, *305*, L15–L22. https://doi.org/10.1152/ajplung.00429.2012

Parfitt, A. M., Drezner, M. K., Glorieux, F. H., Kanis, J. A., Malluche, H., Meunier, P. J., Ott, S. M., & Recker, R. R. (1987). Bone histomorphometry: Standardization of nomenclature, symbols, and units: Report of the ASBMR Histomorphometry Nomenclature Committee. *Journal of Bone and Mineral Research*, *2*(6), 595–610. https://doi.org/10.1002/jbmr.5650020617

Pichetto, M., Arrighi, S., Gobbetti, M., & Romussi, S. (2015). The anatomy of the dog soft palate. III. Histological evaluation of the caudal soft palate in brachycephalic neonates. *Anatomical Record*, *298*(3), 618–623. https://doi.org/10.1002/ar.23054

Rashid, S., Nir, G., Fazli, L., Boag, A. H., Siemens, D. R., Goldenberg, S. L., Abolmaesumi, P., & Salcudean, S. E. (2019). Automatic pathology of prostate cancer in whole mount slides incorporating individual gland classification. *Computer Methods in Biomechanics and Biomedical Engineering: Imaging & Visualization*, *3*, 336–347. https://doi.org/10.1080/21681163.2018.1514280

Rich, L., & Whittaker, P. (2005). Collagen and picrosirius red staining. A polarized light assessment of fibrillar hue and spatial distribution. *Journal of Morphological Sciences*, *22*, 97–104.

Rosendorf, J., Horakova, J., Klicova, M., Palek, R., Cervenkova, L., Kural, T., Hosek, P., Kriz, T., Tegl, V., Moulisova, V., Tonar, Z., Treska, V., Lukas, D., & Liska, V. (2020). Experimental fortification of intestinal

anastomoses with nanofibrous materials in a large animal model. *Scientific Reports*, *10*, 1134. https://doi.org/10.1038/s41598-020-58113-4

Rosendorf, J., Klicova, M., Cervenkova, L., Horakova, J., Klapstova, A., Hosek, P., Palek, R., Sevcik, J., Polak, R., Treska, V., Chvojka, J., & Liska, V. (2021). Reinforcement of colonic anastomosis with improved ultrafine nanofibrous patch: Experiment on pig. *Biomedicines*, *9*, 102. https://doi.org/10.3390/biomedicines9020102

Rosendorf, J., Klicova, M., Cervenkova, L., Palek, R., Horakova, J., Klapstova, A., Hosek, P., Moulisova, V., Bednar, L., Tegl, V., Brzon, O., Tonar, Z., Treska, V., Lukas, D., & Liska, V. (2021). Double–layered nanofibrous patch for prevention of anastomotic leakage and peritoneal adhesions, experimental study. *In Vivo*, *35*, 731–741. https://doi.org/10.21873/invivo.12314

Sadeghinezhad, J., Aghabalazadeh Asl, M., Saeidi, A., & De Silva, M. (2020). Morphometrical study of the cat cerebellum using unbiased design–based stereology. *Anatomia*, *Histologia*, *Embryologia*, *49*, 788–797. https://doi.org/10.1111/ahe.12583

Sadeghinezhad, J., & Nyengaard, J. R. (2021). Morphometry of cervical spinal cord in cat using design–based stereology. *Anatomia*, *Histologia*, *Embryologia*, *50*, 746–755. https://doi.org/10.1111/ahe.12719

Saliba, V., Legido-Quigley, H., Hallik, R., Aaviksoo, A., Car, J., & McKee, M. (2012). Telemedicine across borders: A systematic review of factors that hinder or support implementation. *International Journal of Medical Informatics*, *81*(12), 793–809. https://doi.org/10.1016/j.ijmedinf.2012.08.003

Schindelin, J., Arganda-Carreras, I., Frise, E., Kaynig, V., Longair, M., Pietzsch, T., Preibisch, S., Rueden, C., Saalfeld, S., Schmid, B., Tinevez, J. Y., White, D. J., Hartenstein, V., Eliceiri, K., Tomancak, P., & Cardona, A. (2012). Fiji: An open–source platform for biological–image analysis. *Nature Methods*, *9*, 676–682. https://doi.org/10.1038/nmeth.2019

Schneider, C. A., Rasband, W. S., & Eliceiri, K. W. (2012). NIH Image to ImageJ: 25 years of image analysis. *Nature Methods*, *9*, 671–675. https://doi.org/10.1038/nmeth.2089

Selçuk, M. L., & Tipirdamaz, S. (2020). A morphological and stereological study on brain, cerebral hemispheres and cerebellum of New Zealand rabbits. *Anatomia*, *Histologia*, *Embryologia*, *49*, 90–96. https://doi.org/10.1111/ahe.12489

Slomianka, L., & West, M. J. (2005). Estimators of the precision of stereological estimates: An example based on the CA1 pyramidal cell layer of rats. *Neuroscience*, *136*, 757–767. https://doi.org/10.1016/j.neuroscience.2005.06.086

Smart In Media AG. (2021, September 3). *Virtual microscopy—Overview and definition*. https://www.virtual-microscopy.net

Suchý, T., Šupová, M., Sauerová, P., Verdánová, M., Sucharda, Z., Rýglová, Š., Žaloudková, M., Sedláček, R., & Kalbáčová, M. H. (2015). The effects of different cross–linking conditions on collagen–based nanocomposite scaffolds–an in vitro evaluation using mesenchymal stem cells. *Biomedical Materials*, *10*, 065008. https://doi.org/10.1088/1748-6041/10/6/065008

Tamburro, R., Brunetti, B., Muscatello, L. V., Mantovani, C., & De Lorenzic, D. (2019). Short–term surgical outcomes and histomorphological evaluation of thermal injury following palatoplasty performed with diode laser or air plasma device in dogs with brachycephalic airway obstructive syndrome. *The Veterinary Journal*, *253*, 105391. https://doi.org/10.1016/j.tvjl.2019.105391

Tomášek, P., Tonar, Z., Grajciarová, M., Kural, T., Turek, D., Horáková, J., Pálek, R., Eberlová, L., Králíčková, M., & Liška, V. (2020). Histological mapping of porcine carotid arteries – An animal model for the assessment of artificial conduits suitable for coronary bypass grafting in humans. *Annals of Anatomy*, *228*, 151434. https://doi.org/10.1016/j.aanat.2019.151434

Tonar, Z., Egger, G. F., Witter, K., & Wolfesberger, B. (2008). Quantification of microvessels in canine lymph nodes. *Microscopy Research and Techniques*, *71*, 760–772. https://doi.org/10.1002/jemt.20619

Tonar, Z., Khadang, I., Fiala, P., Nedorost, L., & Kochová, P. (2011). Quantification of compact bone microporosities in the basal and alveolar portions of the human mandible using osteocyte lacunar density and area fraction of vascular canals. *Annals of Anatomy*, *193*, 211–219. https://doi.org/10.1016/j.aanat.2011.02.001.s

Tonarova, P., Lochovska, K., Pytlik, R., & Hubalek Kalbacova, M. (2021). The impact of various culture conditions on human mesenchymal stromal cells metabolism. *Stem Cells International*, *2021*, 6659244. https://doi.org/10.1155/2021/6659244

Tschanz, S., Schneider, J. P., & Knudsen, L. (2014). Design–based stereology: Planning, volumetry and sampling are crucial steps for a successful study. *Annals of Anatomy*, *196*, 3–11. https://doi.org/10.1016/j.aanat.2013.04.011

Van Ginneken, C., Meir, F. V., Sys, S., & Weyns, A. (2002). Stereologic characteristics of pig small intestine during normal development. *Digestive Diseases and Sciences*, *47*(4), 868–878. https://doi.org/10.1023/A:1014768806773

Vatsos, I. N. (2021). Planning and reporting of the histomorphometry used to assess the intestinal health in fish nutrition research—Suggestions to increase comparability of the studies. *Frontiers in Veterinary Science*, *8*, 666044. https://doi.org/10.3389/fvets.2021.666044

West, M. J., Slomianka, L., & Gundersen, H. J. (1991). Unbiased stereological estimation of the total number of neurons in the subdivisions of the rat hippocampus using the optical fractionator. *Anatomical Record*, *231*, 482–497. https://doi.org/10.1002/ar.1092310411

Wolfesberger, B., Tonar, Z., Witter, K., Guija de Arespacohaga, A., Skalicky, M., Walter, I., Thalhammer, J. G., & Egger, G. F. (2008). Microvessel density in normal lymph nodes and lymphomas of dogs and their correlation with vascular endothelial growth factor expression. *Research in Veterinary Science*, *85*, 56–61. https://doi.org/10.1016/j.rvsc.2007.07.008

SUPPORTING INFORMATION

Additional supporting information may be found in the online version of the article at the publisher's website.

How to cite this article: Kolinko, Y., Malečková, A., Kochová, P., Grajciarová, M., Blassová, T., Kural, T., Trailin, A., Červenková, L., Havránková, J., Vištejnová, L., Tonarová, P., Moulisová, V., Jiřík, M., Zavaďáková, A., Tichánek, F., Liška, V., Králíčková, M., Witter, K., & Tonar, Z. (2021). Using virtual microscopy for the development of sampling strategies in quantitative histology and design-based stereology. *Anatomia*, *Histologia*, *Embryologia*, 00, 1–20. https://doi.org/10.1111/ahe.12765

11.3 Supplement III

Rosendorf, J., Horáková J, Klíčová, M., Pálek, R., Červenková, L., **Kural, T.**, Hošek, P., Kříž, T., Tégl, V., Moulisová, V., Tonar, Z., Třeška, V., Lukáš, D., Liška, V. Experimental fortification of intestinal anastomoses with nanofibrous materials in a large animal model. Sci Rep. 2020 Jan 24;10(1):1134. DOI: 10.1038/s41598-020-58113-4.

$IF_{(JCR2020)}$ = 4.380. Q1 (Multidisciplinary Sciences)

https://pubmed.ncbi.nlm.nih.gov/31980716/

SCIENTIFIC REPORTS
nature research

open

Experimental fortification of intestinal anastomoses with nanofibrous materials in a large animal model

Jachym Rosendorf[1,2*], Jana Horakova[4], Marketa Klicova[4], Richard palek[1,2], Lenka cervenkova[2], Tomas Kural[3,5], Petr Hosek[2], Tomas Kriz[2], Vaclav tegl[2,6], Vladimira Moulisova[2], Zbynek tonar[2,5], Vladislav treska[1], David Lukas[4] & Vaclav Liska[1,2]

Anastomotic leakage is a severe complication in gastrointestinal surgery. It is often a reason for reoperation together with intestinal passage blockage due to formation of peritoneal adhesions. Different materials as local prevention of these complications have been studied, none of which are nowadays routinely used in clinical practice. Nanofabrics created proved to promote healing with their structure similar to extracellular matrix. We decided to study their impact on anastomotic healing and formation of peritoneal adhesions. We performed an experiment on 24 piglets. We constructed 3 hand sutured end-to-end anastomoses on the small intestine of each pig. We covered the anastomoses with a sheet of polycaprolactone nanomaterial in the first experimental group, with a sheet of copolymer of polylactic acid with polycaprolactone in the second one and no fortifying material was used in the Control group. The animals were sacrificed after 3 weeks of observation. Clinical, biochemical and macroscopic signs of anastomotic leakage or intestinal obstruction were monitored, the quality of the scar tissue was assessed histologically, and a newly developed scoring system was employed to evaluate the presence of adhesions. The material is easy to manipulate with. There was no mortality or major morbidity in our groups. No statistical difference was found inbetween the groups in the matter of level of peritoneal adhesions or the quality of the anastomoses. We created a new adhesion scoring system. The material appears to be safe however needs to be studied further to prove its' positive effects.

Anastomotic leakage remains one of the major problems in gastrointestinal (GI) surgery[1,2]. It occurs in 3–19% of colorectal surgeries depending on many factors some of which can and some of which cannot be influenced[3–6]. For rectal anastomoses, the reported risk factors include, besides others, male gender, preoperative radiotherapy and so-called low anastomosis[7], i.e. an anastomosis within 5 cm from the anus. One of the most important factors influencing the anastomotic healing has proven to be the oxygenation on the site of the anastomosis. Correct oxygen levels are needed for leukocytes activation, fibroblasts production and angiogenesis, which are essential for wound healing[8]. The technique of construction of GI anastomoses is also very important. Although it has been modified and improved repeatedly throughout the history of modern surgery, the mentioned anastomotic leakage as well as other kinds of complications have not been eradicated completely so far (though their frequency has been lowered noticeably). Various sealing techniques and materials were tested both experimentally and clinically including fibrin patches, fibrin glue, collagen patches, hyaluronic acid derivatives and many others[9–16] as a local barrier protection, while other experiments included systemic administration of various substances[17,18]. The anastomotic leakage occurs in different severity, prolonging the patients' stay in the hospital. Minimal leakage can stay

[1]Department of Surgery, Faculty of Medicine in Pilsen, Charles University, Prague, Czech Republic. [2]Biomedical Center, Faculty of Medicine in Pilsen, Charles University, Prague, Czech Republic. [3]Department of Surgery, University Hospital Regensburg, Regensburg, Germany. [4]Department of Nonwovens, Faculty of Textile Engineering, Technical University in Liberec, Liberec, Czech Republic. [5]Department of Histology and Embryology, Faculty of Medicine in Pilsen, Charles University, Prague, Czech Republic. [6]Department of Anesthesiology and Intensive Care Medicine, Faculty of Medicine in Plzen, Pilsen, Czech Republic. *email: jachymrosendorf@gmail.com

clinically invisible, being detectable only by laboratory markers[19]. The incomplete dehiscence can be approached conservatively by administering antibiotics and parenteral nutrition until the anastomosis is sealed[20–23]. It is usually associated with abdominal drain secretion, abdominal discomfort, temperature elevation, elevation of C-reactive protein and other inflammatory markers[24]. The worst cases need to be approached more radically with relaparotomy bringing a high risk of stomy and higher morbidity and mortality[25,26].

Peritoneal adhesions (PAs) are bonds between peritoneal surfaces of different abdominal organs. They can range from thin films to thick fibrous bonds containing vessels[27]. Some amount of PAs appears after almost every intraabdominal surgical procedure, but also after inflammations, radiotherapy or chemotherapy[28,29]. PAs can be a source of other complications as they cause abdominal discomfort in many patients, decreasing their quality of life in the long term follow-up. Even more serious problem is abdominal passage blockage, which can appear due to PAs in any time of the patients' life from the surgery onwards[29,30]. There are various products on the market designed to decrease the level of postoperative adhesions, none of which is commonly used nowadays in GI surgery to successfully prevent the formation of adhesions while maintaining the GI anastomoses healing process intact. Specific inflammatory responses are crucial for both tissue healing after surgical interventions and adhesion formation; so it is therefore a very difficult task to influence the anastomotic healing positively while trying to decrease the amount of newly formed adhesions. To influence one part of the process in one way while the other one in the opposite way seems to be easier by using some kind of barrier protection rather than a systemic treatment[31].

There are several systems of PA evaluation that focus both on quantity and quality of the adhesions. Coccolini's peritoneal adhesion index divides the abdominal cavity into segments and evaluates the amount of adhesions in each of them separately, while the other systems evaluate adhesions based on their mechanical properties[32–34]; nevertheless, none of these systems grade regional adhesions in the site of anastomosis in the GI tract.

According to the literature, nanomaterials have never been used in attempts to resolve these complications, therefore we decided to test their ability to reinforce GI anastomoses and investigate their effect on the formation of PAs. In our study we focused on non-woven nanofibrous scaffolds. These structures are considered as very interesting in recent years in the field of tissue engineering thanks to their similar morphology to extracellular matrix[17,18]. Srouji S *et al.*[35] have noticed their ability to accelerate tissue regeneration in the site of surgery.

There are several ways how to produce nanofibers. The most appealing method for mass production seems to be electrospinning, which is a method with highly adjustable settings allowing to create a large variety of different products with different shapes and thicknesses of the fibers. It is also a method suitable for high volume production[36]. In the process of electrospinning a liquid polymer solution is dosed to an electrode (spinneret) charged with electric potential, while a collector either grounded or oppositely charged is placed on the opposite side of the apparatus. In the presence of electric field, the drop of the polymer shapes into a so called Taylor's cone from which the material is dragged to the collector. The stream of the solution gets unstable in the process and the solvent evaporates before the polymer hits the collector. The polymer solution forms different types of structures depending on individual settings. The needle-less spinning has been developed lately, allowing production in larger volumes[36,37].

Nanomaterials have been experimentally used in numerous surgical applications to fortify various anatomical structures[38–40]. However, the impact of the nanomaterials on healing in the abdominal cavity and on the formation of PAs has not been described yet. The right material for fabrication must be chosen according to the parameters needed. Biodegradability is a crucial quality. Biodegradable polymers are widely used in human medicine; they have been successfully used even as nanofibrous cloths having the best results when the speed of degradation is similar to the speed of tissue regeneration[41]. The wound healing of an anastomosis on the GI tract takes about 3 weeks, from this point on the scar tissue only matures and remodelation of connective tissue continues for much longer[42]. Polycaprolactone and polylactic acid are approved biocompatible polymers with good mechanical properties and cytocompatibility[43] that are also used for production of different surgical sutures.

Our aim was to investigate whether it is possible to use the nanomaterials in abdominal surgery to determine their influence of the nanomaterials on the healing process of GI anastomosis, and on the formation of PAs. We also aimed to develop a new scoring system for PAs specific for the site of surgery.

Materials and Methods

Nanomaterial preparation. Nanomaterials for our experiment were fabricated via electrospinning on the Nanospider™ machine which is a construct of Technical University of Liberec, Faculty of Textile Enigineering, Department of Nonwovens and Nanofibrous Materials, Czech Republic. Electrospinning has been selected as a method for fabrication of planar fibrous scaffolds as this technique allows large scale production of nanofibers; our team has also wide experience with this technique[39].

We used two types of biocompatible polymers: polycaprolactone (PCL), and a polylactic acid-polycaprolactone copolymer (PLCL). PCL (mean weight = 43000 g/mol, Polysciences) and PLCL (Purasorb PLC 7015, Corbion) were dissolved in chloroform, acetic acid and ethanol solution (8:1:1 volume fractions) to the final concentration of 16% and 10% respectively (concentrations allowing optimal electrospinning properties based on previous research[41]). The solutions were electrospun onto a spun bond (nonwoven cloth underlay) for easy manipulation and application. The material has been sterilised using ethylene oxide (37 °C, Anprolene). This method has been tested before to prove its safety and frugality to the nanomaterial[41].

Material characterization. Scanning electron microscopy (SEM) was employed to obtain images of the fibers; the pictures were analyzed as described in previous work of Horakova *et al.*[41]. Materials were also tested *in vitro* for degradability and mechanical properties[41].

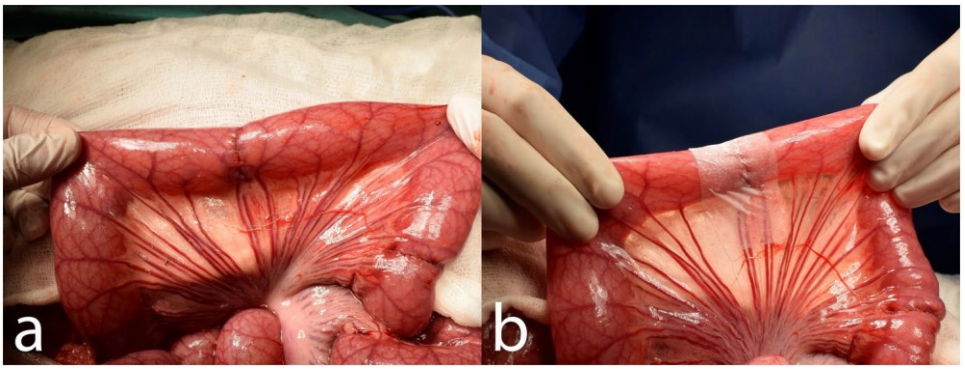

Figure 1. Reinforcing the end-to-end anastomosis on the small intestine in a pig model: (**a**) constructed anastomosis; (**b**) the PCL nanomaterial applied to the site of anastomosis partially covering the mesentery.

Experimental design. All experimental procedures with the use of piglets were described in an experimental protocol approved by the Commission of Work with Experimental Animals at the Medical Faculty of Pilsen, Charles University, and were under control of the Ministry of Education, Youth and Sports of the Czech Republic (project code: MSMT-26570/2017-2). All procedures were performed in compliance to the law of the Czech Republic, which is compatible with the legislation of the European Union.

Healthy male and female Prestice black-pied pigs were randomly allocated to 3 groups using simple randomization (8 animals per each group): PCL group, PLCL group and a control group with no material applied. Each animal was given a unique code. All animals were 12–14 weeks old weighing between 19–35 kg.

Prior to the surgery, the animals were weighed, and intramuscularly premedicated with 10 mg/kg of ketamine (Narkamon, Spofa, Czech Republic), 5 mg/kg of azaperone (Stresnil, Jannssen Phramaceutica, Belgium) and 0,5 mg atropine (Atropin Biotika, Hoechst Biotika, Slovak Republic); general anesthesia was then induced and maintained by intravenous administration of propofol (1% mixture 5–10 mg/kg/h Propofol, Fresenius Kabi, Norway). Fentanyl 1–2 µg/kg/h (Fentanyl Torrex, Chiesi cz, Czech Republic) was used for continuous analgesia. Augmentin 1.2 g as an antibiotic prophylaxis was administered intravenously (GlaxoSmithKline Slovakia, Slovak Republic). A ProPort Plastic Venous Access System with PolyFlow polyurethane catheter (Deltec, Smiths medical, U.S.A.) was implanted and introduced through one of the jugular veins.

We entered the abdominal cavity via an upper middle laparotomy. Three end-to-end anastomoses were constructed on the small intestine in 70, 90 and 110 cm aborally from the duodeno-jejunal junction. We transsected the intestine using monopolar coagulation and constructed a hand sutured anastomosis using MONOSYN 4/0 (Glycolide 72%, Caprolactone 14%, Trimethylencarbonate 14%) double needled polycaprone suture line (B-Braun, Germany), following a standard technique of extramucosal running suture (Fig. 1a). No intestinal resection was performed. A 2 × 5 cm large piece of PCL or PLCL nanomaterial (respecting the group) was placed in the area of the suture, covering the whole surface of the anastomosis (Fig. 1b). No fortifying material was used in the Control group. The intestine was then carefully reposed into the abdominal cavity. Wet swabs were used throughout the procedure for manipulation with the viscera.

The animals were monitored for three weeks by trained blinded caretakers. A fixed realimentation process was scheduled and the ability of the animals to feed according to the schedule was observed. Vomiting was considered as intolerance of the current food dosage. The activity of animals was also monitored.

Blood samples were taken during the experiment at five time points: on day 0 before the application of the material (preoperative baseline sample), exactly two hours after the application of the nanomaterial, on day 7, on day 14, on day 21. Basic biochemical parameters were tracked in these samples (bilirubin, GGT, ALT, AST, ALP, albumin, urea, and creatinine) to see deviations in the animals' metabolism.

We weighed the animals at the end of the observation period, performed laparotomy in full anesthesia again. We inspected the abdominal cavity for changes, PAs (listed organs involved in the adhesions), checked for the presence of free GI content (signs of anastomotic leakage), intestinal strictures, and intestinal diameter growth (signs of GI passage blockage). We acquired photodocumentation, collected samples of the intestine with anastomoses and fixed them into a 10% buffered formalin (cut in the mesenterial line and pinned onto a cork underlay). The second surgery as well as the macroscopic assessment and sample collection were performed by a blinded surgeon. We sacrificed the animals after the sample collection.

Scoring of adhesions. None of the quantitative systems of evaluation of PAs were useful for our experiment as we performed surgery only on a small part of the abdominal cavity and the systems usually score the whole abdomen. Thus we created a new quantitative scoring system for our purposes - a *Perianastomotic adhesions amount score* (PAAS). To evaluate the amount of PAs, we divided the area of the specimen into four equal quarters along the circumference of the intestine. Each segment was assigned zero to two points based on the level of adhesions: zero for no adhesions in the segment, one point for adhesions covering the segment partially and two points for adhesions in the whole length of the segment. This resulted in zero to eight points per anastomosis and zero to twenty four points for one animal (in 12 evaluated segments per animal). The specimen were collected carefully together with the surrounding tissue (depending on the level of adhesions), about 4 cm of the intestine was used for each one. The quality of adhesions was evaluated according to the Zühlke's classification[33]. The

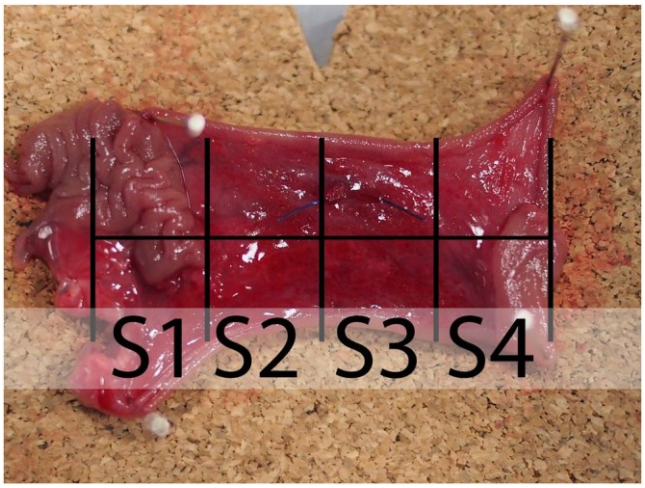

Figure 2. Perianastomotic adhesions amount scoring system for the presence of peritoneal adhesions on the intestine with an anastomosis: The sample (specimen from the Control group) was divided into 4 segments; oral part of the intestine is in the upper side of the image while the aboral part is in the lower part of the image. The area of the suture (the anastomosis itself) is located underneath the horizontal line; scoring of this sample: S1) segment no. 1 scoring 2 points; S2) segment no. 2 scoring 0 points; S3) segment no. 3 scoring 0 points; S4) segment no. 4 scoring 1 point.

intestine was then *ex vivo* transected longitudinally on the mesenteric side, and pinned to a piece of cork. The polarity (oral and aboral part) of the intestine was respected in all measurements (Fig. 2). Each sample was given random alphanumeric code for blinding during the histologic assessment.

Histology. After fixing, we processed the samples by standard paraffin technique. We stained 4 μm thick sections by hematoxylin and eosin for comprehensive overview; Verhoeff's hematoxylin and green trichrome technique was used for staining connective tissues and picrosirius red for visualization of collagen in polarized light. We used immunohistochemical methods for detection of vascular endothelium using Polyclonal Rabbit Anti-Human von Willebrad Factor (A 0082, Dako – Agilent, dilution 1:1000); smooth muscles were detected by Monoclonal Mouse Anti-Human Smooth Muscle Actin (Clone 1A4, M0851, Dako – Agilent, dilution 1:500); for detection of granulocytes and tissue macrophages we used S100A9 Monoclonal Antibody (MAC387, MA1-80446, ThermoFisher Scientific, dilution 1:200).

Stereology. Microscopic images of IHC samples were stereologically assessed. We defined the reference space as the region of intestinal wall without mucosa located 3 mm proximally and 3 mm distally from the center of the anastomosis (contact of muscle layers); the region includes a suture line. We investigated samples qualitatively and quantitatively.

Volume fractions of endothelial cells, of MAC387 positive cells and of collagen within the reference space were assessed by computerized software system (Stereologer, Stereology Resource Center). The microscope used was Nikon Eclipse Ti-U with, camera Promicra camera.

Statistical analysis. Standard frequency tables and descriptive statistics were used to characterize the sample data set. Adhesion scores were analyzed with respect to the group, quadrant and anastomosis position in the intestine (1st, 2nd, and 3rd) using repeated measures ANOVA, thus respecting the order and dependency of the three anastomoses sewn in each piglet. The same method was used to assess the differences between groups in collagen and vWF volume fractions. Volume fraction of MAC 387 was considerably affected by random presence of a stitch in some of the slides. Each piglet was therefore assigned one value for anastomoses with stitches (either the mean of all stitch-positive anastomoses, value of a single stitch-positive anastomosis or a missing value if no stitch-positive anastomoses were observed for that piglet) and one value for anastomoses with no stitches (defined analogically). Two-way main-effect ANOVA was then used to evaluate the differences in MAC827 in relation to group and stitch presence. All reported p values are two-tailed and the level of statistical significance was set at $\alpha = 0.05$. Statistical processing and testing were performed using STATISTICA data analysis software system (Version 12; StatSoft, Inc, 2013; www.statsoft.com).

Results

Two types of biodegradable nanomaterials for anastomosis fortification testing were prepared by electrospinning, the PCL based sheets (Fig. 3a) and the PLCL sheets (Fig. 3b) (Table 1). The material was electrospun on the spun bond underlay that facilitated easy manipulation while using this material during the surgical procedure.

We successfully created a model of intestinal anastomosis on pig with use of PCL and PLCL nanofibrous scaffolds.

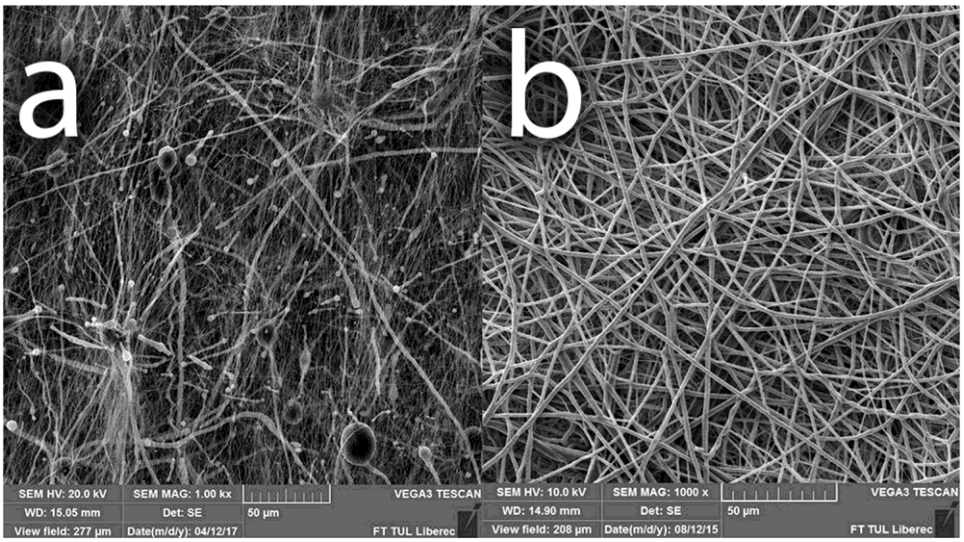

Figure 3. Scanning electron microscopy image of (**a**) the PCL nanomaterial at 1000x magnification and (**b**) the PLCL nanomaterial at 1000x magnification.

	Control Group (n = 8)	PCL Group (n = 8)	PLCL Group (n = 8)	*p*-value between groups (test)
Material fibre thickness	–	325 ± 36 nm	2047 ± 585 nm	–
Material thickness	–	49 ± 5 nm	53 ± 6 nm	–
Macroscopic signs of anastomotic stenosis (count; %)	0; 0%	0; 0%	0; 0%	–
Macroscopic signs of anastomotic leakage (count; %)	0; 0%	0; 0%	0; 0%	–
Mean PAAS score per segment (0–2) (mean ± SEM across pigs)*	0.479 ± 0.086	0.823 ± 0.171	0.688 ± 0.070	0.715 (repeated measures ANOVA)
Incomplete re-epithelisation (count; %)	0; 0%	0; 0%	0; 0%	–
Volume fraction of vWF positive cells [%] (mean ± SEM)	2.22 ± 0.10	2.16 ± 0.16	2.38 ± 0.12	0.690 (repeated measures ANOVA)
Volume fraction of collagen fibres [%] (mean ± SEM)	15.51 ± 2.10	15.67 ± 2.36	11.87 ± 1.91	0.740 (repeated measures ANOVA)
Volume fraction of MAC387 positive cells [%]:				0.550 (two-way ANOVA)
• stitch not in sample (n: mean ± SEM)	8: 0.38 ± 0.09	8: 0.46 ± 0.19	8: 0.21 ± 0.06	
• stitch in sample (n: mean ± SEM)	7: 0.80 ± 0.23	5: 0.67 ± 0.16	6: 0.70 ± 0.27	

Table 1. Summary of the most important results for each group. *Each animal was assigned a score equal to the average of all segment scores in that animal (i.e. 24 segment scores per animal; result theoretically ranging from 0 to 2). Mean and Standard error of the mean (SEM) stated in the table were then calculated from these animal averages.

Both types of material are easy to peel of the spun bond underlay, they can be then easily manipulated with. They adhere to the intestine and hold well on the intestinal wall, yet they can also be rearranged when needed. No further fixation of the materials was necessary.

All animals survived the whole length of the experiment. None of the animals developed either ileus or sepsis. Two animals from the PCL group vomited single time, so the realimentation schedule was not respected in their case. It is worthy to note though they tolerated the feeding from then on. All animals from the Control group and the PLCL group were able to feed according to the schedule, with daily stool and no signs of gastrointestinal passage blockage. The activity of the animals was not decreased in any of the groups throughout the postoperative observation. We did not notice any case of infection of intravenous port in the PCL group; one case of infection of the port appeared in the PLCL group, and two cases were in the Control group. We also noticed one laparotomy wound infection in one of the animals in the PLCL group in a form of an abscess. No intervention was needed.

There were no significant differences in the observed biochemical parameters between the groups and no remarkable deviations from healthy animals (baseline blood sample).

All animals managed to maintain their weight within the range of 5% of their preoperative weight.

There were no signs of GI content leakage within the second surgery in any of the animals (free GI content, thick peritoneal fluid, fibrin films) (Table 1). All of the anastomoses could be found in the reoperation, the nanomaterial remained fixed, covering the suture line completely in all of them. It has been neither absorbed nor dislocated. All anastomoses were sufficient, no visible defects were found in any of them (Fig. 4a–c). PAs involving other organs than the small intestine were found in 3 animals from the Control group, in 5 animals from the PCL

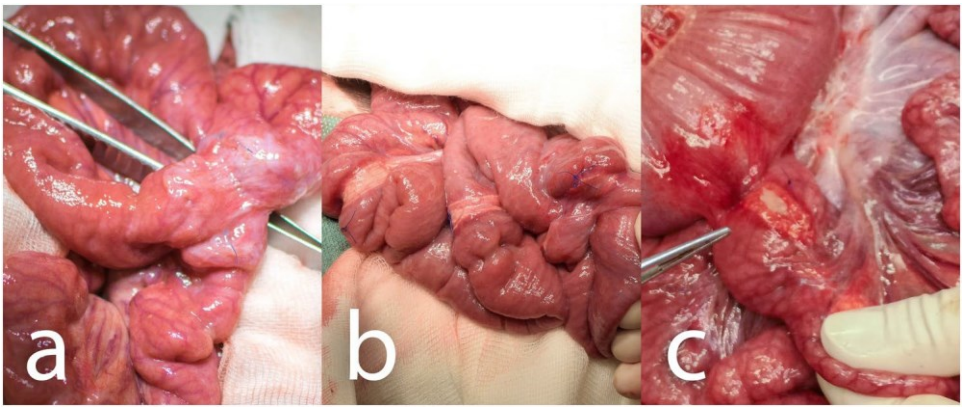

Figure 4. Macroscopic findings in animals of different groups: (**a**) Control group, two anastomoses adhered together, oral parts are marked with a blue suture; (**b**) PCL group, all three anastomoses are visible, the material is clearly visible in the site of application; (**c**) PLCL group, pointing at one of the anastomoses adhering to the colon, oral part is marked with a blue stitch.

group and in 5 animals from the PLCL group. Most of these were adhesions of the left median liver lobe to the incision scar.

The severity of PAs was largely variable within the groups. There was some amount of adhesions in almost all animals in the site of the surgery. Typically, the most adhesions were located within the area of the intestine we manipulated with, connecting the small intestine to the surrounding tissues, mostly only with the small intestine itself (Fig. 5a–c). The adhesions were relatively evenly spread within this area, not surrounding the intestinal circumference in the area of our material or suture line predominantly. The organs we did not manipulate with were usually adhesion-free. The perianastomotic adhesions were in all animals grade Zühlke 2 if present. The adhesions had to be separated by sharp dissection; no clear vascularization was macroscopically visible, though. Only one animal (from the PCL group) didn't develop any perianastomotic adhesions, this was recognized as grade Zühlke 0. The least adhesions according to our scoring system were found in the Control group, ranging from 2 points to 11 per animal (46 points for 8 animals in total), then 66 points for the group PLCL in total (4–11 points per animal) and 79 points for group PCL (0–16 points per animal). Statistical analysis showed these differences between groups as non-significant ($p = 0.715$) (Fig. 6a) (Table 1). The position of the anastomosis (first, second or third) also proved not to be a significant factor ($p = 0.490$) for the amount of adhesions. The most important parameter showed to be the segment of anastomosis while the inner segments (2 and 3) did not show a lot of adhesions, the segments 1 and 4 tended to be heavily adhered ($p<0.001$).

Almost all animals exhibited some level of dilatation of the proximal segments of the small intestine; we observed it in all 8 animals in the PLCL group, in 7 animals in the PCL group, and also in 7 animals in the Control group. Nevertheless, the difference between the groups was not statistically significant.

The material was washed out of the sections during the histological staining process. The presence of the material could be detected on the sections as an empty space surrounded by granulation tissue with a borderline of tissue permeated with empty spaces in the form of single fibers (Fig. 7). We observed no morphological abnormalities in standard histological stainings (Fig. 8), all physiological layers were present in all samples. Also the successful reepithelisation was found in all samples (Table 1). The volume fraction of von Willebrand factor positive cells (endothelial cells) did not show statistically significant differences between the groups ($p = 0.690$) (Fig. 6b), nor did the volume fractions of collagen ($p = 0.740$) (Fig. 6c) and neutrophiles with macrophages ($p = 0.550$) (Fig. 6d) (Table 1).

The section areas containing suture material exhibited significantly higher level of inflammatory cells infiltration than the stitch free sections ($p = 0.001$) (Fig. 6e).

Discussion

To the best of our knowledge, we were the first to use the PCL and PLCL nanofibrous scaffolds in this kind of application. We successfully designed a study to determine whether the material can be used for this purpose. There have been experimental works focusing on utilization of different locoregional types of protection in the site of intestinal anastomosis[9–16], yet no use of nanofibrous scaffolds has been described so far.

We found the material to be very easy to handle and to apply onto the intestine. The fact that there is no need of further fixation to the viscera is very positive as the application form can be a limiting factor when it comes to translation into the clinical practice. The fibrin glue could be an example of material that unnecessarily prolongs the surgery time as it needs to dry for 10 minutes before the surgeon can reinsert the viscera into the abdominal cavity[14,44].

We had no mortality in our study and also no major complications. There were also no clinical changes observed that would suggest development of sepsis or ileus, and the animals managed to maintain their weight; therefore we assume the material does not contribute to postoperative GI obstruction. Most patients develop an anastomotic leakage within the first 2 weeks after the surgery[45,46], we covered three postoperative weeks of observation.

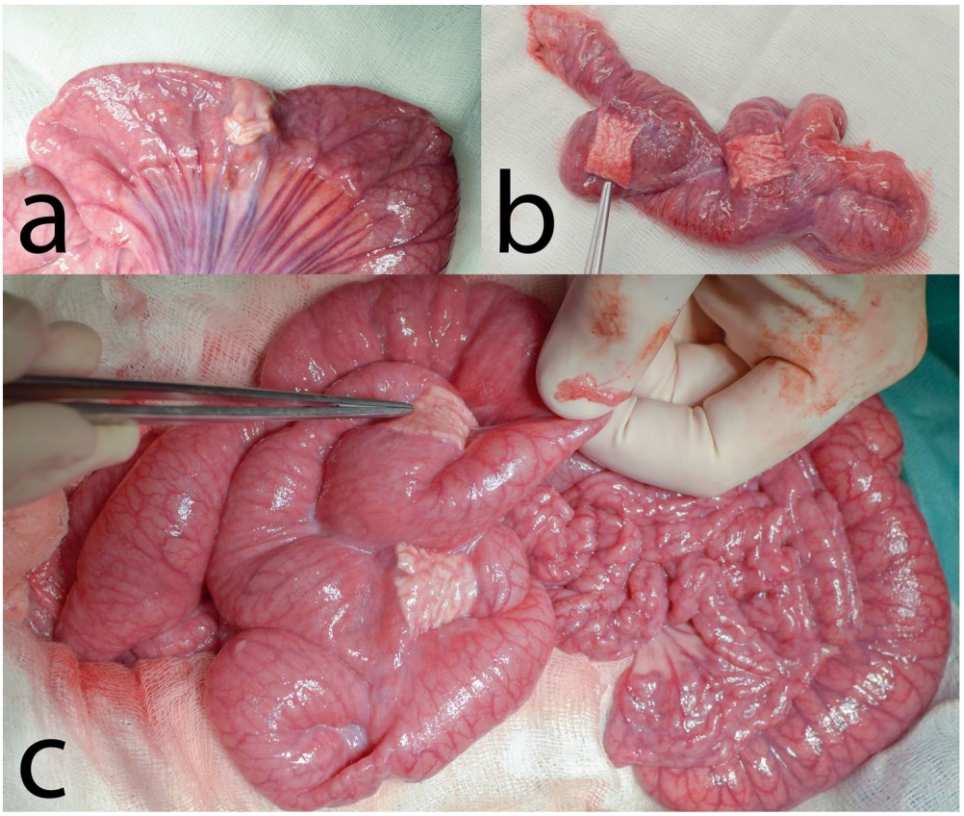

Figure 5. Anastomoses after 3 weeks: (**a**) typical appearance of the small intestine on the 21st postoperative day (PCL group); most of the intestine seems intact with no adhesions, the segments involved in anastomoses are more or less in adhesions, the diameter of the intestine is larger in the proximal segments of the intestine; the material is clearly visible and not dislocated; (**b**) severe adhesions in another animal from the PCL group; (**c**) adhesion free intestine in a different animal from the PCL group.

Nordentoft *et al*. experimented with fibrin coated collagen patches (TachoSil, fibrin sealant) in a pig model of intestinal anastomosis. Two anastomoses per animal were performed on the small intestine after a resection of 2 cm of the intestine. There were no significant differences between the experimental and the Control group in this study in terms of morbidity, mortality and sings of anastomotic leakage as well[10]. In the second study the usage of the same material on a colonic anastomosis showed notable reduction of anastomotic leakage[47]. However, when it comes to clinical use of this material, the fibrin glue does not seem to promote healing as the same authors stated in their review article including 28 studies, only 7 of which revealed a positive effect of the glue[48]. Recently, a clinical study was designed to determine the effect of TachoSil patch in human patients[12]. The study subjected the patients after resection surgery for colorectal cancer to application of the patch over the constructed anastomosis on the large intestine, but was terminated after each of the first eight patients met with complications of different severity. The study concluded that the microbiome of the anastomosis is altered negatively by covering the anastomosis with any kind of material, but did not support this hypothesis with any data.

According to macroscopic findings we can describe the anastomoses from our experiment as well healed. Moreover, we did not observe any morphological changes either in the surrounding tissues or in the whole abdominal cavity, and thus the material seems to be safe to use. The question of the degradation speed remains unanswered at this moment as the material used was always present in the place of application at the end of the experiment. This suggests the material does not have a tendency to slip away but it is also not absorbed as fast as expected. For example a complete reabsorption of the fibrin glue has been described after variable periods ranging from 7 to 20 days[14].

We used the very new *Perianastomotic adhesions amount score* we developed, which accurately describes the quantity of adhesions in the site of an anastomosis on a circular hollow viscus. Some of the systems used in clinical practice consider also the quality of the adhesions, however they evaluate the whole abdominal cavity[32,33]. We did not aim to evaluate the quality macroscopically and mechanically as we assessed the tissue histologically.

The differences in the amount of PAs between the groups were not significant, which can be due to a small size of our experimental groups. The absolute numbers suggest the material increases the amount of PAs in its' surroundings. This can be caused by easy infiltration of the material by peritoneal fibroblasts from both sides of the material because of its structure similar to extracellular matrix as Srouji described earlier[35]. There was also certain amount of adhesions involving different organs than the small intestine, but there was no clinical manifestation associated with those that we know about.

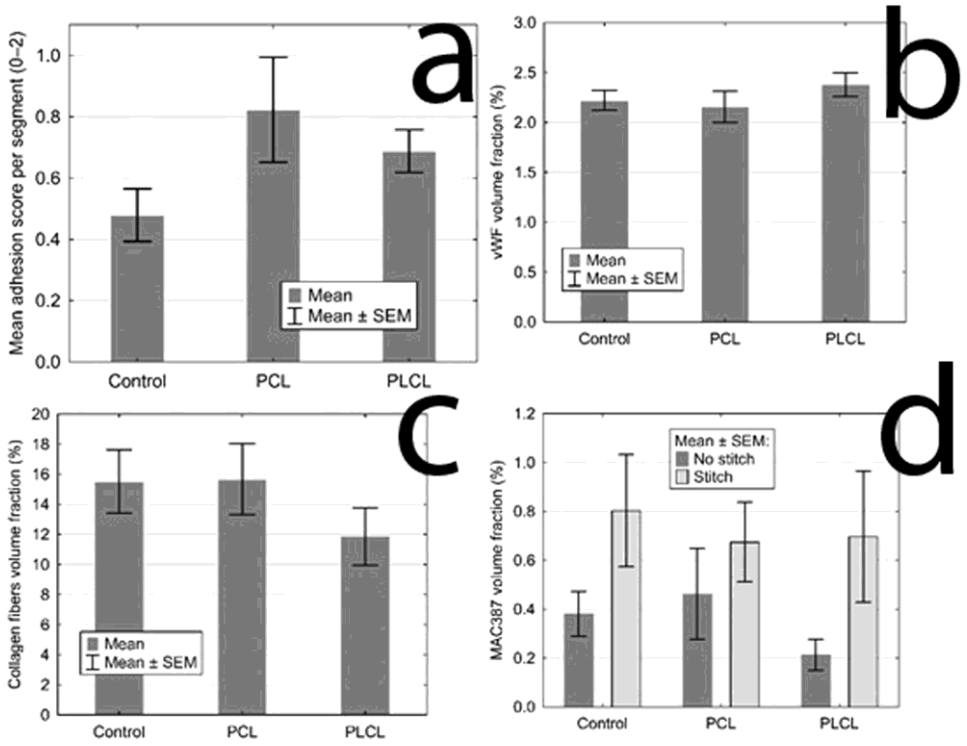

Figure 6. Statistical analysis of quantitative assessment of different parameters: (**a**) The mean adhesion score for each group, the control group scored the lowest with no statistical significance; (**b**) The volume fractions of vWF positively stained area for each groups showing the level of vascularisation, the three groups show the same quality of scar in this aspect; (**c**) The volume fractions of collagen fibres for each group, the three groups show the same quality of scar in this aspect; (**d**) The volume fractions of MAC387 positive area for each group, showing the inflammatory cells infiltration, the presence of a stitch in the section proves to be the only statistically significant factor, the three groups show the same quality of scar in this aspect as well.

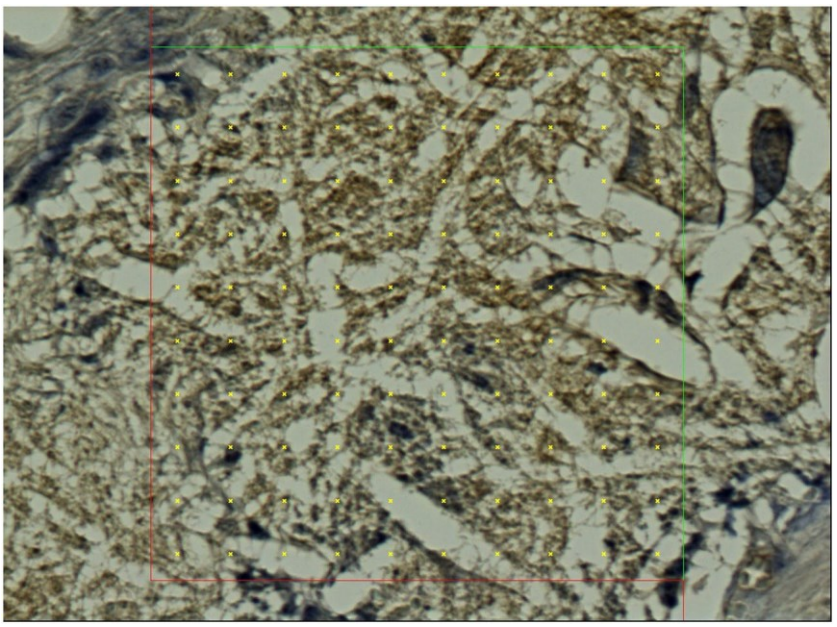

Figure 7. Histological section, PCL group, MAC387 staining: Detail of the marginal zone of the material applied, the empty spaces in the shape of the fibres (stereological grid).

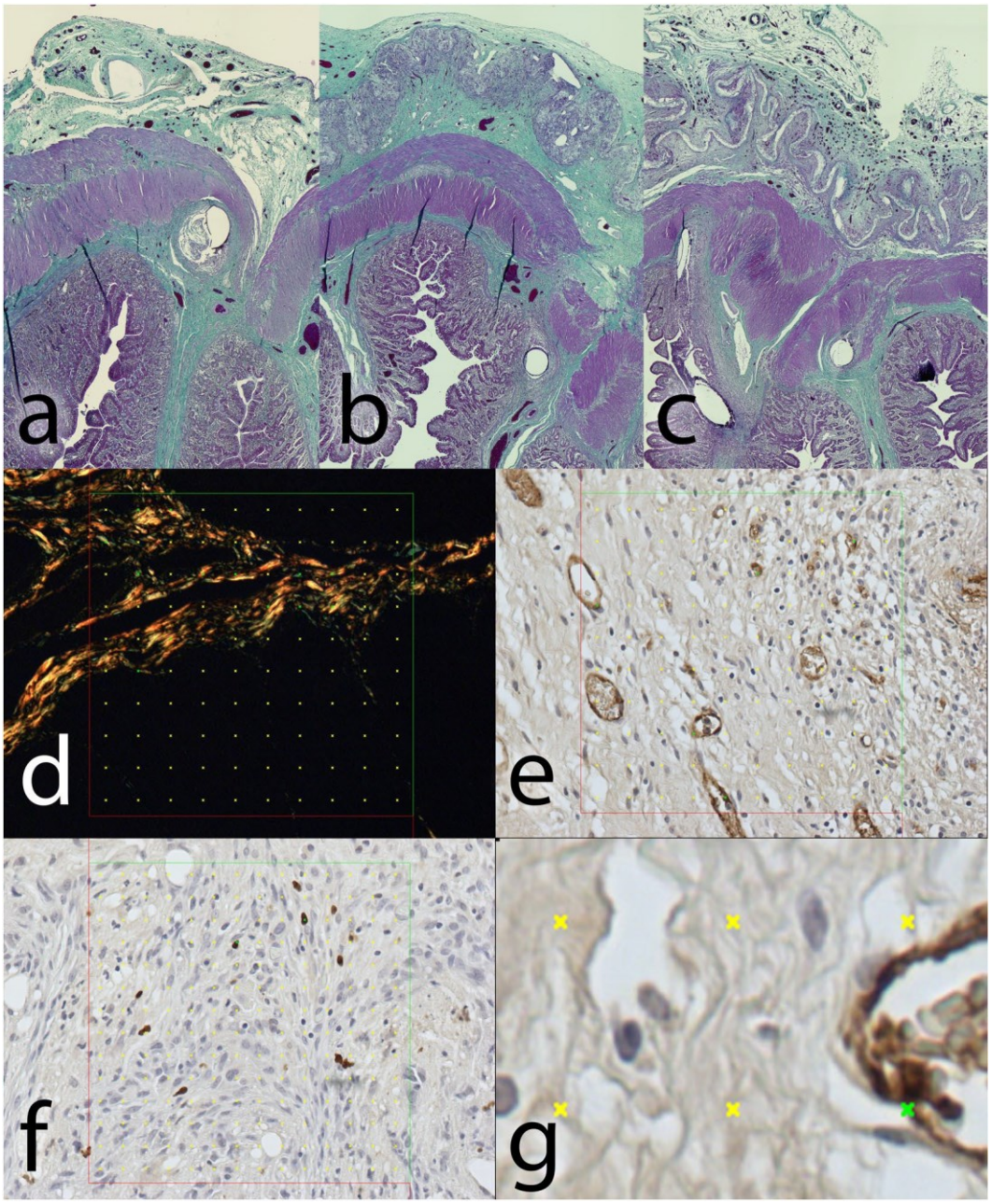

Figure 8. Histological staining of explanted anastomoses: (**a**) Green trichrome: Control group; (**b**) Green trichrome: PCL group, the empty space on the site of application of the nanomaterial can be seen in the upper layer, surrounded by normal granulation tissue; (**c**) Green trichrome: PLCL group, a much thinner empty area can be seen in the upper layer, also surrounded by normal granulation tissue; (**d**) PSR staining, collagen fibres stained yellow, stereological mesh; (**e**) vWF factor staining, the endothelial cells stained brown, stereological grid; (**f**) MAC 387 staining stereology, positive cells stained blue, stereological grid; (**g**) magnification of vWF staining stereology with a positive cross in the upper right corner.

The amount of postoperative adhesions in the peritoneal cavity has been successfully decreased both experimentally and clinically using different substances, usually in a form of gel. Hyaluronic acid based gels or also polycaprolactone based gels can serve as examples[31,49–51]; however, the influence of such materials on the anastomotic healing has not been described and therefore cannot be considered safe in our application.

A very important factor for the formation of adhesions is the material the viscera are manipulated with. Dry swabs damage the peritoneum, cause inflammation and, consequently, adhesion formation[52]. We used wet swabs throughout our experiment. The formation of adhesions should be finished by the end of the three week observation period (although their characteristic may change during the time after this period and the problems they cause can appear much later[42]. To evaluate the clinical impact of all the adhesions formed a longer observation period would be needed.

Even though the materials were dissolved during the process of histological staining, the area of application was clearly visible under a microscope as a tissue-free layer. We followed a standard system of assessment of the healing of an intestinal anastomosis described in different studies[12]. No morphological or any other statistically significant differences were found between the groups using this system. We value this result as positive since we assume that the healing process was not affected in a negative way and that the resulting scar is of the same quality as a physiologically healed one. The system does not evaluate peritoneal adhesions formation, though. As the peritoneal adhesions are certainly a source of many possible complications, their evaluation should be part of an anastomotic healing assessment.

A positive clinical effect could be more pronounced in different experimental settings. Fibrin glue, for example, has been tested in an animal model of complicated colonic anastomosis (severe blood loss, peritonitis), where it showed a positive effect in terms of decreasing morbidity and mortality in the period of 10 postoperative days[52]. The histological assessment of the scar tissue however showed no significant differences between the Control group and the Experimental group on 10th postoperative day measuring also volume fractions of collagen fibers, vWF positive cells and inflammatory reaction[52] (similarly to our results).

A baseline biopsy has not been taken as no intestine was resected. It can be considered a certain limitation of this study. No clinical nor laboratory signs of any pathologies were, however, evident in our animals and no signs of pathologies were found in the final histological specimens either.

Biocompatibility of the materials used in our study was demonstrated by the presence of the granulation tissue of normal quality (according to all measured qualities) surrounding and invading the material.

The level of biodegradation was not to be measured quantitatively as the degradation process of these nanomaterials was described in previous work[41].

All laboratory findings were within the physiological range, which suggests that the material does not cause any systemic disturbances. This was expected because the polymers used for the fabrication of the materials have been in use in clinical medicine for many years.

For more discriminating results a study on a complicated anastomosis should be performed as shown in the works of Tebala *et al.*[53], Zilling *et al.*[44] and Adas *et al.*[17].

Conclusion

We successfully demonstrated that the use of the PCL and PLCL nanofibrous scaffolds in an attempt to fortify an anastomosis on the GI tract is safe. The scaffolds did not influence the amount and quality of scar tissue in the site of anastomosis, and at the same time they did not cause any other kind of complication during our study. From the macroscopic finding they seem to slightly raise the level of adhesions in the site of application, which corresponds to the statement that they promote healing. To be able to assess the adhesion level, we developed and used a novel scoring technique. The material appears to us as a practical and versatile Supporting Material potential of which can be further enhanced for example by adding substances supporting healing like growth factors, antibiotics etc.

The large variability of settings of the fabrication process allows further changes of the material properties.

For the potentially pro-healing qualities of the material, either the PCL or PLCL will be further studied by our team and used as an inner layer of a new double layered patch with an antiadhesive external layer.

Data availability

The authors declare they will supply any existing additional data as soon as possible when requested.

Received: 31 July 2019; Accepted: 9 January 2020;
Published online: 24 January 2020

References

1. Jex, R. K., van Heerden, J. A., Wolff, B. G., Ready, R. L., Ilstrup, D. M. Gastrointestinal Anastomoses Factors Affecting Early Complications, *Ann. Surg.* Aug, **206**(2), 138–41 (1987).
2. Hyman, N., Manchester, T. L., Osler, T., Burns, B. & Cataldo, P. A. Anastomotic Leaks After Intestinal Anastomosis It's Later Than You Think. *Ann. Surg. Feb* **245**(2), 254–8 (2007).
3. Yo, L. S., Consten, E. C., Quarles van Ufford, H. M., Gooszen, H. G. & Gagner, M. Buttressing of the staple line in gastrointestinal anastomoses: overview of new technology designed to reduce perioperative complications. *Dig. Surg.* **23**(5-6), 283–91 (2006).
4. van Rooijen, S. J. *et al.* Definition of colorectal anastomotic leakage: A consensus survey among Dutch and Chinese colorectal surgeons. *World J. Gastroenterol.* **23**(33), 6172–6180 (2017).
5. Slieker, J. C., Daams, F., Mulder, I. M., Jeekel, J. & Lange, J. F. Systematic review of the technique of colorectal anastomosis. *JAMA Surg.* **148**(2), 190–201 (2013).
6. Golub, R., Golub, R. W., Cantu, R. Jr. & Stein, H. D. A multivariate analysis of factors contributing to leakage of intestinal anastomoses. *J. Am. Coll. Surg.* **184**(4), 364–72 (1997).
7. Pommergaard, H. C. *et al.* Preoperative risk factors for anastomotic leakage after resection for colorectal cancer: a systematic review and meta-analysis. *Colorectal Dis.* **16**(9), 662–71 (2014).
8. Boersema, G. S. A. *et al.* Hyperbaric oxygen therapy improves colorectal anastomotic healing. *Int. J. Colorectal Dis.* **31**, 1031–1038 (2016).
9. Khorshidi, H. R. *et al.* Evaluation of the effectiveness of sodium hyaluronate, sesame oil, honey, and silver nanoparticles in preventing postoperative surgical adhesion formation. An experimental study. *Acta Cir. Bras.* **32**(8), 626–632 (2017).
10. Nordentoft, T., Rømer, J. & Sørensen, M. Sealing of gastrointestinal anastomoses with a fibrin glue-coated collagen patch: a safety study. *J. Invest. Surg.* **20**(6), 363–9 (2007).
11. Nordentoft, T. & Holte, K. Preventing Clinical Leakage of Colonic Anastomoses with A Fibrin - Coated Collagen Patch Sealing - An Experimental Study. *Arch Clin Exp Surg.* **3**(4), 201–206.
12. Trotter, J. *et al.* (2018) The use of a novel adhesive tissue patch as an aid to anastomotic healing. *Ann. R. Coll. Surg. Engl.* **100**(3), 230–234 (2014).
13. Aznan, M. I. *et al.* Effect of Tualang honey on the anastomotic wound healing in large bowel anastomosis in rats-A randomized controlled trial. *BMC Complement. Altern. Med.* **23**, 16–28 (2016).

14. Bonanomi, G., Prince, J. M., McSteen, F., Schauer, P. R. & Hamad, G. G. Sealing effect of fibrin glue on the healing of gastrointestinal anastomoses: implications for the endoscopic treatment of leaks. *Surg. Endosc.* **18**(11), 1620–4 (2004).
15. Fajardo, D. A., Amador-Ortiz, C., Chun, J., Stewart, D. & Fleshman, J. W. Evaluation of Bioabsorbable Seamguard for Staple Line Reinforcement in Stapled Rectal Anastomoses. *Surg. Innov.* **19**(3), 288–94 (2012).
16. Boersema, G. S. A. *et al*. Reinforcement of the colon anastomosis with cyanoacrylate glue: a porcine model. *J. Surg. Res.* **217**, 84–91 (2017).
17. Adas, G. *et al*. Treatment of ischemic colonic anastomoses with systemic transplanted bone marrow derived mesenchymal stem cells. *Eur. Rev. Med. Pharmacol. Sci.* **17**(17), 2275–85 (2013).
18. Hirst, N. A. *et al*. Systematic review of methods to predict and detect anastomotic leakage in colorectal surgery. *Colorectal Dis.* **16**(2), 95–109 (2014).
19. Mileski, W. J., Joehl, R. J., Rege, R. V. & Nahrwold, D. L. Treatment of anastomotic leakage following low anterior colon resection. *Arch. Surg.* **123**(8), 968–71 (1988).
20. Sevim, Y., Celik, S. U., Yavarifar, H. & Akyol, C. Minimally invasive management of anastomotic leaks in colorectal surgery. *World J. Gastrointest. Surg. 27* **8**(9), 621–626 (2016).
21. Chadi, S. A. *et al*. Emerging Trends in the Etiology, Prevention, and Treatment of Gastrointestinal Anastomotic Leakage. *J. Gastrointest. Surg.* **20**(12), 2035–2051 (2016).
22. Thomas, M. S. & Margolin, D. A. Management of Colorectal Anastomotic Leak. *Clin. Colon. Rectal Surg.* **29**(2), 138–44 (2016).
23. Blumetti, J. & Abcarian, H. Management of low colorectal anastomotic leak: Preserving the anastomosis. *World J. Gastrointest. Surg. 27* **7**(12), 378–83 (2015).
24. Gessler, B., Eriksson, O. & Angenete, E. Diagnosis, treatment, and consequences of anastomotic leakage in colorectal surgery. *Int. J. Colorectal Dis.* **32**(4), 549–556 (2017).
25. Paliogiannis, P. *et al*. Conservative management of minor anastomotic leakage after open elective colorectal surgery. *Ann. Ital. Chir.* **83**(1), 25–8 (2012).
26. Zhao, R., Li, K., Shen, C. & Zheng, S. The outcome of conservative treatment for anastomotic leakage after surgical repair of esophageal atresia. *J. Pediatr. Surg.* **46**(12), 2274–8 (2011).
27. Beyene, R. T., Kavalukas, S. L. & Barbul, A. Intra-abdominal adhesions. Anatomy, physiology, pathophysiology, and treatment. *Curr. Probl. Surg.* **52**(7), 271–319 (2015).
28. Diamond, M. P. & Freeman, M. L. Clinical implications of postsurgical adhesions. *Hum. Reprod. Update.* **7**(6), 567–76 (2001).
29. van Goor, H. Consequences and complications of peritoneal adhesions. *Colorectal Dis.* **9**(Suppl 2), 25–34 (2007).
30. Ellis, H. The clinical significance of adhesions: focus on intestinal obstruction. *Eur. J. Surg. Suppl.* **577**, 5–9 (1997).
31. Ditzel, M. *et al*. Postoperative adhesion prevention with a new barrier: an experimental study. *Eur. Surg. Res.* **48**(4), 187–93 (2012).
32. Coccolini, F. *et al*. Peritoneal adhesion index (PAI): proposal of a score for the "ignored iceberg" of medicine and surgery. World J. Emerg. Surg. 31;8(1):6 (2013).
33. Zühlke, H. V., Lorenz, E. M., Straub, E. M. & Savvas, V. Pathophysiology and classification of adhesions. *Langenbecks Arch. Chir. Suppl. II Verh. Dtsch. Ges. Chir.* **1990**, 1009–16 (1990).
34. Nair, S. K., Bhat, I. K. & Aurora, A. L. Role of proteolytic enzyme in the prevention of postoperative intraperitoneal adhesions. *Arch Surg.* **108**(6), 849–53 (1974).
35. Srouji, S., Kizhner, T., Suss-Tobi, E., Livne, E. & Zussman, E. 3-D Nanofibrous electrospun multilayered construct is an alternative ECM mimicking scaffold. *J. Mater. Sci. Mater Med.* **19**(3), 1249–55 (2008).
36. Yu, M. *et al*. Recent advances in needleless electrospinning of ultrathin fibers: From academia to industrial production. *Marcomol. Mater. Eng.* **1**, 1–19 (2017).
37. Pokorny, P. *et al*. Effective AC needleless and collectorless electrospinning for yarn production. *Phys. Chem. Chem Phys.* **16**(48), 26816–22 (2014).
38. Dahlin, R. L., Kasper, F. K. & Mikos, A. G. Polymeric nanofibers in tissue engineering. *Tissue Eng. Part. B Rev.* **17**(5), 349–64 (2011).
39. Krchova, S. *et al*. Nanofibers for the wound healing. *Czech Dermatology.* **4**, 234–240 (2014).
40. Yalcin, I. *et al*. Design of polycaprolactone vascular grafts. *J. Ind. Text.* **45**, 1–21 (2014).
41. Horakova, J. *et al*. The effect of ethylene oxide sterilization on electrospun vascular grafts made from biodegradable polyesters. *Mater. Sci. Eng. C. Mater Biol. Appl.* **1**(92), 132–142 (2018).
42. Williams, D. L. & Browder, I. W. Murine models of intestinal anastomoses. In: DiPietro, L. A. & Burns, A. L., (ed) *Wound healing: Methods and protocols*., vol. 10, 1st ed. New Jersey: Humana Press Inc., pp 133–140 (2010).
43. Gunatillake, P. A. & Adhikari, R. Biodegradable synthetic polymers for tissue engineering. *Eur. Cell Mater.* **5**, 1–16 (2003).
44. Zilling, T. L., Jansson, O., Walther, B. S. & Ottosson, A. Sutureless small bowel anastomoses: experimental study in pigs. *Eur. J. Surg.* **165**(1), 61–8 (1999).
45. Li, Y. W. *et al*. Very Early Colorectal Anastomotic Leakage within 5 Post-operative Days: a More Severe Subtype Needs Relaparatomy. *Sci. Rep.* **7**, 39936 (2017).
46. Kosmidis, C. *et al*. Myofibroblasts and colonic anastomosis healing in Wistar rats. *BMC Surg.* **11**, 6 (2011).
47. Nordentoft, T. & Sørensen, M. Leakage of Colon Anastomoses: Development of an Experimental Model in Pigs. *Eur. Surg. Res.* **39**, 14–16 (2007).
48. Nordentoft, T., Pommergaard, H. C., Rosenberg, J. & Achiam, M. P. Fibrin glue does not improve healing of gastrointestinal anastomoses: a systematic review. *Eur. Surg. Res.* **54**(1-2), 1–13 (2015).
49. Gao, X. *et al*. Novel thermosensitive hydrogel for preventing formation of abdominal adhesions. **8**, 2453–63 (2013).
50. Caglayan, E. K., Caglayan, K., Erdogan, N., Cinar, H. & Güngör, B. Preventing intraperitoneal adhesions with ethyl pyruvate and hyaluronic acid/carboxymethylcellulose: a comparative study in an experimental model. *Eur. J. Obstet. Gynecol. Reprod. Biol.* **181**, 1–5 (2014).
51. Kataria, H. & Singh, V. P. Liquid Paraffin vs Hyaluronic Acid in Preventing Intraperitoneal Adhesions. *Indian. J. Surg.* **79**(6), 539–543 (2017).
52. Arung, W., Meurisse, M. & Detry, O. Pathophysiology and prevention of postoperative peritoneal adhesions. *World J. Gastroenterol.* **17**(41), 4545–4553 (2011).
53. Tebala, G. D., Ceriati, F., Ceriati, E., Vecchioli, A. & Nori, S. The use of cyanoacrylate tissue adhesive in high-risk intestinal anastomoses. *Surg. Today.* **25**(12), 1069–72 (1995).

Acknowledgements

This study was supported by the Centrum of Clinical and Experimental liver surgery (UNCE/MED/006), the National Sustainability Program I (NPU I) Nr. LO1503 provided by the Ministry of Education Youth and Sports of the Czech Republic (V.L.).

Author contributions

J. Rosendorf: Acquisition of data, Analysis and interpretation of data, Drafting of manuscript, J. Horakova: Study conception and design, Critical revision of manuscript, M. Klicova: Study conception and design, Critical revision of manuscript, R. Palek: Acquisition of data, L. Cervenkova: Acquisition of data, Analysis and interpretation of data, Drafting of manuscript, T. Kural: Acquisition of data, P. Hosek: Analysis and interpretation of data, Drafting of manuscript, T. Kriz: Acquisition of data, V. Tegl: Acquisition of data, V. Moulisova: Analysis and interpretation of data, Critical revision of manuscript, Z. Tonar: Critical revision of manuscript, V. Treska: Critical revision of manuscript D. Lukas: Study conception and design, V. Liska: Study conception and design, Critical revision of manuscript.

Competing interests

All authors certify they have no affiliations with or involvement in any organization or entity with any financial interest or non-financial interest in the subject of matter or materials in this manuscript.

Additional information

Supplementary information is available for this paper at https://doi.org/10.1038/s41598-020-58113-4.

Correspondence and requests for materials should be addressed to J.R.

Reprints and permissions information is available at www.nature.com/reprints.

Publisher's note Springer Nature remains neutral with regard to jurisdictional claims in published maps and institutional affiliations.

11.4 Supplement IV

Kural, T., Grajciarová, M., Rosendorf, J., Pálek, R., Červenková, L., Malečková, A., Šarčevic, S., Liška, V., Tonar, Z. Histological mapping of healing of the small and large intestine - A quantitative study in a porcine model. Ann Anat. 2023 Apr 1;249:152095. doi: 10.1016/j.aanat.2023.152095.

$IF_{(JCR2021)}$ = 2.976. Q1 (Anatomy&Morphology)

https://pubmed.ncbi.nlm.nih.gov/37011825/

Annals of Anatomy 249 (2023) 152095

Contents lists available at ScienceDirect

Annals of Anatomy

journal homepage: www.elsevier.com/locate/aanat

RESEARCH ARTICLE

Histological mapping of healing of the small and large intestine – A quantitative study in a porcine model

Tomáš Kural [a,b,c], Martina Grajciarová [a,b], Jáchym Rosendorf [b,d], Richard Pálek [b,d], Lenka Červenková [b,e], Anna Malečková [a,b], Sima Šarčevic [b,d], Václav Liška [b,d], Zbyněk Tonar [a,b,*]

[a] Department of Histology and Embryology, Faculty of Medicine in Pilsen, Charles University, alej Svobody 76, 323 00 Pilsen, Czech Republic
[b] Biomedical Center, Faculty of Medicine in Pilsen, Charles University, alej Svobody 76, 323 00 Pilsen, Czech Republic
[c] Arberlandklinik Viechtach, Department of General and Visceral Surgery, Karl-Gareis-Straße 31, 942 34 Viechtach, Germany
[d] Department of Surgery, Faculty of Medicine in Pilsen, Charles University, alej Svobody 76, 323 00 Pilsen, Czech Republic
[e] Department of Pathology, Third Faculty of Medicine, Charles University, Ruská 87, 100 00 Prague, Czech Republic

article info

Article history:
Received 12 January 2023
Received in revised form 2 March 2023
Accepted 22 March 2023
Available online 1 April 2023

Keywords:
Anastomosis
Experimental surgery
Histology
Pig
Small intestine
Large intestine
Stereology

abstract

Background: Gastrointestinal anastomoses are performed in many patients every year. The pathogenesis of aberrant anastomotic healing and the causes of intestinal leakage are not fully understood. The present study gathered and critically evaluated histological quantitative data to deepen current knowledge of anastomotic healing in the small and large intestine and its complications and outline the options for further experimental in vivo research in large porcine animal models.

Methods: Three groups of porcine intestinal anastomoses were compared: small intestine without defect (SI; n = 7), small intestine with an additional defect (SID; n = 8), and large intestine (LI; n = 7). Multilevel sampling (2112 micrographs) and stereological methods were used for histological quantification of proliferation (Ki-67 immunohistochemistry), neutrophil infiltration (myeloperoxidase staining), vascularity (von Willebrand factor) and type I and type III collagen formation (picrosirius red in polarized light) within the region of anastomosis compared to the region outside of anastomosis.

Results: Quantitative histological evaluation revealed the following results. i) Proliferation, vascularity, and collagen, but not neutrophils, were more highly expressed within the anastomosis than outside of the anastomosis region. ii) Porcine large and small intestine were not interchangeable based on histological evaluation of surgical experiments. The presence or absence of an additional experimental defect strongly affected healing, but the healing seemed complete after 21 days. iii) The microscopic structure of small intestine segments was more affected by their proximity to the anastomosis than the structure of large intestine segments.

Conclusions: Histological quantification was more laborious than the previously used semiquantitative scoring system evaluating the healing rate of intestinal anastomoses, but it provided detailed maps of biological processes within individual intestine layers. The primary data collected in the study are open and available for power sample analyses to calculate the minimum numbers of samples justified in future experiments on porcine intestines. The porcine intestine is a promising animal model with translational potential for human surgery.

1. Introduction

1.1. Gastrointestinal anastomoses and leaks

Gastrointestinal anastomoses are performed in thousands of patients annually. However, we do not fully understand the pathogenesis of aberrant anastomotic healing and the causes of intestinal leakage even after a century of research (Binnebösel et al., 2014; Wu et al., 2013). Failure of a gastrointestinal anastomosis leads to

* Correspondence to: Department of Histology and Embryology and Biomedical Center, Faculty of Medicine in Pilsen, Charles University, alej Svobody 76, 323 00 Pilsen, Czech Republic.
E-mail address: tonar@lfp.cuni.cz (Z. Tonar).

https://doi.org/10.1016/j.aanat.2023.152095
0940-9602/

leakage, dehiscence and fistulas, which are major complications after abdominal surgery (Kosmidis et al., 2011). Although the surgical technique has continuously improved, the described incidence of gastrointestinal anastomosis leakage ranges from 2 % to 10 % and is related to increased morbidity (20–30 %) and mortality (7–12 %) (Testini et al., 2014; Rosendorf et al., 2022).

Several risk factors and mechanisms contribute to the occurrence of anastomotic leakage, and the most important are ischemia and technical failure (Testini et al., 2014). Anastomotic leaks are predominantly observed in patients undergoing surgery in high-risk regions of the gastrointestinal tract, such as the rectum and esophagus. Because the anastomotic leak rate in these areas may be excessive (30–40 %), surgeons routinely perform a protective diverting stoma to diminish the risk of intestinal content discharge. This practice necessitates a second operation for closure of the stoma, which itself brings substantial morbidity and increases the risk of anastomotic failure. Therefore, many surgeons and patients choose to leave the stoma as a permanent solution to avoid a second high-risk surgery. Surgeons have accepted that the exact mechanisms of anastomotic failure remain unknown, and anastomotic leaks are at least partially not preventable. There is insufficient motivation for some surgeons to eliminate the routine use of a diverting stoma in lower colorectal surgery (Shogan et al., 2015). However, algorithms are being developed for the early post-operative diagnosis of anastomotic leaks (Jongen et al., 2016).

1.2. Mechanisms of healing and anastomotic failure in intestine layers

A complex and organized cascade of biochemical and cellular events must occur for anastomotic healing (Shaper et al., 2001). The stages of anastomotic healing (Brunicardi et al., 2015) are summarized in Table 1 and were used to justify the choice of parameters for histological quantification. Intestinal anastomotic healing is characterized by a temporary loss of collagen and a transient reduction in intestinal strength (de Roy van Zuidewijn et al., 1986). Submucosal collagen in important for colonic anastomotic integrity (Krarup et al., 2013). Balance in collagen formation and remodeling is crucial for the integrity of the anastomosis, and leakage occurs when lysis prevails over collagen synthesis over time (Hesp et al., 1985). Cyclooxygenase-2 induces prostaglandin E2 formation, and it is a key enzyme in anastomotic healing (Reisinger et al., 2017). Although the healing process is highly similar in all parts of the gastrointestinal tract, the mucosa and serosa are the only layers of the intestinal wall where healing occurs without the formation of scar tissue (Brunicardi et al., 2015).

The functional tunica mucosa facilitates the healing of colonic anastomoses (Bosmans et al., 2017a). Higher rates of anastomotic failure in extraperitoneal parts of the gastrointestinal tract (e.g., esophagus, duodenum or lower third of rectum) were observed in several studies that showed the importance of the serosa in gastrointestinal healing (Brunicardi et al., 2015; Thornton and Barbul, 1997). Correct surgical performance of the suture is crucial for the early integrity of the intestinal anastomosis. Another important feature is good serosal apposition to create optimal conditions for the formation of a watertight fibrin seal on the serosal surface, which minimizes the risk of leakage. This feature is best achieved using an inverting suture technique (Kosmidis et al., 2011; Thornton and Barbul, 1997). However, we did not find any quantitative histological mapping of the microscopic structure of the healing of intestinal anastomoses in large animal models, such as pigs. These studies would help clarify the biological processes that lead to anastomotic leakage and provide starting points for potential preventive interventions (Bosmans et al., 2015).

Table 1
Stages of anastomosis healing according to Brunicardi et al. (2015). The phases overlap in time. Data from previously published studies were used to justify the parameters quantified in the present study.

Phase 1 - Hemostasis and inflammation (from injury to day 3):
Hemostasis precedes and initiates inflammation, which ensures release of chemotactic factors from the wound site. The fibrin clot helps hemostasis and acts as scaffolding for the migration of monocytes and neutrophils into the wound (Braskén, 1991).
Neutrophils colonize the wound 3 h post-injury and peak in number after 12–24 h (Dovi et al., 2003); fibroblasts invade after approx. 48 h (Kivisaari et al., 1975); macrophages are abundant in the wound by 48–96 h post-injury.
Local vasodilation and edema of the intestinal wall in the anastomotic area, especially in the rich submucosal vascular plexus.
Lactate from the initial hypoxia and the oxidative burst of white blood cells (Trabold et al., 2003) stimulates angiogenesis and mitosis via macrophages (Jensen et al., 1986).
Contraction of villi as the first phase of mucosal repair (Blikslager et al., 1997; Moore et al., 1989). Epithelial crawling in the direction of restitution toward the denuded basement membrane initiates the mucosal repair (Dignass et al., 1994).
Enterocytes are exposed to components of the extracellular matrix (fibronectin and laminin) and stimulated by cytokines and growth factors secreted by monocytes (Brunicardi et al., 2015).
Phase 2 - Proliferation (from day 3 to day 14):
Early epithelial restoration of tight junctions between the individual cells re-establishes the mucosal barrier function (Blikslager et al., 1997).
The postoperative edema disappears until day 7 (Braskén, 1991).
Tissue continuity is restored mostly by proliferating and matrix-producing fibroblasts (Brunicardi et al., 2015; Jensen et al., 1986).
Macrophages and fibroblasts produce angiogenic factors (Brunicardi et al., 2015; Clark, 1989). Sufficient oxygen and nutrients supply is necessary for the cell proliferation and matrix synthesis (Hussain et al., 1989). New capillaries may be observed from the third postoperative day (Braskén, 1991).
Type III fibrillar collagen produced from day 3 provides supportive scaffolding for cells and blood vessels in the submucosa, anastomotic line and serosa. Smooth muscle cells and myofibroblasts also synthesize collagen (Brunicardi et al., 2015; Nakamura et al., 2016). Type I collagen production starts at the end of week 1 (Brunicardi et al., 2015).
Myofibroblasts are expressing smooth muscle actin (Darby et al., 1990) and start to contribute to wound contraction between days 7–15 (Darby et al., 1990).
Smooth muscle cells from mesenchymal cells are reestablishing the muscularis layer (Thornton and Barbul, 1997).
Phase 3 - Maturation and remodeling (from day 14 onward):
Collagen level reaches a plateau, but its mechanical strength continues to grow for several more months due to cross-linking (Brunicardi F, 2015;Aznan et al., 2016).
Myofibroblasts undergo apoptosis within the maturing wound (Desmoulière et al., 1995).
Type I collagen starts to prevail, and metalloproteinases, hyaluronidase and the plasminogen activator-plasmin system balance its maturation via collagenolysis (Clark, 1989).
Prolonged presence of neutrophils in the wound delays closure (Dovi et al., 2003).
Macrophages control the local angiogenesis, matrix and collagen synthesis and remodeling by releasing several growth factors and cytokines (Clark, 1989; Feiken et al., 1995).
Number of fibroblasts and blood vessels in the submucosa remains greater than in normal colon (Braskén, 1991).

1.3. Animal models with standardized anastomoses in the small and large intestine

Rodents and rabbits are prominent models in gastrointestinal tract research, including the testing of bioengineered materials, tissue adhesives or the application and injection of enemas that support the healing and strengthening anastomoses (Bosmans et al., 2017a; b; Aznan et al., 2016; Hesp et al., 1985; Kralovic et al., 2022; Krarup et al., 2017; Vakalopoulos et al., 2017). However, the potential of small animal models for translational medicine is limited due to the different sizes, surgical techniques and instruments used in human surgery (Lossi et al., 2016). Therefore, the use of pigs as a large animal model has become more popular due to its anatomical, physiological and genetic comparability to humans (Boersema et al.,

2017; Bonanomi et al., 2004; Nordentoft, 2015). The microscopic structures of the swine and human intestinal walls are very similar, but the intestinal microflorae are different (Zhang et al., 2013). Bosmans et al. (2016) provided a thorough comparison of the pros and cons of the use of animal models for research on anastomoses in the lower gastrointestinal tract.

There are considerable differences in structure, function and microbiome of large intestine between herbivores and omnivores (including humans) (Froidurot and Julliand, 2022). In herbivores, proximal vs. distal colonic regions show different motor patters (Costa et al., 2021). Omnivores usually lack clearly defined anatomical differences between their colonic regions (Costa et al., 2021). The segmentation pattern of the porcine intestine corresponds to an omnivorous species, which makes the species suitable for investigations of healing differences between the small and large intestines. The combination of bacterial contamination and trauma at the site of the anastomosis may lead to thrombosis of the marginal vessels (Cohn and Rives, 1955). Angiographic studies on the degree of vascularization in large and small intestine anastomoses showed a comparable extent of angiogenesis in both types of healing anastomoses (Hesp et al., 1985). There is a significant difference in the speed of small and large intestine mucosal repair. Mucosal repair in the rabbit ileum is complete 7 days after surgery, but mucosal repair and tissue necrosis remain apparent in the colon at that time (Hesp et al., 1985).

1.4. Aims and hypotheses of the present study

Previous studies (Rosendorf et al., 2020, 2021a, 2021b) evaluated samples of the small intestine with an additional artificial defect (SID) and the large intestine with a defect (LID) using semi-quantitative and quantitative scoring systems (e.g., fractions of total collagen, volume fraction of vWF-positive cells and MAC387-positive cells). As the spontaneous healing in young and healthy animals was mostly without any complications that should have been modeled (Rosendorf et al., 2020, 2021a, 2021b), the authors mimicked intestinal leakage observed in human intestine by adding standardized artificial defects to the intestine made with a 7.5 mm diameter draining tube on the antimesenteric side of the anastomosis. The scoring systems used by Rosendorf et al., (2020, 2021a, 2021b) focused on the entire thickness of the intestinal wall, except the mucosa. Our study quantitatively evaluated the individual layers of the intestine and the mucosa in more detail. Semiquantitative scoring was found to be fast, reliable and reproducible (Rosendorf et al., 2020, 2021a, 2021b). However, it considered the entire intestinal wall as a single region of interest. Therefore, this scoring contained no information on the spatial distribution of biological processes, such as leukocyte infiltration, vascularity, and collagen synthesis, within individual intestinal layers.

The present study gathered and critically evaluated histological quantitative data to deepen current knowledge of anastomotic healing in the small and large intestines and its complications and outlined the options for further experimental in vivo research in animal models. We aimed to answer the following questions, which to our knowledge have not been published in a large animal model of intestinal anastomosis healing. The questions are formulated as three (A-C) testable null hypotheses (H_0):

H_0(A): There is no significant difference in proliferation, neutrophilic infiltration, vascularity and collagen formation between the anastomosis and the area outside of the anastomosis.

H_0(B): There is no significant difference in proliferation, neutrophilic infiltration, vascularity and collagen formation between small intestinal anastomosis without a standardized defect (SI), anastomosis in SID, and anastomosis in LID.

H0(C): There are similar correlation patterns in proliferation, neutrophilic infiltration, vascularity and collagen formation between the anastomosis and the area outside of the anastomosis in SI, SID, or LID.

2. Material and methods

2.1. Collection of porcine small and large intestine segments

All paraffin-embedded archived tissue blocks (n = 22) of porcine small and large intestines were obtained from previous studies (Rosendorf et al., 2020, 2021a, 2021b). No animals were sacrificed for the purpose of the present study. Intestinal samples were taken from 12 female and 10 male Prestice Black-Pied pigs aged 12–14 weeks and weighing 24–48 kg. The animal samples were obtained from a project verifying the effect of various nanofibrous structures on the formation of adhesions and healing of resected surfaces and anastomoses. Project No. MSMT-26570/2017–2 was approved by the local ethical authority and the Faculty Committee for the Prevention of Cruelty to Animals. The complete surgical procedure can be found in Rosendorf et al. (2020, 2021a, 2021b). Briefly, transection of the small intestine (SI group: three anastomoses per animal, 70, 90 and 110 cm aborally from the duodeno-jejunal junction; SID group: one anastomosis per animal, 70 cm aborally from the duodeno-jejunal junction) or colon (LID group, approx. 20 cm from the anus) was done. Soft intestinal clamps were used to prevent solid intestinal contents from contaminating the abdominal cavity. The two ends of the transected intestine were cleaned using wet cotton balls. A hand-sewn end-to-end anastomosis was constructed using in the same way as in human patients, i.e., the standard seromuscular running suture (glyconate monofilament 4/0 suture line; Monocryl 4/0, B. Braun Medical s.r.o., Prague, Czech Republic). As mentioned in 1.4, a 7.5 mm-large defect was intentionally left on the antimesenteric side of the anastomosis, simulating a technical fault in two of the three study groups. The postoperative period was without complications, and the pigs were euthanized 21 days after surgery. The samples were divided into 3 groups: a small intestine without a defect (n = 7; control group), a small intestine with a defect (n = 8) and a large intestine with a defect (n = 7). Because Rosendorf et al. (2021a, 2021b) suggested that porcine intestinal anastomoses heal very smoothly and rapidly without additional defects, additional defects were introduced on the antimesenteric side of the anastomosis (7.5 mm diameter) in the SID and LID groups to simulate difficult healing in the human intestine.

2.2. Histological processing and microphotographs

All of the archived paraffin tissue blocks (n = 22) of small and large intestinal samples were cut into 4 µm-thick sections (Leica RM2255 microtome), and these sections were deparaffinized, dehydrated and stained using one histological staining method and three immunohistochemical reactions using Bond RXm autostainer (Leica Biosystems Melbourne Pty Ltd., Melbourne, Australia) using BOND Polymer Refine Detection (see Table 2 for details).

Microphotographs were taken using systematic uniform sampling of the intestinal submucosa, muscularis and subserosa within two regions of interest (ROI), within the anastomosis and outside of the anastomosis (Table 2) (Fig. 1A). The sampling strategy was previously optimized in a pilot study by Kolinko et al. (2021). The anastomosis ROI was defined as the submucosa, muscularis, and subserosa layers of the intestinal wall 3 mm orally and aborally from the center of the anastomosis. The center of the anastomosis was defined as the site of visible suture on the specimen. For specimens with visible disruption of the continuity of the muscle layer or pseudodiverticulum, the anastomosis area was defined as 2 mm

Table 2
Histological staining methods and quantitative parameters. The combination of one histological staining method and three immunohistochemical reactions was used to evaluate the microscopic structures of the individual layers of the intestinal wall. Microphotographs were taken in a systematic, uniform and random manner.

Quantitative parameter (unit)	Staining	Biological significance	Evaluated areas	Objective	Photographs taken
Proliferation index (%)	Immunohistochemistry with an anti-Ki67 antibody (Clone MIB-1, Ready to use, DakoCytomation, Glostrup, Denmark); pretreatment Bond Epitope Retrieval Solution 1 (Leica Biosystems, Newcastle upon Tyne, UK); nuclei counterstained with hematoxylin	The ratio of Ki67-positive nuclei to all nuclei in the reference area.	Individually submucosa, muscularis, subserosa	40x	4
V_V (neutrophils) (-)	Immunohistochemistry with an anti-myeloperoxidase antibody (1:600 dilution, DakoCytomation, Glostrup, Denmark), pretreatment Bond Epitope Retrieval Solution 2 (Leica Biosystems, Newcastle upon Tyne, UK); nuclei counterstained with hematoxylin	The volume fraction of neutrophils. Occasional positivity in lysosomes of monocytes was not considered in our study.	Individually submucosa, muscularis, subserosa	40x	4
Q_A (vascular profiles) (mm^{-2})	Immunohistochemistry with an anti-von Willebrand factor antibody (A 0082, 1:1000 dilution, DakoCytomation, Glostrup, Denmark), pretreatment Bond Epitope Retrieval Solution 2 (Leica Biosystems, Newcastle upon Tyne, UK; nuclei counterstained with hematoxylin	The quantity of vascular profiles per section area.	Individually submucosa, muscularis, subserosa	40x	4
V_V (type I collagen) (-)	Picrosirius red	The volume fraction of type I collagen (yellow-red color under polarized light)	Individually submucosa, muscularis, subserosa	40x	4
V_V (type III collagen) (-)	Picrosirius red	The volume fraction of type III collagen (green color under polarized light)	Individually submucosa, muscularis, subserosa	40x	4

orally and aborally from the edges of the defect (Rosendorf et al., 2020, 2021a, 2021b). To evaluate the proliferation index, fraction of neutrophils, density of vascular profiles and fraction of collagen, four microphotographs were taken using a 40x objective (Olympus Optical Co., Ltd., Tokyo, Japan) (Fig. 1B). The following multilevel sampling was used: four histological sections and stainings were produced from each of the 22 tissue blocks; and three layers in each section (submucosa, muscularis, and subserosa) were photographed separately. This sampling was done in two ROIs (in the anastomosis and outside of the anastomosis) using four micrographs. The total number of micrographs taken and quantified was 2112 (i.e., 22 × 4 × 3 × 2 × 4).

2.3. Stereological quantification

The proliferation index was evaluated as the ratio of Ki67-positive nuclei to all nuclei in the reference area (Fig. 2A). At least 300 nuclei per case were counted when calculating the proliferation index (Nafe et al., 2005). The volume fractions of neutrophils, type I collagen, type III collagen and total collagen were quantified using the stereological point grid and the Cavalieri principle (Fig. 2B, D) (Howard and Reed, 2004; Tonar et al., 2015; extensively tested by Blassova et al., 2019). The number of points hitting the reference area of each case was 204. The fraction was estimated as the ratio of the evaluated structures to the reference area. The two-dimensional density of vascular profiles was evaluated using the unbiased counting frame (Fig. 2C) (Gundersen, 1977). The density was quantified as the number of vascular profiles per reference area. Stereological quantification was performed using Ellipse software (ViDito, Košice, Slovak Republic).

2.4. Statistics

Because some of the datasets did not satisfy the Shapiro–Wilks' normality test, nonparametric methods were used for statistical analyses in the software Statistica Base 11 package (StatSoft, Inc., Tulsa, OK, USA). The Wilcoxon matched pairs test was used to compare the anastomosis vs. outside of the anastomosis areas in paired samples from the same animals (H_0(A) hypothesis). Kruskal-Wallis ANOVA and the post hoc MannꞒWhitney U test were used to compare SI, SID and LID (H_0(B)). Correlations (H_0(C)) were analyzed using the Spearman correlation coefficient. All differences at $p < 0.05$ are reported as significant. It was not necessary to apply the Bonferroni adjustment for multiple tests because we tested, reported, and discussed each of the quantitative parameters separately.

3. Results

All primary morphometric data obtained from the histological quantification are provided in Supplement 1.

3.1. Comparison of anastomotic and outside of anastomotic intestinal sites

All differences between the anastomotic and outside of the anastomosis parts of the small and large intestine are shown in Table 3. For better visualization, the data are also presented graphically in Supplement 2. The anastomosis site had a greater proliferation index in the submucosa (Wilcoxon matched pairs test $p < 0.01$, Suppl. 2A) and the subserosa ($p < 0.05$, Suppl. 2A), density of vascular profiles in the submucosa ($p < 0.001$, Suppl. 2C) and the muscular layer ($p < 0.01$, Suppl. 2C), fraction of type I collagen in the muscular layer ($p < 0.05$, Suppl. 2D), type III collagen in the subserosa ($p < 0.05$, Suppl. 2E), total collagen in the muscular layer

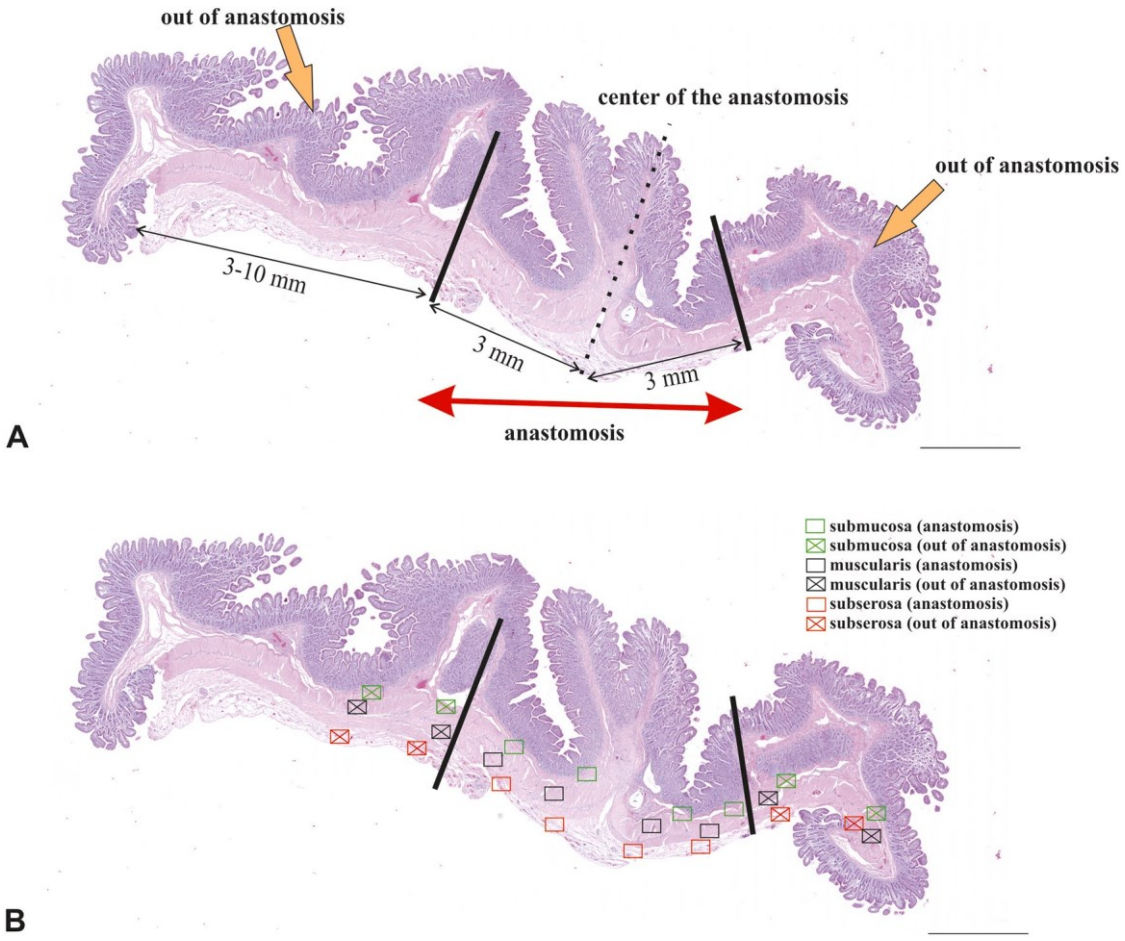

Fig. 1. Division of the intestine into the anastomosis and outside of the anastomosis regions of interest; uniform systematic sampling of the intestinal wall. A - The anastomosis area was defined as the submucosa, muscularis, and subserosa layers of the intestinal wall 3 mm orally and aborally from the center of the anastomosis. The outside of the anastomosis area was the submucosa, muscularis, and subserosa layers of the intestinal wall greater than 3 mm orally and aborally from the center of the anastomosis. B – Four microphotographs were taken separately in the submucosa, muscularis and subserosa within the anastomosis and outside of the anastomosis. Uniform systematic sampling of microphotographs was used. Scale bars, 2000 μm (A, B).

($p < 0.05$, Suppl. 2F) and in the subserosa ($p < 0.05$, Suppl. 2F) compared to outside of the anastomosis.

3.2. Comparison of small intestine without defects, small intestine with defects and large intestine with defects

All differences between SI, SID, and LID in the anastomosis or outside of the anastomosis are shown in Table 4 and Figs. 3–6. For better visualization, the data are also presented graphically in Supplements 3–5.

3.2.1. Anastomosis site

SI had a greater density of vascular profiles in the submucosa (Kruskal-Wallis ANOVA $p < 0.01$) and muscularis ($p < 0.05$) (Suppl. 3C) and a smaller fraction of type III collagen in the submucosa ($p < 0.05$) (Suppl. 3E) compared to SID. SI had a greater density of vascular profiles in the muscularis ($p < 0.01$) (Suppl. 3C) and a smaller fraction of type III collagen (Suppl. 3E) and total collagen (Suppl. 3F) in the submucosa ($p < 0.01$) and the subserosa ($p < 0.01$) than LID. LID had a greater proliferation index in the submucosa ($p < 0.01$) (Suppl. 3A), density of vascular profiles in the submucosa ($p < 0.01$) (Suppl. 3C) and fractions of type I collagen (Suppl. 3D) and total collagen (Suppl. 3F) in the submucosa ($p < 0.01$) than SID.

3.2.2. Outside of the anastomosis

SI had a smaller proliferation index in the subserosa ($p < 0.01$) (Suppl. 4A), fraction of type III collagen in the submucosa ($p < 0.05$) (Suppl. 4E) and a greater fraction of type I collagen in the muscularis ($p < 0.05$) (Suppl. 4D) than SID. SI had a greater density of vascular profiles in the muscularis ($p < 0.01$) (Suppl. 4C) and a smaller fraction of type III collagen (Suppl. 4E) and total collagen (Suppl. 4F) in the submucosa ($p < 0.05$) and the subserosa ($p < 0.01$) than LID. LID had a smaller fraction of neutrophils in the submucosa ($p < 0.05$) and the muscularis ($p < 0.05$) (Suppl. 4B) and a greater fraction of type I collagen in the muscularis ($p < 0.05$) (Suppl. 4D) compared to SID.

3.3. Correlation patterns

All correlations are in three datasheets provided in Supplement 6 separately for SI, SID, and LID and calculated separately for the anastomosis ROI and outside of the anastomosis ROI.

The correlation patterns between the anastomosis ROI and outside of the anastomosis ROI did not overlap in the SI, except for the similar relationship of dominating type I collagen and the total collagen in the subserosa. The correlation patterns found in the anastomosis ROI in SID overlapped in 14 correlations with outside of the anastomosis ROI. The correlation patterns found in the anastomosis ROI overlapped in 6 correlations with outside of the

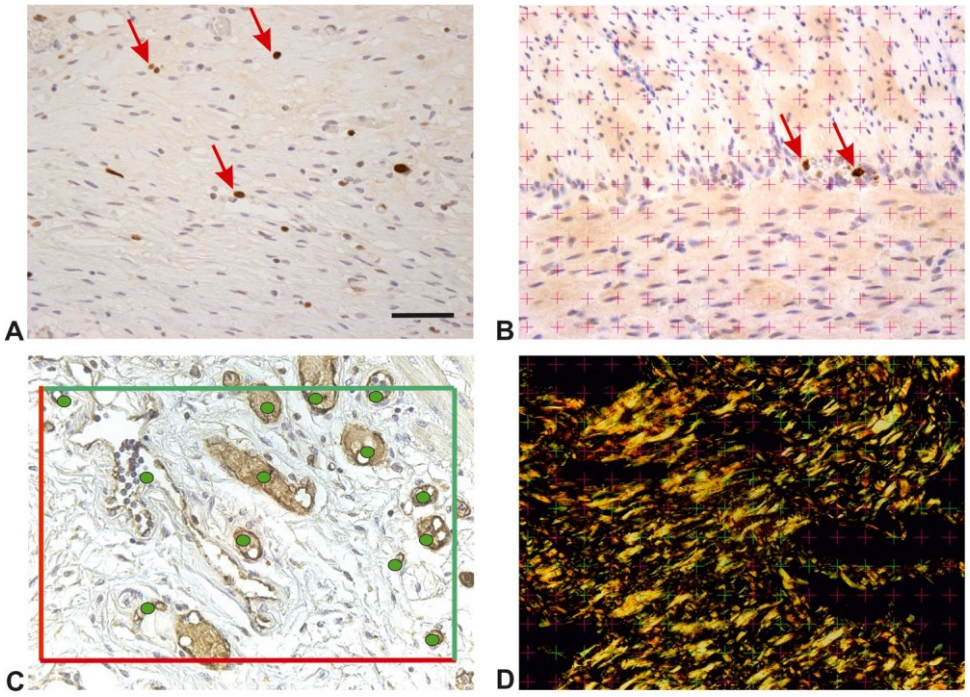

Fig. 2. Quantification of the microscopic structure of the intestinal wall. A – The proliferation index was evaluated as the ratio of Ki67-positive nuclei (brown color, red arrows) to all nuclei in the reference area. B – The fractions of myeloperoxidase-positive cells were evaluated using the stereological point grid and the Cavalieri principle. C – Two-dimensional density of vascular profiles was evaluated using the unbiased counting frame. D – The fractions of type I collagen (yellow–red color), type III collagen (green color) and total collagen were evaluated using the stereological point grid and the Cavalieri principle. Scale bar 50 μm (A-D).

anastomosis ROI in LID. All of these overlapping correlations were related to the fraction of collagens.

4. Discussion

4.1. Proliferation, vascularity, and collagen, but not neutrophils, were more highly expressed in the anastomosis than outside of the anastomosis region

The anastomotic region showed increased proliferation compared to outside of the anastomosis region (Suppl. 2A), which is similar to Grommes et al. (2012). Neutrophilic infiltration (Suppl. 2B) was comparable in all intestine layers within and outside of the anastomosis regions. Rosendorf et al. (2021a, 2021b) also did not find any signs of increased inflammation in the intestinal anastomosis. Our findings suggest that the inflammatory phase of anastomosis healing was complete in the small and large intestines 21 days after surgery. The anastomosis had a greater fraction of collagen (Suppl. 2D–F) in the muscularis and subserosa than outside of the anastomosis region, which suggests that the increased mitotic activity in these layers was accompanied by increase in matrix synthesis.

4.2. The presence of defects matters. Large and small intestine were not interchangeable in experiments

The presence of defects within the small (Table 4A) or the large intestine (Table 4B) was accompanied by decreased vascularity in the submucosa and the muscularis within the anastomosis after 21 days. Similarly, less mature type III collagen prevailed within the submucosa in the anastomoses with defects compared to the anastomoses without defects. These findings may explain the observation by Rosendorf et al. (2021a, 2021b), who reported that porcine intestinal anastomoses without additional standardized defects healed rapidly without any complications, which decreased their experimental value as models for human anastomoses. Additional defects had to be produced to make the healing more realistic and translational for human medicine. Our results suggest that the decreased vascularity and delayed maturation of collagen due to the presence of defects played a major role.

Table 3
Differences between the anastomosis and outside of the anastomosis of the small and large intestine. The anastomotic site had a greater proliferation index in the submucosa (Wilcoxon matched pairs test $p < 0.01$) and subserosa ($p < 0.05$) than outside of the anastomosis. The anastomotic site had a higher density of vascular profiles in the submucosa ($p < 0.001$) and muscular layer ($p < 0.01$). The volume fractions of type I collagen in the muscularis ($p < 0.05$), type III collagen in the subserosa ($p < 0.05$), total collagen in the muscularis ($p < 0.05$) and total collagen in the subserosa ($p < 0.05$) were also greater in the anastomotic site than outside of the anastomosis site. The p values of the Wilcoxon matched pairs tests are shown as * for $p < 0.05$, ** for $p < 0.01$, *** for $p < 0.001$, not statistically significant (n.s.) for $p > 0.05$. ANAS = anastomotic site, OUT ANAS = outside of the anastomosis.

Histological parameter	Submucosa	Muscularis	Subserosa
Proliferation index	ANAS > OUT ANAS ** (p = 0.004)	n.s.	ANAS > OUT ANAS *(p = 0.050)
Neutrophils	n.s.	n.s.	n.s.
Vascular profiles	ANAS > OUT ANAS ***(p = 0.0004)	ANAS > OUT ANAS ** (p = 0.005)	n.s.
Type I collagen	n.s.	ANAS > OUT ANAS *(p = 0.014)	n.s.
Type III collagen	n.s.	n.s.	ANAS > OUT ANAS *(p = 0.010)
Total collagen	n.s.	ANAS > OUT ANAS *(p = 0.014)	ANAS > OUT ANAS *(p = 0.046)

Table 4
Differences between small intestine without defect (SI), small intestine with defect (SID) and large intestine with defect (LID) within the anastomosis and outside of the anastomosis. A – SI had a greater density of vascular profiles in the submucosa (Kruskal-Wallis ANOVA $p < 0.01$) and muscularis ($p < 0.05$) and a smaller fraction of type III collagen in the submucosa ($p < 0.05$) in anastomosis compared to SID. SI had a smaller proliferation index in the subserosa ($p < 0.01$) and fraction of type III collagen in the submucosa ($p < 0.05$) and a greater fraction of type I collagen in the muscularis ($p < 0.05$) outside of the anastomosis than SID. B – SI had a greater density of vascular profiles in the muscularis ($p < 0.01$) and smaller fractions of type III collagen and total collagen in the submucosa ($p < 0.01$) and subserosa ($p < 0.01$) within the anastomosis and outside of the anastomosis compared to LID. C – LID had a greater proliferation index in the submucosa ($p < 0.01$), density of vascular profiles in the submucosa ($p < 0.01$) and fractions of type I collagen and total collagen in the submucosa ($p < 0.01$) in the anastomosis than SID. LID had a smaller fraction of neutrophils in the submucosa and muscularis and a greater fraction of type I collagen in the muscularis ($p < 0.05$) than SID. The p values of the Kruskal-Wallis ANOVA are shown as * for $p < 0.05$, ** for $p < 0.01$, *** for $p < 0.001$, not statistically significant (n.s.) for $p > 0.05$.

A. Small intestine without defect (SI) VS. Small intestine with defect (SID)

	Anastomosis			Outside of the anastomosis		
	Submucosa	**Muscularis**	**Subserosa**	**Submucosa**	**Muscularis**	**Subserosa**
Proliferation index	n.s	n.s	n.s	n.s	n.s	SI < SID *(p = 0.032)
Neutrophils	n.s	n.s	n.s	n.s	n.s	n.s
Vascular profiles	SI > SID *(p = 0.009)	SI > SID ** (p = 0.0015)	n.s	n.s	n.s	n.s
Type I collagen	n.s	n.s	n.s	n.s	SI > SID ** (p = 0.0046)	n.s
Type III collagen	SI < SID ** (p = 0.005)	n.s	n.s	SI < SID ** (p = 0.0014)	n.s	n.s
Total collagen	n.s	n.s	n.s	n.s	n.s	n.s

B. Small intestine without defect (SI) VS. Large intestine with defect (LID)

	Anastomosis			Outside of the anastomosis		
	Submucosa	**Muscularis**	**Subserosa**	**Submucosa**	**Muscularis**	**Subserosa**
Proliferation index	n.s	n.s	n.s	n.s	n.s	n.s
Neutrophils	n.s	n.s	n.s	n.s	n.s	n.s
Vascular profiles	n.s	SI > LID *(p = 0.011)	n.s	n.s	SI > LID *(p = 0.041)	n.s
Type I collagen	n.s	n.s	n.s	n.s	n.s	n.s
Type III collagen	SI < LID *(p = 0.007)	n.s	SI < LID *(p = 0.021)	SI < LID ** (p = 0.002)	n.s	SI < LID *(p = 0.025)
Total collagen	SI < LID *(p = 0.041)	n.s	SI < LID *(p = 0.041)	SI < LID ** (p = 0.002)	n.s	SI < LID *(p = 0.041)

C. Small intestine with defect (SID) vs. Large intestine with defect (LID)

	Anastomosis			Outside of the anastomosis		
	Submucosa	**Muscularis**	**Subserosa**	**Submucosa**	**Muscularis**	**Subserosa**
Proliferation index	SID < LID *(p = 0.032)	n.s	n.s	n.s	n.s	n.s
Neutrophils	n.s.	n.s	n.s	SID > LID *(p = 0.020)	SID > LID *(p = 0.021)	n.s
Vascular profiles	SID < LID *(p = 0.006)	n.s	n.s	n.s	n.s	n.s
Type I collagen	SID < LID *(p = 0.007)	n.s	n.s	n.s	SID < LID ** (p = 0.0046)	n.s
Type III collagen	n.s	n.s	n.s	n.s	n.s	n.s
Total collagen	SID < LID *(p = 0.028)	n.s	n.s	n.s	n.s	n.s

The submucosal healing of the large intestine anastomoses was different than the small intestine anastomoses (Table 4C). The submucosa of the large intestine showed greater proliferation, more vascular profiles, and a greater fraction of type I and total collagen than the small intestine anastomoses. These results suggest that the timing or mechanisms of healing in the small and large intestine are not interchangeable. Our detailed quantification in individual intestinal layers (Supplements 2–4) also revealed that the microscopic picture varied significantly between the layers in proliferation, neutrophilic infiltration, vascularity, and collagen formation.

4.3. Small intestine segments are more affected by their proximity to the anastomosis than large intestine segments

The correlation patterns outside of the anastomosis were different from in the anastomosis in SI without defects (Suppl. 6A). However, the presence of a defect in SID resulted in similar correlation patterns of collagen formation within and outside of the anastomosis (Suppl. 6B). The correlation patterns in SID exceeded the borders of the anastomosis ROI, which suggests that the collagen reparation processes were similar within and outside of the anastomosis. This result indicates that the presence of the defect affected the microscopic composition of the intestine wall beyond the borders of anastomosis, which were set arbitrarily as 3 mm proximally and distally from the anastomosis center. This phenomenon was also found in the large intestine (Suppl. 6C) but to a lesser extent, which suggests that the microscopic composition of the large intestine outside of the anastomosis is less affected by the proximity of the experimental defect. Control samples outside of the anastomosis in the small intestine should be taken further from the anastomosis center than the currently used 3 mm.

4.4. Recommendations and practical implications

The primary data provided in Supplement 1 demonstrate the biological and sampling variability of the histological evaluation. Therefore, the data are suitable and available for subsequent power sample analyses (Chow et al., 2008) to facilitate the calculation of the minimum number of samples when planning experiments of porcine large and small intestine anastomoses.

For studies seeking a rapid evaluation of biomaterials to reinforce intestinal anastomoses or promote healing, fast and robust semi-quantitative histological scoring systems may be the method of choice to measure the outcomes of experimental surgery (Rosendorf et al., 2021a, 2021b). However, a more detailed quantitative histological analysis is advisable for studies of the biological mechanisms of the healing process or studies searching for an explanation of some unusual and surprising findings, as demonstrated in the present paper. Despite the efficiency of stereological methods (Tschanz et al., 2014), quantitative histology is definitely more laborious than semiquantitative scoring. Stereological quantification relies on reproducible and documented sampling of sections and fields of view and requires interactive counting procedures. However, the benefits of stereological quantification include outcomes in the form of continuous variables, which allows for the use of standard statistical procedures.

We found conspicuous differences in the histological picture of individual intestinal layers. Therefore, our results show that it is not advisable to "homogenize" the entire intestine for biological questions related to some of these layers, and the layers should be evaluated separately.

The differences mapped between the quantitative histological parameters, such as proliferation, vascularity, neutrophilic

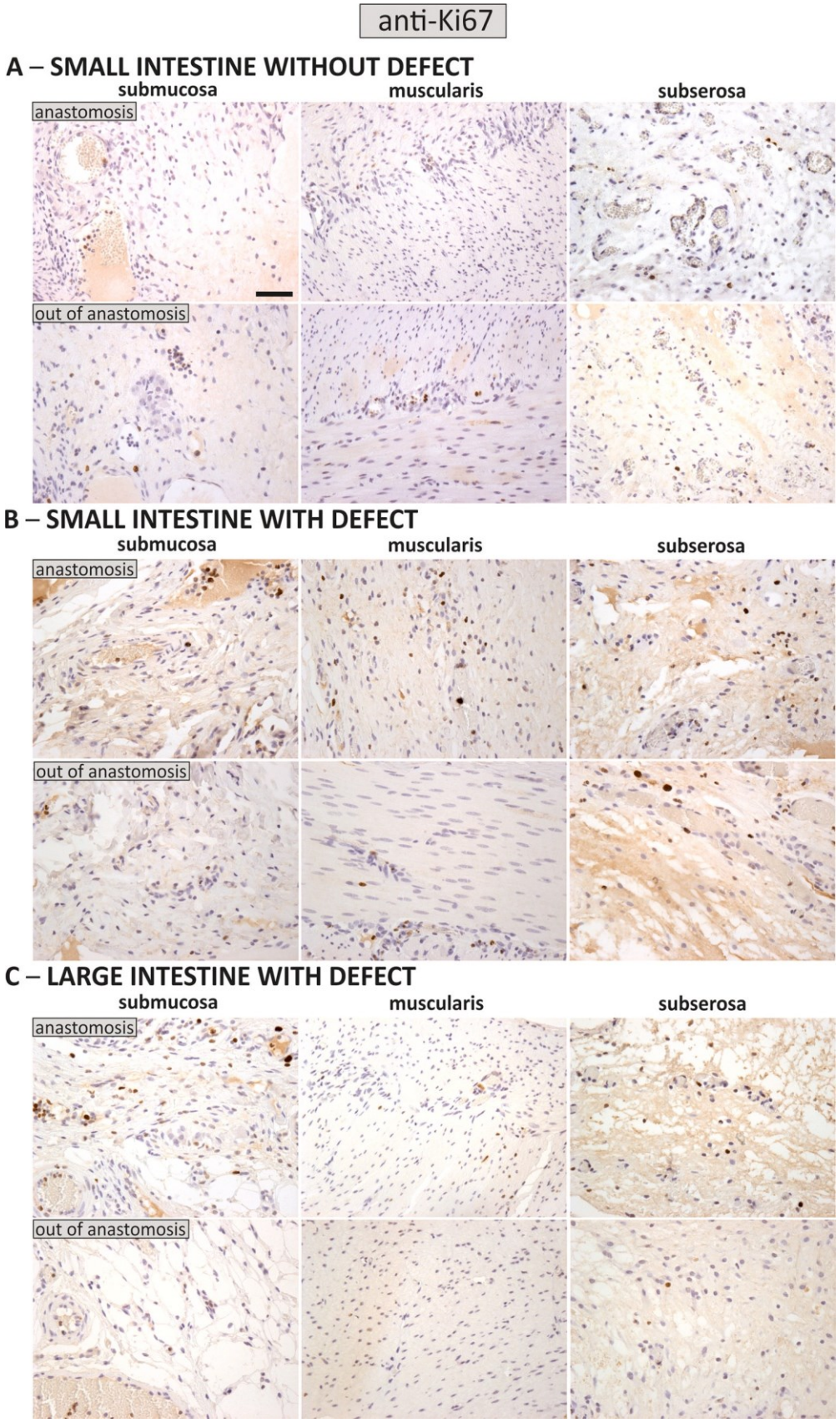

Fig. 3. Differences in proliferation index between small intestine without defect (A), small intestine with defect (B) and large intestine with defect (C) within the anastomosis and outside of the anastomosis. Immunohistochemistry with an anti-Ki67 antibody to evaluate proliferation. Scale bar 50 μm (A-C).

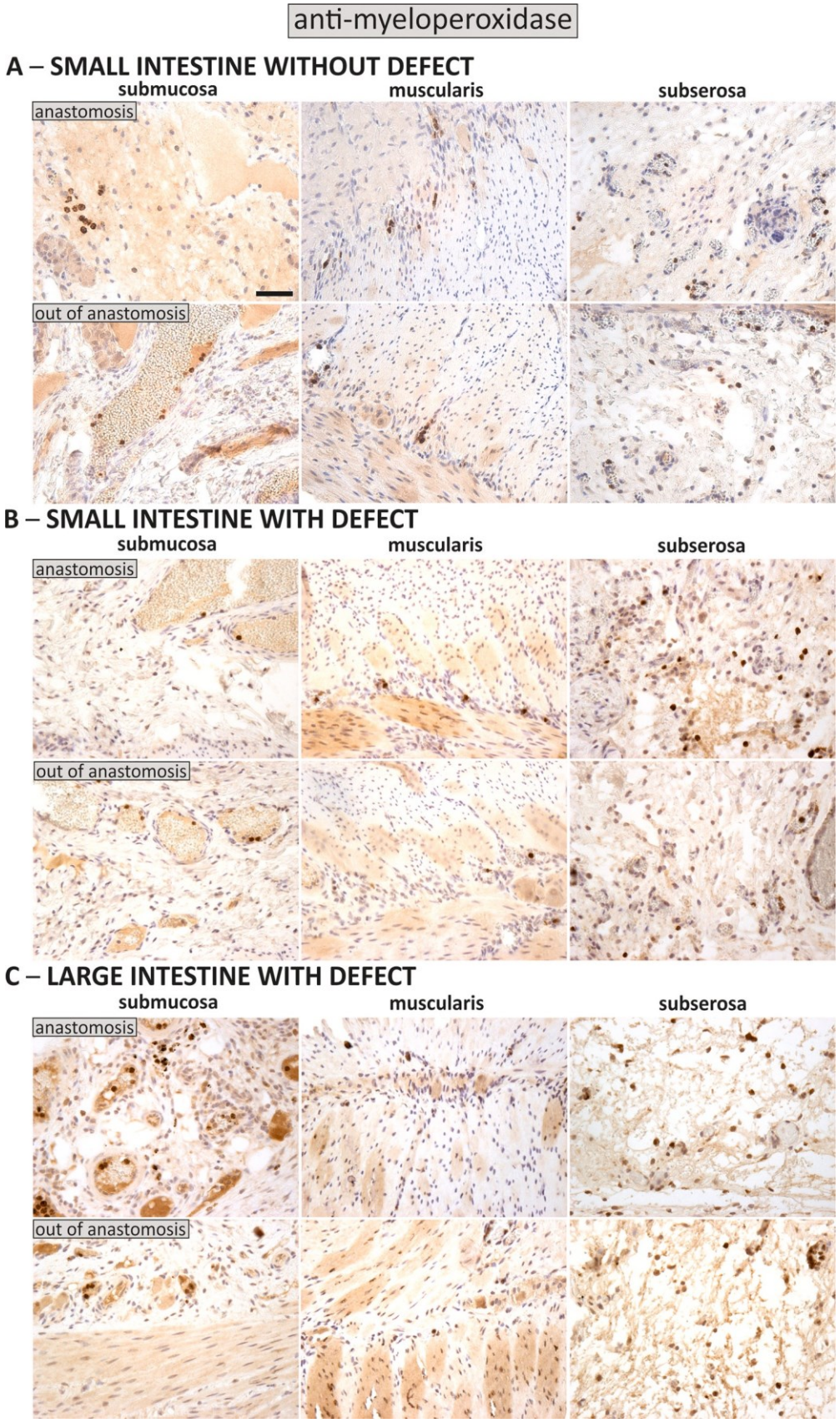

Fig. 4. Differences in neutrophilic infiltration between small intestine without defect (A), small intestine with defect (B) and large intestine with defect (C) within the anastomosis and outside of the anastomosis. Immunohistochemistry with an anti-myeloperoxidase antibody to evaluate neutrophilic infiltration. Scale bar 50 µm (A–C).

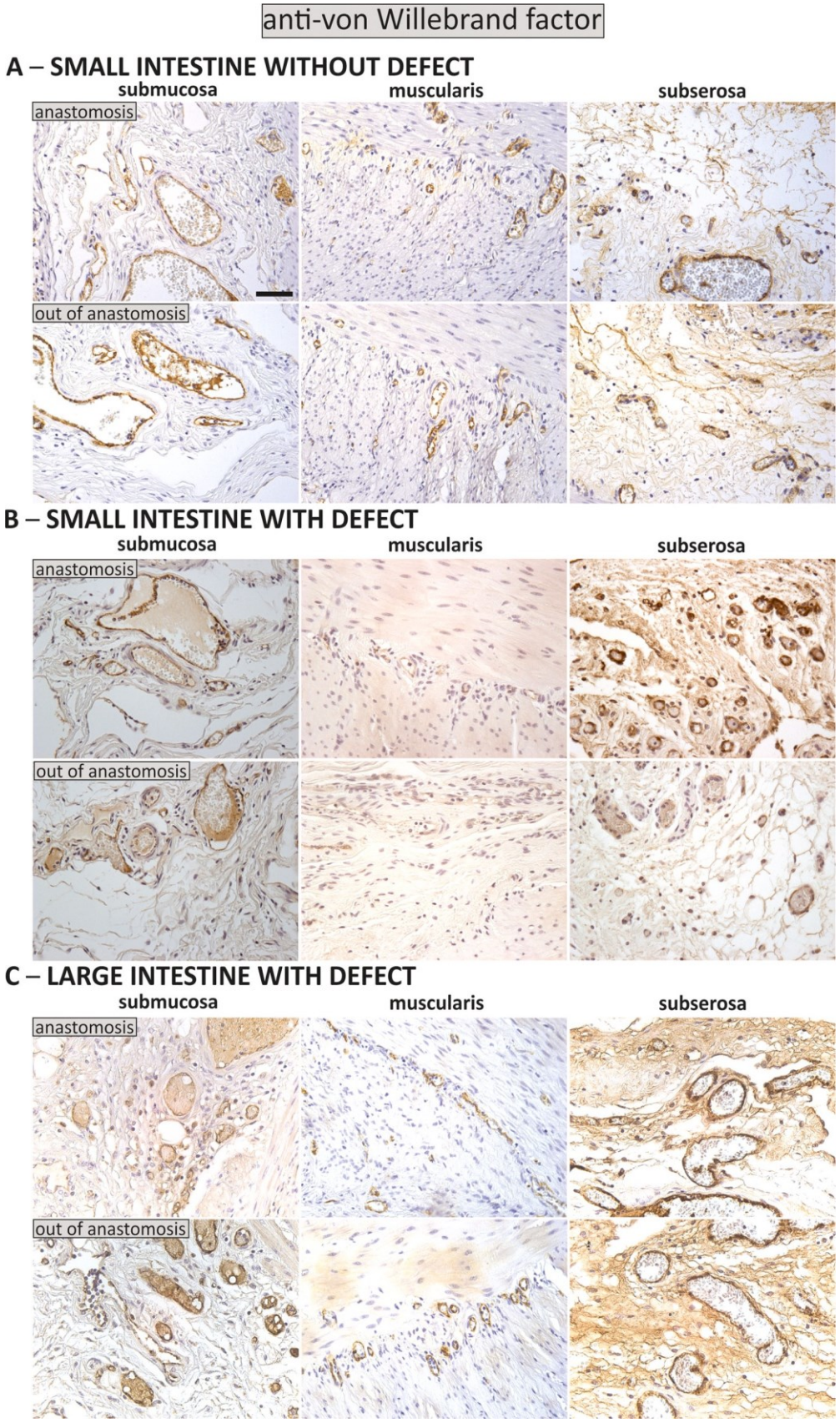

Fig. 5. Differences in vascularity between small intestine without defect (A), small intestine with defect (B) and large intestine with defect (C) within the anastomosis and outside of the anastomosis. Immunohistochemistry with an anti-von Willebrand factor antibody to evaluate vascularity. Scale bar 50 µm (A-C).

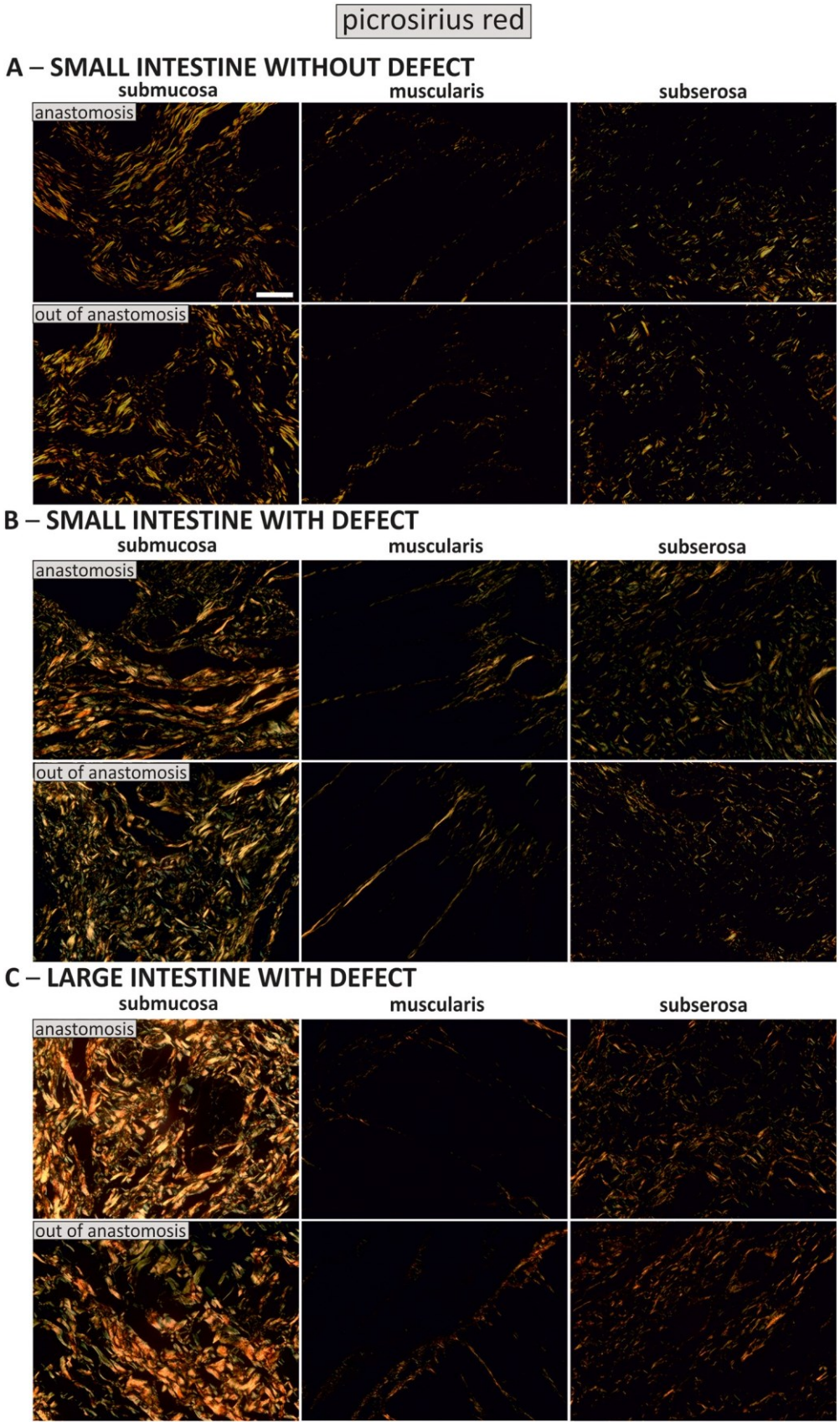

Fig. 6. Differences in the fraction of type I collagen and type III collagen between small intestine without defect (A), small intestine with defect (B) and large intestine with defect (C) within the anastomosis and outside of the anastomosis. Picrosirius red staining to evaluate the fractions of type I collagen (yellow-red color) and type III collagen (green color) and total collagen under polarized light. Scale bar 50 μm (A–C).

infiltration, collagen formation and maturation in the small and large intestines, showed that experiments on porcine small intestine are definitely not interchangeable with the outcomes of experiments in porcine large intestine. Although performing surgery on the small intestine may be technically more feasible for several reasons, such as more mobile intestinal segments due to the mesenteries, a greater length that offers more space for multiple samples per individual, and a smaller risk of contamination than the large intestine, each group of experiments should be evaluated separately to make the outcome more beneficial and realistic for translational medicine.

4.5. Further work and study limitations

To the best of our knowledge, this study is the first study to map the distribution of proliferation, vascularity, neutrophilic infiltration, and collagen formation within the individual layers of porcine SI, SID and LID. However, we are aware of some limitations that must be considered. Although pig is likely the best documented and realistic large animal model for human surgery, healing is generally much faster than typical human patients who need intestinal anastomoses, which often includes oncological and elderly patients with compromised healing (Sparreboom et al., 2018). Moreover, we were able to track down the parameters showing differences between healing of small vs. large intestine. These differences are summarized in Table 4B–C. However, we need to admit that the design of our study does not justify us to draw any conclusions concerning the possible cause of these differences. So far, we can only speculate about factors such as the presence or the absence or intestinal flora, differences in vascular supply resulting in difference leukocyte recruitment, and more.

Further work should include a detailed comparison of proportions (volume fractions and thickness) of individual intestine layers in a porcine model vs. human patients. More histological parameters and markers may be introduced, e.g., mapping of fibroblasts in earlier stages of healing, estimating the fraction of newly formed blood vessels using markers of undifferentiated endothelium, evaluating macrophages, sub-populations of lymphocytes and bacterial contamination in large intestine defects (Belvoncikova et al., 2022). In addition, further work should be focused on changes in the nervous system in the small and large intestine during anastomotic healing, which could help in the study of many intestinal motility disorders such as Hirschrpung's disease (Aggarwal et al., 2002; Klein and Varga, 2020; Kyrklund et al., 2020; Peng et al., 2018; Zhao et al., 2009). Including more time points would improve our knowledge on the healing mechanisms summarized in Table 1 because most previous papers were not based on quantitative histology. The healing process of intestinal anastomoses at different time points using quantitative histology will be examined in our future studies.

5. Conclusions

Quantitative histological evaluation of proliferation, neutrophilic infiltration, vascularity, and collagen formation in 22 samples of porcine small and large intestinal anastomoses revealed the following results. i) Proliferation, vascularity, and collagen, but not neutrophils, were more highly expressed within the anastomosis than outside of the anastomosis region. ii) Porcine large and small intestine were not interchangeable based on histological evaluations of surgical experiments. The presence or absence of an additional experimental defect strongly affected the healing, but the healing seemed complete after 21 days. iii) The microscopic structure of small intestine segments was more affected by proximity to the anastomosis than the structure of large intestine segments.

Histological quantification was more laborious than the semi-quantitative scoring system evaluating the healing rate of intestinal anastomoses, but it provided more detailed maps of biological processes within individual intestine layers. The primary data collected in the present study are available for power sample analyses to calculate the minimum numbers of samples in future experiments on porcine intestines. Experimental studies on large animals are the only option for investigating the anastomotic healing process in the digestive tract, which is surrounded by many unanswered questions. Further studies will provide new methods of targeted prevention and treatment of anastomotic complications based on knowledge of the pathophysiological mechanisms of healing.

Declaration of Competing Interest

The authors declare that they have no known competing financial interests or personal relationships that could have appeared to influence the work reported in this paper.

Acknowledgments

The study was supported by the Charles University Cooperatio Program, research area MED/DIAG. It was also supported by the Project No. NU20J-08-00009, Prevention of intestinal anastomotic leakage and postoperative adhesions using nanofibrous biodegradable materials awarded by The Ministry of Health, Czech Republic. M.G. and A.M. were also supported by Charles University Research Project No. SVV 260 536. T.K. was supported by Charles University Research Project No. SVV 260 651. Skillful technical support from Ms. Jana Dosoudilova and Mr. Jan Javurek is gratefully acknowledged.

Appendix A. Supporting information

Supplementary data associated with this article can be found in the online version at doi:10.1016/j.aanat.2023.152095.

References

Aggarwal, S.K., Yadav, S., Goel, D., Sengar, M., 2002. Combined abdominal and posterior sagittal approach for redo pull-through operation in Hirschsprung's disease. J. Pediatr. Surg. 37, 1156–1159. https://doi.org/10.1053/jpsu.2002.34462

Aznan, M.I., Khan, O.H., Unar, A.O., Tuan Sharif, S.E., Khan, A.H., Syed Abd. Aziz, S.H., Zakaria, A.D., 2016. Effect of Tualang honey on the anastomotic wound healing in large bowel anastomosis in rats-a randomized controlled trial. BMC Complement. Altern. Med. 16, 28. https://doi.org/10.1186/s12906-016-1003-6

Belvoncikova, P., Maronek, M., Gardlik, R., 2022. Gut dysbiosis and fecal microbiota transplantation in autoimmune diseases. Int. J. Mol. Sci. 23, 10729. https://doi.org/10.3390/ijms231810729

Binnebösel, M., Schuler, T., Klink, C.D., Busch, D., Schöb, D.S., von Trotha, K.T., Neumann, U.P., Junge, K., 2014. Influence of CD68+ macrophages and neutrophils on anastomotic healing following laparoscopic sigmoid resection due to diverticulitis. Int. J. Colorectal Dis. 29, 681–688. https://doi.org/10.1007/s00384-014-1855-5

Blassova, T., Tonar, Z., Tomasek, P., Hosek, P., Hollan, I., Treska, V., Molacek, J., 2019. Inflammatory cell infiltrates, hypoxia, vascularization, pentraxin 3 and osteoprotegerin in abdominal aortic aneurysms - a quantitative histological study. PLoS One 14, e0224818. https://doi.org/10.1371/journal.pone.0224818. eCollection 2019.

Blikslager, A.T., Roberts, M.C., Rhoads, J.M., Argenzio, R.A., 1997. Is reperfusion injury an important cause of mucosal damage after porcine intestinal ischemia? Surgery 121, 526–534. https://doi.org/10.1016/s0039-6060(97)90107-0

Boersema, G.S.A., Vennix, S., Wu, Z., Te Lintel Hekkert, M., Duncker, D.-J.G.M., Lam, K.H., Menon, A.G., Kleinrensink, G.-J., Lange, J.F., 2017. Reinforcement of the colon anastomosis with cyanoacrylate glue: a porcine model. J. Surg. Res. 217, 84–91. https://doi.org/10.1016/j.jss.2017.05.001

Bonanomi, G., Prince, J.M., McSteen, F., Schauer, P.R., Hamad, G.G., 2004. Sealing effect of fibrin glue on the healing of gastrointestinal anastomoses: implications for the endoscopic treatment of leaks. Surg. Endosc. 18, 1620–1624. https://doi.org/10.1007/s00464-004-8803-3

Bosmans, J.W., Jongen, A.C., Bouvy, N.D., Derikx, J.P., 2015. Colorectal anastomotic healing: why the biological processes that lead to anastomotic leakage should be revealed prior to conducting intervention studies. BMC Gastroenterol. 15, 180. https://doi.org/10.1186/s12876-015-0410-3

Bosmans, J.W., Jongen, A.C., Birchenough, G.M., Nyström, E.E., Gijbels, M.J., Derikx, J.P., Bouvy, N.D., Hansson, G.C., 2017a. Functional mucous layer and healing of proximal colonic anastomoses in an experimental model. Br. J. Surg. 104, 619–630. https://doi.org/10.1002/bjs.10456

Bosmans, J.W., Jongen, A.C., Boonen, B.T., van Rijn, S., Scognamiglio, F., Stucchi, L., Gijbels, M.J., Marsich, E., Bouvy, N.D., 2017b. Comparison of three different application routes of butyrate to improve colonic anastomotic strength in rats. Int. J. Colorectal Dis. 32, 305–313. https://doi.org/10.1007/s00384-016-2718-z

Bosmans, J.W.A.M., Moossdorff, M., Al-Taher, M., van Beek, L., Derikx, J.P.M., Bouvy, N.D., 2016. International consensus statement regarding the use of animal models for research on anastomoses in the lower gastrointestinal tract. Int. J. Colorectal Dis. 31, 1021–1030. https://doi.org/10.1007/s00384-016-2550-5

Braskén, P., 1991. Healing of experimental colon anastomosis. Eur. J. Surg. 1–51.

Brunicardi, F., Andersen, D., Biliar, T., Dunn, D., Hunter, J., Matthews, J., Pollock, R., 2015. Schwartz's Principles of Surgery, 10th Ed. ⟨https://accessmedicine.mhmedical.com/book.aspx?bookID=2576⟩ (Accessed 21 November 2022).

Chow, S.C., Wang, H., Shao, J., 2008. Sample Size Calculations in Clinical Research, Second ed. Chapman & Hall/CRC Biostatistics Series, Boca Raton.

Clark, R.A., 1989. Wound repair. Curr. Opin. Cell Biol. 1, 1000–1008. https://doi.org/10.1016/0955-0674(89)90072-0

Cohn, I., Rives, J.D., 1955. Antibiotic protection of colon anastomoses. Ann. Surg. 141, 707–717. https://doi.org/10.1097/00000658-195505000-00016

Costa, M., Keightley, L.J., Hibberd, T.J., Wiklendt, L., Dinning, P.G., Brookes, S.J., Spencer, N.J., 2021. Motor patterns in the proximal and distal mouse colon which underlie formation and propulsion of feces. Neurogastroenterol. Motil. Off. J. Eur. Gastrointest. Motil. Soc. 33, e14098. https://doi.org/10.1111/nmo.14098

Darby, I., Skalli, O., Gabbiani, G., 1990. Alpha-smooth muscle actin is transiently expressed by myofibroblasts during experimental wound healing. Lab. Invest. 63, 21–29.

Desmoulière, A., Redard, M., Darby, I., Gabbiani, G., 1995. Apoptosis mediates the decrease in cellularity during the transition between granulation tissue and scar. Am. J. Pathol. 146, 56–66.

Dignass, A., Lynch-Devaney, K., Kindon, H., Thim, L., Podolsky, D.K., 1994. Trefoil peptides promote epithelial migration through a transforming growth factor beta-independent pathway. J. Clin. Invest. 94, 376–383. https://doi.org/10.1172/JCI117332

Dovi, J.V., He, L.-K., DiPietro, L.A., 2003. Accelerated wound closure in neutrophil-depleted mice. J. Leukoc. Biol. 73, 448–455. https://doi.org/10.1189/jlb.0802406

Feiken, E., Rømer, J., Eriksen, J., Lund, L.R., 1995. Neutrophils express tumor necrosis factor-alpha during mouse skin wound healing. J. Invest. Dermatol. 105, 120–123. https://doi.org/10.1111/1523-1747.ep12313429

Froidurot, A., Julliand, V., 2022. Cellulolytic bacteria in the large intestine of mammals. Gut Microbes 14, 2031694. https://doi.org/10.1080/19490976.2022.2031694

Grommes, J., Binnebösel, M., Klink, C., von Trotha, K., Schleimer, K., Jacobs, M., Neumann, U., Krones, C., 2012. Comparison of intestinal microcirculation and wound healing in a rat model. J. Invest. Surg.: Off. J. Acad. Surg. Res. 26. https://doi.org/10.3109/08941939.2012.692759

Gundersen, H.J.G., 1977. Notes on the estimation of the numerical density of arbitrary profiles: the edge effect. J. Microsc. 111, 219–223. https://doi.org/10.1111/j.1365-2818.1977.tb00062.x

Hesp, W.L., Hendriks, T., Schillings, P.H., Lubbers, E.J., de Boer, H.H., 1985. Histological features of wound repair: a comparison between experimental ileal and colonic anastomoses. Br. J. Exp. Pathol. 66, 511–518.

Howard, V., Reed, M., 2004. Unbiased Stereology: Three-Dimensional Measurement in Microscopy. Garland Science.

Hussain, M.Z., Ghani, Q.P., Hunt, T.K., 1989. Inhibition of prolyl hydroxylase by poly (ADP-ribose) and phosphoribosyl-AMP. Possible role of ADP-ribosylation in intracellular prolyl hydroxylase regulation. J. Biol. Chem. 264, 7850–7855.

Jensen, J.A., Hunt, T.K., Scheuenstuhl, H., Banda, M.J., 1986. Effect of lactate, pyruvate, and pH on secretion of angiogenesis and mitogenesis factors by macrophages. Lab. Invest. 54, 574–578.

Jongen, A.C., Bosmans, J.W., Kartal, S., Lubbers, T., Sosef, M., Slooter, G.D., Stoot, J.H., van Schooten, F.J., Bouvy, N.D., Derikx, J.P., 2016. Predictive factors for anastomotic leakage after colorectal surgery: study protocol for a prospective observational study (REVEAL Study). JMIR Res. Protoc. 5, e90. https://doi.org/10.2196/resprot.5477

Kivisaari, J., Vihersaari, T., Renvall, S., Niinikoski, J., 1975. Energy metabolism of experimental wounds at various oxygen environments. Ann. Surg. 181, 823–828.

Klein, M., Varga, I., 2020. Hirschsprung's disease—recent understanding of embryonic aspects, etiopathogenesis and future treatment avenues. Medicine 56, 611. https://doi.org/10.3390/medicina56110611

Kolinko, Y., Malečková, A., Kochová, P., Grajciarová, M., Blassová, T., Kural, T., Trailin, A., Červenková, L., Havránková, J., Vištejnová, L., Tonarová, P., Moulisová, V., Jiřík, M., Zavaďáková, A., Tichánek, F., Liška, V., Králíčková, M., Witter, K., Tonar, Z., 2021. Using virtual microscopy for the development of sampling strategies in quantitative histology and design-based stereology. Anat. Histol. Embryol. https://doi.org/10.1111/ahe.12765

Kosmidis, C., Efthimiadis, C., Anthimidis, G., Basdanis, G., Apostolidis, S., Hytiroglou, P., Vasiliadou, K., Prousalidis, J., Fahantidis, E., 2011. Myofibroblasts and colonic anastomosis healing in Wistar rats. BMC Surg. 11, 6. https://doi.org/10.1186/1471-2482-11-6

Kralovic, M., Vjaclovsky, M., Tonar, Z., Grajciarova, M., Lorenzova, J., Otahal, M., Necas, A., Hoch, J., Amler, E., 2022. Nanofiber fractionalization stimulates healing of large intestine anastomoses in rabbits. IJN 17, 6335–6345. https://doi.org/10.2147/IJN.S364888

Krarup, P.-M., Eld, M., Heinemeier, K., Jorgensen, L.N., Hansen, M.B., Ågren, M.S., 2013. Expression and inhibition of matrix metalloproteinase (MMP)-8, MMP-9 and MMP-12 in early colonic anastomotic repair. Int. J. Colorectal Dis. 28, 1151–1159. https://doi.org/10.1007/s00384-013-1697-6

Krarup, P.-M., Eld, M., Jorgensen, L.N., Hansen, M.B., Ågren, M.S., 2017. Selective matrix metalloproteinase inhibition increases breaking strength and reduces anastomotic leakage in experimentally obstructed colon. Int. J. Colorectal Dis. 32, 1277–1284. https://doi.org/10.1007/s00384-017-2857-x

Kyrklund, K., Sloots, C.E.J., de Blaauw, I., Bjørnland, K., Rolle, U., Cavalieri, D., Francalanci, P., Fusaro, F., Lemli, A., Schwarzer, N., Fascetti-Leon, F., Thapar, N., Johansen, L.S., Berrebi, D., Hugot, J.-P., Crétolle, C., Brooks, A.S., Hofstra, R.M., Wester, T., Pakarinen, M.P., 2020. ERNICA guidelines for the management of rectosigmoid Hirschsprung's disease. Orphanet J. Rare Dis. 15, 164. https://doi.org/10.1186/s13023-020-01362-3

Lossi, L., D'Angelo, L., De Girolamo, P., Merighi, A., 2016. Anatomical features for an adequate choice of experimental animal model in biomedicine: II. Small laboratory rodents, rabbit, and pig. Ann. Anat. 204, 11–28.

Moore, R., Carlson, S., Madara, J.L., 1989. Villus contraction aids repair of intestinal epithelium after injury. Am. J. Physiol. 257, G274–G283. https://doi.org/10.1152/ajpgi.1989.257.2.G274

Nafe, R., Schlote, W., Schneider, B., 2005. Histomorphometry of tumour cell nuclei in astrocytomas using shape analysis, densitometry and topometric analysis. Neuropathol. Appl. Neurobiol. 31, 34–44. https://doi.org/10.1111/j.1365-2990.2004.00599.x

Nakamura, H., Yokoyama, Y., Uehara, K., Kokuryo, T., Yamaguchi, J., Tsuzuki, T., Nagino, M., 2016. The effects of bevacizumab on intestinal anastomotic healing in rabbits. Surg. Today 46, 1456–1463. https://doi.org/10.1007/s00595-016-1342-4

Nordentoft, T., 2015. Sealing of gastrointestinal anastomoses with fibrin glue coated collagen patch. Dan. Med. J. 62, B5081.

Peng, C.-H., Chen, Y.-J., Pang, W.-B., Zhang, T.-C., Wang, Z.-M., Wu, D.-Y., Wang, K., 2018. STROBE-anastomotic leakage after pull-through procedure for Hirschsprung disease. Medicine 97, e13140. https://doi.org/10.1097/MD.0000000000013140

Reisinger, K.W., Schellekens, D.H., Bosmans, J.W., Boonen, B., Hulsewé, K.W., Sastrowijoto, P., Derikx, J.P., Grootjans, J., Poeze, M., 2017. Cyclooxygenase-2 is essential for colorectal anastomotic healing. Ann. Surg. 265, 547–554. https://doi.org/10.1097/SLA.0000000000001744

Rosendorf, J., Horakova, J., Klicova, M., Palek, R., Cervenkova, L., Kural, T., Hosek, P., Kriz, T., Tegl, V., Moulisova, V., Tonar, Z., Treska, V., Lukas, D., Liska, V., 2020. Experimental fortification of intestinal anastomoses with nanofibrous materials in a large animal model. Sci. Rep. 10, 1134. https://doi.org/10.1038/s41598-020-58113-4

Rosendorf, J., Klicova, M., Cervenkova, L., Horakova, J., Klapstova, A., Hosek, P., Palek, R., Sevcik, J., Polak, R., Treska, V., Chvojka, J., Liska, V., 2021a. Reinforcement of colonic anastomosis with improved ultrafine nanofibrous patch: experiment on pig. Biomedicines 9, 102. https://doi.org/10.3390/biomedicines9020102

Rosendorf, J., Klicova, M., Cervenkova, L., Palek, R., Horakova, J., Klapstova, A., Hosek, P., Moulisova, V., Bednar, L., Tegl, V., Brzon, O., Tonar, Z., Treska, V., Lukas, D., Liska, V., 2021b. Double-layered nanofibrous patch for prevention of anastomotic leakage and peritoneal adhesions, experimental study. Vivo 35, 731–741. https://doi.org/10.21873/invivo.12314

Rosendorf, J., Klicova, M., Herrmann, I., Anthis, A., Cervenkova, L., Palek, R., Treska, V., Liska, V., 2022. Intestinal anastomotic healing: what do we know about processes behind anastomotic complications. Front. Surg. 9, 904810. https://doi.org/10.3389/fsurg.2022.904810. eCollection 2022.

de Roy van Zuidewijn, D.B., Wobbes, T., Hendriks, T., Klompmakers, A.A., de Boer, H.M., 1986. The effect of antineoplastic agents on the healing of small intestinal anastomoses in the rat. Cancer 58, 62–66. https://doi.org/10.1002/1097-0142(19860701)58:1<62::aid-cncr2820580112>3.0.co;2-x

Shaper, K.R., Savage, F.J., Hembry, R.M., Boulos, P.B., 2001. Regulation of matrix metalloproteinases in a model of colonic wound healing in a rabbit. Dis. Colon. Rectum 44, 1857–1866. https://doi.org/10.1007/BF02234468

Shogan, B.D., Belogortseva, N., Luong, P.M., Zaborin, A., Lax, S., Bethel, C., Ward, M., Muldoon, J.P., Singer, M., An, G., Umanskiy, K., Konda, V., Shakhsheer, B., Luo, J., Klabbers, R., Hancock, L.E., Gilbert, J., Zaborina, O., Alverdy, J.C., 2015. Collagen degradation and MMP9 activation by Enterococcus faecalis contribute to intestinal anastomotic leak. Sci. Transl. Med. 7, 286ra68. https://doi.org/10.1126/scitranslmed.3010658

Sparreboom, C.L., van Groningen, J.T., Lingsma, H.F., Wouters, M.W.J.M., Menon, A.G., Kleinrensink, G.-J., Jeekel, J., Lange, J.F., Dutch ColoRectal Audit group, 2018. Different risk factors for early and late colorectal anastomotic leakage in a nationwide audit. Dis. Colon Rectum 61, 1258–1266. https://doi.org/10.1097/DCR.0000000000001202

Testini, M., Gurrado, A., Portincasa, P., Scacco, S., Marzullo, A., Piccinni, G., Lissidini, G., Greco, L., De Salvia, M.A., Bonfrate, L., Debellis, L., Sardaro, N., Staffieri, F., Carratù, M.R., Crovace, A., 2014. Bovine pericardium patch wrapping intestinal anastomosis improves healing process and prevents leakage in a pig model. PLoS One 9, e86627. https://doi.org/10.1371/journal.pone.0086627

Thornton, F.J., Barbul, A., 1997. Healing in the gastrointestinal tract. Surg. Clin. N. Am. 77, 549–573. https://doi.org/10.1016/s0039-6109(05)70568-5

Tonar, Z., Kochova, P., Cimrman, R., Perktold, J., Witter, K., 2015. Segmental differences in the orientation of smooth muscle cells in the tunica media of porcine aortae. Biomech. Model. Mechanobiol. 14, 315–332. https://doi.org/10.1007/s10237-014-0605-5

Trabold, O., Wagner, S., Wicke, C., Scheuenstuhl, H., Hussain, M., Rosen, N., Seremetiev, A., Becker, H., Hunt, T., 2003. Lactate and oxygen constitute a fundamental regulatory mechanism in wound healing. Wound Repair Regen.: Off. Publ. Wound Heal. Soc. [and] Eur. Tissue Repair Soc. 11, 504–509. https://doi.org/10.1046/j.1524-475X.2003.11621.x

Tschanz, S., Schneider, J.P., Knudsen, L., 2014. Design-based stereology: planning, volumetry and sampling are crucial steps for a successful study. Ann. Anat. 196, 3–11. https://doi.org/10.1016/j.aanat.2013.04.011

Vakalopoulos, K.A., Bosmans, J.W.A.M., van Barneveld, K.W.Y., Vogels, R.R.M., Boersema, G.S.A., Wu, Z., Gijbels, M.J.J., Jeekel, J., Kleinrensink, G.J., Bouvy, N.D., Lange, J.F., 2017. Impact of tissue adhesives on the prevention of anastomotic leakage of colonic anastomoses: an in vivo study. Int. J. Colorectal Dis. 32, 961–965. https://doi.org/10.1007/s00384-017-2834-4

Wu, Z., Vakalopoulos, K.A., Kroese, L.F., Boersema, G.S.A., Kleinrensink, G.J., Jeekel, J., Lange, J.F., 2013. Reducing anastomotic leakage by reinforcement of colorectal anastomosis with cyanoacrylate glue. Eur. Surg. Res. 50, 255–261. https://doi.org/10.1159/000350383

Zhang, Q., Widmer, G., Tzipori, S., 2013. A pig model of the human gastrointestinal tract. Gut Microbes 4, 193–200. https://doi.org/10.4161/gmic.23867

Zhao, L., Cheng, Z., Dhall, D., Doherty, T.M., Frykman, P.K., 2009. A novel corrective pullthrough surgery in a mouse model of Hirschsprung's disease. J. Pediatr. Surg. 44, 759–766. https://doi.org/10.1016/j.jpedsurg.2008.06.006